LEABHARLANN CHOLÁISTE NA TRÍONÓIDE, BAILE ÁTHA CLIATH | TRINITY COLLEGE LIBRARY DUBLIN
Ollscoil Átha Cliath | The University of Dublin

Terms and Conditions of Use of Digitised Theses from Trinity College Library Dublin

Copyright statement

All material supplied by Trinity College Library is protected by copyright (under the Copyright and Related Rights Act, 2000 as amended) and other relevant Intellectual Property Rights. By accessing and using a Digitised Thesis from Trinity College Library you acknowledge that all Intellectual Property Rights in any Works supplied are the sole and exclusive property of the copyright and/or other IPR holder. Specific copyright holders may not be explicitly identified. Use of materials from other sources within a thesis should not be construed as a claim over them.

A non-exclusive, non-transferable licence is hereby granted to those using or reproducing, in whole or in part, the material for valid purposes, providing the copyright owners are acknowledged using the normal conventions. Where specific permission to use material is required, this is identified and such permission must be sought from the copyright holder or agency cited.

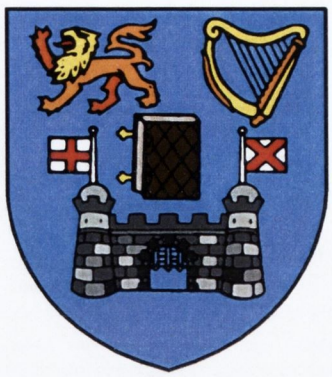
Liability statement

By using a Digitised Thesis, I accept that Trinity College Dublin bears no legal responsibility for the accuracy, legality or comprehensiveness of materials contained within the thesis, and that Trinity College Dublin accepts no liability for indirect, consequential, or incidental, damages or losses arising from use of the thesis for whatever reason. Information located in a thesis may be subject to specific use constraints, details of which may not be explicitly described. It is the responsibility of potential and actual users to be aware of such constraints and to abide by them. By making use of material from a digitised thesis, you accept these copyright and disclaimer provisions. Where it is brought to the attention of Trinity College Library that there may be a breach of copyright or other restraint, it is the policy to withdraw or take down access to a thesis while the issue is being resolved.

Access Agreement

By using a Digitised Thesis from Trinity College Library you are bound by the following Terms & Conditions. Please read them carefully.

I have read and I understand the following statement: All material supplied via a Digitised Thesis from Trinity College Library is protected by copyright and other intellectual property rights, and duplication or sale of all or part of any of a thesis is not permitted, except that material may be duplicated by you for your research use or for educational purposes in electronic or print form providing the copyright owners are acknowledged using the normal conventions. You must obtain permission for any other use. Electronic or print copies may not be offered, whether for sale or otherwise to anyone. This copy has been supplied on the understanding that it is copyright material and that no quotation from the thesis may be published without proper acknowledgement.



Theoretical Studies of Carbon Nanotubes Interacting with Magnetic Atoms.

by

David Kirwan

A Thesis Submitted for the Degree of Doctor of Philosophy

School of Physics

University of Dublin
Trinity College

TRINITY COLLEGE
10 AUG 2009
LIBRARY DUBLIN
THESIS
8815

Declaration

This thesis has not previously been submitted as an exercise for a degree at this or any other University. It is my own work, except where I have specifically referred to published or unpublished work undertaken in collaboration with others. In these cases their contributions have been duly acknowledged in the text.

The library may lend or copy this thesis on request.

Summary

The past twenty years have seen an enormous increase in interest in the properties of low dimensional systems. Carbon nanotubes are an example of one such system. They possess remarkable physical properties which it is hoped could be exploited in a variety of applications. One of the more novel of these lies in the nascent field of spintronics, wherein the superlative electronic properties of nanotubes would be utilised within a magnetic environment. Motivated by these factors, the thesis presents a theoretical study of the properties of nanotubes interacting with randomly distributed transition metal atoms. This is an attempt to replicate the real physical situation in which magnetic catalyst particles, left over from the formation of nanotubes, often remain adsorbed on the surface or occupying defect sites within the tube.

The thesis is divided into two broad and complimentary areas. The first part examines the Indirect exchange coupling (IEC), which dominates the magnetic ordering in systems of particles interacting with a metallic host. The second studies the Magnetoresistance (MR) in these system, in an attempt to see whether the transport properties can be significantly altered by the application of an external magnetic field.

Since the ultimate aim was to treat large quantities of randomly placed impurities, it was necessary to develop a light-weight theoretical description of the system. Such an approach has the added benefit of introducing a degree of physical and mathematical transparency. Green Function methods provide a powerful and flexible technique for treating the presence of disorder by describing the changes to the electronic structure of the host arising from interactions with impurities. In addition, carbon nanotubes are well described within a single band tight-binding picture. Consequently, in the case of pristine armchair and zigzag nanotubes it is possible to develop a set of closed form analytic expressions for the Green Function between any two lattice sites, which greatly expedited many of the calculations performed.

In many low dimensional systems, when ferromagnetic layers are placed in contact with a metallic host a long range magnetic ordering is known to develop between the layers, even at separations where their dipolar interaction should be negligible. This is known as Indirect exchange coupling and is mediated by the presence of de-

localised conduction electrons in the host. In general, as the separation between the impurities is changed the coupling displays two robust characteristics: an oscillation between preferential ferromagnetic/anti-ferromagnetic alignment and an overall long range decay. The decay rate is predicted to decrease with decreasing dimension. Due to their metallicity and low dimensionality, nanotubes present a unique system in which to test the veracity of such predictions. These were examined in the case of pairs of transition metal atoms interacting with a nanotube. In line with the predictions the coupling was seen to exhibit very long range, in general. However, the oscillatory character of the coupling was absent. This was shown to result from a commensurability effect between the momentum of a conduction electron travelling along the tube and the lattice spacing. The application of a small gate voltage was sufficient to break the commensurability – by slightly changing the momentum of the electron – and the oscillations were restored.

The standard theory of IEC predicts that the qualitative features of the coupling are properties of the host metal and independent of the specifics of the impurity or the particular interaction with the host. As a result, for a given non-magnetic metal, the characteristics of IEC coupling are generally very robust. For nanotubes, however, this ubiquity was not observed. Specifically, the rate of decay was found to be highly sensitive to the location of an adsorbed impurity within the host. When placed at the centre of a hexagon of carbon atoms interference effects arise which greatly reduce the range of the coupling. These could easily be identified within the physically transparent framework adopted. Furthermore, these interference effects are characteristics of the honeycomb lattice of graphene and not limited to achiral nanotubes. The standard theoretical approach used to extract the decay rate in indirectly coupled systems was unable to account for the observed short range, and it was therefore necessary to propose a natural extension to this theory.

In the second part of the thesis attention turned to the magneto-transport properties of nanotubes in the presence of large numbers of transition metal atoms. The use of nanotubes in potential spintronic applications is dependent on being able to bring about substantial changes in conductance with the application of an external magnetic field. This is typically measured by the Magnetoresistance (MR). The cases of substitutional and adsorbed impurities were studied. Motivated by the earlier results, the effect of changing the position of the adsorbed impurities within the host was also examined. It was found that the MR could be very large, particularly for substitutional impurities, although the magnitude was seen to depend on the magnetic moment of the individual atomic species. Manganese atoms, which were highly spin-polarised, displayed enormous MR. By contrast, the MR in the case of Nickel doping was substantially smaller. Adsorbed impurities were also capable of displaying large values of MR. However, impurities adsorbed centrally had no effect

on the ballistic character of the conductance through a nanotube. In effect, electrons propagating through the tube were unaware of the presence of the impurities. This could be accounted for by the same interference effect which resulted in such weak coupling when impurities were placed in these positions. This emphasised the link between IEC and MR and the existence of such an effect could have important implications for the development of spintronic devices based on such systems.

Acknowledgements

Studying for a PhD is certainly a major undertaking; far greater than I initially appreciated. For providing assistance along the way, a number of people deserve specific mention.

Firstly, I would like to acknowledge those people I have collaborated with directly: Dr Mauro Ferreira, Dr Claudia Rocha and Dr Antonia Costa. I would particularly like to thank my supervisor Mauro for his considerable help and patience over the past four (...and a half...) years. It is often said that the supervisor sets the tone for the group. If this is true, then I am sincerely grateful to him for providing such a pleasant and convivial working environment.

I also thank our erstwhile postdoc Claudia for all her assistance, both in performing calculations and in explaining the many aspects of transport theory. Thanks as well to Dr Tom Archer and Dr Miguel Oliveira for the great deal of help they provided in matters computational. There are certainly advantages to sharing an office with senior group postdocs. I would also like to acknowledge the contributions of Science Foundation Ireland for funding this little endeavour, as well as the Trinity Centre for High Performance Computing and Stefano Sanvito and his group for providing computational facilities. These may not have been required all that often, but when they were, they were there. My former classmate and fellow *maurite* Dr. Andrew Wall deserves thanks for his help in proofreading part of the thesis. I must not forget to express my gratitude to the remainder of Mauro's students and the wider computational spintronics group, both past and present, primarily for providing participants for the coffee breaks that are so crucial to a physicist's working day.

Finally, on a personal level I would like to thank my parents for all their support and for indulging their son the perpetual student. Perhaps they felt he couldn't remain a student forever. Time will tell, I suppose.

Contents

1 Introduction **1**

1.1 Carbon Nanotubes 1

1.1.1 Structure of Carbon Nanotubes 1

1.1.2 Electronic Properties 3

1.1.3 Additional Physical Properties 5

1.2 Indirect Exchange Coupling 6

1.3 Giant-Magnetoresistance 9

1.4 Nanotubes Based Electronics 10

1.5 Magnetically Doped Nanotubes 11

1.6 Outline of Thesis 12

2 Mathematical tools - Green Function Methods, Dyson's Equation and the Lloyd Formula. **15**

2.1 Introduction 15

2.2 Green Functions 16

2.3 Dyson's Equation 18

2.3.1 Substitutional Atom 20

2.3.2 Adsorbed Atom 22

2.4 Lloyd Formula 23

2.5 Recursive Methods 25

2.5.1 Bulk Green Function Propagators 28

2.6 The Recursive Method applied to Carbon Nanotubes 31

2.6.1 2 Substitutional Impurities 34

2.6.2 Adsorbed Atoms 36

2.7 Summary and Conclusions 39

3 Electronic Structure of Achiral Nanotubes **41**

3.1 Graphene 42

3.2 Nanotubes 44

3.2.1 Poles 46

3.2.2 Armchair Nanotubes 49

3.2.3 Zigzag Nanotubes 51
3.3 Analytic Green Function Propagators for Semi-infinite Tubes 54
3.3.1 Armchairs 54
3.3.2 Zigzags 58
3.4 Summary of Chapter 65

4 Indirect Exchange Coupling on Carbon Nanotubes 67
4.1 Introduction 67
4.2 Direct Exchange and the Hubbard Hamiltonian 68
4.3 Carbon Nanotube Mediated Indirect Exchange 71
4.4 Asymptotic Limit 74
4.5 Results 78
4.5.1 Armchair Nanotubes 78
4.5.2 Zigzag Nanotubes 83
4.5.3 Effect of changing the Exchange Potential, V_x 86
4.6 Summary of Chapter 91

5 Suppression of Indirect Exchange Coupling on Carbon Nanotubes 93
5.1 Ab-initio Results 93
5.2 Failure of the Asymptotic Approximation 93
5.3 Effects of Changing Adatom Location 95
5.3.1 Armchair Nanotubes 97
5.3.2 Zigzag Tubes 99
5.4 Results 102
5.5 Graphene and Chiral Tubes 106
5.6 Symmetry Breaking 110
5.7 Summary and Conclusions 114

6 Transport Properties of Magnetically Doped Carbon Nanotubes 117
6.1 Introduction 117
6.2 Kubo Formula 120
6.3 Monte Carlo Methods 125
6.4 Parameterisation of the Hamiltonian 128
6.5 T-matrix Expansion 132
6.6 Results/Analysis 134
6.6.1 Adsorbed Impurities 134
6.6.2 Substitutional Impurities 142
6.7 Chapter Summary and Conclusions 150

7 Conclusions **153**

7.1 Extensions and Future Work 156

A Differentiation of the Log of an Operator **159**

B Proof that $\mathrm{Tr}(\log(A)) = \log(\det(A))$ **161**

C Imaginary-Axis Integration **163**

D Phase factor $\phi(E)$ **for a Nanotube** **167**

E Expression for the Generalised On-site Green function Propagator **169**

List of Figures

1.1 A graphene lattice with primitive unit vectors given by $\mathbf{a}_1$ and $\mathbf{a}_2$. The hatched box is the primitive unit cell of graphene. The wrapping direction for a (N,N) armchair nanotube is given by the blue line and for a (N,0) zigzag by the red line. In either case the longitudinal axis of the tube, indicated by the hatched lines, lies perpendicular to this direction. 2

1.2 Structure of achiral nanotubes. The top image is of a (6,6) armchair nanotube, the bottom shows a (9,0) zigzag tube. The two cases are distinguished by their transverse cross section. 3

1.3 Real (left) and reciprocal (right) space lattice of graphene. $\mathbf{a}_1$ and $\mathbf{a}_2$ are the graphene primitive lattice vectors with $\mathbf{b}_1$ and $\mathbf{b}_2$ the corresponding reciprocal lattice vectors. The lattices are equivalent under rotation of $\pi/2$ radians. The points comprising the Fermi-Surface of graphene are indicated by the black squares. 3

1.4 A plot of the local density of states for (a) a (5,5) armchair nanotube (b) a (9,0) metallic (black line) and a (7,0) semi-conducting (red line) zigzag nanotube. The energy is given in arbitrary units 4

1.5 Band structure and conductance for (a) a (5,5) armchair nanotube and (b) a (6,0) zigzag nanotube. In each case there are two bands crossing the Fermi-Surface. Including spin degeneracy this gives a total conductance of $4\,e^2/h$. The wavevector k is in units $1/a$, where a is the lattice constant of graphene. 5

1.6 A schematic representation of a magnetic multi-layer, in which 2 ferromagnetic regions are embedded in a metallic host. The blue areas represent ferromagnetic regions consisting of M atomic layers. These layers are separated by D layers of the host metal. 7

1.7 Typical oscillatory behaviour of IEC as a function of spacer separation, D. $J(D)$ is the coupling between the layers, written in terms of arbitrary units. 8

2.1 Schematic representation of a substitutional atom embedded in a host. Here the host is represented as a simple linear chain although this does not involve any loss of generality. 21

2.2 Schematic representation of an adsorbed atom attached to an infinite host. Here the host is represented by a simple linear chain although this involves no loss of generality. 22

2.3 A schematic diagram illustrating the RGF technique. Block 2 is attached to the end of the existing structure which terminates at block 1. In the figure there are four orbitals per block. 26

2.4 Schematic representation of a semi-infinite nanostructure grown recursively. The structure is decomposed into rectangular blocks extending from $-\infty$ and terminating at block 0. The propagator between an element on block i and j is sought. If $i < j$ then the structure is initially grown as far as i, extended to j and finally connected to the $-j$ block structure on the right. If $i > j$ then a finite $-i+1$ block structure is grown from the right. It is then extended as far as j and finally connected to the semi-infinite structure grown from the left, terminating at $j-1$. The dashed lines indicate that the right side structure can also extend to $+\infty$. . . 28

2.5 A finite (4,4) armchair nanotube. The figure shows the nanotube being grown by progressively attaching isolated rings to the existing tube. 31

2.6 Primitive unit cells of (a) an armchair and (b) a zigzag nanotube. N such cells are joined together to form a nanotube ring. 31

2.7 Recursively generated Green Function propagators. (a) is the diagonal propagator for a (6,0) zigzag. The imaginary part is the local density of states. The singularities at $E = \pm\gamma$ are characteristics of (2N,0) tubes. (b) shows a general off-diagonal propagator on a (6,6) armchair nanotube. In this case the lattice sites are located at (r_1, a_1) and $(r_1 + 3, a_1 - 2)$, with r describing the ring and a the intra-ring site. Only the separation is significant. All units are written in terms of the nearest neighbour hopping γ. For clarity, $\eta = 1 \times 10^{-3}$. 33

2.8 A section of an *unwrapped* (2,2) armchair nanotube hosting 2 substitutional impurities. The tube is initially broken into 2 semi-infinite regions and a central 5 ring region containing the impurities. 34

2.9 Centrally located impurities in an armchair nanotube. By convention the impurities are initially attached to the ring immediately to their right. Intra-ring connections are represented by the solid lines, inter-ring connections by dashed lines. There are seen to be two distinct locations for the impurities within each primitive unit cell. 37

3.1 (a) Portion of a graphene lattice. The primitive vectors in the $\mathbf{a_1}$ and $\mathbf{a_2}$ directions are shown. Each cell encloses two atoms, labelled 1 (black) and 2 (white). (b) Fermi-surface of graphene. $\mathbf{b_1}$ and $\mathbf{b_2}$ are the reciprocal lattice vectors of graphene. $\mathbf{b}_A$ and $\mathbf{b}_Z$ are vectors along the direction of quantisation for armchair and zigzag nanotubes respectively 42

3.2 A closed integration contour in the upper half k-space plane. k_i marks the position of a pole of $f(k)$ lying in the UHP. The integrand vanishes along the upper contour. The net contribution to Eq.(3.19) from the left and right contours is zero due to the assumed periodicity of the function. 47

3.3 Real and imaginary parts of the on-site Green Function for a (4,4) armchair nanotube. The solid lines are the analytic results. For comparison the same propagator, generated recursively, is overlaid. The number of points has been reduced to aid the comparison. The agreement is seen to be perfect. 50

3.4 Real and imaginary parts of the off-site Green Function for a (4,4) armchair given by $\Delta\ell = -4,\ \Delta j = 5,\ \Delta s = -1$. The solid lines are the analytic results and the points are the recursive results. The agreement is seen to be perfect. 50

3.5 Real and imaginary parts of an off-site Green Function propagator of a semi-conducting (4,0) tube. The lattice sites are separated by $\Delta\ell = 4,\ \Delta j = 4,\ \Delta s = 0$. The solid lines are the analytic results. Included for comparison are selected points of the same propagator generated recursively. 53

3.6 Real and imaginary parts of an off-site Green Function of a metallic (6,0) tube. The lattice sites are separated by $\Delta\ell = -2,\ \Delta j = 2,\ \Delta s = 0$. The sites lie along the same line of carbon atoms in the tube's transverse direction. The solid lines are the analytic results. For comparison, the recursive results have been overlaid. The predicted bound state at $E = \pm t_0(\gamma)$ is found to be present in both approaches. 53

3.7 Cut plane of graphene. The electronic density vanishes along the green line. The blue square identifies the armchair unit ring (c.f. fig. 2.6) with the intra-ring atoms numbered as shown. 54

3.8 Green Function propagator G(-2, 2; -5, 1), between atom 2 on ring -2 and atom 1 on ring -5 of a semi-infinite (4,4) armchair calculated analytically (solid lines) and recursively (points). 56

3.9 On-site Green Function G(-3,3; -3, 3) of atom 3 on ring -3. The nanotube is a semi-infinite (4,4) armchair. The propagator has been calculated analytically (solid lines) and recursively (points). 57

3.10 Cut plane of graphene. There is no electronic density along the green line. The blue square identifies the zigzag ring, which was introduced in figure 2.6. 58

3.11 Green Function propagator G(-1,1;-5,1), between atom 1 on ring -1 and atom 1 on ring -5 on a (3,0) zigzag, calculated analytically (solid lines) and recursively (points). 60

3.12 Green Function propagator G(0,2;-1,8), between atom 2 on the surface and ring -1, atom 8 on a (4,0) semi-conducting zigzag, calculated analytically (solid lines) and recursively (points). 61

3.13 On-site Green Function propagator G(2,5;2,5) on a (6,0) metallic zigzag. η has been increased to 1×10^{-2} for clarity. The results of both the analytic (solid lines) and recursive (points) calculations are overlaid. Note the presence of bounds states at $E = \pm t_0(\gamma)$. 62

3.14 Surface Green Function propagator G(0,2;0,6) on a (0,6) metallic zigzag. η has been increased to 1×10^{-2} for clarity. Surprisingly the analytic and recursive results are not in agreement. The analytic formula is unable to produce the bound state at $E = 0$. 63

3.15 Surface Green Function propagator G(0,2;0,6) on a (0,6) metallic zigzag. η has been increased to 1×10^{-2} for clarity. The solid lines were generated using the modified expression given by Eq.(3.65). This recovers the agreement between the analytic and recursive results. 65

4.1 An illustration of a quantum well. The system is represented as a simple linear chain. The black atoms belong to the metallic, non-magnetic host. The green atoms are magnetic and conduction electrons are subject to a spin-split potential, V_x, at these sites. 68

4.2 Two possible transition metal atom/nanotube interactions: (a) A (6,6) armchair with 2 adsorbed impurities. In this chapter the impurities are assumed to be located above individual carbon atoms. (b) A (6,6) armchair with 2 impurities occupying substitutional positions within the nanotube. In both cases, the separation between the impurities is D, which is normally measured as an integer number of nanotube rings. 71

4.3 A comparison of the integrand in Eq.(4.18) along the real (left panel) and imaginary (right panel) energy axis. The simulation was performed on a (7,7) armchair with 2 substitutional impurities separated by 50 rings. The energy is given in units of the carbon-carbon hopping energy, $\gamma(t_0)$. 75

4.4 Real (black line/green dots) and imaginary (red line/blue dots) components of $\ln(1+4V_x^2 G^{\uparrow}_{AB} G^{\downarrow}_{BA})$ as a function of D on a $(5,5)$ armchair for 2 different values of E_F. The left panel shows $E_F = 0.0$, the right $E_F = -0.5\,\gamma$, where γ is the carbon-carbon hopping energy. In both cases the integrand is given by the solid lines. The dotted lines are the sum over the Fourier coefficients $m, n = -2, -1, 0, 1, 2$. The only contributions come from $(n, m) = (0, 2), (2, 0), (1, 1)$. The contribution from higher coefficients is negligible. For $E_F = 0.0$, the imaginary part of the integrand is seen to be zero. 78

4.5 Propagating wavevectors for armchair and zigzag nanotubes as a function of the Fermi-Energy: (a) armchair with $E_F = 0$ (b) armchair with $E_F \neq 0$ (c) zigzag with $E_F = 0$ (d) zigzag with $E_F \neq 0$. For armchair nanotubes, changing E_F is seen to break the commensurability between the plus and minus wavevectors. . . 79

4.6 $J(D)$ for a $(5,5)$ armchair with 2 substitutional impurities at $E_F = 0.0$ for cases where the impurities reside on the same sublattice of graphene (black line) and on different sublattices (red line). The inset shows a log-log plot of the coupling. The decay is seen to be $1/D$. The magnitude of the coupling is given in terms of an arbitrary energy unit and the separation in the number of nanotube rings separating the impurities. 79

4.7 $J(D)$ for a $(5,5)$ armchair nanotube with 2 substitutional impurities at $E_F = -0.5\gamma$. The impurities reside on the same sublattice. Coupling is measured in arbitrary units, the separation in number of nanotube rings. The inset is a log-log plot of the coupling. It confirms that the rate of decay is 1/D. 80

4.8 J(D) for a (5,5) armchair with 2 adsorbed impurities. (a) $E_F = 0$. (b) $E_F = -0.5\gamma$. The coupling $J(D)$ is plotted in arbitrary units and D refers to the number of armchair rings separating the impurities. 82

4.9 $J(D)$ for a $(6,0)$ zigzag at $E_F = 0.0$ with two adsorbed impurities. The black line represents the case where the impurities lie on the same sublattice, the red line the case where the impurities lie on different sublattices. The log-log plot shown in the inset confirms that the asymptotic rate of decay is $1/D$. 83

4.10 $J(D)$ for a $(6,0)$ zigzag at $E_F = 0.0$ with two adsorbed impurities. The separation is allowed assume non-integer values (red line), revealing the underlying oscillatory nature of the coupling. The black line shows the coupling with D restricted to integer values. J is measured in arbitrary units. 84

4.11 $J(D)$ for a $(6,0)$ zigzag with two substitutional impurities at $E_F = 0.0$ (black line), $E_F = 0.1\gamma$ (red line), $E_F = 0.2\gamma$ (blue line). Doping the tube reveals the underlying oscillatory character of the coupling. J is measured in arbitrary units, D is the separation in nanotube rings. 85

4.12 $J(D)$ for a $(7,0)$ semi-conducting zigzag with two adsorbed impurities at $E_F = 0.0$ (black line) and $E_F = 0.3\gamma$ (red line). J is measured in arbitrary units and D is the separation in nanotube rings. 85

4.13 $J(D)$ for a (5,5) armchair with two adsorbed impurities at $E_F = 0.0$ for several values of V_x : 0.5γ (black), 1.0γ (red), 1.5γ (green). J is measured in arbitrary units, D is the separation in nanotube rings. 86

4.14 Coupling as a function of V_x on a (6,0) zigzag with two adsorbed impurities at $E_F = 0$. Two limiting regimes are evident: For small V_x the coupling increases quadratically while for large splittings the decoupling decreases quadratically. . . 87

4.15 Coupling on a (6,0) zigzag nanotube with two adsorbed impurities for different values of V_x: Black line $3.5\,\gamma$; red line $4.0\,\gamma$; green line 4.5γ. $E_F = 0.10\gamma$. The effect of changing V_x is merely to scale the oscillation. 88

4.16 Coupling on a (6,0) zigzag nanotube with two adsorbed impurities for different values of V_x. Black line $0.3\,\gamma$; red line $0.4\,\gamma$; green line $0.5\,\gamma$; blue line $1.5\,\gamma$. The Fermi-energy is set at $E_F = 0.10\gamma$. In this regime the phase and shape of the coupling shows some sensitivity to the value of V_x. 89

4.17 Coupling as a function of V_x for two substitutional impurities on a (6,0) zigzag at $E_F = 0.05\gamma$. The impurity separation is 50 layers. 90

4.18 Coupling on a (6,0) zigzag nanotube with two substitutional impurities for different values of V_x at $E_F = 0.05\gamma$. Black line $V_x = 10.0\,\gamma$; red line $20.0\,\gamma$; green line $30.0\,\gamma$; blue line $40.0\,\gamma$. As $V_x \to \infty$ a non sinusoidal profile develops. This results from higher order contributions in $\mathcal{G}_{ab}(D)$ and represents deviations from the predictions of RKKY theory. 91

5.1 Three possible locations for an adatom (green) within a host nanotube: (a) atop a single carbon atom (b) a bridge site between atoms (c) at the centre of a hexagon of carbon atoms. 96

5.2 Two armchair nanotube hexagons separated in the longitudinal direction by $D\,\mathbf{a}_Z$. When impurities are centrally located they interact with host atoms on three adjacent lines of carbon atoms: $-1\,,0\,,1$. The atoms are labelled from 1-6 in a counterclockwise direction. 97

5.3 Two hexagons of carbon atoms belonging to a zigzag nanotube. The hexagons are separated by a distance $|\ell + j|\mathbf{a}_A$, along the tube's longitudinal axis. The carbon atoms are labelled in the graphene basis used in chapter 3. The foremost atom on hexagon A is overlaid with the origin of the underlying graphene sheet. There is no restriction that the circumferential separation must equal zero, as might be concluded from the figure. 100

5.4 Coupling (in arbitrary units) as a function of separation for an armchair nanotube with the impurities placed in the atop (black line) and bridge (red line) positions. The inset is log-log plot of the coupling, confirming its long range character. . . . 102

5.5 Coupling as a function of separation for an armchair nanotube with the impurities placed in the hexagonal position. The inset is a log-log plot which confirms the rapid decay. 103

5.6 Coupling as a function of separation for metallic zigzag nanotube with the impurities placed in the hexagonal position. The inset is a log-log plot which confirms the rapid decay. 103

5.7 2 centrally located impurities in a graphene sheet. Each atom is in contact with 6 lattice atoms, labelled 1,2,...,6 in a counter-clockwise direction. Atom 1 is fixed at the origin of the sheet. The 2 hexagons are displaced by a vector $\mathbf{R} = \ell\mathbf{a}_1 + j\mathbf{a}_2$. 107

5.8 Coupling as a function of D for the case of a centrally placed atom (black line) and the case in which the hopping, t_3, between the impurity and hexagon atom 3 has been changed by 5%. 113

5.9 Log-log plot of coupling as a function of D for the case of centrally located impurities (black line) and the case in which the hopping, t_3, between the impurity and hexagon atom 3 has been changed by 5%. The guide lines show the respective asymptotic decay rates. 114

6.1 A section of a doped (6,6) nanotube. The large atoms represent substitutional impurities randomly distributed about the nanotube. 118

6.2 Illustration of transport through an armchair nanotube. The nanotube extends to infinity in both directions. The armchair unit ring is shown by the hatched box. This contains carbon atoms as well as potentially orbital and spin degrees of freedom. The left overlayer extends from $-\infty$ and terminates between ring 0 and ring 1. The conductance can be calculated by considering current elements crossing this imaginary boundary. 120

6.3 Magnetism at the site of impurity atoms is represented by introducing a spin-split potential. The separation between the bands is given by V_{x}, centred about the dashed line ϵ_a. 128

6.4 A schematic representation of a nanostructure. The system is broken into 3 sections with the central region comprising a series of N, possibly disordered layers. The left and right sections are semi-infinite leads. The central region couples to the leads via the surface layer and the effect of the leads can be incorporated into a self energy term, $\Sigma_{L,R}$, which is equal to the surface Green Function at each of the surfaces. 131

6.5 Conductance and MR vs impurity concentration on a 200 ring long (5,5) armchair. $E_F = 0$. The impurities are in the atop position. Top panel shows the average MR (solid line/circles) and the average MR* (hatched line). The lower panel shows the average conductance with $H > 0$ (red line) and $H = 0$ (blue line). . . . 135

6.6 Conductance vs concentration of impurities on a 200 ring long (5,5) armchair. $E_F = -0.5$eV. The impurities are in the atop position. Top panel shows the average MR (solid line/circles) and the average MR* (hatched line). The lower panel shows the average conductance with $H > 0$ (red line) and $H = 0$ (blue line). 135

6.7 Channel decomposed conductance for the case of $E_F = -0.5\,\text{eV}$. The two solid/circle lines represent the down-down (black line) and up-up (red line) contributions for the case of $H > 0$. When $H = 0$ the conductance channels are allowed to mix. These are shown by the three solid/square lines. The down-down (blue) and up-up (green) components are now approximately equal. Scatterings between the up and down channels (indigo) reduce the conductance. The dotted and hatched lines are visual fittings of the down-down curve (black) and the up-up curve (red) for the case of $H > 0$. 137

6.8 Conductance and MR vs E_F on a 160 ring long (5,5) armchair. The concentration of Mn impurities is 3.33%. The lower panel shows the conductance with $H > 0$ (red line) and $H = 0$ (blue line). The hatched line represents the effect of applying a gate voltage without changing the overall magnetisation. The upper panel shows the E_F dependence of the MR. 138

6.9 Channel decomposed conductance for the case in figure 6.8. The circles represent the down- (black) and up- (red) spin channels with $H > 0$. The squares are for the case with no applied field. The down-down (blue) and up-up (green) channels are degenerate. The violet line is the conductance arising from spin-flip scatterings. The hatched line is half the total conductance with $H > 0$. 138

6.10 (5,5) nanotube with 200 rings. c=1% (40 impurities). Impurities are in the centre position. In the lower panel the red and blue lines show the conductance with $H > 0$ and $H = 0$ respectively. The dashed green line shows the conductance in the aligned configuration on a more densely plotted energy mesh. The upper panel shows MR (solid line/circles) and MR* (hatched line) as a function of E_F. . 140

6.11 Conductance and MR vs concentration, c, for armchair nanotubes doped with substitutional Mn impurities. $E_F = 0$. The nanotube is 200 rings long. For each case the upper panel shows MR (solid line/circles) and MR* (hatched line) and the lower panel shows the average conductance with $H > 0$ (red line) and $H = 0$ (blue line). 142

6.12 Conductance and MR as a function of concentration on a (7,7) armchair nanotube substitutionally doped with Ni impurities. The nanotube is 200 rings long. In the lower panel, the red line shows the conductance in an applied field, the blue line is the conductance with zero field. The upper panel shows MR (solid line/circles) and MR* (hatched line). 143

6.13 Ensemble averaged magnetisation vs concentration for a (7,7) armchair nanotube doped with substitutional Ni (black line) and Mn (red line) impurities 144

6.14 Coupling vs longitudinal separation for substitutional (a) Ni and (b) Mn impurities. In both cases the black line is the coupling when both impurities are placed on the same sublattice of graphene and the red line is for the case when they are placed on different sublattices 144

6.15 Channel decomposed conductance for a (7,7) armchair with substitutionally doped Mn impurities: With $H > 0$, the down-down channel is given by the black line and the up-up channel by the red. The same two channels for $H = 0$ are given respectively by the green and blue lines. The up-down channel (violet line) carries no current. 145

6.16 An example of frustration effects: (a) 3 magnetic moments are placed on the same sublattice and each has a preferential AFM coupling (blue) (b) the preferential AFM coupling is between moments placed on different sublattices. As a result no frustration need occur since the intra-sublattice moments now prefer to adopt a FM alignment (green). 146

6.17 Coupling, $J_{\bullet\bullet}$, as a function of occupation, n. It is possible to identify regions, denoted by n_c, where the ground state will not be frustrated. The positions of Mn and Ni are indicated by the green ellipse and blue square respectively. 147

6.18 Band decomposed conductance vs E_F for a (7,7) armchair doped with 0.8% substitutional Mn impurities. The conductance channels with $H > 0$ are shown by the black and red lines (circles). The three bands corresponding to $H = 0$ are shown by the blue, green and violet lines (squares). 148

6.19 Conductance and MR vs E_F for a (7,7) for the case shown in figure 6.18. The MR (black line) is given in the upper panel. The conductance with $H > 0$ (red line) and $H = 0$ (blue line) are shown in the lower panel. The hatched line is the value of MR*, calculated using the ensemble average conductance. 148

6.20 Conductance as a function of E_F on a (7,7) armchair nanotube substitutionally doped with 0.5% Ni impurities. The nanotube is 199 rings long. The lower panel shows the channel decomposed conductance: black and red lines (circles) for $H > 0$ and green, blue and violet (squares) for $H = 0$. The upper panel shows the total conductance for $H > 0$ (black) and $H = 0$ (red). 149

C.1 Contour of integration. The integrand is assumed to vanish along the semi-circular contour, labelled as 3. The black dots mark the locations of poles of the function in the lower half plane. 163

List of Tables

5.1 Table of coupling values, $\Delta E = E(FM) - E(AFM)$, for two Mn impurities adsorbed on a (4,4) armchair nanotube and two Ni impurities substituted in a (6,0) zigzag tube. The impurities are separated along the tube's longitudinal axis in units of the lattice constant: $a = 2.44\mathring{A}$ for armchairs and $a = 4.23\mathring{A}$ for zigzags. 105

5.2 Decaying exponent, α, as a function of number of interacting cells, n, for the three cases shown in table 5.1. 106

6.1 Table of self consistent parameters. The two transition metal atoms for which values were available are Manganese and substitutionally doped Nickel. $\langle n \rangle_0$ and $\langle m \rangle_0$ are the occupation and magnetisation obtained from *ab-initio* simulations. J is the pairwise coupling between two impurities placed on the tube at a specified distance. $\langle m \rangle$ is the self consistent value of the magnetisation. t is the host/impurity hopping and ϵ_a locates the centre of the exchange split level with respect to the nanotube band centre. 130

6.2 *Ab-initio* results for pairs of Ni and Mn impurities located on different graphene sublattices. In both cases, the switching is seen to induce a change in the sign of the coupling. 147

Chapter 1

Introduction

1.1 Carbon Nanotubes

The discovery of carbon nanotubes has occurred as a result of an increasing ability and desire to manipulate materials on an ever smaller scale. As the size of these materials reach limiting dimensions, their inherent quantum mechanical nature begins to play a significant role. Carbon fibres have long been used in applications, particularly in areas which require strong, light-weight and thermally conductive materials. As synthesis and refinement techniques improved, coarse carbon fibres gave way to ultra-thin strands. At the limit of this process stood hollow tubes of graphene, which were discovered by Iijima in 1991[1]. The initial observation was of a series of co-axially aligned tubes; or what would later be called multi-walled nanotubes (MWNT). These were comprised of cylindrical objects, a single atomic layer thick, with diameter ranging from 4-30 nm and lengths extending up to a micrometer. Not long after, individual, or single-walled nanotubes (SWNT) were successfully isolated[2].

This discovery stimulated an enormous research effort into carbon nanotubes which has continued for almost two decades. This is due, primarily, to their superlative physical properties. Not only are they mechanically robust and light-weight, but they also display uniquely sensitive and tunable electronic properties. Combined with the increased interest in utilising the properties of low dimensional systems, this has created tantalising possibilities for the use of nanotubes in a whole host of applications as diverse as ultra-small electronic devices and bullet proof vests.

1.1.1 Structure of Carbon Nanotubes

The structure of a carbon nanotube is normally described in terms of its underlying graphene lattice. Graphene consists of an infinite plane of carbon atoms arranged in a honeycomb pattern. When individual graphene layers are stacked on top of

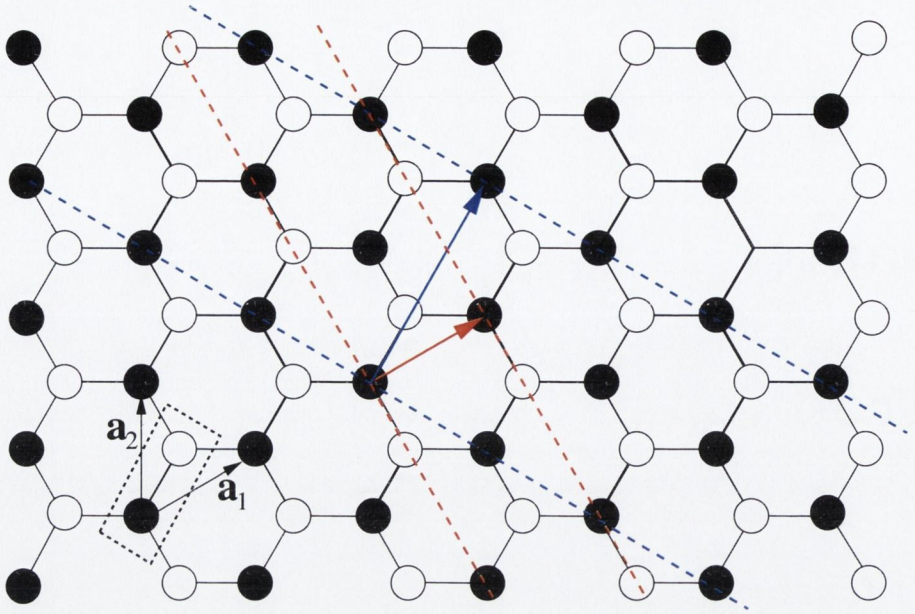


Figure 1.1: A graphene lattice with primitive unit vectors given by $\mathbf{a}_1$ and $\mathbf{a}_2$. The hatched box is the primitive unit cell of graphene. The wrapping direction for a (N,N) armchair nanotube is given by the blue line and for a (N,0) zigzag by the red line. In either case the longitudinal axis of the tube, indicated by the hatched lines, lies perpendicular to this direction.

one another and coupled by weak Van der Walls forces, they form a well known and commonplace material: graphite.

An individual carbon atom has six electrons. Two of these are deep core electrons and the remainder lie in the valence band. When carbon atoms are placed in an aggregate, the electrons can form a variety of bonds which will give rise to different crystalline structures. For graphene (graphite), three of the valence electrons ($2s$, $2p_x$, $2p_y$) form in-plane or σ-bonded sp^2 hybridised orbitals. These are extremely strong covalent bonds which are responsible for the hexagonal structure of the graphene sheet. The remaining p_z (or π-bonded) orbital is oriented out of the plane of the sheet and thus by symmetry cannot couple to the σ-bonded orbitals. A second possibility is that all four valence electrons will form sp^3 hybridised bonds. The material that results from such bonding is diamond.

Figure 1.1 shows the honeycomb lattice of graphene. This can be viewed as a bi-partite lattice consisting of two periodic triangular lattices; or equivalently as a single triangular lattice with two carbon atoms per unit cell. The primitive vectors for the lattice are normally given by $\mathbf{a}_1$ and $\mathbf{a}_2$ and the intra-cell atoms are labelled as 1(black) and 2(white).

A carbon nanotube is derived from graphene by rolling the sheet up in a particular direction. As seen from figure 1.1 there are an infinite number of possible wrapping directions, defined by $\mathbf{C}_h = n\,\mathbf{a}_1 + m\,\mathbf{a}_2$. The integers m and n are the chiral indices and uniquely define each tube. Nanotubes are typically divided into two basic symmetry classes: achiral and chiral. A nanotube is said to be achiral

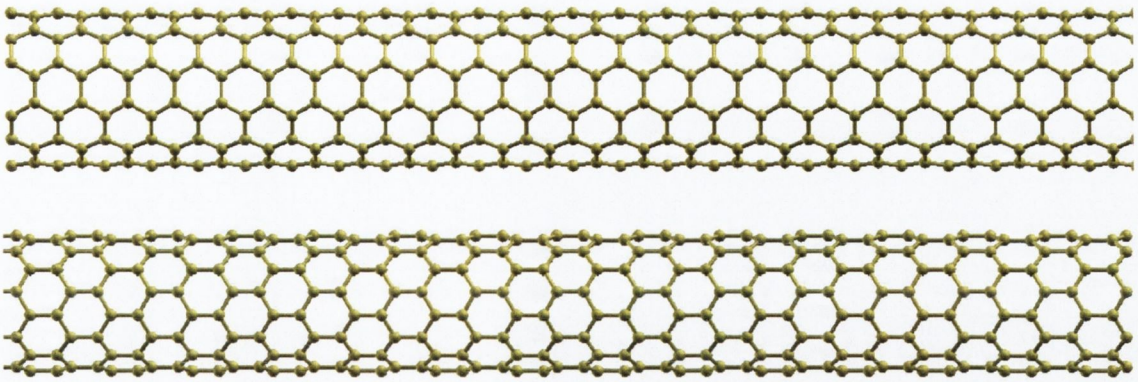


Figure 1.2: Structure of achiral nanotubes. The top image is of a (6,6) armchair nanotube, the bottom shows a (9,0) zigzag tube. The two cases are distinguished by their transverse cross section.

if it displays mirror (or inversion) symmetry. This is only satisfied by nanotubes with chiral indices (m, m) and $(m, 0)$. These are shown in *unwrapped* form in figure 1.1 and are known respectively as armchair and zigzag nanotubes. The names derive from the shape of their respective cross sectional profiles. Figure 1.2 shows the physical or *wrapped* tubes when viewed along their longitudinal axis. For all other pairs of indices the nanotubes display a twisting symmetry and the image cannot be superimposed exactly onto the original structure. These are known collectively as the chiral nanotubes. A consequence of the twisting character is that the unit cell for chiral tubes is typically much larger than for achiral tubes.

1.1.2 Electronic Properties

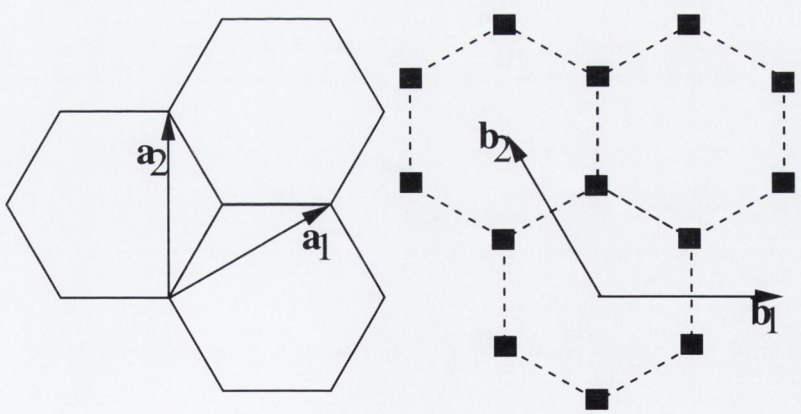
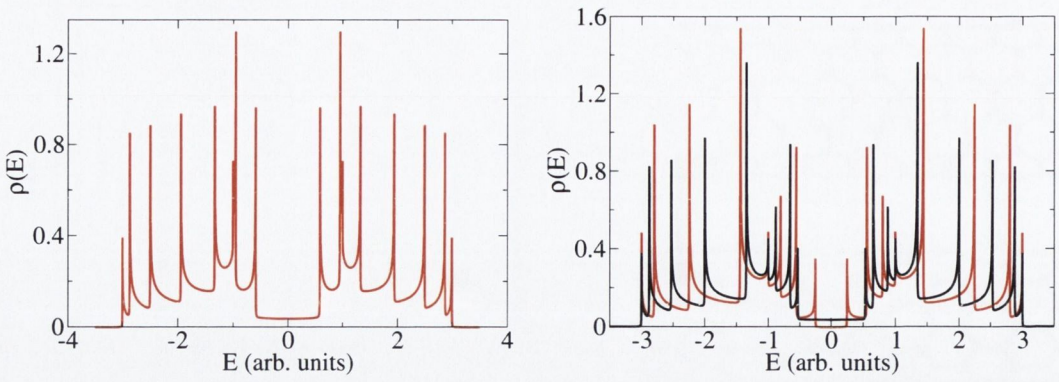


Figure 1.3: Real (left) and reciprocal (right) space lattice of graphene. $\mathbf{a}_1$ and $\mathbf{a}_2$ are the graphene primitive lattice vectors with $\mathbf{b}_1$ and $\mathbf{b}_2$ the corresponding reciprocal lattice vectors. The lattices are equivalent under rotation of $\pi/2$ radians. The points comprising the Fermi-Surface of graphene are indicated by the black squares.

The imposition of the boundary condition in the $\mathbf{C}_h$ direction quantises the momentum component of an electron along the tube's circumferential direction. This reduces the 2-D band structure of graphene to a series of 1-D energy bands.



(a) (b)

Figure 1.4: A plot of the local density of states for (a) a (5,5) armchair nanotube (b) a (9,0) metallic (black line) and a (7,0) semi-conducting (red line) zigzag nanotube. The energy is given in arbitrary units

The decoupling of the σ and π electrons leads to a significant simplification. The σ energy bands are known to lie far from the Fermi-Energy and can often be ignored. By contrast the π bands lie close to the Fermi-Energy. Curvature effects resulting from wrapping the tube will introduce non-zero overlaps between these π orbitals, however, except in cases of very small diameter nanotubes (which are structurally unstable anyhow) these overlaps can normally be neglected.

The quantisation of the allowed momenta leads to an extreme sensitivity of the electronic properties of the nanotube to the wrapping direction. Such sensitivity arises due to the unique character of the Fermi-Surface of graphene, shown in figure 1.3. This is not in fact a surface but rather a series of isolated points located at the vertices of the First Brillouin zone. If one of the quantisation lines intersects the Fermi-Surface then the tube is metallic; otherwise it is semi-conducting. The general condition for observing metallicity is that the difference in the chiral indices, $n - m$, be a multiple of 3. As a result, one third of nanotubes are metallic and two thirds are semi-conducting. For achiral nanotubes: armchairs are always metallic, one third of zigzags are metallic, with two thirds semi-conducting. The focus in this thesis is primarily on achiral nanotubes. This is mainly because their high degree of symmetry means they can be treated in a particularly straightforward and transparent fashion. From the point of view of probing electronic properties this should not be unduly limiting since the achiral tubes are both semi-conducting and metallic. Figure 1.4 shows the density of states for each of these cases. The spikes in the plots are known as Van-Hove singularities. These are the hallmark of a 1-D system and occur at energies where the Fermi-velocity dE/dk vanishes. At the centre of the band there is plateau, the width of which decreases with increasing diameter. The number of states in the plateau is inversely proportional to the diameter of the nanotube.

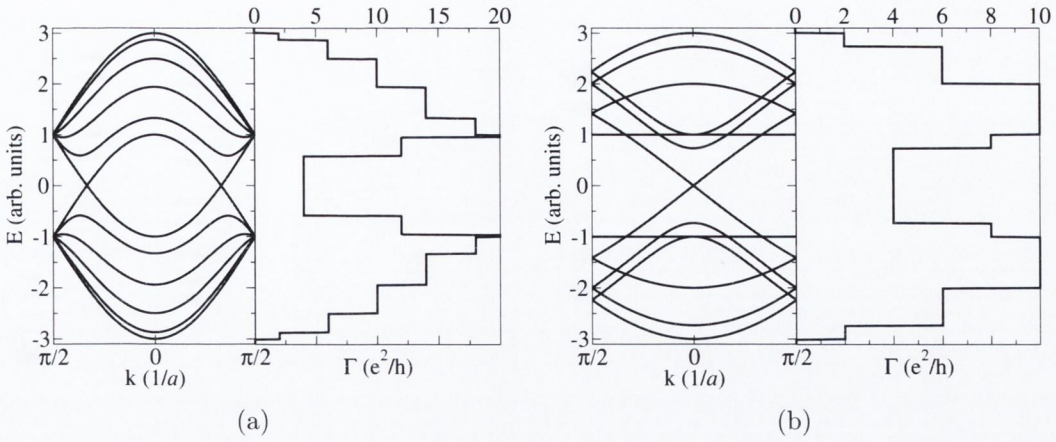


Figure 1.5: Band structure and conductance for (a) a (5,5) armchair nanotube and (b) a (6,0) zigzag nanotube. In each case there are two bands crossing the Fermi-Surface. Including spin degeneracy this gives a total conductance of $4\,e^2/h$. The wavevector k is in units $1/a$, where a is the lattice constant of graphene.

Figure 1.5 shows both the π band structure and the corresponding conductance for an armchair and zigzag nanotube. In chapter 3 the electronic structure of both graphene and carbon nanotubes will be examined in considerable detail. For the moment we note that only two of these bands cross the Fermi-Surface at $E_F = 0$. Since the transport is ballistic, the conductance around this energy is given by $\Gamma = 4\Gamma_0$, where $\Gamma_0 = e^2/h$ is the quantum of conductance. The additional factor of two arises from spin degeneracy. Each time a channel enters (or leaves) the energy window the conductance increases (or drops) by $2\Gamma_0$.

Perhaps the most important property of nanotubes is that they are stable against the Peierls distortion[3], a symmetry breaking effect which normally destroys the metallicity of a 1-D structure. Experiments on the electrical conductivity of single walled nanotubes showed that they behave as quantum wires[4]. In particular, the observed conductance plateaus as a function of the bias voltage demonstrated that the nanotubes were behaving as ballistic conductors[5]. The existence of a such a robust quantum wire offers enormous potential for technological application.

This thesis is concerned exclusively with the electronic properties of nanotubes. However, interest in nanotubes is not limited solely to these. Before concluding this section, we will briefly summarise some of their other properties.

1.1.3 Additional Physical Properties

In addition to their striking electronic properties, nanotubes also display remarkable mechanical properties. The carbon-carbon bond found in a graphene is the strongest occurring in nature. Experiments on ropes of single walled nanotubes predict a Young's Modulus of around 1TPa[6], which is approximately one order of magnitude greater than steel. In addition, nanotubes show remarkable flexibility and tend,

when strained, to buckle or kink rather than break. It was found that nanotubes could be bent reversibly up to a very high angle[7]. Such structural robustness is a desirable trait for components in a host of objects as varied as atomic force microscope tips and next generation liquid crystal displays.

Nanotubes are also expected to exhibit high thermal conductivity due to their stiff sp^2 bonds. Recent experiments on the thermal properties of single walled carbon nanotubes have found a room temperature thermal conductivity of in excess of 2000-3000 W/mK[8][9]. This is comparable with the thermal conductivity of diamond, which is one of the best thermal conductors. The ability to transport heat efficiently is essential to designing modern electronic components and is yet another desirable characteristic possessed by nanotubes.

The 1-D character of semi-conducting nanotubes gives rise to strong optical transitions occurring at frequencies corresponding to the separation of the two Van-Hove singularities closest to the band centre. These are known as E_{11} transitions and result from radiative recombination between electrons and holes. Since the location of the singularities is dependent on the diameter and chirality, fluorescence measurements have been proposed as a technique for characterising nanotubes[10]. The fact that nanotubes can emit light opens up many interesting possibilities for ultra-small photonic devices. Carbon nanotubes have many potential advantages as solid state optical devices: They possess a direct bandgap, so no momentum transfer need accompany any radiative processes. They are also naturally ambipolar, which means that both electrons and holes can be injected into them at the same time. Additionally the confinement of the electrons along the tube forces recombinations to take place, leading to enhanced light emission[11]. The sensitivity of the electronic properties of a nanotube to its chirality and diameter opens the path to the development of tunable, ultra-small optical devices.

1.2 Indirect Exchange Coupling

As a material is reduced in size, to the point that one or more of its dimensions is only a number of atomic layers wide, deviations from bulk behaviour start to become important. These deviations result from quantum mechanical effects. Loosely speaking, these tend to manifest themselves by the introduction of instability, and a general sharpening of features, as a system becomes confined. As an example, we might consider the Van-Hove singularities introduced in the previous section. When the confinement is relaxed, these effects tend to average out and the properties of the bulk material are recovered. As fabrication techniques have improved over the last 20 years, and as the constant drive towards miniaturisation leads to ever smaller devices, it has become possible to approach the dimensions necessary

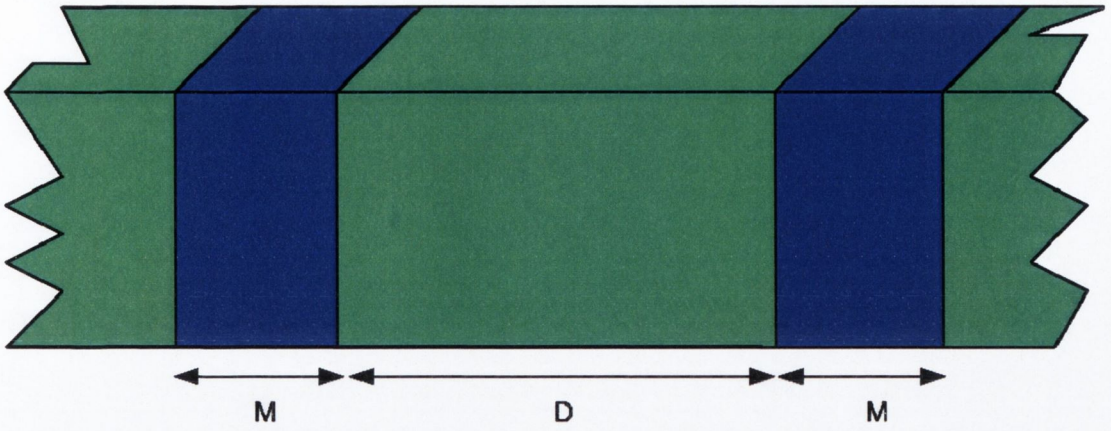


Figure 1.6: A schematic representation of a magnetic multi-layer, in which 2 ferromagnetic regions are embedded in a metallic host. The blue areas represent ferromagnetic regions consisting of M atomic layers. These layers are separated by D layers of the host metal.

to expose these effects. Practically, this presents a number of problems which are normally described as resulting from reaching the fundamental limits of materials and devices. However, these effects also present significant opportunities. An early example of a low dimensional effect that has proved both useful and exploitable is known as Indirect exchange coupling (IEC).

Indirect exchange coupling (alternatively Interlayer exchange coupling) was first discovered in magnetic multi-layered systems. These comprise ultra-thin layers of ferromagnetic materials separated by a metallic host and are schematically illustrated in figure 1.6. The low dimensionality manifests itself both in the extremely thin width of the magnetic layers and the finite separation between them. The initial observation involved a multilayer consisting of two Fe regions separated by a Cr spacer. Quite surprisingly, it was found that the Fe layers coupled anti-ferromagnetically[12]. Subsequent experiments with Fe/Cr and Co/Ru found that the coupling actually oscillated as a function of the width of the spacer material[13]. Remarkably, the oscillation period seemed more or less unaffected by the choice of magnetic layers[14]. The coupling was also observed to decay quite slowly at very low temperatures: as the inverse square of the separation. The typical coupling strengths were far too large to be attributable to dipolar interactions[15]. Figure 1.7 shows the typical behaviour of the IEC as a function of the spacer separation D.

An explanation for the effect was provided by Edwards[16][17] using what became known as the Quantum Well Theory. In this theory, the magnetic ordering is driven by the conduction electrons of the host metal. From a physical perspective the oscillations arose from the confinement of these electrons within the finite regions. This confinement leads to the quantisation of the electron energy levels. The positions of these levels are determined by the width, D, of the spacer region. The oscillation results from these quantised energy levels crossing the Fermi-Energy in

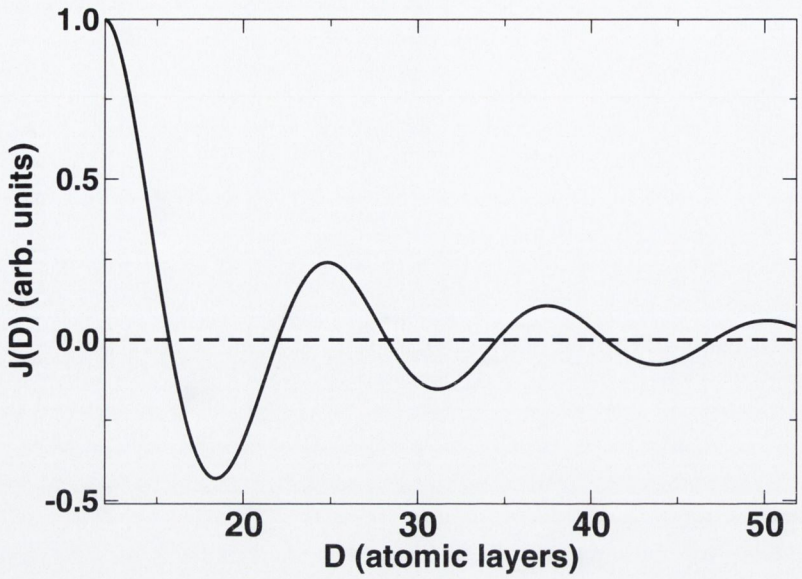


Figure 1.7: Typical oscillatory behaviour of IEC as a function of spacer separation, D. $J(D)$ is the coupling between the layers, written in terms of arbitrary units.

a cyclical fashion, in response to changes in the width of the spacer. This model was capable of reproducing most of the features observed in the experiments, in particular the rate of decay and the period of the oscillation.

The explanation in terms of coupling mediated by conduction electrons bore an obvious similarity to the Ruderman-Kittel-Kasuya-Yosida (RKKY) interaction[18]. This also viewed the interaction between magnetic moments as arising from the presence of conduction electrons, and the coupling is written in terms of effective direct coupling, $J(\mathbf{r}_i - \mathbf{r}_j)\mathbf{s}_i \cdot \mathbf{s}_j$, between two moments i and j. This had been originally proposed as an explanation for IEC. However a naive application of the theory predicted oscillation periods that were far too short. Bruno proposed a generalisation of the RKKY theory which was capable of producing the required long period oscillations by including the effect of the discrete spacer thickness[19][20]. Subsequently, it was shown that the RKKY theory was in fact an approximation to the Quantum Well Theory, correct to second order[21]. When higher order terms were significant the RKKY picture is unable to replicate features of the more general theory, notably the appearance of non-trivial oscillation periods[22].

Although the Quantum Well Picture successfully accounted for the observed $1/D^2$ decay, the theory predicted more generally that this decay rate was dependent on the dimensionality of the system. Lower dimensional metallic systems should exhibit an even longer range decay, as the underlying quantum mechanical nature of the coupling was more sharply exposed. For a 1-D metal the decay would be as slow as $1/D$. It was only with the discovery of carbon nanotubes that such a limit became accessible.

1.3 Giant-Magnetoresistance

It may not seem surprising that the resistance of a ferromagnetic metal might be altered by the presence of an applied magnetic field. The extent of the change is known as the Magnetoresistance (MR) and is typically defined as the fractional change in resistance resulting from the application of a field ($MR = [R(H) - R(0)]/R(0)$). However, in a normal ferromagnet, the internal field acting on a given moment is far stronger that the field which can be applied. As a result, the primary effect of the field is to rotate the direction of magnetisation relative to current direction. This is known as anisotropic magnetoresistance (AMR) and experiments on ferromagnets typically yield an AMR of about 2%[23]. By contrast, in the magnetic multi-layered systems introduced in the previous section, the coupling between the layers is comparatively weak. As a result they are capable of exhibiting a much larger MR. The initial experiment on a Fe/Cr multilayer reported the resistivity of the structure was reduced by a factor of two when the Fe layers were aligned[24]. Subsequent experiments with the same system found a value of 220%[25].

In systems exhibiting large or Giant-magnetoresistance (GMR), the crucial point is that the relative orientation of the moments can be changed. The Indirect exchange coupling facilitates the observation of GMR since, by choosing the spacer thickness appropriately, the magnetic layers will align anti-ferromagnetically. A relatively small magnetic field will therefore be sufficient to align them. IEC is however not necessary for observing Giant-magnetoresistance since alternative approaches such as layer pinning and using materials with different magnetic coercivities have latterly been employed. The large change in resistance arises from spin dependent scattering at the magnetic/metallic interfaces in the materials. We can consider an analogy with an optical polariser which provides an over-simplified yet instructive explanation for the GMR[26]. Assuming that only those electrons with spin anti-parallel to the local magnetisation are scattered at the interface, then with both moments aligned one of the spin channels can propagate through the structure without any scattering. Conversely, with the two layers anti-aligned both spin channels are subject to significant scattering at one of the interfaces. In this way, it is evident that the Indirect exchange coupling and Giant-magnetoresistance are related phenomena. They both arise from scattering of conduction electrons of the host metal as they pass through the magnetic regions.

From an applied standpoint, the discovery of Giant-magnetoresistance has been of enormous importance, especially in the area of magnetic storage. The first hard disk utilising the effect was produced in 1997 and quickly became the industry standard. The importance of the discovery was recognised with the award of the 2007 Nobel Prize in Physics jointly to Albert Fert and Peter Grünberg for their

pioneering experiments in the area.

1.4 Nanotubes Based Electronics

The primary motivation behind research in carbon nanotubes is the development of working nanoscale devices. As the fundamental limits of conventional silicon-based electronic devices become exposed, much effort is being expended in the development of new classes of nano-materials. Carbon nanotubes, with their many remarkable properties, are at the forefront of these attempts.

One of the most straightforward approaches is to utilise the properties of nanotubes directly, in conventional electronic devices akin to current silicon-based ones. An advantage of this approach is that it may ease the introduction of nanotubes into technological applications. Semi-conducting tubes have recently been incorporated as components in field effect transistors and as light emitting diodes. The fact that conductance in nanotubes is ballistic should in principle lead to faster devices. Additionally, they have high mobility and they have a smooth surface so that there are no dangling bonds that trap charge. The first transistor based on a single carbon nanotube was produced in 1998[27][28]. In 2003, it was demonstrated that a nanotube based FET device could operate close to the ballistic conductance limit at room temperature[29].

A closely related area is the production of solid state optical devices such as LED's. These are semi-conducting materials which emit light due to electron-hole recombinations, a process known as electro-luminescence. Nanotubes can act as naturally ambipolar semi-conductors in which both holes and electrons can be injected simultaneously. Therefore the source of the emission is not confined to the interface between n and p type regions, as with a conventional semiconductor, but can actually be tuned with a gate voltage. An overview of the use of carbon nanotubes in conventional electronics was recently given in reference[30][31].

A major aim of research in the area of nanotechnology is the development of spintronic devices, which use the spin rather than the charge of the electron. Unlike conventional transistors, which use a gate voltage to turn the device on and off, the spin based analogy would use the relative orientation of magnetic layers to control the current through the device. In recent years a number of prototype devices have been created with a nanotube placed between two ferromagnetic electrodes. Clean carbon nanotubes possess two useful characteristics in this context: a long spin scattering length ($\sim$ 100nm) and a high Fermi-Velocity ($\sim 10^6$m/s) which reduces the time required to travel between the electrodes. In this way it is hoped that spin information could be preserved between injection and extraction. One of the first experiments in this area placed a multiwall nanotube between Co electrodes

and found a magnetoresistance of 9%, which was seen as a promising result[32]. Recently, a similar experiment using perovskite manganite electrodes reported the much larger value of 61%[33].

1.5 Magnetically Doped Nanotubes

One of the more promising routes to application is the possibility of altering the electronic properties of the nanotube through interactions with atoms and molecules. Of particular interest from the point of view of spintronics is the interaction of transition metal atoms with nanotubes. These atoms (especially Ni, Co and Fe) play a crucial role as catalyst particles in the formation of nanotubes[34]. Even after extensive purification these impurities can remain in the vicinity of the tube, either adsorbed on the surface or occupying a substitutional position within the nanotube. From the theoretical side, numerous *ab-initio* calculations have been performed on the stability and magnetic properties of transition metal atoms, both adsorbed on[35][36][37][38] and substituted in[39] carbon nanotubes. These results demonstrate a wide array of possibilities for functionalisation of nanotubes.

At the same time, the interaction of nanotubes with magnetic objects is not limited to isolated atoms. A number of other possible routes have been proposed. These include contacting a nanotube to a magnetic substrate[40][41]; filling nanotubes with magnetic nanoparticles[42][43][44]; defect induced magnetism[45][46]; building transition metal nanotube tips[47].

At present, the crucial problem restricting the development of nanotube electronics is the issue of controllability. Standard fabrication techniques produce a plethora of tubes with a wide range of diameters and chiralities. Furthermore, the tubes are inclined to form bundles attracted by the intertube Van der Walls forces. Disentangling these bundles without damaging the tubes is a serious technical challenge, as is isolating specific tubes according to their desired electronic properties. Additional problems are faced in attempting to connect nanotubes to external electrodes. Although the experiments described above have produced devices based on individual single and multi-walled nanotubes, these were created more as proof of concept than as working devices. It will be some time before nanotubes appear as common components in nanodevices. This will require the ability to create an abundance of tubes, cheaply, reliably and with a high degree of structural perfection.

In the face of these difficulties, theoretical methods can provide an invaluable tool in identifying potential routes to application. These methods are free from the practical difficulties affecting experiment: it is possible to study the properties of individual pristine nanotubes of a given diameter and chirality. Additionally, theoretical methods are well suited to studying the effects of doping on carbon

nanotubes. In this thesis, we shall investigate the interaction of transition metal atoms with carbon nanotubes. Magnetic ordering in low dimensional systems is of fundamental interest, and nanotubes provide a particularly rich playground in which some of these properties can be explored. At the same time, they are also a rare example of a quantum wire and the effect of disorder on their transport properties is of significant applied interest.

1.6 Outline of Thesis

The thesis is comprised of seven chapters. In chapter 2 the general theoretical framework is introduced. This mainly involves the treatment of disorder using Green Function methods. These methods provide access to the change in the global density of states resulting from the disorder, and from which the change in a wide array of physical quantities can be deduced. The formalism is in no way restricted to treating carbon nanotubes or any particular kind of nanotube/impurity interaction. The presentation throughout the chapter will reflect this. It is only in the final section that armchair and zigzag nanotubes are specified, and then only as a concrete example of the implementation of Recursive Green Function techniques.

The focus in chapter 3 is on the electronic structure of graphene and by extension carbon nanotubes. These are treated within a simple π-band model. Within a single band approach it is possible to examine the electronic properties of nanotubes in a very transparent way. Specifically, in the case of achiral tubes, it allows for the development of closed form analytic expressions for the lattice Green Function propagators. The lattice propagators are of crucial importance in determining the electronic properties of disordered systems and the existence of the analytic expressions is of enormous benefit in expediting calculations. Despite extensive treatments of carbon nanotubes within a single-band representation, these closed form analytic expressions had previously not been derived. Additionally, they provide a useful physical picture with which to explore electron propagation. In the final section, analogous expressions are also derived for semi-infinite achiral nanotubes.

Building on the theoretical framework developed in the previous two chapters, in chapter 4 and 5 attention turns to magnetic ordering of pairs of impurity atoms interacting with nanotubes. Chapter 4 begins with a review of the exchange interaction in metals; particularly Indirect exchange coupling and the Quantum Well Theory. This is then applied to nanotubes. By switching between armchair to zigzag nanotubes the effect of the host on the coupling can be explored. The fact that the magnetic character derives from individual atoms as opposed to ferromagnetic layers introduces an extra degree of freedom in the problem: the location of the impurity within the host. This is explored in chapter 5.

Chapter 6 is concerned with the transport properties of magnetically doped nanotubes. Whereas in the previous two chapters the nanotube was interacting with a pair of impurity atoms, in this chapter the tube is in contact with a large number of randomly distributed impurity atoms. This is an attempt to replicate the real physical situation more closely. *Ab-initio* calculations on systems with individual or pairs of atoms are used to parameterise the model so that it represents the effect of coupling real transition metal atoms to the tube. The transport calculations are performed using the Kubo Formula. With an expression for the conductance it is an easy matter to calculate the Magnetoresistance. Before doing this it is necessary to determine the ground state orientation of the magnetic moments, which is accomplished with the aid of Monte Carlo methods.

In Chapter 7 the main results of the thesis are summarised and possible extensions to the work are presented.

Chapter 2

Mathematical tools - Green Function Methods, Dyson's Equation and the Lloyd Formula.

2.1 Introduction

In this chapter most of the basic mathematical techniques which will be used throughout the thesis are introduced.

As a motivation we consider the problem of how a foreign object interacts with a host material. The interaction between the host and the foreign body manifests itself as a change in the density of states. In particular, how is the electronic structure of the system affected by such an interaction? As far as the electronic structure is concerned, the effect of introducing an interaction between a foreign body and a host manifests itself as a change in the density of states. Once the density of states is known it is then a straightforward task to calculate a variety of physical quantities, such as the occupation number, charge transfer and the total energy. To arrive at these values it is necessary to develop a machinery for calculating both the density of states and changes to the density of states. The tools for accomplishing this task are Green Function methods.

The Green Function is directly related to the local density of states (LDOS). For periodic systems, calculating the LDOS is an easy enough task, at least in principle. However the great power of Green Function methods is that they are capable of going far beyond such a restrictive case and provide a framework for the treatment of disordered systems. This is achieved using a simple but powerful expression known as Dyson's Equation. Dyson's Equation provides an expression for the changing LDOS arising from the interaction between the host and a foreign object. The foreign object could be a substrate, a group of itinerant atoms or even

another host. Furthermore, by exploiting special sum rules it is possible to rewrite Dyson's Equation in a form that gives direct access to the change in the global density of states (DOS) arising from the interaction, without having to explicitly determine the DOS of either the decoupled or coupled systems. This is known as the Lloyd Formula method[48]. In this chapter we will look at properties of the Green Function, show how they relate to the density of states and derive both Dyson's Equation and the Lloyd Formula.

2.2 Green Functions

Perhaps one of the most important quantities in mesoscopic physics is the Green Function[49]. Throughout this thesis it underpins all the calculations performed. The Green Function is a solution of a linear differential equation, relating a response function to a source term. In our case the linear differential equation is the Schrodinger Equation. Once the Green Function is known the equation is essentially solved. In Solid State Physics, one of the primary benefits of Green Function methods is that they provide direct access to the density of states. Additionally, in transport calculations, the Green Function describes the propagation of electrons through a conductor. In a general sense, the Green Function is a two-point correlation function which allows us to express the response at point B to a perturbation at point A. This makes it particularly suited to treating the disordered systems which we intend to consider here.

In problems in Condensed Matter Physics, the Green Function is typically defined as

$$G^{(\pm)} = \lim_{\eta \to 0}[(E \pm i\eta)\hat{I} - \hat{H}]^{-1} \quad . \tag{2.1}$$

$\hat{H}$ is the Hamiltonian chosen to represent the system, $\hat{I}$ is the identity operator and E is the energy. The quantity η plays the role of an imaginary part added to the energy. Its presence is necessary to ensure that the Green Function is properly defined around the eigenvalues of the Hamiltonian. The presence of this non-zero imaginary quantity destroys the Hermicity of the operator and consequently the Green Function is not a physical observable. The limit can be taken in a positive (retarded) or negative (advanced) sense denoted by $\pm$. This distinction has a physical significance: the retarded Green Function describes propagation away from the site of the perturbation while the advanced Green Function describes propagation towards the perturbation. This distinction will only be relevant later on when considering transport properties. As a tool for calculating the density of states we are free to adopt either definition and duly choose to work with the retarded propagator. To

see how Eq.(2.1) relates to the density of states we assume that the state vectors $|\Psi_\mu\rangle$ form a complete set of eigenvectors of $\hat{H}$. Then, defining the eigenvalues as ϵ_μ,

$$\hat{H} = \sum_\mu |\Psi_\mu\rangle \, \epsilon_\mu \, \langle\Psi_\mu| \quad . \tag{2.2}$$

Inserting in Eq.(2.1) gives,

$$\hat{G} = \lim_{\eta\to 0} \sum_\mu |\Psi_\mu\rangle \frac{1}{E + i\eta - \epsilon_\mu} \langle\Psi_\mu| \quad . \tag{2.3}$$

It should perhaps be mentioned at this point that the Green Function is a general operator, defined by the specific form of Hamiltonian H. Depending on the level of complexity required we can use either a free electron, a tight-binding or more intensive *ab-initio* Hamiltonians. Throughout this thesis most of our calculations will be based on a Tight-Binding Hamiltonian. For that reason, all the results in this chapter will be presented for Hamiltonians that are written in terms of linear combinations of atomic orbitals.

If the Hamiltonian is described by a basis of localised orbitals $|j\rangle$, centred on site j, then the projection of these vectors onto Eq.(2.3) gives

$$\langle j|\hat{G}|j'\rangle = \lim_{\eta\to 0} \sum_\mu \langle j|\Psi_\mu\rangle \frac{1}{E + i\eta - \epsilon_\mu} \langle\Psi_\mu|j'\rangle \tag{2.4}$$

$$= \lim_{\eta\to 0} \sum_\mu \langle j|\Psi_\mu\rangle \frac{E - i\eta - \epsilon_\mu}{(E - \epsilon_\mu)^2 + \eta^2} \langle\Psi_\mu|j'\rangle \quad . \tag{2.5}$$

Taking the imaginary part and setting $j = j'$,

$$-\frac{1}{\pi}\mathrm{Im}\langle j|\hat{G}|j\rangle = \lim_{\eta\to 0} \sum_\mu |\langle j|\Psi_\mu\rangle|^2 \frac{\eta}{(E - \epsilon_\mu)^2 + \eta^2} \quad . \tag{2.6}$$

From the definition of the Dirac Delta function,

$$\delta(x) = \frac{1}{\pi} \lim_{a\to 0} \frac{a}{x^2 + a^2} \quad , \tag{2.7}$$

it follows that,

$$-\frac{1}{\pi}\mathrm{Im}\,\langle j|\hat{G}|j\rangle = \sum_\mu |\langle j|\Psi_\mu\rangle|^2 \delta(E - \epsilon_\mu) \quad . \tag{2.8}$$

This is precisely the definition of the local density of states at site j. Once this is known the task of calculating physical quantities such as occupation number, charge transfer and energy change is essentially accomplished. Unfortunately, things are not quite that simple: In Eq.(2.8) we have assumed the eigenstates of the system, $|\Psi_\mu\rangle$,

are known. If the system displays simple translational invariance then the eigenvectors are given by Bloch's Theorem. When translational invariance is broken, say by the introduction of impurities, the Bloch wavevectors are no longer eigenvectors of the system. In this context the Green Function approach is invaluable since using Eq.(2.1) we can relate the propagators of the disordered system to those of the clean system without having to directly determine the eigenvectors of the former; a task which normally involves constructing large supercells. The procedure for doing this is known as Dyson's Equation. Its derivation is extremely simple and is presented in the next section.

2.3 Dyson's Equation

Written in its most general form, Dyson's Equation simply relates the Green Function, $\hat{G}$, associated with a Hamiltonian $\hat{H} = \hat{H}_0 + \hat{V}$ to the Green Function, $\hat{\mathcal{G}}$, associated with H_0. $\hat{V}$ is a perturbation potential relating the two systems. Its derivation follows easily from Eq.(2.1).

$$\hat{G} = \left((E + i\eta)\hat{I} - (\hat{H}_0 + \hat{V})\right)^{-1} \tag{2.9}$$

$$= \left(\hat{\mathcal{G}}^{-1} - \hat{V}\right)^{-1} \tag{2.10}$$

$$= (\hat{I} - \hat{\mathcal{G}}\hat{V})^{-1}\hat{\mathcal{G}} \quad . \tag{2.11}$$

Multiplying from the left by $(\hat{I} - \hat{\mathcal{G}}\hat{V})$ we arrive at the concise form,

$$\hat{G} = \hat{\mathcal{G}} + \hat{\mathcal{G}}\,\hat{V}\,\hat{G} \quad . \tag{2.12}$$

This is Dyson's Equation in its most commonly encountered form. We assume for the moment that the propagators of the unperturbed system are already known. Calculation of the corresponding propagators for the perturbed system is complicated somewhat by the presence of the operator $\hat{G}$ on both the left and right hand sides of the above equation.

To proceed further we assume that the perturbation potential $\hat{V}$ affects a finite number $(n_1, n_2, ..., n_N)$ of localised atomic orbitals $|j\rangle$. These can represent atomic sites, intra-atomic orbitals or spin degrees of freedom. No further assumption about the specific nature of the interaction need be made at this time. In particular, referring to a perturbation $\hat{V}$ often carries the connotation that the perturbation is weak. This is not necessarily true. Eq.(2.12) is valid for any perturbation regardless of the magnitude. If the effect is weak then Eq.(2.12) can be expanded as a power

series.

$$\hat{G} = \hat{\mathcal{G}} + \hat{\mathcal{G}}\hat{V}\hat{\mathcal{G}} + \hat{\mathcal{G}}\hat{V}\hat{\mathcal{G}}\hat{V}\hat{\mathcal{G}} + \cdots \quad , \tag{2.13}$$

and truncated after only a few terms.

Writing the perturbation operator $\hat{V}$ in this localised basis

$$\hat{V} = \sum_{i,j=1}^{N} |n_i\rangle \, V_{ij} \, \langle n_j| \quad , \tag{2.14}$$

and

$$\hat{G} = \hat{\mathcal{G}} + \sum_{i,j=1}^{N} \hat{\mathcal{G}} \, |n_i\rangle \, V_{ij} \, \langle n_j| \, \hat{G} \quad . \tag{2.15}$$

In order to obtain an expression for the matrix elements of G in terms of the known elements $\mathcal{G}$ we project the state vectors $\{|n_k\rangle\}$ onto the operator $\hat{G}$ from the left,

$$\langle n_k| \, \hat{G} = \langle n_k| \, \hat{\mathcal{G}} + \sum_{i,j=1}^{N} \langle n_k|\hat{\mathcal{G}}|n_i\rangle V_{ij} \, \langle n_j| \, \hat{G} \quad . \tag{2.16}$$

Collecting terms in $\langle n_j| \, \hat{G}$,

$$\sum_{j=1}^{N} \left(\delta_{jk} - \sum_{i=1}^{N} \langle n_k|\hat{\mathcal{G}}|n_i\rangle V_{ij} \right) \langle n_j| \, \hat{G} = \langle n_k| \, \hat{\mathcal{G}} \quad . \tag{2.17}$$

It is common to define an $N \times N$ dimensional matrix $T^{-1} = I - [\mathcal{G}][V]$, where $[\mathcal{G}]$ and $[V]$ are the $N \times N$ matrices containing the elements $\langle n_i|\hat{\mathcal{G}}|n_j\rangle$ and $\langle n_i|\hat{V}|n_j\rangle$. Then

$$T^{-1} = \delta_{jk} - \sum_{i=1}^{N} \langle n_k|\hat{\mathcal{G}}|n_i\rangle V_{ij} \quad , \tag{2.18}$$

and

$$\sum_{j=1}^{N} T_{ij}^{-1} \, \langle n_j| \, \hat{G} = \langle n_i| \, \hat{\mathcal{G}} \quad . \tag{2.19}$$

Inverting gives,

$$\langle n_i| \, \hat{G} = \sum_{j=1}^{N} T_{ij} \, \langle n_j| \, \hat{\mathcal{G}} \quad . \tag{2.20}$$

Substituting Eq.(2.20) in Eq.(2.15) allows us write a general expression for the operator $\hat{G}$ in terms of matrix elements of the unperturbed Green Function $\hat{\mathcal{G}}$,

$$\hat{G} = \hat{\mathcal{G}} + \sum_{i,j,k=1}^{N} \hat{\mathcal{G}} \left|n_i\right\rangle V_{ij} T_{jk} \left\langle n_k\right| \hat{\mathcal{G}} \quad . \tag{2.21}$$

We can write the operator $\hat{G}$ as the dyadic product[1]

$$\hat{G} = \hat{\mathcal{G}} + \hat{\mathcal{G}} \begin{pmatrix} |n_1\rangle \\ |n_2\rangle \\ \vdots \\ |n_N\rangle \end{pmatrix} \begin{pmatrix} V_{11} & V_{12} & \cdots & V_{1N} \\ V_{21} & V_{22} & \cdots & V_{2N} \\ \vdots & \vdots & \ddots & \vdots \\ V_{N1} & V_{N2} & \cdots & V_{NN} \end{pmatrix} \times \tag{2.22}$$

$$\times \begin{pmatrix} T_{11} & T_{12} & \cdots & T_{1N} \\ T_{21} & T_{22} & \cdots & T_{2N} \\ \vdots & \vdots & \ddots & \vdots \\ T_{N1} & T_{N2} & \cdots & T_{NN} \end{pmatrix} \begin{pmatrix} \langle n_1| & \langle n_2| & \cdots & \langle n_N| \end{pmatrix} \hat{\mathcal{G}} \quad , \tag{2.23}$$

and the individual matrix elements can be written as

$$G_{jj'} = \mathcal{G}_{jj'} + \sum_{t,u,v=1}^{N} \mathcal{G}_{jn_t} V_{tu} T_{uv} \mathcal{G}_{n_v j'} \quad . \tag{2.24}$$

Eq.(2.24) gives an expression for any Green Function propagator of the total Hamiltonian H in terms of the propagators of the reference Hamiltonian H_0. All we need to do is form the appropriate matrices $[\mathcal{G}]$ and $[V]$. Generally speaking the perturbation will either change the on-site energy $\langle j|\hat{V}|j\rangle = \epsilon_j$, alter the hopping $\langle j|\hat{V}|j \pm 1\rangle = t_{j,j\pm1}$ between neighbouring sites or a combination of both.

In order to illustrate the formalism we explicitly show the calculation for the case of a single substitutional atom and a single adatom attached to an infinite host.

2.3.1 Substitutional Atom

In the case of a single substitutional atom, one host atom ($j = N$ say) is replaced by an atom from a different chemical species. The electronic structure of the host, in the absence of the impurity, is described by the operator $\hat{\mathcal{G}}$. Again, at this point, it is not necessary to be more specific about the nature of the host. In figure 2.1 the host

[1] A dyadic product is a matrix of the form $\mathrm{x}\, U \mathrm{x}^T$, where x is an N vector and U an $N \times N$ matrix. It is similar in form to a standard inner product $\mathrm{x}^T U \mathrm{x}$, except that the transpose occurs to the right. Whereas an inner product takes a vector x and returns a scalar, a dyadic product returns an $N \times N$ matrix.

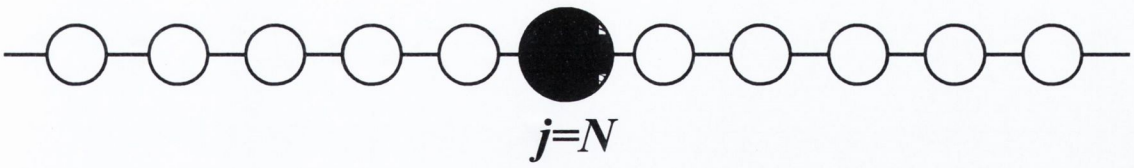


Figure 2.1: Schematic representation of a substitutional atom embedded in a host. Here the host is represented as a simple linear chain although this does not involve any loss of generality.

is implicitly represented by a linear chain. This involves no loss of generality, since in the expressions below we make no assumptions about the form of the operator $\hat{\mathcal{G}}$. In later chapters $\hat{\mathcal{G}}$ will describe a carbon nanotube.

Except at the site of the impurity, each atom is represented by an energy level $\langle j|\hat{H}|j\rangle = \epsilon_0$ and nearest neighbour hopping $t = \langle j|\hat{H}|j \pm 1\rangle$. In the simplest case the effect of the impurity is to change the on-site potential at site $j = N$: $\epsilon_0 \rightarrow \epsilon_N = \epsilon_0 + \lambda$. The matrix $[V]$ has a single non zero element $\langle 0|\hat{V}|0\rangle = \lambda$. Assuming the propagators for the isolated host are known, we can use Eq.(2.24) to write down an expression for the propagators of the composite system. Since the perturbation is limited to the site $j = N$ the matrix T reduces to the scalar,

$$T = \frac{1}{1 - \langle N|\hat{\mathcal{G}}|N\rangle\langle N|\hat{V}|N\rangle} \quad , \tag{2.25}$$

and Eq.(2.15) gives,

$$G_{jj'} = \mathcal{G}_{jj'} + \mathcal{G}_{jN}\frac{\langle N|\hat{V}|N\rangle}{1 - \langle N|\hat{\mathcal{G}}|N\rangle\langle N|\hat{V}|N\rangle}\mathcal{G}_{Nj'} \tag{2.26}$$

$$= \mathcal{G}_{jj'} + \mathcal{G}_{jN}\frac{\lambda}{1 - \lambda\mathcal{G}_{NN}}\mathcal{G}_{Nj'} \quad . \tag{2.27}$$

Expanding the denominator in powers in λ gives some physical meaning to the above expression. The propagator between sites j and j' in the presence of the impurity can be regarded as the sum of direct propagation between the two sites and propagation via the impurity site N. Each power of λ represents a higher order interaction. Since there is only a single impurity present, these higher interactions can only occur at the impurity site. If additional impurities were present the interaction could involve an increasing number of intermediate steps. If the expansion parameter is small then these higher order interactions are negligible. We shall return to this viewpoint in section 6.5. From a computational standpoint, such a truncated expansion it is not particularly useful since it is far simpler to invert the matrix for T directly. Nevertheless; it provides a nice physical picture for visualising the propagation of electrons through a disordered system.

2.3.2 Adsorbed Atom

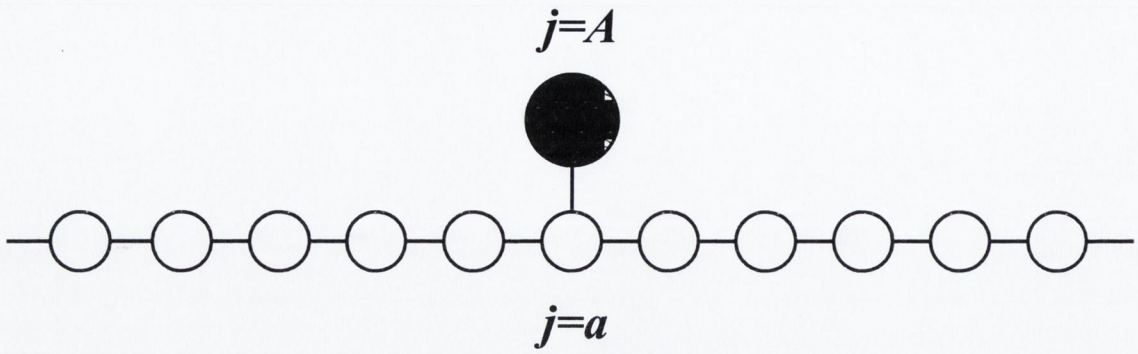


Figure 2.2: Schematic representation of an adsorbed atom attached to an infinite host. Here the host is represented by a simple linear chain although this involves no loss of generality.

In the case of an adsorbed atom the reference system consists of a generic host and an isolated impurity located an infinite distance away. The system is shown schematically in figure 2.2. Again, the expressions are in no way restricted to the case of a simple linear chain. The isolated impurity is characterised by a single orbital described by a state vector $|A\rangle$ .The effect of the perturbation $\hat{V}$ is to bring the impurity into the vicinity of the host. We represent this interaction by allowing a non-zero hopping, t, to develop between the impurity and one of the host atoms, $j = a$ say. In this case $\{|j\rangle\}, |A\rangle$ form a basis for the Hilbert Space and $\hat{V} = t(|A\rangle\langle a| + |a\rangle\langle A|)$. The perturbation now affects two atomic orbitals and the matrix $[V]$ becomes,

$$[V] = \begin{pmatrix} \langle a|\hat{V}|a\rangle & \langle a|\hat{V}|A\rangle \\ \langle A|\hat{V}|a\rangle & \langle A|\hat{V}|A\rangle \end{pmatrix} = \begin{pmatrix} 0 & t \\ t & 0 \end{pmatrix} \quad . \tag{2.28}$$

It follows that

$$[T] = \left[\begin{pmatrix} 1 & 0 \\ 0 & 1 \end{pmatrix} - \begin{pmatrix} \mathcal{G}_{aa} & \mathcal{G}_{aA} \\ \mathcal{G}_{Aa} & \mathcal{G}_{AA} \end{pmatrix} \begin{pmatrix} 0 & t \\ t & 0 \end{pmatrix} \right]^{-1} \tag{2.29}$$

$$= \frac{\begin{pmatrix} 1 - t\,\mathcal{G}_{Aa} & t\,\mathcal{G}_{aa} \\ t\,\mathcal{G}_{AA} & 1 - t\,\mathcal{G}_{aA} \end{pmatrix}}{1 - t(\mathcal{G}_{aA} + \mathcal{G}_{Aa}) + t^2(\mathcal{G}_{aA}\mathcal{G}_{Aa} - \mathcal{G}_{AA}\mathcal{G}_{aa})} \tag{2.30}$$

Substituting in Eq.(2.24) gives,

$$G_{jj'} = \mathcal{G}_{jj'} + t\left(\frac{\mathcal{G}_{ja}\, t\mathcal{G}_{AA}\, \mathcal{G}_{aj} + \mathcal{G}_{ja}\, t(1 - t\mathcal{G}_{aA})\, \mathcal{G}_{Aj'}}{1 - t(\mathcal{G}_{aA} + \mathcal{G}_{Aa}) + t^2(\mathcal{G}_{aA}\mathcal{G}_{Aa} - \mathcal{G}_{AA}\mathcal{G}_{aa})} \right. \tag{2.31}$$

$$\left. + \frac{\mathcal{G}_{jA}\, t(1 - t\mathcal{G}_{Aa})\, \mathcal{G}_{aj'} + \mathcal{G}_{jA}\, t\mathcal{G}_{aa}\, \mathcal{G}_{Aj'}}{1 - t(\mathcal{G}_{aA} + \mathcal{G}_{Aa}) + t^2(\mathcal{G}_{aA}\mathcal{G}_{Aa} - \mathcal{G}_{AA}\mathcal{G}_{aa})} \right) .$$

For a perturbation involving more than two atomic orbitals, it is generally nec-

essary to invert the matrix using numerical techniques.

2.4 Lloyd Formula

Many of the calculations in the first part of this thesis ultimately involve calculating changes in total energy resulting from a perturbation $\hat{V}$ to the reference Hamiltonian $\hat{H}_0$. The intention may be to compute the binding energy of an impurity, or the magnetic coupling between impurities. Irrespective of the specifics of the interaction, the energy difference is defined as

$$\Delta E = E - E_0 \quad . \tag{2.32}$$

Since the reference system is usually an infinite host and the perturbation is confined to a few atomic orbitals, the energy difference would be expected to be small with respect to the total energy of either system. Consequently direct evaluation of the separate energies can be difficult, or at best inefficient. What is desirable is a method that can calculate the energy difference directly, without having to calculate the total energy explicitly. This can be accomplished using the Lloyd Formula Method, which we now derive.

The energy difference can be written by

$$\Delta E = \int_{-\infty}^{E_F} dE\, E[\rho(E) - \rho_0(E)] \quad , \tag{2.33}$$

with ρ and ρ_0 representing the density of states of the composite and reference systems respectively. Since the reference system is assumed to be infinite, and the perturbation is restricted to a finite number of distinct sites, the Fermi Energy (E_F) can be regarded as fixed (although to guarantee charge conservation we sometimes have to allow a small, unphysical change to occur[50]). The change in the global density of states, $\rho(E) - \rho_0(E)$, can be written as a sum over the LDOS, which can in turn be written in terms of on-site Green Function elements. Therefore,

$$\Delta\rho = -\frac{1}{\pi}\mathrm{Im}\sum_j [G_{jj}(E) - \mathcal{G}_{jj}(E)] \quad . \tag{2.34}$$

As seen in the previous section, the quantity $G_{jj}(E) - \mathcal{G}_{jj}(E)$ is easily evaluated using Eq.(2.24). If the perturbation is localised to N atomic orbitals n_a,

$$G_{jj} - \mathcal{G}_{jj} = \sum_{a,b,c=1}^{N} \mathcal{G}_{jn_a} V_{ab} T_{bc} \mathcal{G}_{n_c j} \quad . \tag{2.35}$$

Summing over all atomic orbitals gives,

$$\sum_j (G_{jj} - \mathcal{G}_{jj}) = \sum_{a,b,c=1}^{N} \left(\sum_j \mathcal{G}_{n_c j} \mathcal{G}_{j n_a} \right) V_{ab} T_{bc} \quad . \tag{2.36}$$

Since the orbitals j form a complete set, it is possible to write

$$\sum_j \mathcal{G}_{n_c j} \mathcal{G}_{j n_a} = \sum_j \langle n_c | \hat{\mathcal{G}} | j \rangle \langle j | \hat{\mathcal{G}} | n_a \rangle = \langle n_c | \hat{\mathcal{G}} \left(\sum_j |j\rangle \langle j| \right) \hat{\mathcal{G}} | n_a \rangle = \langle n_c | \hat{\mathcal{G}}^2 | n_a \rangle \quad . \tag{2.37}$$

Therefore,

$$\sum_j (G_{jj} - \mathcal{G}_{jj}) = \sum_{a,b,c=1}^{N} \langle n_c | \hat{\mathcal{G}}^2 | n_a \rangle V_{ab} T_{bc} \quad . \tag{2.38}$$

Additionally, it is easily seen from Eq.(2.1) that,

$$\hat{\mathcal{G}}^2 = -\frac{d}{dE} \hat{\mathcal{G}} \quad , \tag{2.39}$$

so that,

$$\Delta G := \sum_j (G_{jj} - \mathcal{G}_{jj}) = -\mathrm{Tr}[\mathcal{G}' V T] \quad , \tag{2.40}$$

where $\mathcal{G}', V$ and T are $N \times N$ matrices and $\mathcal{G}'$ is defined to be the matrix $[\mathcal{G}'_{ab}] = \frac{d[G_{ab}]}{dE}$.

Assuming the perturbation $\hat{V}$ has no energy dependence, then from the definition of T we have $T^{-1} = I - \mathcal{G}V$, so that

$$\frac{dT}{dE}^{-1} = -\frac{d\hat{\mathcal{G}}}{dE} V \quad , \tag{2.41}$$

and

$$\frac{d\hat{\mathcal{G}}}{dE} = -\frac{dT}{dE}^{-1} V^{-1} \quad . \tag{2.42}$$

Thus, $\hat{\mathcal{G}}' \hat{V} \hat{T} = -\frac{d\hat{T}^{-1}}{dE} \hat{T}$ and

$$\Delta G = \mathrm{Tr}[\frac{dT}{dE}^{-1} T] = \mathrm{Tr} \frac{d}{dE} \log(T^{-1}) = \frac{d}{dE} \mathrm{Tr} \log(\hat{I} - \hat{\mathcal{G}} \hat{V}) \quad . \tag{2.43}$$

The proof that $\mathrm{Tr}(\log \hat{X})' = \mathrm{Tr}[\hat{X}' \hat{X}] = \mathrm{Tr}[\hat{X} \hat{X}']$ for an operator $\hat{X}$, where the prime denotes the derivative, is given in appendix A. The expression for $\Delta\rho$ is now given

by,

$$\Delta\rho = -\frac{1}{\pi}\mathrm{Im}[\Delta G] \tag{2.44}$$

$$= -\frac{1}{\pi}\mathrm{Im}\frac{d}{dE}\mathrm{Tr}\log(I - \mathcal{G}V) \quad . \tag{2.45}$$

Additionally, as shown in appendix B, $\mathrm{Tr}(\log(1 - \mathcal{G}V)) = \log(\det(1 - \mathcal{G}V))$ so that in its canonical form, the Lloyd Formula is given by,

$$\Delta\rho(E) = -\frac{1}{\pi}\mathrm{Im}\frac{d}{dE}\log(\det(I - \mathcal{G}(E)V)) \quad . \tag{2.46}$$

Eq.(2.46) demonstrates that $\Delta\rho$ can be written in terms of an energy derivative. This is a particularly attractive way to proceed since calculating most physical observables involves an integration over energy. The change in the occupation number ΔN can thus be written down.

$$\Delta N(E_F) = -\frac{1}{\pi}\mathrm{Im}\log(\det(I - \mathcal{G}(E)V))\Big|_{E_F} \quad . \tag{2.47}$$

Returning to the change in total energy; this is given by,

$$\Delta E = \int_{-\infty}^{E_F} dE\, E\, \Delta\rho(E) \tag{2.48}$$

$$= E_F\Delta N(E_F) + \frac{1}{\pi}\int_{-\infty}^{E_F} dE\, \mathrm{Im}\log(\det(I - \mathcal{G}(E)V)) \tag{2.49}$$

$$= \frac{1}{\pi}\int_{-\infty}^{E_F} dE\, \mathrm{Im}\log(\det(I - \mathcal{G}V)) \tag{2.50}$$

The last of these equations comes from requiring that the charge in the system be conserved. This reflects the physical condition that the total charge should not change as a result of bringing the two systems into contact. However, the condition that $\Delta N = 0$ will normally not be satisfied automatically. In such cases it can be viewed as a constraint on the allowed parameterisation[51][52]. Otherwise, as discussed in reference [50], it is necessary to allow for a small unphysical change in the Fermi-Energy, $E_F \rightarrow E_F + \delta E_F$.

2.5 Recursive Methods

Eq.(2.46) is written in terms of Green Function propagators of the reference $\mathcal{G}$ and the perturbation matrix V. Since the latter is known, all that remains is to calculate the former. The reference system will in general comprise either a periodic host or an underlying periodic host which has some disorder already associated with

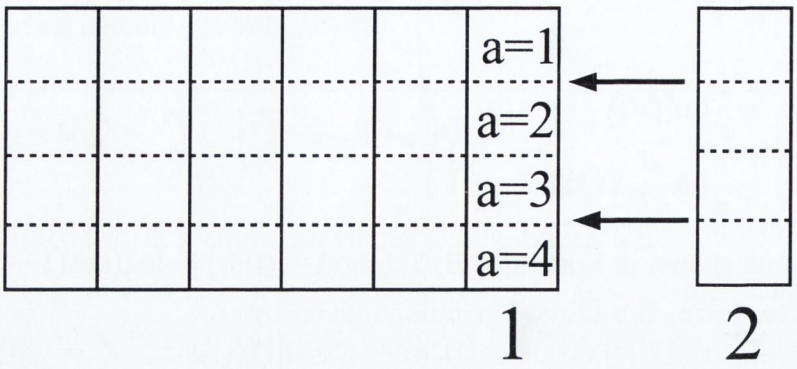


Figure 2.3: A schematic diagram illustrating the RGF technique. Block 2 is attached to the end of the existing structure which terminates at block 1. In the figure there are four orbitals per block.

it. There are two ways to proceed: If the host is translationally invariant and has only a single orbital per atom it is normally possible to produce closed form analytic expressions for the propagators. Chapter 3 is devoted to developing these expressions for armchair and zigzag nanotubes. These can then be inserted in Eq.(2.24) to yield the required propagators for the reference system in Eq.(2.46). Alternatively, a Recursive Green Function (RGF) approach can be used to calculate the propagators of the reference system without recourse to the underlying periodic host. The approach is once again based on Dyson's Equation. It is conceptually simple, quick to implement and very portable. It will prove particularly useful in chapter 6 when calculating transport properties of doped nanotubes. At its heart it involves a renormalisation technique which allows us to calculate the Green Function at the surface of a semi-infinite structure without having to directly invert the infinite dimensional Hamiltonian. We can then combine two semi-infinite sections to calculate the bulk propagators. The structure is decomposed into a number of blocks which are initially isolated from each other. Each block contains N atomic sites as well as possible orbital and spin degrees of freedom. Importantly, these blocks need not be equivalent, although they should reflect some basic periodic structure of the host. We then successively connect adjacent blocks. The surface of a semi-infinite host is reached when the addition of a extra block produces no effect on the matrix elements at the surface. This is merely a definition and does not involve any trickery. For all intents and purposes a structure extends to infinity when the surface atoms have no sense of the presence of the opposite boundary.

The generic structure is represented as a system of rectangular blocks in figure 2.3. The propagators are generated as follows. Assume the Hamiltonian for each isolated block, H_i, is known. Adjacent blocks are then connected by $N \times N$ matrices $t_{i,i+1}$ and $t_{i+1,i}$. The indices represent the order in which the blocks are attached. The first connects the atoms on block i to those on $i+1$; the second connects the elements in the opposite sense. Because of the Hermicity of the overall Hamiltonian

they are related by $t_{i+1,i} = t^{\dagger}_{i,i+1}$.

Successive blocks are added using Dyson's Equation. Starting with a single block, we add a second to the right of the first. This is directly analogous to the method demonstrated in section 2.3.2 for treating single atoms adsorbed at the surface of the host. The only difference is that all scalar quantities are replaced by matrices. In this sense the perturbation can be regarded as adsorbing an additional block at the end of the existing structure. The sites affected by this adsorption are $|1,a\rangle, |2,b\rangle$ where $a,b = 1,2,\cdots,N$. The first index labels a given block and the second the particular atom within the block. The perturbation can then be written as,

$$\hat{V} = \sum_{a,b=1}^{N} |1,a\rangle\, V_{1a,2b}\, \langle 2,b| = |1\rangle\, t_{12}\, \langle 2| \quad . \tag{2.51}$$

As defined above, $t_{12} = [t_{12}]_{ab}$ is a hopping matrix containing all the hopping element $1 \rightarrow 2$. Writing the perturbation in this general form allows the derivation to proceed in exactly the same way as in the scalar case; the only difference being that when dealing with matrices the order in which operations occur must be preserved exactly. Using Dyson's Equation,

$$\langle 2|\hat{G}|2\rangle = \langle 2|\hat{\mathcal{G}}|2\rangle + \langle 2|\hat{\mathcal{G}}|2\rangle t_{21} \langle 1|\hat{G}|2\rangle \tag{2.52}$$

$$\langle 1|\hat{G}|2\rangle = \langle 1|\hat{\mathcal{G}}|2\rangle + \langle 1|\hat{\mathcal{G}}|1\rangle t_{12} \langle 2|\hat{G}|2\rangle \quad . \tag{2.53}$$

Combining the two equations gives an expression for the surface elements, $\langle 2|\hat{G}|2\rangle$, of the updated structure in terms of surface elements, $\langle 1|\hat{\mathcal{G}}|1\rangle$, of the original structure. The elements of $\langle 2|\hat{\mathcal{G}}|2\rangle$ are propagators between sites on the isolated block. We label this as R_2 with the subscript chosen to preserve the continuity of the indices. Then defining $S_1 = \langle 1|\hat{\mathcal{G}}|1\rangle$ and $S_2 = \langle 2|\hat{G}|2\rangle$,

$$S_2 = R_2 + R_2 t_{21} S_1 t_{12} S_2 \tag{2.54}$$

$$= (I - R_2 t_{21} S_1 t_{12})^{-1} R_2 \tag{2.55}$$

$$= (R_2^{-1} - t_{21} S_1 t_{12})^{-1} \quad . \tag{2.56}$$

S_i is the surface Green Function of the structure that extends to as far as block i. If the initial structure contains only a single block, then $R_1 = S_1$.

The surface elements are in general generated according to the formula,

$$S_L = (I - R_0 t_{RL} S_L t_{LR})^{-1} R_0 \quad , \tag{2.57}$$

which recursively updates the Surface Green Function as additional blocks are added. The subscript 'L' indicates that the structure is being grown from the left. t_{LR}, t_{RL}

connect adjacent blocks in the sense of left to right and right to left, respectively. R_0 is the Green Function matrix of the isolated block. The surface propagator for an equivalent structure grown from the right can be calculated by changing the order of t_{RL} and t_{LR}.

$$S_R = (I - R_0 t_{LR} S_R t_{RL})^{-1} R_0 \quad . \tag{2.58}$$

Eq.(2.57) and Eq.(2.58) are not limited to adsorbing isolated blocks. Suppose the initial structure consists of two finite or semi-infinite regions. The left side terminates at block 0, the right side at 1. Assuming we know the surface propagators S_0 and S_1 then it is possible to calculate the bulk propagator, G_{11}, using Eq.(2.57) with R_0 replaced by S_1,

$$G_{11} = (I - S_1 t_{10} S_0 t_{01})^{-1} S_1 \quad . \tag{2.59}$$

If S_0, S_1 represent the surface of two semi-infinite regions then G_{11} is the matrix of bulk propagators between all the intra-block elements of the infinite structure. The extension to a general bulk propagator is given in the next section.

2.5.1 Bulk Green Function Propagators

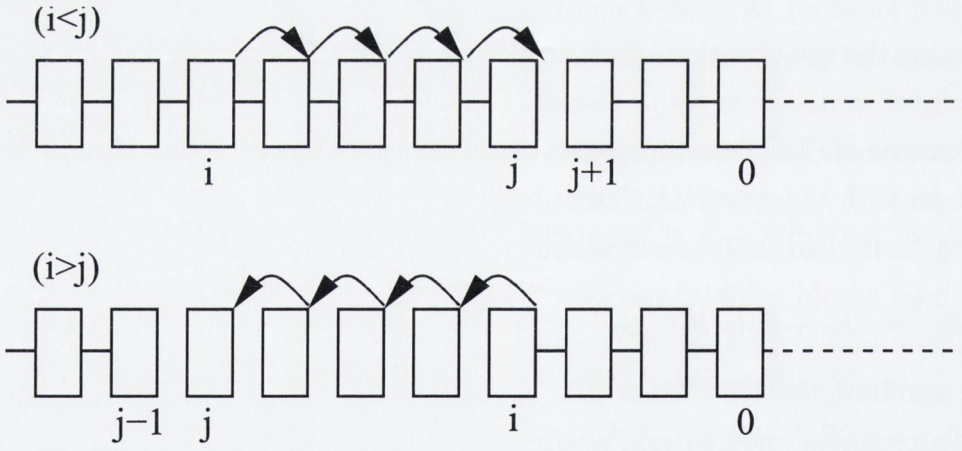


Figure 2.4: Schematic representation of a semi-infinite nanostructure grown recursively. The structure is decomposed into rectangular blocks extending from $-\infty$ and terminating at block 0. The propagator between an element on block i and j is sought. If $i < j$ then the structure is initially grown as far as i, extended to j and finally connected to the $-j$ block structure on the right. If $i > j$ then a finite $-i+1$ block structure is grown from the right. It is then extended as far as j and finally connected to the semi-infinite structure grown from the left, terminating at $j-1$. The dashed lines indicate that the right side structure can also extend to $+\infty$.

In this section we use a methodology presented in[53] to calculate an arbitrary bulk propagator G_{ij} between any 2 sites on a general infinite or semi-infinite nanostructure. The desired sites are assumed to be located on block i and block j. We will

initially consider a semi-infinite host. Once the method for generating semi-infinite propagators is known the extension to a fully infinite system is trivial.

We assume that the host is semi-infinite, grown from the left (i.e. $(-\infty, 0]$). This is shown in figure 2.4. Assume that $j > i$ then the propagator,

$$\begin{aligned} G^j_{i,j} &= G^{j-1}_{i,j-1}\, t_{j-1,j}\, G^j_{j,j} && (2.60)\\ &= G^{j-1}_{i,j-1}\, t_{j-1,j}\, S^j && (2.61)\\ &= G^{j-2}_{i,j-2}\, t_{j-2,j-1}\, S^{j-1}\, t_{j-1,j}\, S^j && (2.62)\\ &\;\;\vdots \\ &= S^i\, t_{i,i+1}\, S^{i+1}\, t_{i+1,i+2} \cdots S^{j-1}\, t_{j-1,j}\, S^j \quad . && (2.63) \end{aligned}$$

The superscript indicates the rectangular block at which the host terminates at each step. This could also be viewed as starting with the host connected as far as i and progressively adding blocks until j is reached. For cases where each block is identical then $S^j = S_L$, $t_{j-1,j} = t_{LR}$ and we write

$$G^j_{i,j} = (S_L t_{LR})^{j-i} S_L \quad . \tag{2.64}$$

Next, we construct the surface Green Function for the $-j$ block structure, grown from the right, connecting blocks $[j+1, 0]$. We label the surface Green Function as S_R. All that remains is to connect the 2 structures. Note that if $j = 0$ we have already calculated the required Green Function. In this case we can set $S_R = 0$. Alternatively, if the structure is infinite, then S^R is just the semi-infinite surface element generated from the right using Eq.(2.58). Combining the two subsections, we have the following:

$$\begin{aligned} G_{i,j} &= G^j_{i,j} + G^j_{i,j}\, t_{j,j+1}\, G_{j+1,j} && (2.65)\\ G_{j+1,j} &= G^j_{j+1,j+1}\, t_{j+1,j}\, G_{j,j} && (2.66)\\ G_{j,j} &= G^j_{j,j} + G^j_{j,j}\, t_{j,j+1}\, G_{j+1,j} \quad . && (2.67) \end{aligned}$$

Inserting the last of these equations in the second gives,

$$\begin{aligned} G_{j+1,j} &= (I - G^j_{j+1,j+1} t_{j+1,j} G^j_{j,j} t_{j,j+1})^{-1} G^j_{j+1,j+1} t_{j+1,j} G^j_{j,j} \\ &= (I - S_R\, t_{RL}\, S_L\, t_{LR})^{-1}\, S_R\, t_{RL}\, S_L \quad . && (2.68) \end{aligned}$$

Inserting this expression in the first equation,

$$G_{i,j} = G^j_{i,j} + G^j_{i,j} t_{LR} (I - S_R t_{RL} S_L t_{LR})^{-1} S_R t_{RL} S_L \quad , \tag{2.69}$$

with $G^j_{i,j}$ given by Eq.(2.63). This gives an expression for generating the propagator

between any two sites, subject to the restriction that the propagator is towards the surface.

Alternatively, if $i > j$, we generate the $-j+1$ block structure coming from the right and connect this to the semi infinite structure terminating at block $j-1$. We begin by calculating the S^i element which is the surface propagator of the $-i+1$ block structure grown from the right. In cases where the system is fully infinite, then S^i is the surface Green Function propagator for a structure grown from the right using Eq.(2.58). To this structure we add an additional $i-j$ blocks which gives,

$$G^j_{i,j} = S^i t_{i,i-1} S^{i-1} t_{i-1,i-2} \cdots S^j \quad . \tag{2.70}$$

This is identical to Eq.(2.63) except that the order of the hopping matrices t_{RL} and t_{LR} have been reversed. Also S^i is now the surface of a finite $-i+1$ block structure. Again, if the finite structure contains no impurities we can write,

$$G^j_{i,j} = (S_R t_{RL})^{i-j} S_R \quad . \tag{2.71}$$

All that remains is to connect the two structures. This involves the calculation of the element $G_{j-1,j}$, which in analogy to Eq.(2.68) can be written as,

$$G_{j-1,j} = (I - S_L t_{LR} S_R t_{RL})^{-1} S_L t_{LR} S_R \quad . \tag{2.72}$$

Hence for $i > j$,

$$G_{i,j} = G^j_{i,j} + G^j_{i,j} t_{RL} (I - S_L t_{LR} S_R t_{RL})^{-1} S_L t_{LR} S_R \quad , \tag{2.73}$$

with $G^j_{i,j}$ given by Eq.(2.70).

Finally, we consider the case where $i = j$. In this case we generate a $-i+1$ block structure from the right, in accordance with the method for the $i > j$ case. Then all that remains is to connect this to the surface emanating from the left.

$$G_{ii} = (I - S_R t_{RL} S_L t_{LR})^{-1} S_R \tag{2.74}$$

Using Eq.(2.69, 2.73, 2.74) as appropriate we can determine the Green Function propagator between any two sites on the semi-infinite structure.

For the case of fully infinite hosts these equations still apply, the only modification being that the structure initially grown from the right is no longer finite. If anything this simplifies matters since the distance from the surface is no longer important.

2.6 The Recursive Method applied to Carbon Nanotubes

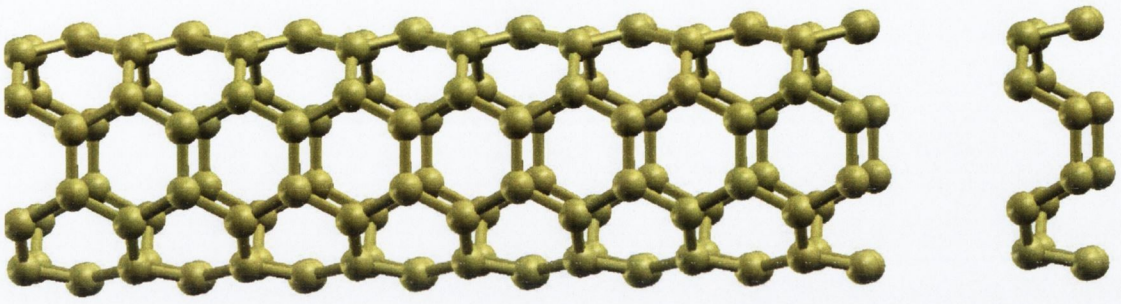


Figure 2.5: A finite (4,4) armchair nanotube. The figure shows the nanotube being grown by progressively attaching isolated rings to the existing tube.

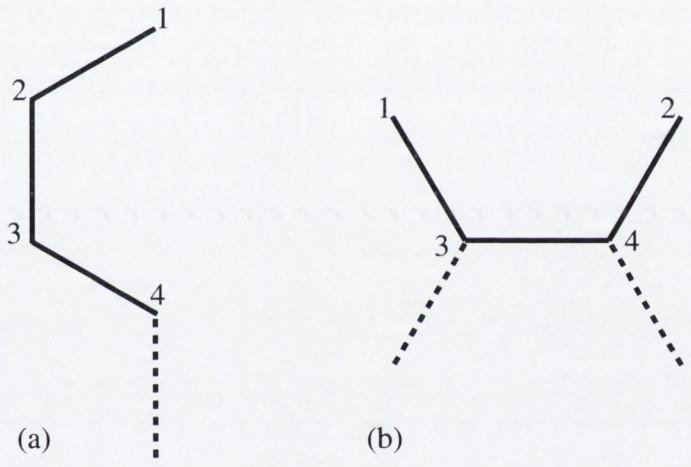


Figure 2.6: Primitive unit cells of (a) an armchair and (b) a zigzag nanotube. N such cells are joined together to form a nanotube ring.

The preceding section has been general in the sense that the particular structure of the infinite or semi-infinite host was not specified. This was so as to avoid unnecessarily restricting the generality of the method; the effect of the particular choice of host is merely to define the matrices H_0 and t_{LR}. To illustrate the method a little more clearly we examine the specific example of a nanotube host.

With a nanotube, the rectangular blocks of figure 2.4 are replaced by rings of carbon atoms, as shown in figure 2.5 for the case of an armchair nanotube. For armchair and zigzag nanotubes, each ring is comprised of N unit cells, each of which contains four atoms. The Hamiltonian, H_0, for each of these isolated rings is

easily written down.

$$H_0 = \begin{pmatrix} H_1 & t_{12} & 0 & 0 & \cdots & 0 & t_{1N} \\ t_{21} & H_2 & t_{23} & 0 & \cdots & 0 & 0 \\ 0 & t_{32} & H_3 & t_{34} & \cdots & 0 & 0 \\ \vdots & \vdots & \vdots & \vdots & \ddots & \vdots & \vdots \\ 0 & 0 & 0 & 0 & \cdots & H_{N-1} & t_{N-1N} \\ t_{N1} & 0 & 0 & 0 & \cdots & t_{NN-1} & H_N \end{pmatrix} . \tag{2.75}$$

Each of the elements in this array is a 4×4 matrix. The block diagonal elements, H_i, are the individual Hamiltonians for each primitive unit cell. These primitive unit cells are shown in figure 2.6. The matrices t_{ij} describes the interaction between primitive cells. It has generally been assumed that the interactions extend only as far as adjacent cells, although this restriction need not apply. The two terms t_{1N}, t_{N1} in the upper and lower corners join the opposite ends of the ring.

For armchair nanotubes the primitive cell Hamiltonian is given by

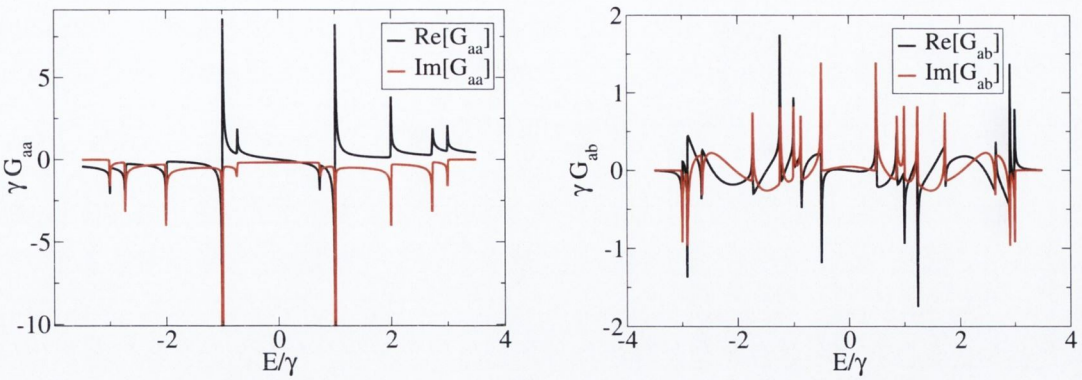
$$H_i = \begin{pmatrix} \epsilon_{i_1} & t & 0 & 0 \\ t & \epsilon_{i_2} & t & 0 \\ 0 & t & \epsilon_{i_3} & t \\ 0 & 0 & t & \epsilon_{i_4} \end{pmatrix} . \tag{2.76}$$

Eq.(2.76) is the Hamiltonian for a simple 4 atom chain. There is no requirement that any of the hopping elements, t, between neighbouring sites be equivalent (i.e. t should strictly be written as $(t_i)_{jk}$). For zigzags, the unit cell has a more complicated topology and the primitive cell Hamiltonian is,

$$H_i = \begin{pmatrix} \epsilon_{i_1} & 0 & t & 0 \\ 0 & \epsilon_{i_2} & 0 & t \\ t & 0 & \epsilon_{i_3} & t \\ 0 & t & t & \epsilon_{i_4} \end{pmatrix} \tag{2.77}$$

As illustrated in figure 2.6, the ring generated by this primitive cell actually consists of two lines of atoms connected along $3 \leftrightarrow 4$, $7 \leftrightarrow 8$ etc. We could also have used a ring comprised of a simple chain, analogous to Eq.(2.76). However the hopping matrices between adjacent rings would then differ for every second ring. This does not present any intrinsic difficulty but from the point of view of portability, it is desirable to retain a situation where adjacent rings are connected by a common hopping matrix.

The adjacent rings are connected by hopping matrices t_{LR} and t_{RL}. For nanotubes these matrices are block diagonal, i.e. they only connect the same unit cell



(a) (6,0) zigzag

(b) (6,6) armchair

Figure 2.7: Recursively generated Green Function propagators. (a) is the diagonal propagator for a (6,0) zigzag. The imaginary part is the local density of states. The singularities at $E = \pm\gamma$ are characteristics of (2N,0) tubes. (b) shows a general off-diagonal propagator on a (6,6) armchair nanotube. In this case the lattice sites are located at (r_1, a_1) and $(r_1 + 3, a_1 - 2)$, with r describing the ring and a the intra-ring site. Only the separation is significant. All units are written in terms of the nearest neighbour hopping γ. For clarity, $\eta = 1 \times 10^{-3}$.

on adjacent rings.

$$t_{LR} = \begin{pmatrix} t_1 & 0 & 0 & \cdots & 0 \\ 0 & t_2 & 0 & \cdots & 0 \\ 0 & 0 & t_3 & \cdots & 0 \\ \vdots & \vdots & \vdots & \ddots & \vdots \\ 0 & 0 & 0 & \cdots & t_N \end{pmatrix} . \tag{2.78}$$

The matrices t_i are primitive hopping matrices. Using the primitive cells in figure 2.6 we see that for armchairs they are given by,

$$t_i = \begin{pmatrix} 0 & t & 0 & 0 \\ 0 & 0 & 0 & 0 \\ 0 & 0 & 0 & 0 \\ 0 & 0 & t & 0 \end{pmatrix} \tag{2.79}$$

and for zigzags,

$$t_i = \begin{pmatrix} 0 & 0 & 0 & 0 \\ t & 0 & 0 & 0 \\ 0 & 0 & 0 & 0 \\ 0 & 0 & 0 & 0 \end{pmatrix} . \tag{2.80}$$

It is then merely a matter of inserting the matrices H_0 and t_{LR} in Eqs.(2.57, 2.58, 2.69, 2.73 and 2.74) to determine the appropriate propagator for an armchair or zigzag nanotube.

As an illustrative example, figure 2.7 shows the diagonal propagator for a (6,0)

zigzag nanotube and a general inter-ring element on a (6,6) armchair. In chapter 3 the propagators for pristine nanotubes generated using recursive methods will be compared with those evaluated using analytic methods.

In the final section of this chapter we look at the treatment of disorder within the recursive method. We consider the concrete example of a (2,2) armchair nanotube doped in turn with substitutional and adsorbed impurities. The choice of a (2,2) nanotube is merely for ease of representation. The procedure for generalising to larger tubes should be obvious.

2.6.1 2 Substitutional Impurities

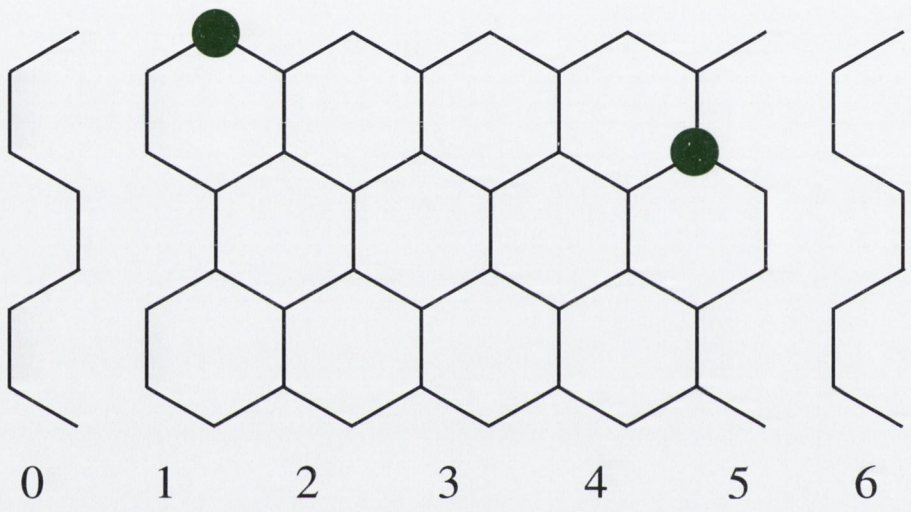


Figure 2.8: A section of an *unwrapped* (2,2) armchair nanotube hosting 2 substitutional impurities. The tube is initially broken into 2 semi-infinite regions and a central 5 ring region containing the impurities.

A (2,2) armchair has an 8 atom ring. We set the carbon on-site energy equal to ϵ_0 and the impurity on-site to λ. If we assume that the 2 impurities are located on ring 1, atom 1 and ring 5, atom 3 (c.f. fig.2.6), then for all other rings the isolated ring Hamiltonian H_0 is given by,

$$H_0 = \left(\begin{array}{cccc|cccc} \epsilon_0 & t & 0 & 0 & 0 & 0 & 0 & t \\ t & \epsilon_0 & t & 0 & 0 & 0 & 0 & 0 \\ 0 & t & \epsilon_0 & t & 0 & 0 & 0 & 0 \\ 0 & 0 & t & \epsilon_0 & t & 0 & 0 & 0 \\ \hline 0 & 0 & 0 & t & \epsilon_0 & t & 0 & 0 \\ 0 & 0 & 0 & 0 & t & \epsilon_0 & t & 0 \\ 0 & 0 & 0 & 0 & 0 & t & \epsilon_0 & t \\ t & 0 & 0 & 0 & 0 & 0 & t & \epsilon_0 \end{array}\right) . \tag{2.81}$$

The corresponding Green Function for an isolated ring is $R_0 = (EI - H_0)^{-1}$. The ring Hamiltonians H_1 and H_5 for the two rings hosting the impurities are given by,

$$H_1 = \left(\begin{array}{cccc|cccc} \epsilon_0+\lambda & t & 0 & 0 & 0 & 0 & 0 & t \\ t & \epsilon_0 & t & 0 & 0 & 0 & 0 & 0 \\ 0 & t & \epsilon_0 & t & 0 & 0 & 0 & 0 \\ 0 & 0 & t & \epsilon_0 & t & 0 & 0 & 0 \\ \hline 0 & 0 & 0 & t & \epsilon_0 & t & 0 & 0 \\ 0 & 0 & 0 & 0 & t & \epsilon_0 & t & 0 \\ 0 & 0 & 0 & 0 & 0 & t & \epsilon_0 & t \\ t & 0 & 0 & 0 & 0 & 0 & t & \epsilon_0 \end{array}\right) \tag{2.82}$$

$$H_5 = \left(\begin{array}{cccc|cccc} \epsilon_0 & t & 0 & 0 & 0 & 0 & 0 & t \\ t & \epsilon_0 & t & 0 & 0 & 0 & 0 & 0 \\ 0 & t & \epsilon_0+\lambda & t & 0 & 0 & 0 & 0 \\ 0 & 0 & t & \epsilon_0 & t & 0 & 0 & 0 \\ \hline 0 & 0 & 0 & t & \epsilon_0 & t & 0 & 0 \\ 0 & 0 & 0 & 0 & t & \epsilon_0 & t & 0 \\ 0 & 0 & 0 & 0 & 0 & t & \epsilon_0 & t \\ t & 0 & 0 & 0 & 0 & 0 & t & \epsilon_0 \end{array}\right) . \tag{2.83}$$

When connecting armchair rings from left to right, the hopping matrix is given by Eq.(2.79)

$$t_{LR} = \left(\begin{array}{cccc|cccc} 0 & t & 0 & 0 & 0 & 0 & 0 & 0 \\ 0 & 0 & 0 & 0 & 0 & 0 & 0 & 0 \\ 0 & 0 & 0 & 0 & 0 & 0 & 0 & 0 \\ 0 & 0 & t & 0 & 0 & 0 & 0 & 0 \\ \hline 0 & 0 & 0 & 0 & 0 & t & 0 & 0 \\ 0 & 0 & 0 & 0 & 0 & 0 & 0 & 0 \\ 0 & 0 & 0 & 0 & 0 & 0 & 0 & 0 \\ 0 & 0 & 0 & 0 & 0 & 0 & t & 0 \end{array}\right) . \tag{2.84}$$

Setting $S_L = R_0$, Eq.(2.57) is applied recursively until the convergence condition $S_L - R_0 t_{RL} S_L t_{LR} S_L = R_0$ is satisfied. The semi-infinite structure is assumed to terminate at ring 0. Applying Eq.(2.58) gives the surface Green Function coming from the right, which terminates at ring 6. The disordered region lies in between, as shown in figure 2.8. Since we wish to calculate the propagator between the two impurities, we first extend the left structure to encompass the rings 1-5. Using Eq.(2.63) we calculate $G^{(5)}_{1,5}$ where the superscript indicates that the structure now

terminates at ring 5. The bulk propagator $G_{1,5}$ is obtained by substituting the expression for $G^{(5)}_{1,5}$ in Eq.(2.69). The required propagator is given by the element (1,3) of the matrix $G_{1,5}$.

2.6.2 Adsorbed Atoms

The treatment of adsorbed atoms is slightly more complicated since in this case the dimension of the matrix will change for rings hosting the impurity. In addition there are a number of positions at which the impurities may wish to locate: either attached to a single carbon atom or at the centre of a hexagon of carbon atoms. Assume first that the impurity is attached to atom 1 on ring 1 with a hopping t'. In this case H_1 is a 9×9 matrix,

$$H_1 = \left(\begin{array}{cccccccc|c} \epsilon_0 & t & 0 & 0 & 0 & 0 & 0 & t & t' \\ t & \epsilon_0 & t & 0 & 0 & 0 & 0 & 0 & 0 \\ 0 & t & \epsilon_0 & t & 0 & 0 & 0 & 0 & 0 \\ 0 & 0 & t & \epsilon_0 & t & 0 & 0 & 0 & 0 \\ 0 & 0 & 0 & t & \epsilon_0 & t & 0 & 0 & 0 \\ 0 & 0 & 0 & 0 & t & \epsilon_0 & t & 0 & 0 \\ 0 & 0 & 0 & 0 & 0 & t & \epsilon_0 & t & 0 \\ t & 0 & 0 & 0 & 0 & 0 & t & \epsilon_0 & 0 \\ \hline t' & 0 & 0 & 0 & 0 & 0 & 0 & 0 & \epsilon_0 + \lambda \end{array}\right) \tag{2.85}$$

The impurity only affects ring 1. However the dimensions of the matrices t_{10} and t_{01} must be altered to apply Eq.(2.57), namely,

$$S_1 = [(E\,I - H_1) - t_{10} S_0 t_{01}]^{-1} \quad . \tag{2.86}$$

Since $EI - H_1$ is a 9×9 matrix, t_{10} must become the 9×8 matrix formed by affixing a row of zero to t_{RL}. The adjoint matrix t_{01} is therefore an 8×9 matrix which ensures the product $t_{10} S_0 t_{01}$ has the correct dimension.

If the impurity is located at a centre site the situation is complicated still further. As seen from figure 2.9, the impurity now affects two adjacent rings. By convention we assume that the site is actually attached to the left of the rightmost of these two rings, labelled ring 1. There are 2 distinct positions within each primitive cell of the ring: either attached to atoms $2, 3$ or $3, 4, 5, 6$. The ring Hamiltonian in the first of these cases is given by,

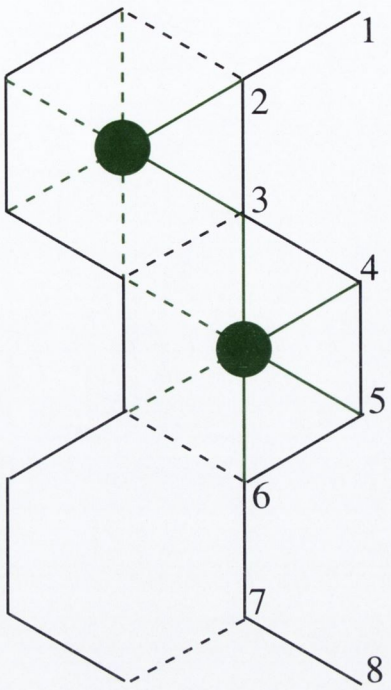


Figure 2.9: Centrally located impurities in an armchair nanotube. By convention the impurities are initially attached to the ring immediately to their right. Intra-ring connections are represented by the solid lines, inter-ring connections by dashed lines. There are seen to be two distinct locations for the impurities within each primitive unit cell.

$$H_1 = \left(\begin{array}{cccccccc|c} \epsilon_0 & t & 0 & 0 & 0 & 0 & 0 & t & 0 \\ t & \epsilon_0 & t & 0 & 0 & 0 & 0 & 0 & t' \\ 0 & t & \epsilon_0 & t & 0 & 0 & 0 & 0 & t' \\ 0 & 0 & t & \epsilon_0 & t & 0 & 0 & 0 & 0 \\ 0 & 0 & 0 & t & \epsilon_0 & t & 0 & 0 & 0 \\ 0 & 0 & 0 & 0 & t & \epsilon_0 & t & 0 & 0 \\ 0 & 0 & 0 & 0 & 0 & t & \epsilon_0 & t & 0 \\ t & 0 & 0 & 0 & 0 & 0 & t & \epsilon_0 & 0 \\ \hline 0 & t' & t' & 0 & 0 & 0 & 0 & 0 & \epsilon_0 + \lambda \end{array}\right) \tag{2.87}$$

and in the second case by,

$$H_1 = \left(\begin{array}{cccccccc|c} \epsilon_0 & t & 0 & 0 & 0 & 0 & 0 & t & 0 \\ t & \epsilon_0 & t & 0 & 0 & 0 & 0 & 0 & 0 \\ 0 & t & \epsilon_0 & t & 0 & 0 & 0 & 0 & t' \\ 0 & 0 & t & \epsilon_0 & t & 0 & 0 & 0 & t' \\ 0 & 0 & 0 & t & \epsilon_0 & t & 0 & 0 & t' \\ 0 & 0 & 0 & 0 & t & \epsilon_0 & t & 0 & t' \\ 0 & 0 & 0 & 0 & 0 & t & \epsilon_0 & t & 0 \\ 0 & 0 & 0 & 0 & 0 & 0 & t & \epsilon_0 & 0 \\ \hline 0 & 0 & t' & t' & t' & t' & 0 & 0 & \epsilon_0 + \lambda \end{array}\right) . \tag{2.88}$$

The matrix t_{01} becomes the 8×9 matrix,

$$t_{01} = \left(\begin{array}{cccccccc|c} 0 & t & 0 & 0 & 0 & 0 & 0 & 0 & t' \\ 0 & 0 & 0 & 0 & 0 & 0 & 0 & 0 & t' \\ 0 & 0 & 0 & 0 & 0 & 0 & 0 & 0 & t' \\ 0 & 0 & t & 0 & 0 & 0 & 0 & 0 & t' \\ 0 & 0 & 0 & 0 & 0 & t & 0 & 0 & 0 \\ 0 & 0 & 0 & 0 & 0 & 0 & 0 & 0 & 0 \\ 0 & 0 & 0 & 0 & 0 & 0 & 0 & 0 & 0 \\ 0 & 0 & 0 & 0 & 0 & 0 & t & 0 & 0 \end{array}\right) , \tag{2.89}$$

since atoms 1, 2, 3, 4 on ring 0 now connect the adsorbed atom attached to ring 1. The second case shown in figure 2.9, in which atoms 4 and 5 on ring 0 connect with the impurity, is given by,

$$t_{01} = \left(\begin{array}{cccccccc|c} 0 & t & 0 & 0 & 0 & 0 & 0 & 0 & 0 \\ 0 & 0 & 0 & 0 & 0 & 0 & 0 & 0 & 0 \\ 0 & 0 & 0 & 0 & 0 & 0 & 0 & 0 & 0 \\ 0 & 0 & t & 0 & 0 & 0 & 0 & 0 & t' \\ 0 & 0 & 0 & 0 & 0 & t & 0 & 0 & t' \\ 0 & 0 & 0 & 0 & 0 & 0 & 0 & 0 & 0 \\ 0 & 0 & 0 & 0 & 0 & 0 & 0 & 0 & 0 \\ 0 & 0 & 0 & 0 & 0 & 0 & t & 0 & 0 \end{array}\right) \tag{2.90}$$

If a given ring hosts more than one impurity then the dimension of the relevant matrices are increased accordingly.

2.7 Summary and Conclusions

In this chapter, all of the basic theoretical machinery that will be employed throughout the thesis was introduced. The methods were based on Green Function techniques. The Green Function was defined and its relationship to the LDOS (d_j) of an individual atomic orbital localised at a site j was shown. Importantly, it also provides direct access to the change in d_j resulting when two sub-systems, initially isolated, are brought into contact. Moreover, it was shown that the change in d_j could be summed explicitly, even with an infinite number of orbitals present. This yields the change in the global density of states, which is fundamental to evaluating changes in a wide range of physical properties of the system. As such, the Green Function is the key quantity underpinning all of these calculations. The presentation in the chapter emphasised the generality of Green Function methods. In particular, all the results can easily be extended to include the effects of multiple orbitals per atom and spin degrees of freedom. The second of these will become important in later chapters.

The second part of the chapter was concerned with technical matters: specifically the development of a method of generating the Green Function matrix elements. The approach chosen was the Recursive Green Function method. This was shown to be a portable technique, well suited to the treatment of nanostructures, since the lateral dimensions of such systems are normally quite small. They are particularly useful for treating systems with a large numbers of impurities, because unlike most approaches, the computational overhead scales with the size of the nanostructure rather than the number of impurities. In the final section the treatment of achiral nanotubes within this framework was shown explicitly.

There is an alternative approach to generating these propagators which proves useful when the matrix elements of the underlying, pristine host are already known. This makes use of Eq.(2.24). The propagators for the pristine system are inserted in this equation to yield the required Green Function propagators for the composite system. In systems with only a few impurities this method is normally far more efficient than the recursive approach, since now the computational overhead scales with the number of impurities rather than the size of host. In addition to being equivalent, the two approaches are actually complimentary since, depending on the specifics of the problem, one is normally more appropriate than the other.

For a pristine achiral nanotube, analytic expressions can be derived for the propagators within a single band model. As a result, when the number of impurities is comparatively small, Eq.(2.24) provides an extremely efficient route to evaluating the updated propagators. The next chapter is dedicated to deriving these expressions.

Chapter 3

Electronic Structure of Achiral Nanotubes

In the previous chapter we introduced Dyson's Equation and the Lloyd Formula method for evaluating many characteristic properties of systems hosting disorder of some kind. Central to the calculation of any of these properties are the lattice Green Function elements of the underlying, pristine host. Normally these are determined by either brute force k-space integration or alternatively by using the recursive methods outlined in chapter 2. We have already seen from Eq.(2.24) that in a disordered system, the required number of matrix elements increases quadratically with the number of impurities. As a result, evaluating the propagators numerically, although by no means prohibitive, can become a time consuming process when the number of impurities is large. Such calculations would be greatly facilitated by the existence of analytic expressions for the pristine Green Function propagators, since these would almost entirely remove the computational overhead in the problem. In the current chapter we will derive closed form expressions for the Green Function propagators between any two sites on an achiral nanotube. The existence of these expressions is a consequence of the particularly simple description of a nanotube in terms of the decoupled π electrons. It is a simple enough matter to extend these expressions to the lattice propagators of semi-infinite nanotubes, and potentially to finite tubes or nanoribbons. The expressions for semi-infinite nanotubes will prove of considerable use when we come to consider the transport properties of nanotubes.

A second advantage of the analytic expressions is that they provide a clear physical description of electron propagation through the nanotube. This interpretation is consistently useful in analysing the features observed throughout this work.

The derivation is essentially straightforward, although the bipartite nature of the graphene lattice does complicate the details. The resulting expressions appear somewhat convoluted although, as stated, they prove invaluable in expediting our calculations. This fact alone justifies the energy expended in their derivation. We

begin by calculating the electronic structure of graphene.

3.1 Graphene

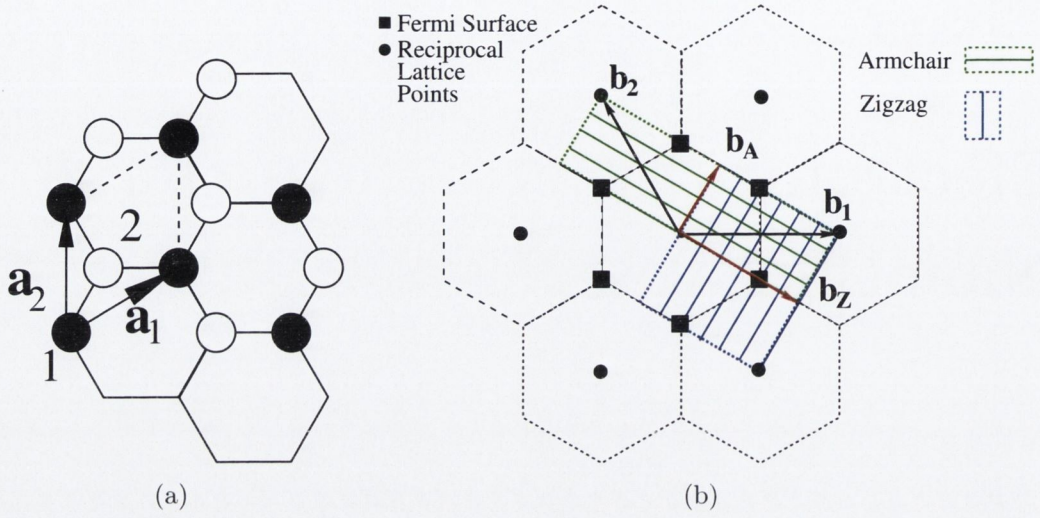


Figure 3.1: (a) Portion of a graphene lattice. The primitive vectors in the $\mathbf{a}_1$ and $\mathbf{a}_2$ directions are shown. Each cell encloses two atoms, labelled 1 (black) and 2 (white). (b) Fermi-surface of graphene. $\mathbf{b_1}$ and $\mathbf{b_2}$ are the reciprocal lattice vectors of graphene. $\mathbf{b}_A$ and $\mathbf{b}_Z$ are vectors along the direction of quantisation for armchair and zigzag nanotubes respectively

The structure of a graphene lattice is shown in figure 3.1(a). Graphene has a bipartite lattice which is normally treated as an underlying triangular Bravais lattice with a two atom unit cell. The location of any carbon atom is described by the triple (ℓ, j, s) where ℓ, j specify the position of the unit cell, $\mathbf{r} = \ell\mathbf{a}_1 + j\mathbf{a}_2$, and $s = 1, 2$ labels the intra-cell atom.

Within a single band tight-binding model, the Hamiltonian is written in a basis of localised orbitals, $|\mathbf{r}, s\rangle$, representing each of the sites in the lattice. The carbon atoms have 4 valence electrons. Three of these form strong sp^2 hybridised bonds. The fourth electron (p_z) is oriented in a plane perpendicular to the lattice. By symmetry this orbital is rigorously decoupled from the other in-plane orbitals and can be treated separately. The in-plane σ-bonded bands lie far from the Fermi-Energy and can be neglected to a good approximation.

The non-zero elements of the Hamiltonian are assumed to extend only to nearest neighbouring sites. This introduces two parameters: ϵ_0, the on-site potential for a p_z-electron on a carbon atom and t_0 (alternatively γ) which represents the probability of an electron hopping to a neighbouring atom.

With this simplification, the Hamiltonian can be written as,

$$\begin{aligned}\hat{H} &= \sum_{\mathbf{r}} \left(\sum_{s=1}^{2} |\mathbf{r}, s\rangle \, \epsilon_0 \, \langle \mathbf{r}, s| \right) \\ &+ |\mathbf{r}, 1\rangle \, t_0 \left(\langle \mathbf{r}, 2| + \langle \mathbf{r} - \mathbf{a}_1, 2| + \langle \mathbf{r} - \mathbf{a}_2, 2| \right) \\ &+ |\mathbf{r}, 2\rangle \, t_0 \left(\langle \mathbf{r}, 1| + \langle \mathbf{r} + \mathbf{a}_1, 1| + \langle \mathbf{r} + \mathbf{a}_2, 1| \right) \quad . \end{aligned} \tag{3.1}$$

Using Bloch's Theorem the eigenvectors are given by,

$$|\mathbf{k}, \alpha\rangle = \frac{1}{\sqrt{N_c}} \sum_{\mathbf{r}} \sum_{s=1}^{2} e^{i\mathbf{k}\cdot\mathbf{r}} A_s \, |\mathbf{r}, \mathbf{s}\rangle \quad . \tag{3.2}$$

N_c is a normalisation factor representing the number of unit cells in the infinite graphene lattice. Applying Eq.(3.2) to Eq.(3.1) gives rise to the characteristic equation,

$$\begin{pmatrix} \epsilon_0 & t^*(\mathbf{k}) \\ t(\mathbf{k}) & \epsilon_0 \end{pmatrix} \begin{pmatrix} A_1 \\ A_2 \end{pmatrix} = \lambda \begin{pmatrix} A_1 \\ A_2 \end{pmatrix} \quad , \tag{3.3}$$

where $t(\mathbf{k}) = t_0(1 + e^{i\mathbf{k}\cdot\mathbf{a}_1} + e^{i\mathbf{k}\cdot\mathbf{a}_2})$. Solving Eq.(3.3) yields the dispersion relation,

$$\begin{aligned}\epsilon_{\pm}(\mathbf{k}) &= \epsilon_0 \\ &\pm |t_0| \sqrt{3 + 2\cos(\mathbf{k}\cdot\mathbf{a}_1) + 2\cos(\mathbf{k}\cdot\mathbf{a}_2) + 2\cos(\mathbf{k}\cdot(\mathbf{a}_1 - \mathbf{a}_2))} \quad , \end{aligned} \tag{3.4}$$

with corresponding eigenvectors,

$$|\mathbf{k}, \pm\rangle = \frac{1}{\sqrt{2N_c}} \sum_{\mathbf{r}} e^{i\mathbf{k}\cdot\mathbf{r}} \left(|\mathbf{r}, 1\rangle \pm e^{i\phi(\mathbf{k})} \, |\mathbf{r}, 2\rangle \right) \quad . \tag{3.5}$$

The phase factor is defined by $e^{i\phi(\mathbf{k})} = t(\mathbf{k})/|t(\mathbf{k})|$.

The eigenvectors form an orthonormal basis in which the Hamiltonian is diagonal,

$$\hat{H} = \sum_{\mathbf{k}} \sum_{\alpha=\pm} |\mathbf{k}, \alpha\rangle \, \epsilon_\alpha(\mathbf{k}) \, \langle \mathbf{k}, \alpha| \quad . \tag{3.6}$$

In Eq.(2.1) the Green Function operator was defined as

$$\hat{G} = \lim_{\eta \to 0} ((E + i\eta)\hat{I} - \hat{H})^{-1} \quad . \tag{3.7}$$

The limit will be dropped in subsequent expressions, as will specific mention to η, but the Green Function should nevertheless be viewed in the limit of $\eta \to 0$. Using Eq.(3.6), the Hamiltonian $\hat{H}$ is already written in a diagonal representation and it

is thus a trivial matter to invert the operator, giving

$$\widehat{G}(E) = \sum_{\mathbf{k}} \sum_{\alpha=\pm} |\mathbf{k}, \alpha\rangle \frac{1}{E + i\eta - \epsilon_\alpha(\mathbf{k})} \langle \mathbf{k}, \alpha| \quad . \tag{3.8}$$

Eq.(3.8) is the eigenvector, or reciprocal space, representation of the Green Function operator. The sum over $\mathbf{k}$ extends over all states in the First Brillouin zone of graphene, which is shown in figure 3.1(b). The basis vectors, $\mathbf{b}_1$ and $\mathbf{b}_2$, are defined in the usual way by the conditions $\mathbf{a}_i \cdot \mathbf{b}_i = 1$ and $\mathbf{a}_i \cdot \mathbf{b}_j = 0$.

We are primarily interested in the lattice representation of the Green Function. This arises from projecting the operator onto the set of real space orbitals,

$$\langle \mathbf{r}, s|\hat{G}|\mathbf{r}', s'\rangle = \sum_{\mathbf{k}} \sum_{\alpha=\pm} \langle \mathbf{r}, s|\mathbf{k}, \alpha\rangle \frac{1}{E + i\eta - \epsilon_\alpha(\mathbf{k})} \langle \mathbf{k}, \alpha|\mathbf{r}', s'\rangle \quad . \tag{3.9}$$

Again, $\mathbf{r}$ and $\mathbf{r}'$ label any two carbon atoms and $s, s' \in \{1, 2\}$ is the intra-cell index. The projection of the lattice vector onto each of the eigenvectors is,

$$\langle \mathbf{r}, 1|\mathbf{k}, \pm\rangle = \sqrt{\tfrac{1}{2N_c}}\, e^{i\mathbf{k}\cdot\mathbf{r}} \quad \langle \mathbf{r}, 2|\mathbf{k}, \pm\rangle = \pm\sqrt{\tfrac{1}{2N_c}}\, e^{i(\mathbf{k}\cdot\mathbf{r} + \phi(\mathbf{k}))} \quad . \tag{3.10}$$

Finally, summing over α gives the expression for the Green Function propagator between any two sites on a graphene lattice,

$$\langle \mathbf{r}, s|\hat{G}|\mathbf{r}', s'\rangle = \frac{1}{N_c} \sum_{\mathbf{k}} \frac{e^{i\mathbf{k}\cdot(\mathbf{r}-\mathbf{r}')}}{(E - \epsilon_0)^2 - |t(\mathbf{k})|^2} \times \begin{cases} (E - \epsilon_0) & , \quad s = s' \\ t^*(\mathbf{k}) & , \quad s, s' = 1, 2 \\ t(\mathbf{k}) & , \quad s, s' = 2, 1 \end{cases} \tag{3.11}$$

with the correct multiplicative factor determined by $s - s'$.

3.2 Nanotubes

The electronic structure of a carbon nanotube is derived from that of graphene by the imposition of an appropriate boundary condition. This quantises the component of momentum along the tube's circumferential direction: $\mathbf{C}_h$. For armchair nanotubes the circumferential vector is $\mathbf{C}_h = N\mathbf{a}_A = N(\mathbf{a}_1 + \mathbf{a}_2)$; for zigzags it lies in the orthogonal direction $\mathbf{C}_h = N\mathbf{a}_Z = N(\mathbf{a}_1 - \mathbf{a}_2)$. The finite integer N describes the circumference of the tube. In the notation of the last chapter this is the number of primitive nanotube cells in the nanotube ring. Written in terms of the chiral indices, (m, n), the armchairs are described by the pair (N, N) and the zigzags by $(N, -N)$. The second case differs from the standard $(N, 0)$ notation used for zigzags, with the circumferential vector in the $\mathbf{a}_1$ direction. The resulting nanotubes will be equivalent since the two directions are equal under a rotation of the graphene sheet

by $\pi/3$ radians, although the propagator between a given pair of lattice sites will obviously depend on the particular choice of wrapping direction. A description in terms of (N, N) and $(N, -N)$ has been selected so that the circumferential directions for both tubes are orthogonal, which allows for the treatment of both cases within a common framework. However, throughout the thesis, whenever a zigzag nanotube is labelled by chiral indices, the canonical form will be adopted. This is done so as to maintain a relation to the standard notation. Thus, for the purpose of calculating matrix elements, a $(N, 0)$ tube should always be understood as actually representing a $(N, -N)$ tube.

The condition $\mathbf{C}_h \cdot \mathbf{k} = 2\pi n$ discretises the allowed values of momentum along the tube's circumferential direction. To better reflect this condition we introduce a new set of reciprocal lattice vectors, $\mathbf{b}_A, \mathbf{b}_Z$, where

$$\begin{aligned} \mathbf{b}_A &= \frac{1}{2}(\mathbf{b}_1 + \mathbf{b}_2) \\ \mathbf{b}_Z &= \frac{1}{2}(\mathbf{b}_1 - \mathbf{b}_2) \,. \end{aligned} \tag{3.12}$$

The momentum components are related by,

$$\begin{aligned} k_A &= k_1 + k_2 \\ k_Z &= k_1 - k_2 \,. \end{aligned} \tag{3.13}$$

Thus, for armchair nanotubes k_A is quantised according to $k_A^n = 2\pi n/N$ while for zigzags k_Z is quantised according to $k_Z^n = 2\pi n/N$ (c.f. fig. 3.1(b)). Nanotubes, as cylindrical objects are most naturally described in terms of orthogonal basis vectors. One describes the longitudinal position along the tube, the other the circumferential. This is seen in the expression for $t(\mathbf{k})$ where the basis transformation decouples the two momenta components,

$$\begin{aligned} |t(\mathbf{k})|^2 &= t_0^2(3 + 2\cos(k_1) + 2\cos(k_2) + 2\cos(k_1 - k_2)) \\ &= t_0^2\left(1 + 4\cos(k_A/2)\cos(k_Z/2) + 4\cos^2(k_Z/2)\right) \,. \end{aligned} \tag{3.14}$$

As seen in figure 3.1(b), the area enclosed by $-\pi \leq k_{A,Z} \leq \pi$ is half that of the First Brillouin Zone of graphene. This is because the new lattice vectors $\mathbf{a}_A$ and $\mathbf{a}_Z$ enclose a four atom unit cell. Rewriting Eq.(3.11) on terms of these new momenta we find,

$$\begin{aligned} \langle \ell, j, s|\hat{G}|\ell', j', s'\rangle &= \frac{1}{N_c}\sum_{k_a, k_z} \frac{e^{i[\frac{k_A}{2}(\Delta\ell + \Delta j) + \frac{k_Z}{2}(\Delta\ell - \Delta j)]}}{(E - \epsilon_0)^2 - |t(k_A/2, k_Z/2)|^2} \\ &\times \begin{cases} E - \epsilon_0 & , \quad s = s' \\ t_0(1 + e^{i\frac{(k_A + k_Z)}{2}\Delta s} + e^{i\frac{(k_A - k_Z)}{2}\Delta s}) & , \quad s \neq s' \end{cases} \end{aligned} \tag{3.15}$$

where $\Delta\ell = \ell - \ell'$, $\Delta j = j - j'$ and $\Delta s = s - s'$.

As we have seen, the corresponding expressions for nanotubes result from quantising the appropriate transverse momentum component, $k^n_{A,Z}$, and then summing over all the allowed states along the longitudinal direction. Since the latter component remains unquantised this involves an integration over k for each mode index n. We take the First Brillouin zone of graphene to extend from $[0, 2\pi)$ in the circumferential direction and $[0, 4\pi)$ in the longitudinal direction. Converting the sum into an integral along the longitudinal component,

$$\frac{1}{N_c}\sum_{\mathbf{k}} = \frac{1}{N}\sum_{k_C}\frac{1}{2N_L}\sum_{k_L} \rightarrow \frac{1}{4N\pi}\sum_{m=1}^{N}\int_{-2\pi}^{2\pi} \quad . \tag{3.16}$$

The factor of 2 in the second expression arises because the area enclosed by the primitive nanotube vectors $\mathbf{a}_A$ and $\mathbf{a}_Z$ contains 4 carbon atoms, whereas $\mathbf{a}_1 \times \mathbf{a}_2$ contains only 2. For armchair tubes Eq.(3.15) then becomes,

$$\begin{aligned}\langle \ell, j, s|\hat{G}|\ell', j', s'\rangle &= \frac{1}{2\pi N}\sum_{m=1}^{N}\int_{-\pi}^{\pi} dk_Z \frac{e^{i[\frac{m\pi}{N}(\Delta\ell+\Delta j)+k_Z(\Delta\ell-\Delta j)]}}{(E-\epsilon_0)^2 - |t(\frac{m\pi}{N}, k_Z)|^2} \\ &\times \begin{cases} E-\epsilon_0 & , \ s = s' \\ t_0(1+2e^{i\frac{m\pi}{N}\Delta s}\cos(k_Z)) & , \ s \neq s' \end{cases} \quad . \end{aligned} \tag{3.17}$$

For zigzag tubes,

$$\begin{aligned}\langle \ell, j, s|\hat{G}|\ell', j', s'\rangle &= \frac{1}{2\pi N}\sum_{m=1}^{N}\int_{-\pi}^{\pi} dk_A \frac{e^{i[k_A(\Delta\ell+\Delta j)+\frac{m\pi}{N}(\Delta\ell-\Delta j)]}}{(E-\epsilon_0)^2 - |t(k_A, \frac{m\pi}{N})|^2} \\ &\times \begin{cases} E-\epsilon_0 & , \ s = s' \\ t_0(1+2e^{ik_A\Delta s}\cos(\frac{m\pi}{N})) & , \ s \neq s' \end{cases} \quad . \end{aligned} \tag{3.18}$$

All that remains is to evaluate the integrals. The general method for doing so is outlined in the next section.

3.2.1 Poles

Eq.(3.17) and Eq.(3.18) are integrals of the form

$$I(D) = \frac{1}{2N\pi}\int_{-\pi}^{\pi} dk \frac{e^{ikD}}{f(k)} \quad , \tag{3.19}$$

where $f(k)$ is an even, periodic function with period 2π. Such integrals are normally evaluated using the Residue Theorem of complex analysis[54]. In essence this involves allowing k to become a complex valued variable and then finding the zeros of the denominator of $f(k)$. These zeros are known as poles and are written as k_i.

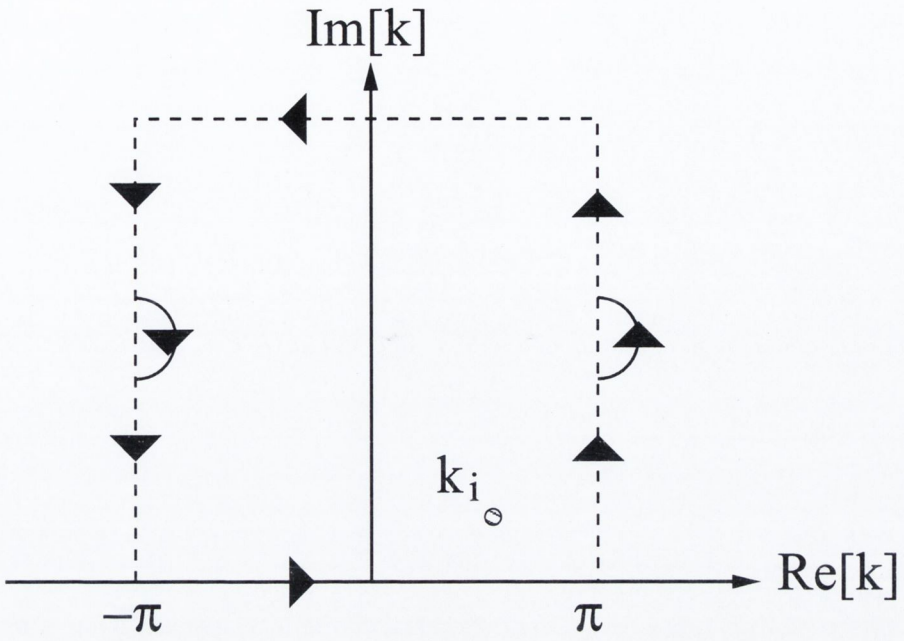


Figure 3.2: A closed integration contour in the upper half k-space plane. k_i marks the position of a pole of $f(k)$ lying in the UHP. The integrand vanishes along the upper contour. The net contribution to Eq.(3.19) from the left and right contours is zero due to the assumed periodicity of the function.

Assume, for the moment, that they do not lie on the real axis. Then, if $D \geq 0$, the integrand will vanish in the Upper Half Plane(UHP), in which $\mathrm{Im}(k) > 0$. If we consider the contour shown in figure 3.2, the integrand cancels along the zone boundaries (due to the integrand's periodicity) and the integration reduces to a sum of the residues over the N poles in the UHP[54],

$$I(D) = \frac{2\pi i}{2\pi N} \sum_{i=1}^{N} \frac{e^{ik_i D}}{\frac{df(k)}{dk}\Big|_{k_i}} \quad . \tag{3.20}$$

For the case $D < 0$ the analysis is exactly the same except the contributing poles are now $k_i' = -k_i$ and we pick up an overall minus sign since the contour is now traversed in the clockwise direction. Because $f(k)$ is an even function, $f'(k)$ is odd and

$$I(-|D|) = -\frac{2\pi i}{2\pi N} \sum_{i=1}^{N} \frac{e^{-ik_i'|D|}}{\frac{df(k)}{dk}|_{k_i'}} = \frac{2\pi i}{2\pi N} \sum_{i=1,N} \frac{e^{ik_i|D|}}{\frac{df(k)}{dk}|_{k_i}} = I(|D|) \quad . \tag{3.21}$$

Thus, the integral $I(D)$ is symmetric under $D \rightarrow -D$ and we can always consider D to be positive.

Of course the actual value of the residue and the number of contributing poles will depend on the particular form of $f(k)$ and this will be different for each nanotube. The presence of the non-zero imaginary energy, η, ensures that the poles reside off

the real axis[1]. For armchair and zigzag nanotubes, with respective quantisation in the k_A and k_Z directions the zeros of $f(k)$ are defined by of the following equations,

$$\begin{aligned}
\cos(k_Z) &= -\frac{1}{2}\cos(\frac{m\pi}{N}) \pm \frac{1}{2}\sqrt{\left(\frac{E+i\eta-\epsilon_0}{t_0}\right)^2 - \sin^2(\frac{m\pi}{N})} \quad (a.n.) \\
\cos(k_A) &= \frac{1}{4\cos(\frac{m\pi}{N})}\left[\left(\frac{E+i\eta-\epsilon_0}{t_0}\right)^2 - 1 - 4\cos^2(\frac{m\pi}{N})\right] \quad (z.n.) \quad . \quad (3.22)
\end{aligned}$$

The second expression is not valid when $m/N = 1/2$, which occurs for zigzag nanotubes when N is even.

Each solution of Eq.(3.22) is an equation of the form $\cos(k_m(E)) = w(m, E)$. It is easily seen that the values of k_m satisfying $k_m(E) = \cos^{-1}(w(m, E))$ are separated by 2π. Thus, for a giving solution, exactly one pole resides within the contour. With an armchair nanotube, for each value of E and m there are two branches to consider. For zigzags there is single pole. In each case the poles are then defined by $k_m(E) = k_1(E) + ik_2(E) = \cos^{-1}(w(E, m))$ subject to the constraint that $k_2 > 0$ and $-\pi < k_1 \leq \pi$.

We can introduce a pair of analogous functions, $I^{A,Z}(m, D)$, for armchair and zigzag tubes. The subscript m labels the transverse mode and D is the integer separation between rings in the longitudinal direction. The integral is then given by Eq.(3.20). Explicitly,

$$\begin{aligned}
I^A(m, D) &= \frac{1}{2\pi N}\int_{-\pi}^{\pi} dk \frac{e^{ikD}}{(E-\epsilon_0)^2 - t_0^2(1 + 4\cos(\frac{m\pi}{N})\cos(k) + 4\cos^2(k))} \\
&= \frac{i}{4Nt_0^2}\sum_{p=\pm}\frac{e^{ik_m^p(E)|D|}}{[\cos(\frac{m\pi}{N}) + 2\cos(k_m^p(E))]\sin(k_m^p(E))} \quad , \quad (3.23)
\end{aligned}$$

and

$$\begin{aligned}
I^Z(m, D) &= \frac{1}{2\pi N}\int_{-\pi}^{\pi} dk \frac{e^{ikD}}{(E-\epsilon_0)^2 - t_0^2(1 + 4\cos(\frac{m\pi}{N})\cos(k) + 4\cos^2(\frac{m\pi}{N}))} \\
&= \frac{i}{4Nt_0^2}\frac{e^{ik_m(E)|D|}}{\cos(\frac{m\pi}{N})\sin(k_m(E))} \quad . \quad (3.24)
\end{aligned}$$

The integrals in Eq.(3.17) and Eq.(3.18) have now been evaluated. All that remains is to write down the final form of the propagators.

[1]which is perhaps not so surprising since this quantity ensures that the Green Function is well defined.

3.2.2 Armchair Nanotubes

From Eq.(3.17), the calculation of a general matrix element for an armchair nanotube results from the evaluation of the $I^A(m, \Delta\ell - \Delta j)$ and $I^A(m, \Delta\ell - \Delta j \pm \Delta s)$ integrals. Distinguishing the cases of $\Delta s = 0$ and $\Delta s \neq 0$,

$$\begin{aligned}
\langle \ell, j, s|\hat{G}|\ell' j', s\rangle &= \frac{i}{4Nt_0^2}(E + i\eta - \epsilon_0)\sum_{m=1}^{N} e^{i\frac{m\pi}{N}(\Delta\ell+\Delta j)} \\
&\times \sum_{p=1}^{2} \frac{e^{ik_m^p(E)|\Delta\ell-\Delta j|}}{[\cos(\frac{m\pi}{N}) + 2\cos(k_m^p(E))]\sin(k_m^p(E))} \\
\langle \ell, j, s|\hat{G}|\ell' j', s'\rangle &= \frac{i}{4Nt_0}\sum_{m=1}^{N} e^{i\frac{m\pi}{N}(\Delta\ell+\Delta j)} \\
&\times \sum_{p=1}^{2}\left(\frac{e^{ik_m^p(E)|\Delta\ell-\Delta j|}}{[\cos(\frac{m\pi}{N}) + 2\cos(k_m^p(E))]\sin(k_m^p(E))}\right. \\
&+ \left. e^{i\frac{m\pi}{N}\Delta s}\frac{e^{ik_m^p(E)|\Delta\ell-\Delta j+\Delta s|} + e^{ik_m^p(E)|\Delta\ell-\Delta j-\Delta s|}}{[\cos(\frac{m\pi}{N}) + 2\cos(k_m^p(E))]\sin(k_m^p(E))}\right) \qquad (3.25)
\end{aligned}$$

Each of the $2N$ modes propagate with an energy dependent wavevector $k_m^p(E)$. For the case where $\Delta\ell - \Delta j = 0$ the propagator behaves slightly differently due to the presence of the modulus sign. In this case, we can write

$$1 + 2e^{i\frac{\pi m}{N}}e^{ik} = 1 + 2e^{i\frac{\pi m}{N}}\cos(k) + 2ie^{i\frac{\pi m}{N}}\sin(k) \quad . \qquad (3.26)$$

It follows that

$$\frac{1 + 2e^{i\frac{\pi m}{N}}e^{ik}}{\left(\cos(\frac{m\pi}{N}) + 2\cos(k)\right)\sin(k)} = \frac{1 + 2e^{i\frac{\pi m}{N}}\cos(k)}{\left(\cos(\frac{m\pi}{N}) + 2\cos(k)\right)\sin(2k)} + 2i\frac{e^{i\frac{\pi m}{N}}}{\cos(\frac{m\pi}{N}) + 2\cos(k)} \quad . \qquad (3.27)$$

Summing over the $p = \pm$ contributions in the second term we get,

$$\begin{aligned}
& 2ie^{i\frac{\pi m}{N}}\left(\frac{1}{\cos(\frac{m\pi}{N}) + 2\cos(k^+)} + \frac{1}{\cos(\frac{m}{N}\pi) + 2\cos(k^-)}\right) \qquad (3.28) \\
= \; & 2ie^{i\frac{\pi m}{N}}\frac{2\cos(\frac{m\pi}{N}) + 2(\cos(k^+) + \cos(k^-))}{(\cos(\frac{m\pi}{N}) + 2\cos(k^-))(\cos(\frac{m\pi}{N}) + 2\cos(k^+))} \quad . \qquad (3.29)
\end{aligned}$$

From Eq.(3.22), $2(\cos(k^+) + \cos(k^-)) = -\cos(\frac{m\pi}{N})$ so that the total contribution from the second term is zero.

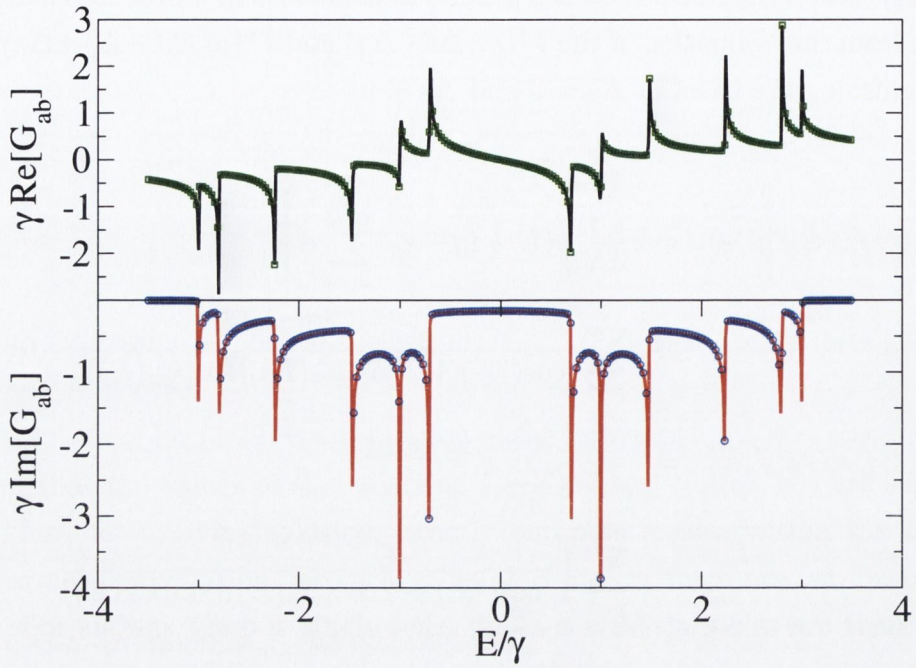


Figure 3.3: Real and imaginary parts of the on-site Green Function for a (4,4) armchair nanotube. The solid lines are the analytic results. For comparison the same propagator, generated recursively, is overlaid. The number of points has been reduced to aid the comparison. The agreement is seen to be perfect.

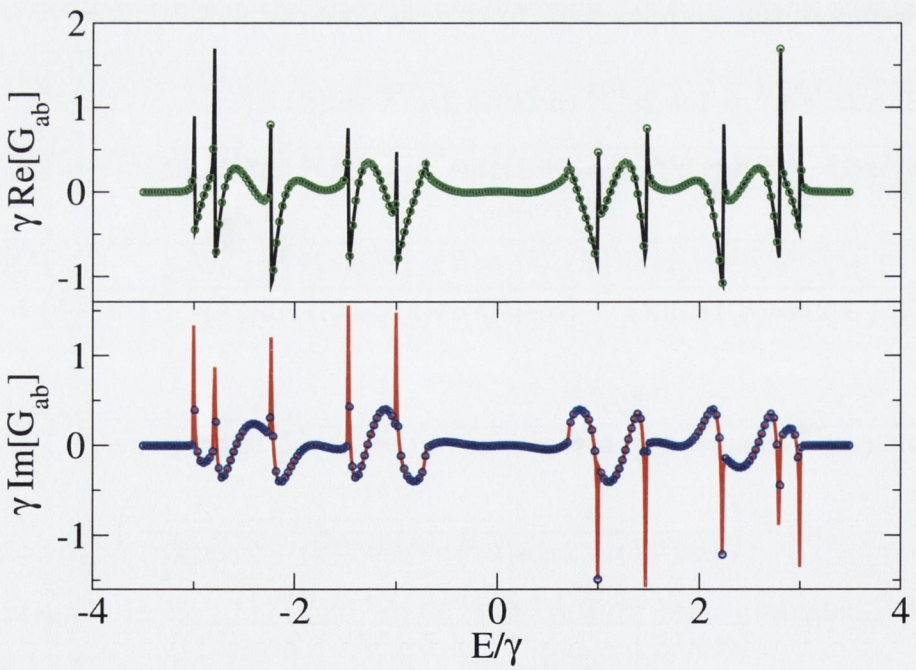


Figure 3.4: Real and imaginary parts of the off-site Green Function for a (4,4) armchair given by $\Delta\ell = -4$, $\Delta j = 5$, $\Delta s = -1$. The solid lines are the analytic results and the points are the recursive results. The agreement is seen to be perfect.

This enables us to write Eq.(3.25) in its final form,

$$\begin{aligned}
\langle \ell, j, s|\hat{G}|\ell' j', s\rangle &= \frac{i}{Nt_0^2}(E+i\eta-\epsilon_0)\sum_{m=1}^{N} e^{i\frac{m\pi}{N}(\Delta\ell+\Delta j)} \\
&\times \sum_{p=1}^{2} \frac{e^{ik_m^p(E)|\Delta\ell-\Delta j|}}{[\cos(\frac{m\pi}{N})+2\cos(k_m^p(E))]\sin(k_m^p(E))} \\
\langle lj, s|\hat{G}|l' j', s'\rangle &= \frac{i}{Nt_0}\sum_{m=1}^{N} e^{i\frac{m\pi}{N}(\Delta\ell+\Delta j)} \\
&\times \sum_{p=1}^{2} \frac{e^{ik_p(E,m)|\Delta\ell-\Delta j|}(1+2e^{i\frac{m\pi}{N}\Delta s}\cos(k))}{[\cos(\frac{m\pi}{N})+2\cos(k_m^p(E))]\sin(k_m^p(E))} \quad . \qquad (3.30)
\end{aligned}$$

The factor $1+2e^{i\frac{m\pi}{N}\Delta s}\cos(k)$ satisfies $|1+2e^{i\frac{m\pi}{N}\Delta s}\cos(k)|^2 = (E/t_0)^2$. The above equations represent the contribution from the $2N$ propagating modes at the given energy. They can be written in the form

$$\langle lj, s|\hat{G}|l' j', s\rangle = \sum_m \chi_m(\Delta\ell+\Delta j)e^{ik_m|\Delta\ell-\Delta j|} \quad . \qquad (3.31)$$

Each mode contributes a term which oscillates with the longitudinal separation to the total Green Function. This form emphasises that the nanotube is a 1-D conductor with a finite cross sectional area described by χ_m. This finite cross section gives rise to the additional propagating modes. However, a nanotube differs from a general quasi 1-D conductor in that most of the wavevectors are evanescent at any given energy. Close to the Fermi-Energy only two modes give extended contributions. This is easily seen by re-writing the first term in Eq.(3.22) as

$$\left(2\cos(k_m^{\pm})+\cos(\frac{m\pi}{N})\right)^2+\sin^2(\frac{m\pi}{N}) = (E+i\eta)^2/t_0^2 = -(\eta/t_0)^2 \approx 0 \quad . \qquad (3.32)$$

This can only be satisfied if both terms on the left are separately zero, which requires that m be some multiple of N.

Figures 3.3 and 3.4 are plots of Eq.(3.30) for two different lattice sites. The points overlaid correspond to the same propagator calculated using the recursive methods of chapter 2. These are more sparsely plotted to allow for clear comparison. The graphs show that the results of the analytic and recursive methods are in exact agreement.

3.2.3 Zigzag Nanotubes

For zigzags, Eq.(3.18) involves evaluation of the integrals $I^Z(m, \Delta\ell+\Delta j)$ and $I^Z(m, \Delta\ell+\Delta j+\Delta s)$.

$$\langle \ell, j, s|\hat{G}|\ell', j', s'\rangle = \frac{i}{4Nt_0^2}\sum_{m=1}^{N}\frac{e^{i\frac{m\pi}{N}(\Delta\ell-\Delta j)}}{\cos\left(\frac{m\pi}{N}\right)\sin(k_m(E))} \times \begin{cases} (E+i\eta-\epsilon_0)\ e^{ik_m(E)|\Delta\ell+\Delta j|} & s=s' \\ t_0\left(2\cos\left(\frac{m\pi}{N}\right)e^{ik_m(E)|\Delta\ell+\Delta j+\Delta s|}\right. & \\ \left.+\ e^{ik_m(E)|\Delta\ell+\Delta j|}\right) & s\neq s' \end{cases} \tag{3.33}$$

Separation of the terms $|\Delta\ell+\Delta j+\Delta s|$ as $|\Delta\ell+\Delta j|+\Delta s$ is not as simple as in the case of armchairs, since the propagators are no longer symmetric under changes in the sign of the longitudinal separation $\Delta\ell+\Delta j \rightarrow -(\Delta l+\Delta j)$.

There is also a peculiarity to be considered for even N zigzag nanotubes. For $m = N/2$ the denominator in $I^Z(m, D)$ loses its k-dependence. Physically, this corresponds to two dispersionless bands, located at $E = \pm t_0$. These bands were previously seen in figure 1.5(b). The k-space integration is trivial in this case and only gives a non-zero contribution when $\Delta\ell = -\Delta j$, which corresponds to both sites lying on the same line of atoms in the transverse direction of the tube. In this case we add a term,

$$\frac{1}{N}\frac{e^{i\pi\Delta\ell}}{(E+i\eta-\epsilon_0)^2-t_0^2}\begin{cases} E+i\eta-\epsilon_0 & s=s' \\ t_0 & s\neq s' \end{cases} \qquad m=\frac{N}{2}\ , \tag{3.34}$$

to Eq.(3.33).

As with armchairs not all of the wavemodes will contribute at the Fermi-Energy; indeed, for zigzags, depending on the diameter of the tube there may be no extended state at all. This is seen from the second expression in Eq.(3.22),

$$\left(2\cos(\frac{m\pi}{N})+\cos(k_m)\right)^2+\sin^2(k_m) = -(\eta/t_0)^2 \approx 0 \quad . \tag{3.35}$$

This is just Eq.(3.32) with the order of k and $\frac{m\pi}{N}$ reversed. For it to hold N must be a multiple of 3 and $k_m \approx m\pi$, so that only the $n = N, 2N$ modes contribute.

Figures 3.5 and 3.6 show the propagators calculated using Eq.(3.33). In both cases the agreement with the recursive propagators is seen to be exact. In figure 3.6, the lattice sites lie on the same line in tube's transverse direction (i.e. they lie at equivalent vertices on the zigzag chain). For both the analytic and recursive cases, the bound state predicted by Eq.(3.34) is clearly visible.

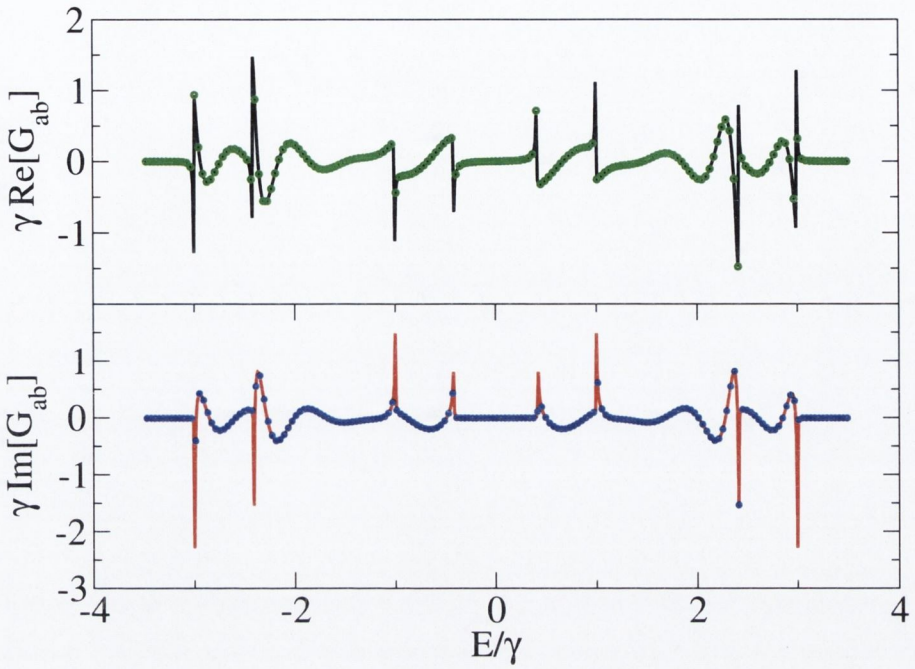


Figure 3.5: Real and imaginary parts of an off-site Green Function propagator of a semiconducting (4,0) tube. The lattice sites are separated by $\Delta\ell = 4$, $\Delta j = 4$, $\Delta s = 0$. The solid lines are the analytic results. Included for comparison are selected points of the same propagator generated recursively.

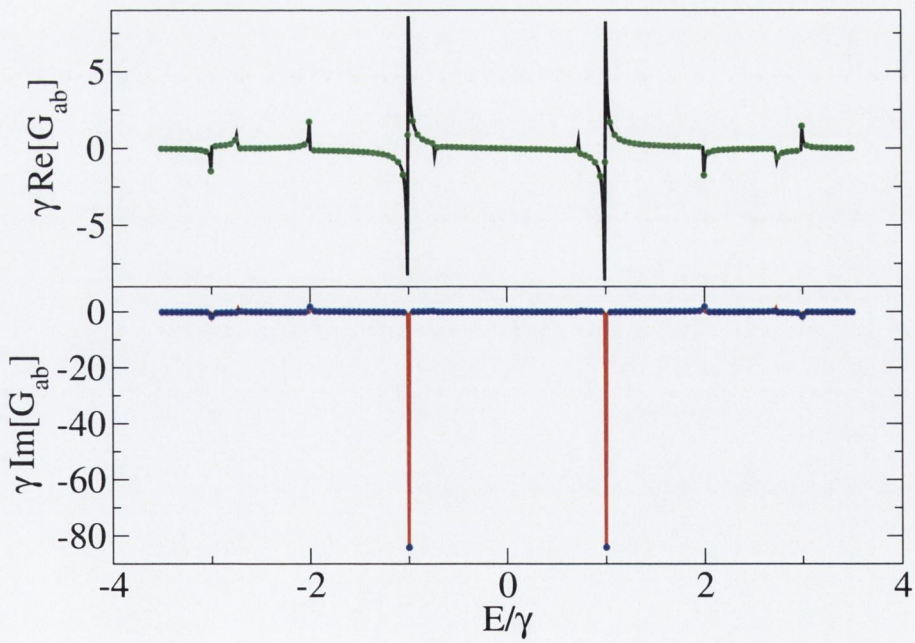


Figure 3.6: Real and imaginary parts of an off-site Green Function of a metallic (6,0) tube. The lattice sites are separated by $\Delta\ell = -2$, $\Delta j = 2$, $\Delta s = 0$. The sites lie along the same line of carbon atoms in the tube's transverse direction. The solid lines are the analytic results. For comparison, the recursive results have been overlaid. The predicted bound state at $E = \pm t_0(\gamma)$ is found to be present in both approaches.

3.3 Analytic Green Function Propagators for Semi-infinite Tubes

The treatment outlined above is easily extended to provide closed form expressions for propagators between sites on semi-infinite tubes. These will be used later on in transport calculations, where the leads in the system will be represented by semi-infinite nanotubes. A second case in which they would conceivably prove useful is in describing nanotube heterojunctions: composite tubes formed by connecting two nanotubes of differing diameters or chiralities[55].

A semi-infinite graphene sheet is not translationally invariant and hence Bloch's Theorem cannot be applied directly. Nevertheless by forming superpositions of the eigenvectors of the infinite tube which give rise to zero electronic density along the line defining the surface, we can replicate the electronic structure of the semi-infinite case. This superposition will generate additional terms in the expression; however the form of each term will be unchanged from those given by Eq.(3.23) and Eq.(3.24). Therefore once the new eigenvectors are determined it is a simple matter to write down the Green Function.

3.3.1 Armchairs

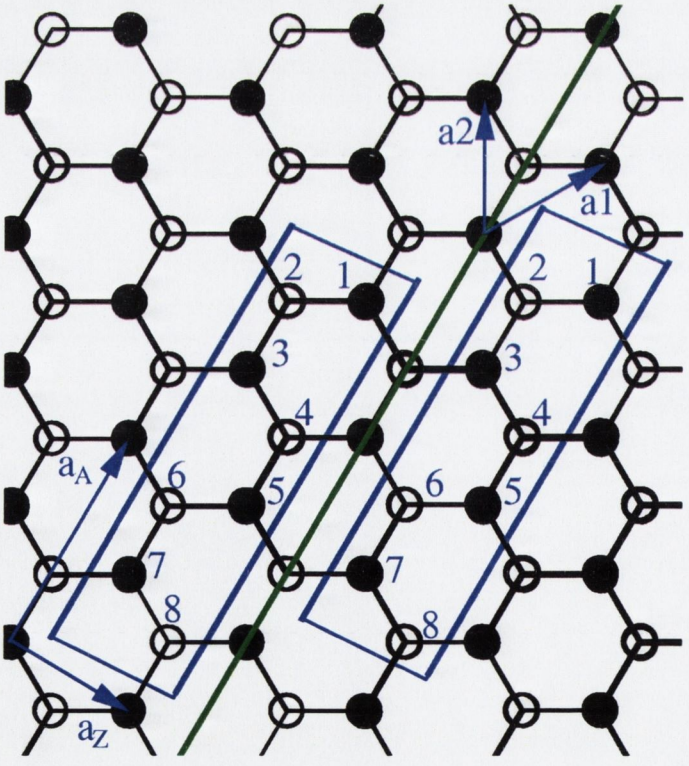


Figure 3.7: Cut plane of graphene. The electronic density vanishes along the green line. The blue square identifies the armchair unit ring (c.f. fig. 2.6) with the intra-ring atoms numbered as shown.

For armchairs we define the eigenvectors representing the semi-infinite tube as follows: Writing Eq.(3.5) in terms of the basis vectors $\mathbf{b}_A, \mathbf{b}_z$, it is not difficult to see that $|k_A, k_Z, \pm\rangle$ and $|k_A, -k_Z, \pm\rangle$ are eigenvectors of $\hat{H}$ with the same eigenvalue: $\epsilon_\pm(k_A, k_Z)$. Hence any linear combination of these states will also be an eigenvector with the same eigenvalue. We attempt to construct a new orthonormal set of eigenvectors such that the probability of finding an electron in the state $|\Psi_\mathbf{k}, \pm\rangle$ vanishes for $s = 1, 2$ along the line $\ell = j$. This line is shown in figure 3.7. To this end we define

$$\begin{aligned} |\Psi(k_A, k_Z), \pm\rangle &= \frac{1}{\sqrt{2}}\left(|k_A, k_Z, \pm\rangle - |k_A, -k_Z, \pm\rangle\right) \\ &= \frac{1}{\sqrt{4N_c}} \sum_{\ell,j} e^{i\frac{k_A}{2}(\ell+j)} \Big[\left(e^{i\frac{k_Z}{2}(\ell-j)} - e^{-i\frac{k_Z}{2}(\ell-j)}\right) |\mathbf{r}, 1\rangle \\ &\pm e^{i\phi(\mathbf{k})} \left(e^{i\frac{k_Z}{2}(\ell-j)} - e^{-i\frac{k_Z}{2}(\ell-j)}\right) |\mathbf{r}, 2\rangle \Big] \quad . \end{aligned} \tag{3.36}$$

The real space projection onto these eigenvectors is,

$$\langle \mathbf{r}, 1|\Psi_\mathbf{k}, \pm\rangle = \frac{i}{\sqrt{N_c}} \sin\left(\frac{k_Z}{2}(\ell - j)\right) e^{i\frac{k_A}{2}(\ell+j)} \tag{3.37}$$

$$\langle \mathbf{r}, 2|\Psi_\mathbf{k}, \pm\rangle = \pm\frac{i}{\sqrt{N_c}} \sin\left(\frac{k_Z}{2}(\ell - j)\right) e^{i\frac{k_A}{2}(\ell+j)} e^{i\phi(\mathbf{k})} \quad . \tag{3.38}$$

As required, the probability density $|\langle \ell, j, s|\Psi(k_A, k_Z), \pm\rangle|^2$ is zero along the line $j = \ell$. This defines the surface of the armchair nanotube.

For compactness the following definitions are introduced: $\Sigma\ell = \ell + \ell'$, $\Delta\ell = \ell - \ell'$, $\Sigma j = j + j'$, $\Delta j = j - j'$, $\Delta s = s - s'$. For an infinite tube the propagators depend only on the separation of the sites and not on their absolute positions. This is no longer the case for a semi-infinite tube since the surface breaks the overall translational invariance of the system. The propagators now depend not only on the separation of the sites but on their absolute location within the tube. This is reflected by the addition of the terms in $\Sigma\ell$ and Σj.

Projecting the lattice sites onto the Green Function operator gives exactly the same relation as Eq.(3.9), only with $|\mathbf{k}, \pm\rangle$ replaced by $|\Psi_\mathbf{k}, \pm\rangle$,

$$\langle \mathbf{r}, s|\hat{G}|\mathbf{r}', s'\rangle = 2\sum_\mathbf{k} \frac{\langle \mathbf{r}, s|\Psi_\mathbf{k}, +\rangle\langle\Psi_\mathbf{k}, +|\mathbf{r}', s'\rangle}{(E - \epsilon_0)^2 - |t(\mathbf{k})|^2} \begin{cases} E - \epsilon_0 & s - s' = 0 \\ |t(\mathbf{k})| & s - s' \neq 0 \end{cases} .$$

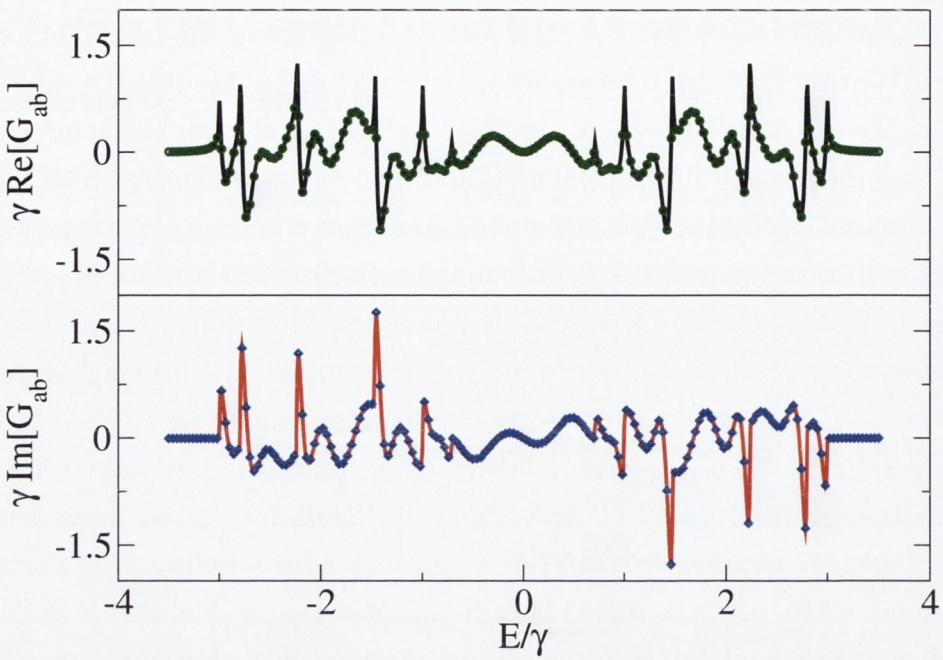


Figure 3.8: Green Function propagator G(-2, 2; -5, 1), between atom 2 on ring -2 and atom 1 on ring -5 of a semi-infinite (4,4) armchair calculated analytically (solid lines) and recursively (points).

The projections are given by,

$$\begin{aligned}\langle \mathbf{r}, s|\Psi_{\mathbf{k}}, \pm\rangle\langle\Psi_{\mathbf{k}}, \pm|\mathbf{r}', s\rangle &= \frac{1}{4N_c}\left(e^{i\frac{k_Z}{2}(\Delta\ell-\Delta j)} - e^{i\frac{k_Z}{2}(\Sigma\ell-\Sigma j)} + c.c.\right) \\ &\times\ e^{i\frac{k_A}{2}(\Delta\ell+\Delta j)} \qquad (3.39)\\ \langle \mathbf{r}, s|\Psi_{\mathbf{k}}, \pm\rangle\langle\Psi_{\mathbf{k}}, \pm|\mathbf{r}', s'\rangle &= \pm\frac{1}{4N_c}\left(e^{i\frac{k_Z}{2}(\Delta\ell-\Delta j)} - e^{i\frac{k_Z}{2}(\Sigma\ell-\Sigma j)} + c.c.\right) \\ &\times\ e^{i\frac{k_A}{2}(\Delta\ell+\Delta j)}e^{i\phi(\mathbf{k})\Delta s} \quad . \qquad (3.40)\end{aligned}$$

c.c. denotes the complex conjugate. Each term is still of the form $I^A(m, D)$; specifically $I^A(m, \Delta\ell - \Delta j)$ and $I^A(m, \Sigma\ell - \Sigma j)$. The complex conjugates in Eq.(3.40) provide a simple multiplicative factor, due to the invariance of $I^A(m, D)$ under $D \to -D$. It is now merely a case of writing down the expression for the propagators. For intra-sublattice terms ($s = s'$),

$$\begin{aligned}\langle \ell j, s|\hat{G}|\ell', j', s\rangle &= \frac{i}{4Nt_0^2}(E + i\eta - \epsilon_0)\sum_{m=1}^{N} e^{i\frac{m\pi}{N}(\Delta\ell+\Delta j)} \\ &\times \sum_{p=1}^{2}\frac{e^{ik_m^p(E)|\Delta\ell-\Delta j|} - e^{ik_m^p(E)|\Sigma\ell-\Sigma j|}}{[\cos(\frac{m\pi}{N}) + 2\cos(k_m^p(E))]\sin(k_m^p(E))} \quad . \qquad (3.41)\end{aligned}$$

The treatment of the inter-sublattice terms ($s \neq s'$) is exactly the same although the number of terms involved leads to a somewhat messy looking expression. There are 6 separate integrals: $I^A(m, \Delta\ell - \Delta j)$, $I^A(m, \Delta\ell - \Delta j \pm \Delta s)$, $I^A(m, \Sigma\ell - \Sigma j)$,

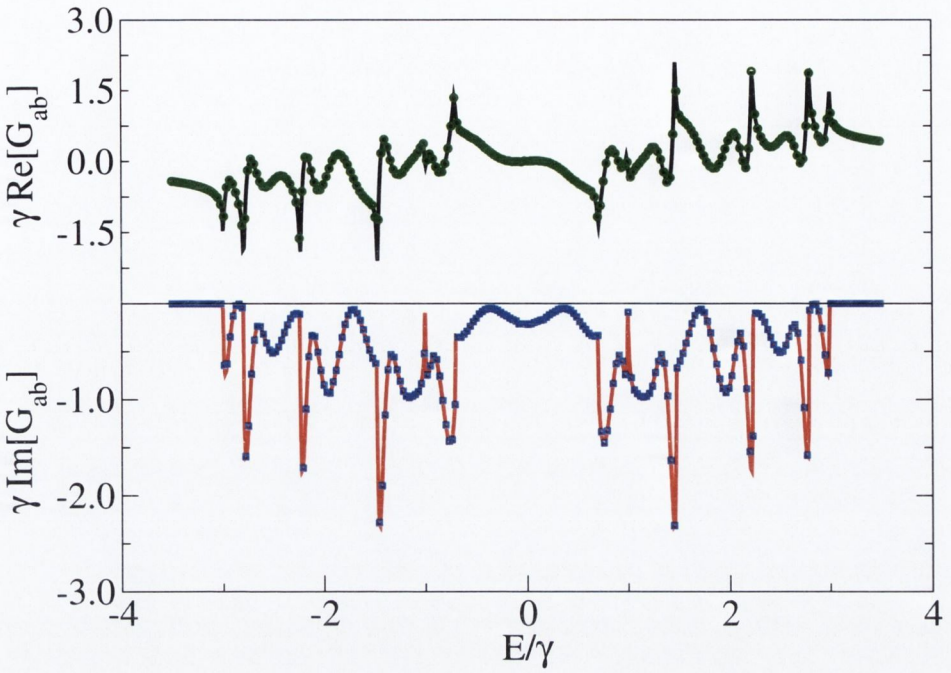


Figure 3.9: On-site Green Function G(-3,3;-3,3) of atom 3 on ring -3. The nanotube is a semi-infinite (4,4) armchair. The propagator has been calculated analytically (solid lines) and recursively (points).

$I^A(m, \Sigma\ell - \Sigma j \pm \Delta s)$ leading to,

$$\begin{aligned}
\langle \ell, j, s|\hat{G}|\ell', j', s'\rangle &= \frac{i}{4Nt_0}\sum_{n=1}^{N} e^{i\frac{m\pi}{N}(\Delta\ell+\Delta j)} \sum_{p=1}^{2} \frac{e^{ik_m^p(E)|\Delta\ell-\Delta j|} - e^{ik_m^p(E)|\Sigma\ell-\Sigma j|}}{[\cos(\frac{m\pi}{N}) + 2\cos(k_m^p)]\sin(k_m^p)} \\
&+ e^{i\frac{m\pi}{N}\Delta s}\left(\frac{e^{ik_m^p(E)|\Delta\ell-\Delta j+1|} - e^{ik_m^p(E)|\Sigma\ell-\Sigma j+1|}}{[\cos(\frac{m\pi}{N}) + 2\cos(k_m^p(E))]\sin(k_m^p(E))} \right. \\
&+ \left. \frac{e^{ik_m^p(E)|\Delta\ell-\Delta j-1|} - e^{ik_m^p(E)|\Sigma\ell-\Sigma j-1|}}{[\cos(\frac{m\pi}{N}) + 2\cos(k_m^p(E))]\sin(k_m^p(E))} \right) \quad . \qquad (3.42)
\end{aligned}$$

The same considerations used to simplify the expressions for infinite armchair tubes apply here and leads to much simplified form for the propagators. The final result is then given by,

$$\begin{aligned}
\langle \ell, j, s|\hat{G}|\ell', j', s\rangle &= \frac{i}{4Nt_0^2}(E + i\eta - \epsilon_0)\sum_{m=1}^{N} e^{i\frac{m\pi}{N}(\Delta\ell+\Delta j)} \\
&\times \sum_{p=1}^{2} \frac{e^{ik_m^p(E)|\Delta\ell-\Delta j|} - e^{ik_m^p(E)|\Sigma\ell-\Sigma j|}}{[\cos(\frac{m\pi}{N}) + 2\cos(k_m^p(E))]\sin(k_m^p(E))} \\
\langle \ell, j, s|\hat{G}|\ell', j', s'\rangle &= \frac{i}{4Nt_0}\sum_{n=1}^{N} e^{i\frac{m\pi}{N}(\Delta\ell+\Delta j)} \sum_{p=1}^{2}(1 + 2e^{i\frac{m\pi}{N}\Delta s}\cos(k_m^p)) \\
&\times \frac{e^{ik_m^p(E)|\Delta\ell-\Delta j|} - e^{ik_m^p(E)|\Sigma\ell-\Sigma j|}}{[\cos(\frac{m}{N}\pi) + 2\cos(k_m^p(E))]\sin(k_m^p(E))} \quad . \qquad (3.43)
\end{aligned}$$

Figures 3.8 and 3.9 show comparisons between the analytic propagator determined by Eq.(3.43) and the same propagators calculated recursively. The first shows a general off-site propagator between atoms on 2 distinct armchair rings, the second is for a given on-site propagator. The recursive results are plotted more sparsely over energy to facilitate the comparison, but as in the infinite case, the two methods are seen to be in perfect agreement.

3.3.2 Zigzags

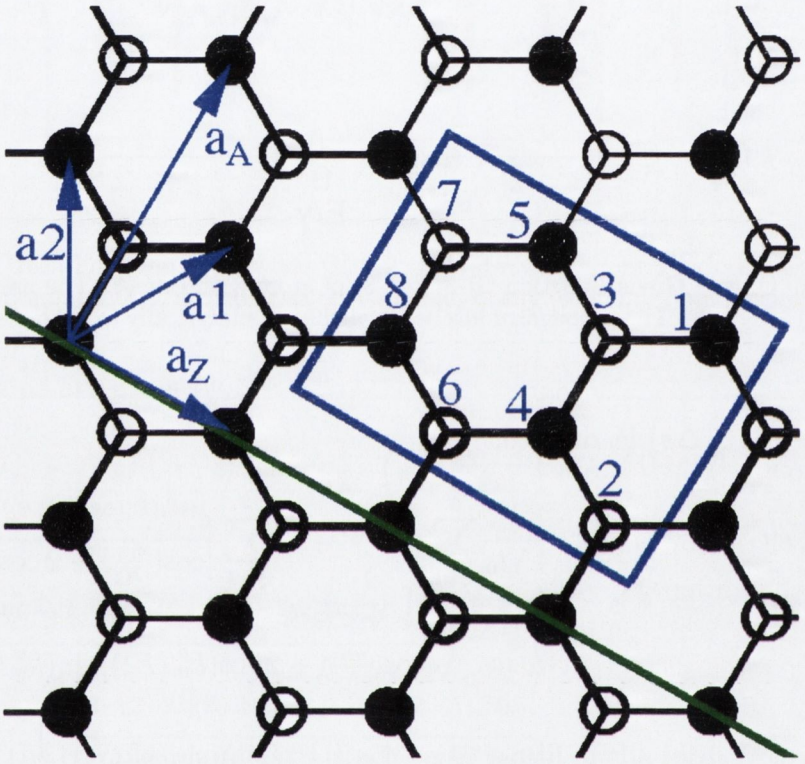


Figure 3.10: Cut plane of graphene. There is no electronic density along the green line. The blue square identifies the zigzag ring, which was introduced in figure 2.6.

We now calculate the Green Function propagators for semi-infinite zigzag nanotubes. In doing so we expose a limitation of the standing-wave method of constructing eigenvectors, which is relevant to the surface propagators.

For zigzags, the appropriate condition is that the electronic density along the line $\mathbf{a}_z$, with $s = 1$ should be zero. This line is shown in figure 3.10. Writing the phase factor appearing in Eq.(3.5) in terms of the basis vectors $\mathbf{b}_A, \mathbf{b}_Z$,

$$t(k_A, k_Z) = t_0(1 + e^{ik_Z/2} + e^{ik_A/2}) = t_0(1 + 2\cos(k_Z/2)e^{ik_A/2}) \quad . \tag{3.44}$$

The approach is the same as in the previous section. We form a superposition of

degenerate eigenvectors,

$$|\Psi(k_A, k_Z), \pm\rangle = \frac{1}{\sqrt{2}} \left(|k_A, k_Z, \pm\rangle - |-k_A, k_Z, \pm\rangle \right) \quad . \tag{3.45}$$

However for zigzags, $t(k_A, k_z) = 1 + \cos(k_Z/2) e^{ik_A/2} = t^*(-k_A, k_Z)$, and thus,

$$\begin{aligned} |\Psi(k_A, k_Z), \pm\rangle &= \frac{1}{\sqrt{4N}} \sum_{\ell,j} e^{i\frac{k_Z}{2}(\ell - j)} \Big[\left(e^{i\frac{k_A}{2}(\ell+j)} - e^{-i\frac{k_A}{2}(\ell+j)} \right) |\mathbf{r},\, 1\rangle \\ &\pm \left(e^{i\phi(\mathbf{k})} e^{i\frac{k_A}{2}(\ell+j)} - e^{-i\phi(\mathbf{k})} e^{-i\frac{k_A}{2}(\ell+j)} \right) |\mathbf{r},\, 2\rangle \Big] \end{aligned} \tag{3.46}$$

The projection of a lattice vector onto a given eigenvector is given by

$$\langle \mathbf{r}\ , 1 | \Psi_{\mathbf{k}}\ , \pm\rangle = \frac{i}{\sqrt{N}} \sin\left(\frac{k_A}{2}(\ell + j) \right) e^{i\frac{k_Z}{2}(l-j)} \tag{3.47}$$

$$\langle \mathbf{r}\ , 2 | \Psi_{\mathbf{k}}\ , \pm\rangle = \frac{\pm i}{\sqrt{N}} \sin\left(\frac{k_A}{2}(\ell + j) + \phi(\mathbf{k}) \right) e^{i\frac{k_Z}{2}(l-j)} \quad . \tag{3.48}$$

The probability density, $|\langle \ell, j, 1 | \Psi(k_A, k_Z), \pm\rangle|^2$, is thus seen to be zero along the line $j = -\ell$. This line defines the surface of the zigzag nanotube. However, unlike armchairs, this surface condition breaks the symmetry between the $s = s' = 1$ and $s = s' = 2$ propagators and also breaks the inversion symmetry of the lattice as a whole. From figure 3.10, the lower half of the lattice now has dangling bonds at its surface. We confine ourselves to the other half: for which $\ell + j \geq 0$.

The projection elements are,

$$\begin{aligned} \langle \mathbf{r}, 1 | \Psi_{\mathbf{k}}, \pm\rangle \langle \Psi_{\mathbf{k}}, \pm | \mathbf{r}', 1\rangle &= \frac{1}{4N_c} \left(e^{i\frac{k_A}{2}(\Delta\ell + \Delta j)} - e^{i\frac{k_A}{2}(\Sigma\ell + \Sigma j)} + c.c. \right) \\ &\times\ e^{i\frac{k_Z}{2}(\Delta\ell - \Delta j)} \end{aligned} \tag{3.49}$$

$$\begin{aligned} \langle \mathbf{r}, 2 | \Psi_{\mathbf{k}}, \pm\rangle \langle \Psi_{\mathbf{k}}, \pm | \mathbf{r}', 2\rangle &= \frac{1}{4N_c} \left(e^{i\frac{k_A}{2}(\Delta\ell + \Delta j)} - e^{i\frac{k_A}{2}(\Sigma\ell + \Sigma j)} e^{2i\phi} + c.c. \right) \\ &\times\ e^{i\frac{k_Z}{2}(\Delta\ell - \Delta j)} \end{aligned} \tag{3.50}$$

$$\begin{aligned} \langle \mathbf{r}, s | \Psi_{\mathbf{k}}, \pm\rangle \langle \Psi_{\mathbf{k}}, \pm | \mathbf{r}', s'\rangle &= \pm \frac{1}{4N_c} \left(e^{i\frac{k_A}{2}(\Delta\ell + \Delta j)} e^{i\phi\Delta s} - e^{i\frac{k_A}{2}(\Sigma\ell + \Sigma j)} e^{i\phi} + c.c. \right) \\ &\times\ e^{i\frac{k_Z}{2}(\Delta\ell - \Delta j)} \end{aligned} \tag{3.51}$$

For the $s = s' = 1$ case the propagators are given by,

$$\begin{aligned} \langle \ell, j, 1 | \hat{G} | \ell', j', 1\rangle &= \frac{i}{4Nt_0^2} (E + i\eta - \epsilon_0) \sum_{m=1}^{N} e^{i\frac{m\pi}{N}(\Delta\ell - \Delta j)} \\ &\times\ \frac{e^{ik_m(E)|\Delta\ell + \Delta j|} - e^{ik_m(E)|\Sigma\ell + \Sigma j|}}{\sin(k_m)\cos(\frac{m\pi}{N})} \end{aligned} \tag{3.52}$$

Figure 3.11 shows a comparison between the analytic and recursive methods for the

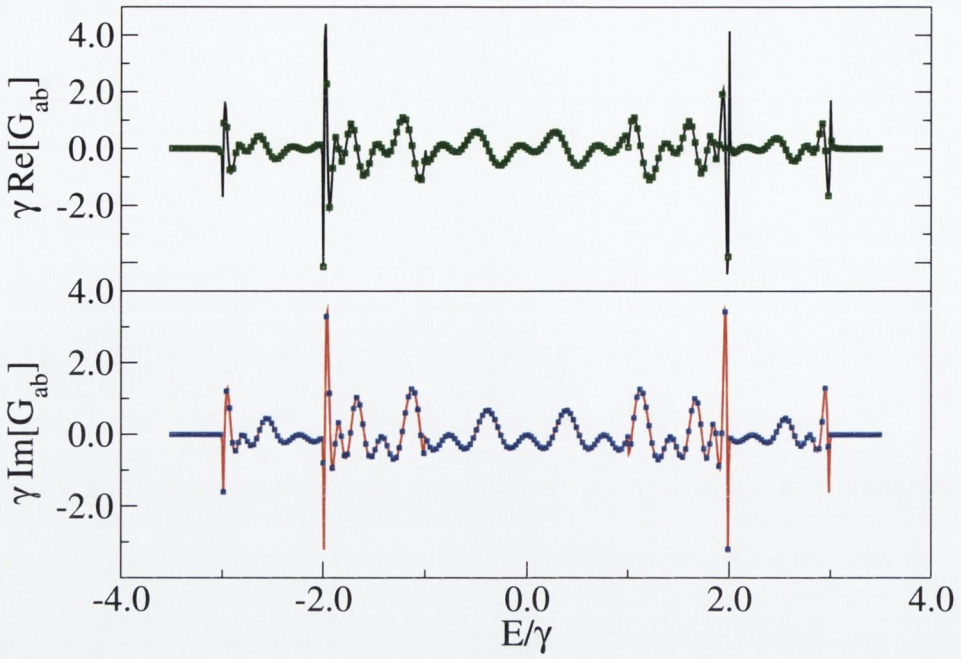


Figure 3.11: Green Function propagator G(-1,1;-5,1), between atom 1 on ring -1 and atom 1 on ring -5 on a (3,0) zigzag, calculated analytically (solid lines) and recursively (points).

off-site propagator between two $s = 1$ sites. The agreement are once again seen to be perfect.

For $s = s' = 2$, the standard form of the integral, $I^Z(m, D)$, is changed due to the presence of the factor $e^{2i\phi} = t/t^*$. To determine what effect this will have on the contour integral we must first examine whether this modified integrand has any additional poles. The denominator of the phase factor will certainly have zeros but these are also zeros of the numerator so the behaviour of the quotient is indeterminate. As a result, we need to examine what happens as the denominator tends to zero. If this occurs at k_0, then since t and t^* are both analytic function we can write,

$$\frac{t}{t^*} = \frac{t(k_0) + [t(k_0)]'(k - k_0) + \cdots}{t^*(k_0) + [t^*(k_0)]'(k - k_0) + \cdots} \quad . \tag{3.53}$$

Since $(t^*)' = -t'$,

$$\lim_{k \to k_0} \frac{t(k)}{t^*(k)} = -1 \quad , \tag{3.54}$$

and consequently the factor does not contribute any additional terms to the integral. It remains to be seen how it behaves as $\mathrm{Im}(k) \to \infty$. Since $1/t^*(k)$ is a bounded function it will not stop the integrand vanishing in the UHP. Therefore, this factor

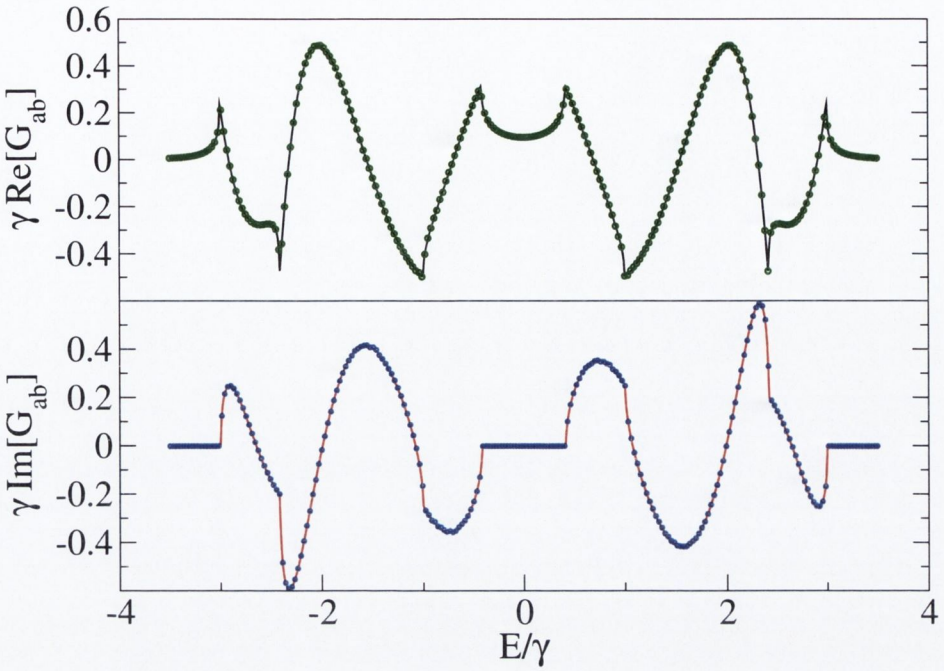


Figure 3.12: Green Function propagator G(0,2;-1,8), between atom 2 on the surface and ring -1, atom 8 on a (4,0) semi-conducting zigzag, calculated analytically (solid lines) and recursively (points).

simply introduces a multiplicative term to the matrix element,

$$\begin{aligned}\langle \ell, j, 2|\hat{G}|\ell', j', 2\rangle &= \frac{i}{4Nt_0^2}(E+i\eta-\epsilon_0)\sum_{m=1}^{N} e^{i\frac{m\pi}{N}(\Delta\ell-\Delta j)}\left(\frac{e^{ik_m|\Delta\ell+\Delta j|}}{\sin(k_m)\cos(\frac{m\pi}{N})}\right. \\ &- \left.\frac{t(k_m)}{t^*(k_m)}\frac{e^{ik_m|\Sigma\ell+\Sigma j|}}{\sin(k_m)\cos(\frac{m\pi}{N})}\right) \quad . \end{aligned} \tag{3.55}$$

In figure 3.12 the off-site propagator between two $s = 2$ sites is shown. The modified formula given by Eq.(3.55) gives a perfect agreement with the recursively generate propagator.

The intra-lattice case $s \neq s'$ has the standard denominator, $I^z(m, D)$ and the propagators are given by,

$$\begin{aligned}\langle \ell j, s|\hat{G}|\ell' j', s'\rangle &= \frac{i}{4Nt_0}\sum_{m=1}^{N} e^{\pi i\frac{m}{N}(\Delta\ell+\Delta j)} \\ &\times \left(\frac{e^{ik_m|\Delta\ell+\Delta j|}+2\cos(\frac{m\pi}{N})e^{ik_m|\Delta\ell+\Delta j+\Delta s|}}{\sin(k_m)\cos(\frac{m\pi}{N})}\right. \\ &- \left.\frac{e^{ik_m|\Sigma\ell+\Sigma j|}+2\cos(\frac{m\pi}{N})e^{ik_m|\Sigma\ell+\Sigma j+1|}}{\sin(k_m)\cos(\frac{m\pi}{N})}\right) \end{aligned} \tag{3.56}$$

The modulus sign around the Σ terms are no longer strictly necessary since these terms are positive. Also, note that in the last term is $\Sigma\ell+\Sigma j+1$ and not $\Sigma\ell+\Sigma j+\Delta s$.

As with infinite zigzag tubes, the case of $m = N/2$ has to be treated separately.

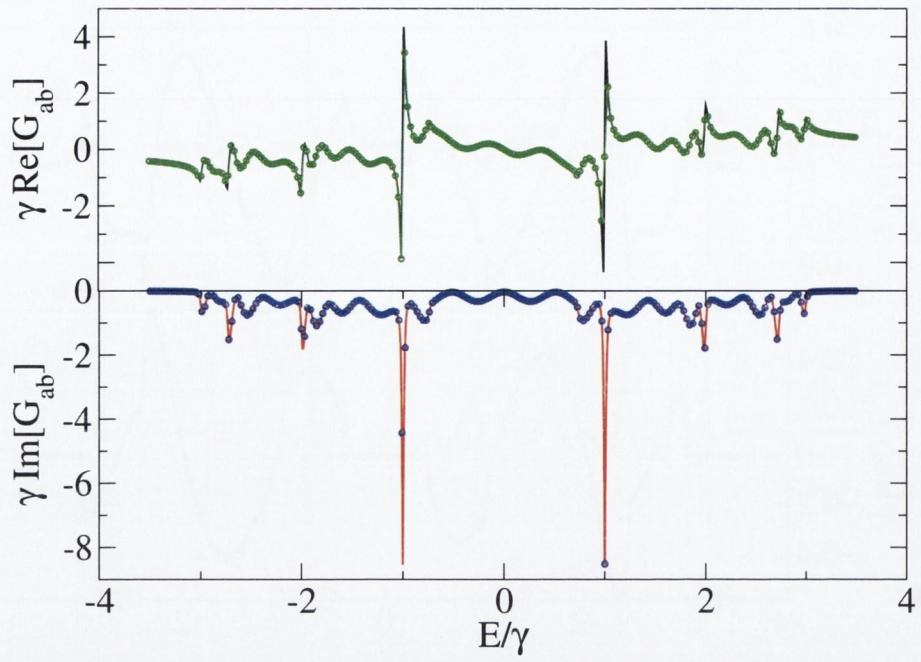


Figure 3.13: On-site Green Function propagator G(2,5;2,5) on a (6,0) metallic zigzag. η has been increased to 1×10^{-2} for clarity. The results of both the analytic (solid lines) and recursive (points) calculations are overlaid. Note the presence of bounds states at $E = \pm t_0(\gamma)$.

If $\Delta\ell + \Delta j = 0$ and $\Sigma\ell + \Sigma j \neq 0$ then we add

$$\frac{1}{Nt_0^2} e^{i\pi\Delta\ell} \frac{1}{(E + i\eta - \epsilon_0)^2 - t_0^2} \begin{cases} E + i\eta - \epsilon_0 & s - s' = 0 \\ t_0 & s - s' \neq 0 \end{cases} , \tag{3.57}$$

as appropriate.

The condition $\Delta\ell + \Delta j = 0$ is satisfied when the two points lie on a line parallel to the surface. $\Sigma\ell + \Sigma j = 0$ is only satisfied if both points lie on the surface of the tube. The presence of these bound states is confirmed by figure 3.13. Once again the comparison between the recursive and analytic approaches shows complete agreement.

For $s = s' = 2$ the form of the integral for the Σ terms has been seen to differ from the standard form by a factor $e^{2i\phi} = t/t^*$. However as seen from figure 3.14, this case also exhibits a perplexing feature: when the index N is even, the recursively generated surface propagators exhibit a bound state located at $E = 0$. This corresponds to the case of $\Sigma\ell + \Sigma j = 0$ and $\Delta\ell + \Delta j = 0$. The expression given by Eq.(3.55) is unable to reproduce such a feature. A resolution to this situation can be found by recognising that in constructing the wave-functions, all we have required is that the probability density vanishes along a given line. For most cases this is sufficient to generate the correct propagators for a semi-infinite system. However it is not clear if these wavevectors are actually eigenvectors of the semi-infinite Hamiltonian. This is particularly relevant for zigzags since, when the

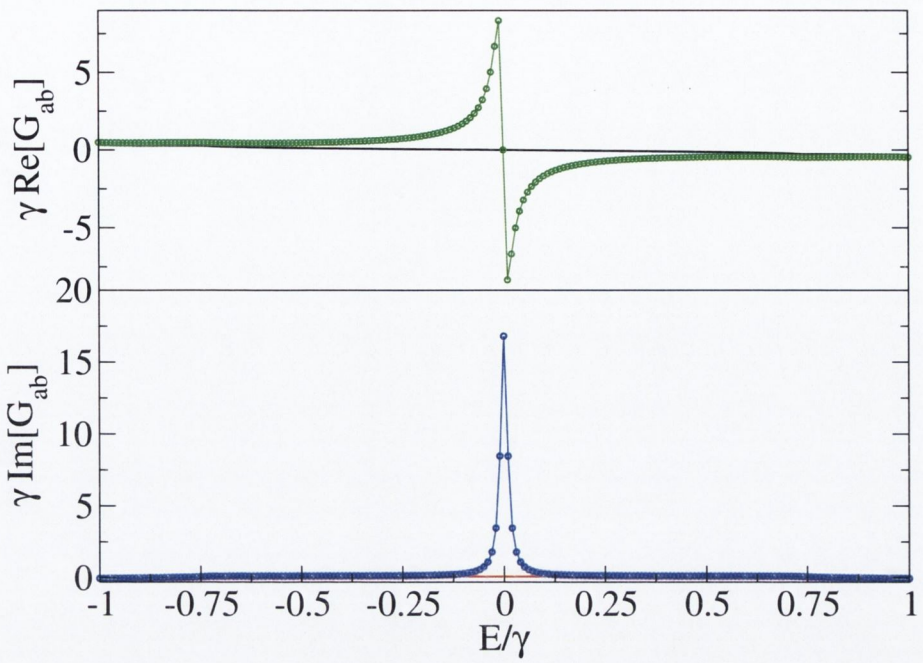


Figure 3.14: Surface Green Function propagator G(0,2;0,6) on a (0,6) metallic zigzag. η has been increased to 1×10^{-2} for clarity. Surprisingly the analytic and recursive results are not in agreement. The analytic formula is unable to produce the bound state at $E = 0$.

index N is even, the zigzag tube has two degenerate bands. The fact that the bound states are only present for even values of N suggests that they somehow arise from the dispersionless bands. To see how these might be important, we write the lattice sites along the surface in a basis of eigenvectors of the fully infinite system,

$$|\ell, -\ell, 1\rangle = \frac{1}{\sqrt{2N_c}} \sum_{m=1}^{N} \sum_{k} e^{-2i\ell\frac{m\pi}{N}} (|m, k, +\rangle + e^{-i\phi(m,k)} |m, k, -\rangle) \tag{3.58}$$

$$|\ell, -\ell, 2\rangle = \frac{1}{\sqrt{2N_c}} \sum_{m=1}^{N} \sum_{k} e^{-2i\ell\frac{m\pi}{N}} (|m, k, +\rangle - e^{-i\phi(m,k)} |m, k, -\rangle) \quad . \tag{3.59}$$

This was accomplished by inverting Eq.(3.5) and setting $\mathbf{k} = k\,\mathbf{b}_A + 2\pi m/N\,\mathbf{b}_Z$. Summing over all lattice sites lying along the surface,

$$\begin{aligned} \sum_{\ell=1}^{N} e^{2i\ell\frac{n\pi}{N}} |\ell, -\ell, 2\rangle &= \frac{1}{\sqrt{2N_c}} \sum_{m,\ell=1}^{N} \sum_{k} e^{2i(n-m)\frac{\pi}{N}\ell} (|m, k, +\rangle - e^{-i\phi(m,k)} |m, k, -\rangle) \\ &= \frac{N}{\sqrt{2N_c}} \sum_{k} (|n, k, +\rangle - e^{-i\phi(n,k)} |n, k, -\rangle) \quad . \end{aligned} \tag{3.60}$$

Setting $n = N/2$ gives,

$$\sum_{\ell=1}^{N} e^{i\ell\pi} |\ell, -\ell, 2\rangle = \frac{N}{\sqrt{2N_c}} \sum_{k} (|N/2, k, +\rangle - |N/2, k, -\rangle) \quad . \tag{3.61}$$

Defining the states given in Eq.(3.61) as,

$$|x_s\rangle = \frac{1}{\sqrt{N}} \sum_{\ell=1}^{N} e^{i\pi\ell} |\ell, -\ell, s\rangle \tag{3.62}$$

then, since the states are dispersionless, $\hat{H}|x_2\rangle = t_0|x_1\rangle$. However $|x_1\rangle = 0$ since the basis vectors $|\ell, -\ell, 1\rangle$ do not correspond to sites on the semi-infinite tube. Therefore the state $|x_2\rangle$ can be regarded as a state in the kernel of $\hat{H}$, that is the set of all non-zero vectors $|x\rangle$ satisfying $\hat{H}|x\rangle = 0$. It follows that $(E\hat{I} - \hat{H})|x_2\rangle = E|x_2\rangle$ and applying $\hat{G}$ we have

$$\hat{G}|x_2\rangle = \frac{1}{E}|x_2\rangle \quad . \tag{3.63}$$

The component of the Green Function operator that satisfies Eq.(3.63) is

$$\hat{G}_s = |x_2\rangle \frac{1}{E} \langle x_2| \quad . \tag{3.64}$$

The subscript, s, indicates that this is a surface contribution to the Green Function. The analytic formula gives an accurate expression for the lattice propagators, $\hat{G}_b$, in the bulk. To recover complete agreement with the recursive results, we write the total Green Function as $\hat{G} = \hat{G}_b - \hat{G}_s$. Explicitly,

$$\langle \ell, j, s|\hat{G}|\ell', j', s'\rangle = \langle \ell, j, s|\hat{G}_b|\ell', j, s'\rangle - \frac{1}{N} \sum_{\ell,\ell'=1}^{N} \frac{e^{i\pi(\ell-\ell')}}{E} \delta_{-\ell,j}\delta_{-\ell',j'}\delta_{s,2}\delta_{s',2} \tag{3.65}$$

In figure 3.15 we plot the propagator between the same two surface sites as figure 3.14 using the modified propagator, Eq.(3.65). The analytic and recursive methods are now in perfect agreement since the contribution from $\hat{G}_s$ provides the bound state found in the recursive result. Similar bound states are known to exist at the Fermi-Energy along the surface of zigzag edged nanoribbons [56][57]. In so far as we are concerned with infinite nanotubes these states are not relevant. However they could be important in transport calculations which make use of zigzag leads. In these cases the leads couple to the conductor via the surface element of the semi-infinite nanotube.

The lesson of Eq.(3.65) is the need to be careful when constructing expressions for semi-infinite structures using the standing-wave method outlined in this section. While it works perfectly well for the majority of cases, it should always be borne in mind that we are not explicitly inverting the Hamiltonian for a semi-infinite tube; the only requirement made is that the electronic density vanish along the surface. For the case of zigzag nanotubes it seems that the analytic treatment does not correctly

address the effect of breaking the symmetry of the tube on the dispersionless bands.

The analytic treatment of a semi-infinite zigzag nanotube has been far trickier than expected. Firstly, the surface condition caused the form of the integrand to change from the standard form given by Eq.(3.24) in the case where $s, s' = 2$. The correct expression required only a small modification to the existing formula. Far more alarming was the discrepancy between the analytic and recursive methods in the case of surface propagators. This was seen to result from degeneracy in the electronic structure occurring with even N tube, leading to the appearance of bound states on the surface of the tube.

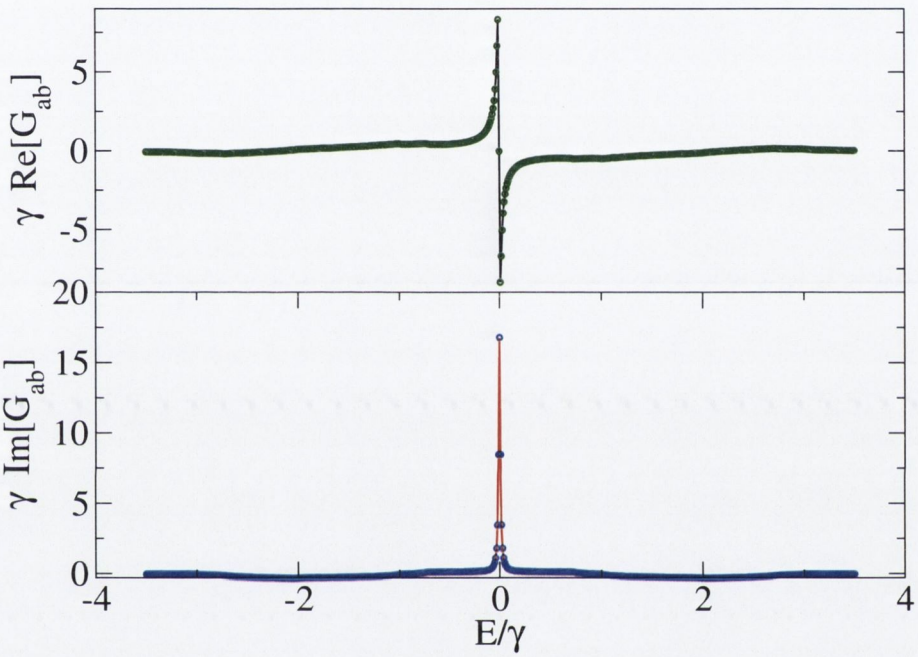


Figure 3.15: Surface Green Function propagator G(0,2;0,6) on a (0,6) metallic zigzag. η has been increased to 1×10^{-2} for clarity. The solid lines were generated using the modified expression given by Eq.(3.65). This recovers the agreement between the analytic and recursive results.

3.4 Summary of Chapter

In this chapter we have derived a set of closed-form expressions for lattice Green Function propagators for both infinite and semi-infinite achiral tubes. These expressions are extremely useful: both as a computational expedient and in providing a physical picture of electron propagation through disordered nanotubes. This picture will be utilised in addressing the effects encountered in chapter 5. Despite the seeming complexity, the derivations were quite straightforward. The Hamiltonian for graphene was diagonalised within a single band tight-binding model. This defined the Green Function operator. The corresponding operators for nanotubes were deduced by introducing the appropriate quantisation of the allowed wavevec-

tors. Projecting the operator onto a set of real space vectors, all that remained was to integrate over the unquantised wavevectors.

These expressions were then extended to semi-infinite propagators. Although a semi-infinite nanotube lacks strict translational invariance, it is nevertheless possible to replicate the electronic structure by constructing superpositions of eigenstates of the infinite tubes, using a standing-wave approach. As a consequence of this relation, the k-space integrals were, for the most part, exactly the same as for the infinite tubes. It was then simply a matter of writing down the closed form expressions for the lattice propagators in direct analogy to the infinite propagators. For zigzags, a limitation of the standing-wave approach was found.

These expressions, combined with the results of the previous chapter, provide all the components necessary to begin calculating changes to the density of states arising from the interaction of a nanotube with transition metal atoms. We are interested in the indirect coupling between the atoms which results from this interaction. This will be the focus of the next chapter.

Chapter 4

Indirect Exchange Coupling on Carbon Nanotubes

4.1 Introduction

In chapter 1 we introduced the Indirect exchange coupling (IEC) which, at very low temperatures, is responsible for the long range magnetic ordering in magnetic multilayers. The typical oscillatory behaviour of the coupling was illustrated in figure 1.7. It was stated that these features could be understood within a standard RKKY picture of coupling mediated by conduction electrons or, more generally, using the Quantum Well Theory. In both of these approaches the coupling can be viewed as resulting from interaction of the magnetic regions with the conduction electrons of the host. In the latter the features of the IEC can be fully explained by the band profile of the multilayer system. Within the magnetic regions the electrons are subject to a spin dependent potential, which differs from that of the host. This is shown in figure 4.1. The presence of the potential wells quantises the allowed energies of the electrons in the system. As the width, D, of the spacer is changed these levels move up and down with respect to the Fermi-Energy and this ultimately gives rise to an oscillatory coupling. The coupling is calculated by summing over all the levels lying below the Fermi-Energy and then determining the energy difference between the case where the two wells are aligned and where the band profiles in one of the regions are reversed. This sum introduces the required decay of the coupling as a function of D.

The original derivation of the theory[16] treated the multilayer as a series of infinite magnetic planes stacked on top of one another to form a thin film. The decay of the coupling was seen to be $1/D^2$ and was in perfect agreement with experiment. However, a corollary to the theory was that if the system could be confined in the transverse directions, then the range of the coupling would be even

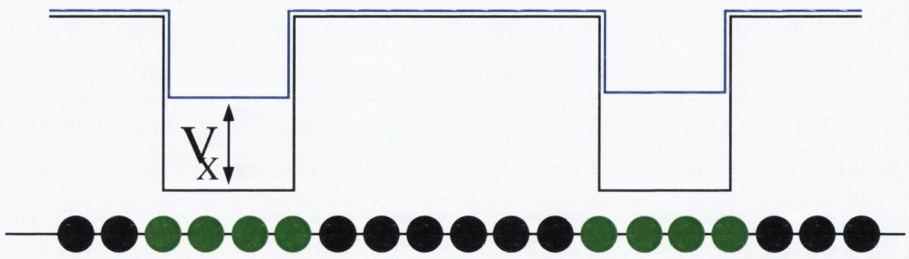


Figure 4.1: An illustration of a quantum well. The system is represented as a simple linear chain. The black atoms belong to the metallic, non-magnetic host. The green atoms are magnetic and conduction electrons are subject to a spin-split potential, V_x, at these sites.

longer. In 1-D the rate would be as slow as $1/D$. It is for this reason that carbon nanotubes become very relevant to the study of IEC. They are, at present, the only example of a stable, highly conductive quasi 1-D system. They have also been shown to interact strongly with magnetic impurities, particularly transition metal atoms. As such they contain all the necessary ingredients required to display IEC. Thus, in this chapter, we consider the IEC with a nanotube host. In place of the magnetic layers the interaction will be between a pair of transition metal atoms. The atoms are assumed to be well separated so that dipolar interactions can be neglected. The atoms can attach to the tube in two ways: with the impurity adsorbed at the surface of the tube, or as a substitutional replacement to one of the host carbon atoms. Both cases are illustrated in figure 4.2. By changing the separation, D, along the longitudinal axis of the tube we can observe the properties of the IEC in a manner similar to the one employed in the study of multilayers. Continuing this analogy, we are interested primarily in the following: (1) the rate of decay, (2) the period of oscillation, (3) whether the qualitative features of the coupling are dependent on the chirality of the tube and (4) whether the effect of switching between substitutional and adsorbed impurities leads to qualitative differences in the coupling.

Before turning to this problem, the next section provides a brief review of the Coulomb interaction and shows how, when treated in the most simple manner possible, this gives rise to the spin dependent potential wells used in the Quantum Well Theory.

4.2 Direct Exchange and the Hubbard Hamiltonian

Ferromagnetism in transition metals results from an exchange term arising from the Coulomb interaction between d-electrons in neighbouring ions. For a system of N

electrons, the Coulomb interaction,

$$H_{e-e} = \sum_{i,j=1}^{N} \frac{e^2}{|\mathbf{r}_i - \mathbf{r}_j|} \quad , \tag{4.1}$$

is a function of the two electron coordinates $\mathbf{r}_i$ and $\mathbf{r}_j$. In contrast, the ionic potential was a function of only a single electron coordinate. Quantum mechanically, a many body Hamiltonian like the one shown in Eq.(4.1) is correctly described by a set of fermionic operators using the language of second quantisation. We will refrain from utilising this formulation since we shall not be treating many body effects explicitly. A thorough introduction to second quantisation can be found in any treatment of the quantum theory of magnetism (see, for example, reference[58]).

In operator form, the individual terms in the sum in Eq.(4.1) can be written as,

$$H_{12} = \sum_{i,j,\ell,k} \left\langle n_i, n_j \left| \frac{e^2}{r_{12}} \right| n_k, n_\ell \right\rangle \sum_{\sigma,\sigma'} |n_i, \sigma\rangle \otimes |n_j, \sigma\rangle \langle n_k, \sigma'| \otimes \langle n_\ell, \sigma'| \quad . \tag{4.2}$$

The presence of $\otimes$ may well be an abuse of notation but it does emphasise that we are no longer dealing with a single particle Hamiltonian. The state vector $|n_i, \sigma\rangle$ represents an electron of spin σ located at lattice site i and, to a first approximation, the sum extends over nearest neighbour ions. The term in angle brackets is the expectation value of the Coulomb term given by,

$$\left\langle n_i, n_j \left| \frac{e^2}{r_{12}} \right| n_k, n_\ell \right\rangle = \int d\mathbf{r}_1 \int d\mathbf{r}_2 \, \psi_i^*(\mathbf{r}_1) \, \psi_j^*(\mathbf{r}_2) \frac{e^2}{|\mathbf{r}_1 - \mathbf{r}_2|} \psi_k(\mathbf{r}_1) \psi_\ell(\mathbf{r}_2) \tag{4.3}$$

where ψ_i is a localised wavefunction centred about site i.

The non-zero contributions to Eq.(4.2) come from setting $i = j = k = \ell$; $i = \ell$, $j = k$ and $i = k$, $j = \ell$. If we consider only the intra-atomic term, then Eq.(4.2) can be written as,

$$H_{12} = U \sum_i \sum_{\sigma,\sigma'} \hat{n}_{i,\sigma} \, \hat{n}_{i,\sigma'} \quad . \tag{4.4}$$

U is the Coulomb integral, obtained from Eq.(4.3) by setting all the indices equal to one another. The operator $\hat{n}_{i,\sigma} = |n_i, \sigma\rangle\langle n_i, \sigma|$ is the occupation of the state with spin σ localised at site i. Only those terms with $\sigma' \neq \sigma$ are non-zero. This is a consequence of the Pauli principle, which requires that the electronic wavefunction vanishes when electrons of the same spin are placed in the same atomic orbital. Eq.(4.4) is known as the Hubbard Hamiltonian. Written in this form it is still a many body Hamiltonian and cannot be solved using the single particle approaches of the previous chapters. Notwithstanding this fact, the standard approach assumes

that, to first order, the exchange interaction can be treated as a single particle effect. This is the Hartree-Fock (HF) approximation, and results from first writing

$$\hat{n}_{i,\sigma} = \langle n_{i\sigma} \rangle + (\hat{n}_{i\sigma} - \langle n_{i\sigma} \rangle) \quad , \tag{4.5}$$

where $\langle n_i \rangle$ is the expectation value for the occupation number. Eq.(4.5) is trivially true. The approximation comes from assuming that the term in parenthesis is small, then

$$\hat{n}_{i,\sigma}\hat{n}_{i,-\sigma} \approx \langle n_{i,\sigma} \rangle \hat{n}_{i,-\sigma} + \langle n_{i,-\sigma} \rangle \hat{n}_{i,\sigma} - \langle n_{i,\sigma} \rangle \langle n_{i,-\sigma} \rangle \quad . \tag{4.6}$$

The Coulomb term has been written in terms of single particle states $|i,\sigma\rangle \langle i,\sigma|$. The last term shifts the band centre of the magnetic atoms by $\epsilon_a = -U \sum_i \langle n_{i,\sigma} \rangle \langle n_{i,-\sigma} \rangle$. If the average number of electrons per ion is $\langle n_i \rangle = \langle n_{i,\uparrow} \rangle + \langle n_{i,\downarrow} \rangle$ and the magnetisation $\langle m_i \rangle = \langle n_{i,\uparrow} \rangle - \langle n_{i,\downarrow} \rangle$ then,

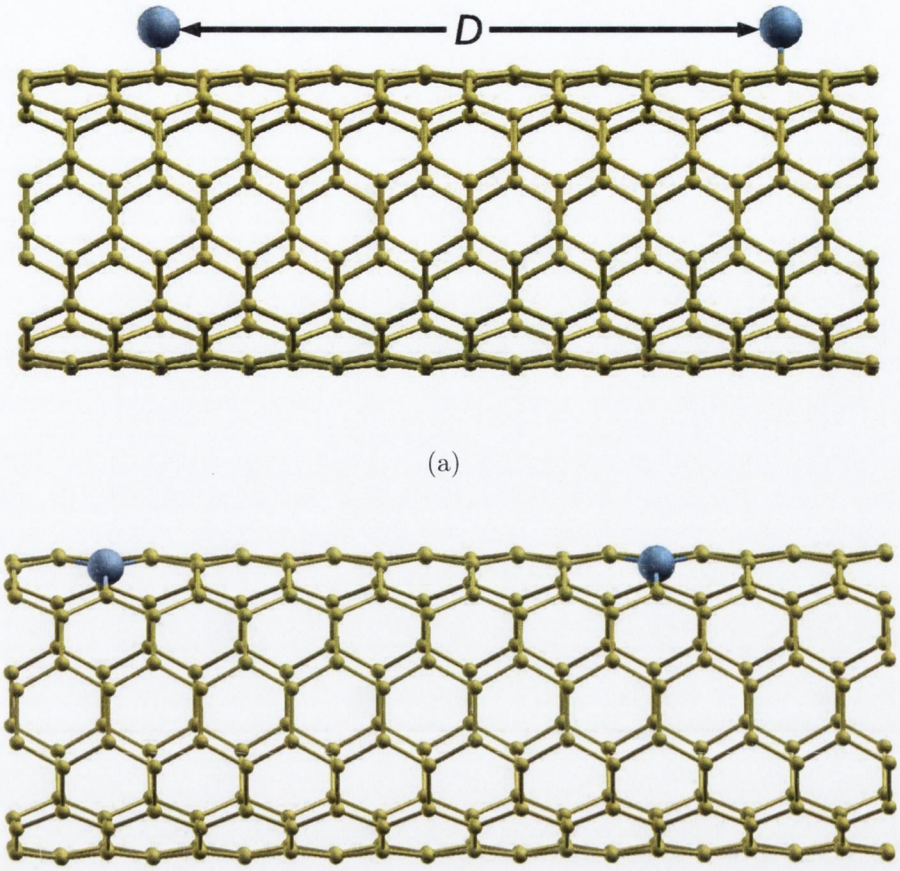
$$H_{HF} = \sum_{i,\sigma} \epsilon_{i,\sigma} |i\sigma\rangle\langle i,\sigma| \quad , \tag{4.7}$$

with,

$$\epsilon_{i,\sigma} = \epsilon_a + \frac{U}{2}\langle n_i \rangle - (-1)^{\sigma}\frac{U}{2}\langle m_i \rangle \quad . \tag{4.8}$$

The HF equation has each electron interacting with an effective field generated by the electron of opposite spin. The magnetic moment manifests itself as an exchange energy $V_{\mathrm{x}} = U\langle m \rangle$ which breaks the degeneracy of the spin bands at the site of the magnetic atoms. The electrons are thus subject to a spin dependent potential. The Hamiltonian is then easily treated using the methods outlined in chapter 2.

Returning to Eq.(4.2), the case for which $i = k$ and $j = \ell$ is known as the exchange term. This is a quantum interference effect, which involves electrons at a given site exchanging their spin. When properly treated within a second quantisation approach (see for example reference [59]), this gives rise to a coupling between adjacent ions. The coupling can be written as $J_{ij}\mathbf{s}_i \cdot \mathbf{s}_j$, where $J_{ij} = \langle n_i, n_j | e^2/r_{12} | n_i, n_j \rangle$ and $\mathbf{s}_i$ describes the orientation of the magnetic moment at site i. Since it arises from a direct coupling of adjacent ions it is known as the direct interaction. As we have seen, when magnetic ions are embedded in a metal, a second type of interaction can occur. In this case, the magnetic interaction is present even when the ions are far apart and the direct interaction is negligible. As a result it is known as Indirect Exchange.



(a)

(b)

Figure 4.2: Two possible transition metal atom/nanotube interactions: (a) A (6,6) armchair with 2 adsorbed impurities. In this chapter the impurities are assumed to be located above individual carbon atoms. (b) A (6,6) armchair with 2 impurities occupying substitutional positions within the nanotube. In both cases, the separation between the impurities is D, which is normally measured as an integer number of nanotube rings.

4.3 Carbon Nanotube Mediated Indirect Exchange

The results of the last section show that the presence of a magnetic moment can be represented, within a mean field approximation, by an exchange potential localised at the site of the moment. This is a particularly convenient approach for treating indirect exchange, since it results from the presence of delocalised conduction electrons which are well described by a band picture. In this picture, the conduction electrons are subjected to an exchange split potential at the site of the impurities. If the conduction electrons belong to a carbon nanotube and the magnetic moments are transition metal atoms separated by a distance D, as shown in figure 4.2, then the Hamiltonian of the combined system can be written as,

$$\hat{H} = \hat{H}_{\mathrm{NT}} + \sum_{\sigma=\downarrow\uparrow} \hat{H}^{\sigma}_{\mathrm{INT}} \quad . \tag{4.9}$$

$\hat{H}_{\rm NT}$ is the Hamiltonian for an isolated nanotube and following the approach of the previous chapter is treated within a single band tight-binding picture. $\hat{H}^{\sigma}_{\rm INT}$, it is the spin-dependent contribution from the impurity atoms. The expression for $\hat{H}^{\sigma}_{\rm INT}$ depends on the type of interaction. For adsorbed impurities it is the sum of a spin-dependent Hamiltonian $\hat{H}^{\sigma}_{\rm IMP}$, representing two isolated magnetic impurities, and a term $\hat{H}^{\sigma}_{\rm NT-IMP}$ which couples the impurities to the nanotube. If the impurity sites are labelled as $j = A$ and $j = B$, then $\hat{H}^{\sigma}_{\rm IMP} = |A\ \sigma\rangle\, \lambda^{\sigma}_{A}\, \langle A\ \sigma| + |B\ \sigma\rangle\, \lambda^{\sigma}_{B}\, \langle B\ \sigma|$ is the Hamiltonian for the two isolated atoms with on-site energies shifted by $\lambda^{\sigma}_{A}, \lambda^{\sigma}_{B}$ with respect to the nanotube band centre. The index σ labels the distinct spin split levels. $\hat{H}_{\rm NT-IMP} = |a\ \sigma\rangle\, t\, \langle A\ \sigma| + |b\ \sigma\rangle\, t\, \langle B\ \sigma| + c.c.$ couples the impurities to the tube. a, b are the host atoms in contact with the impurities and t is the adatom/tube hopping. Here, it is assumed that adsorbed impurities interact directly with individual nanotube atoms (c.f. figure 4.2(a)). In the next chapter this restriction will be relaxed. For substitutional impurities, the on-site energies at a, b are altered directly and $\hat{H}^{\sigma}_{\rm INT} = |a{=}A\ \sigma\rangle\, \lambda^{\sigma}_{a}\, \langle a{=}A\ \sigma| + |b{=}B\ \sigma\rangle\, \lambda^{\sigma}_{b}\, \langle b{=}B\ \sigma|$. Inverting the Hamiltonian gives the Green Function for the system. Using Dyson's Equation the lattice propagators for the nanotube/atom composite, G_{ij}, can be written in terms of the propagators, $\mathcal{G}_{ij}$, of the isolated tube.

The coupling between the moments is defined as the total energy required to rotate moment B relative to moment A by an angle $\theta = \pi$. More generally, we consider the energy required to rotate the moment by an arbitrary angle θ,

$$\Delta E(\theta) = E(\theta) - E(\theta = 0) \quad . \tag{4.10}$$

The value of the coupling is recovered by setting $\theta = \pi$. This amounts to calculating the energy difference arising from the spin perturbation, $\hat{V} = -V_{\rm x}[(\cos(\theta) - 1)\hat{\sigma}_z + \sin(\theta)\hat{\sigma}_x]$, which induces the rotation of the magnetic moment. $\hat{\sigma}_z$ and $\hat{\sigma}_x$ are the usual Pauli matrices. By convention the up-spin band has been chosen to lie below the down-spin band.

Since we are dealing with an infinite nanotube we work with the Grand Canonical Ensemble. Then the energy change is given by the change in the Thermodynamic Potential[58],

$$\Delta\Omega = -k_B T \int_{-\infty}^{\infty} dE \ln(1 + e^{-(E-E_F)/k_B T}) \Delta\rho(E, D) \quad . \tag{4.11}$$

Integrating by parts and using Eq.(2.46) for the change in the density of states,

$$\Delta\Omega = \frac{1}{\pi} \int_{-\infty}^{\infty} dE\, \frac{1}{1 + e^{(E-E_F)/k_B T}}\, \mathrm{Im} \ln\left(\det(1 - G(E, D)V)\right) \quad . \tag{4.12}$$

Here, G, is the Green Function for the reference system, which corresponds to two magnetic moments initially aligned along the z-direction ($\theta = 0$). Because the presence of the magnetic moments break the spin degeneracy of the electrons, the propagator, G_{BB}, of the rotated moment must be written in terms of its various spin components,

$$(1 - GV) = \begin{pmatrix} 1 & 0 \\ 0 & 1 \end{pmatrix} - V_{\mathrm{x}} \begin{pmatrix} G^{\uparrow\uparrow}_{BB} & 0 \\ 0 & G^{\downarrow\downarrow}_{BB} \end{pmatrix} \begin{pmatrix} 1 - \cos(\theta) & \sin(\theta) \\ \sin(\theta) & \cos(\theta) - 1 \end{pmatrix} \quad (4.13)$$

The superscripts $\uparrow, \downarrow$ refer to spin up and down electrons. With the moments in a collinear alignment there is no mixing between spin-bands and G is diagonal in spin space. Evaluating the determinant,

$$\begin{aligned} \Delta\Omega(\theta, D) &= \frac{1}{\pi} \int_{-\infty}^{\infty} dE\, f(E)\, \mathrm{Im}\ln[\det(I - G(E, D)V)] & (4.14) \\ &= \frac{1}{\pi} \int_{-\infty}^{\infty} dE\, f(E)\, \mathrm{Im}\ln[1 - V_{\mathrm{x}}(1 - \cos\theta)(G^{\uparrow\uparrow}_{BB} - G^{\downarrow\downarrow}_{BB}) & (4.15) \\ &- 2V_{\mathrm{x}}^2\, G^{\uparrow\uparrow}_{BB}(E, D) G^{\downarrow\downarrow}_{BB}(E, D)(1 - \cos\theta)] \quad . & (4.16) \end{aligned}$$

$f(E) = (1 + e^{(E - E_F)/k_B T})^{-1}$ is the Fermi-Dirac function. Using Dyson's Equation to express the up-spin propagators in terms of the down-spin,

$$G^{\uparrow\uparrow}_{BB} = G^{\downarrow\downarrow}_{BB} - 2V_{\mathrm{x}}(G^{\downarrow\downarrow}_{BB} G^{\uparrow\uparrow}_{BB} + G^{\downarrow\downarrow}_{BA} G^{\uparrow\uparrow}_{AB}) \quad , \quad (4.17)$$

leads to the final expression for the coupling,

$$\Delta\Omega(\pi, D) = \frac{1}{\pi} \int_{-\infty}^{\infty} dE f(E)\, \mathrm{Im}\ln(1 + 4V_{\mathrm{x}}^2\, G^{\uparrow\uparrow}_{AB}(E, D)\, G^{\downarrow\downarrow}_{BA}(E, D)) \quad . \quad (4.18)$$

Writing the coupling in this form emphasises that the Indirect Exchange results from electrons propagating backward and forward between A and B. Dyson's equation can be used to write the propagators, $G^{\sigma\sigma}_{AB}$, in terms of propagators of the isolated nanotube. These expressions will differ for the cases of substitutional and adsorbed impurities shown in figure 4.2. They are given respectively by,

$$\begin{aligned} G^{\sigma\sigma}_{ab} &= \frac{\mathcal{G}_{ab}}{(1 - \mathcal{G}_{aa}\lambda^{\sigma}_{a})(1 - \mathcal{G}_{bb}\lambda^{\sigma}_{b}) - \mathcal{G}_{ab}\lambda^{\sigma}_{b}\mathcal{G}_{ba}\lambda^{\sigma}_{a}} & (4.19) \\ G^{\sigma}_{AB} &= \frac{t^2\, \mathcal{G}^{\sigma}_{AA}\mathcal{G}_{ab}\mathcal{G}^{\sigma}_{BB}}{(1 - t^2\, \mathcal{G}^{\sigma}_{AA}\mathcal{G}_{aa})(1 - t^2\, \mathcal{G}^{\sigma}_{BB}\mathcal{G}_{bb}) - t^4\, \mathcal{G}^{\sigma}_{AA}\mathcal{G}_{ab}\mathcal{G}^{\sigma}_{BB}\mathcal{G}_{ba}} & (4.20) \end{aligned}$$

In either case, the dependence on the separation, D, is contained entirely in the lattice-lattice propagators $\mathcal{G}_{ab}(D), \mathcal{G}_{ba}(D)$ of the pristine tube. As a result of the analytic expressions developed previously – specifically Eq.(3.30) and Eq.(3.33) – these propagators are already known. Therefore the integrand in Eq.(4.18) can be

evaluated with virtually no computational overhead.

Nevertheless; difficulties arise with the numerical integration over E, since the low dimensionality of the system introduces Van Hove singularities of the type seen in figure 1.4. Treating these singularities correctly requires an extremely fine integration mesh. In addition, the impurities can introduce resonances far below the Fermi-Energy. By imposing an arbitrary cut off in the lower bound of the integral we need to be careful to ensure that all such bound states are properly included. Failure to do so can result in spurious biasing in the sign of the coupling as D increases[21]. Fortunately, these difficulties can be circumvented by using the analytic[1] properties of the Green Function, which ensure that the determinant is always an analytic function in the upper half energy plane(UHP). As a consequence, we are free to replace the integration over real energy with an integration along the imaginary energy axis. Along the imaginary axis the behaviour of the function is very smooth. Figure 4.3 shows the integrand along both directions. The benefit of integration along the imaginary energy axis is clear. The recipe for switching between a real and imaginary axis integration is outlined in appendix C. In its final form the energy integral, at zero temperature, is given by,

$$-J(D) = \Delta\Omega(D) = -\frac{1}{\pi}\int_0^\infty dE \ln\left|1 + 4V_x^2\, G^{\uparrow}_{AB}(E_F + iE, D)\, G^{\downarrow}_{BA}(E_F + iE, D)\right| \tag{4.21}$$

The coupling, $J(D)$, is defined as the negative of the energy change $\Delta\Omega$, so that a positive coupling value indicates a preferred anti-ferromagnetic alignment. When the separation D is large it is possible to evaluate the integral using a semi-analytical method. Using this approach it becomes possible to identify general features of the coupling, notably the period of oscillation and rate of decay.

4.4 Asymptotic Limit

Edwards *et. al.*[16] presented a semi-analytic approach to performing the integral in Eq.(4.18) for multilayered systems. This gave immediate access to certain features of the coupling: particularly the decay rate and periodicity. Their argument was quite general and can also be applied to the case of nanotubes. First of all, we make use of an observation from the previous section: the only separation dependence in the integrand of Eq.(4.18) arises from the propagators $\mathcal{G}_{ab}(D), \mathcal{G}_{ba}(D)$. In chapter 3 we have seen that these propagators oscillate as a function of D with an energy dependent period, $2\pi/k$, determined by the propagating wavevector at that energy.

[1]By analytic, it is meant that a function has no singular points.

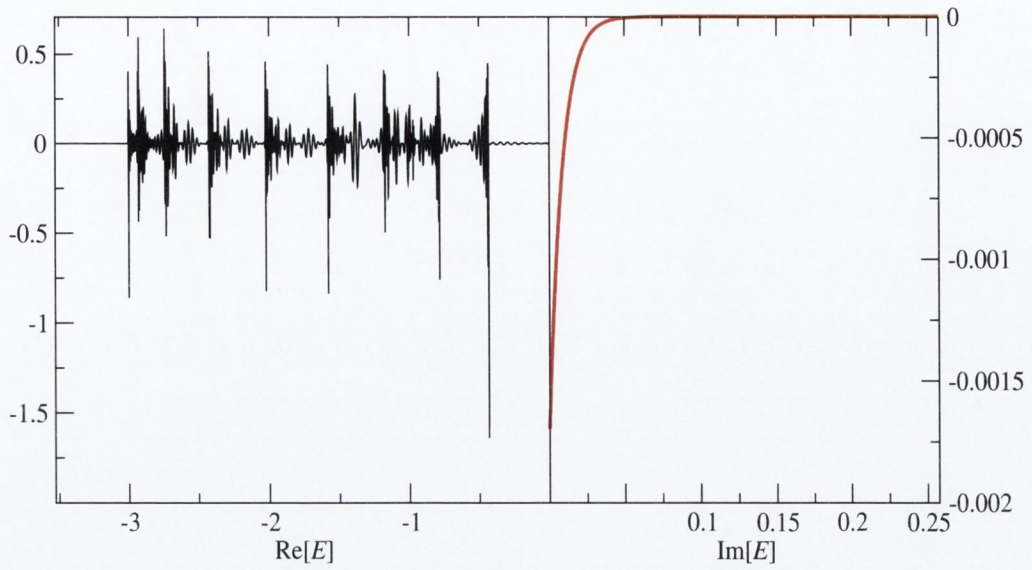


Figure 4.3: A comparison of the integrand in Eq.(4.18) along the real (left panel) and imaginary (right panel) energy axis. The simulation was performed on a (7,7) armchair with 2 substitutional impurities separated by 50 rings. The energy is given in units of the carbon-carbon hopping energy, $\gamma(t_0)$.

Of course, for nanotubes there are $2N$ propagating wavevectors k_i for each energy. However we overlook this fact for the moment and assume the propagator oscillates with a single period. In that case the integrand can be expanded in a Fourier Series as a function of D, that is,

$$\frac{1}{\pi}\ln[1+4V_x^2 G^{\uparrow}_{AB}(E,D)G^{\downarrow}_{BA}(E,D)] = C_m(E)e^{imk(E)D} \quad , \tag{4.22}$$

where

$$C_m(E) = \frac{k(E)}{2\pi}\int_{-\frac{\pi}{k(E)}}^{\frac{\pi}{k(E)}} dD\,\frac{1}{\pi}\ln[1+4V_x^2 G^{\uparrow}_{AB}(E,D)G^{\downarrow}_{BA}(E,D)]e^{-imk(E)D} \quad . \tag{4.23}$$

Eq.(4.18) can thus be written as

$$J(D) = \mathrm{Im}\int_{-\infty}^{\infty} dE\,\frac{1}{1+e^{\beta(E-E_F)}}\sum_m C_m(E)\,e^{imk(E)D} \quad , \tag{4.24}$$

where $\beta = 1/k_BT$ is the inverse temperature. Solving this integral involves making use of the Residue Theorem introduced in the previous chapter. The logarithm is analytic and therefore so are the Fourier Coefficients. Since the propagators $\mathcal{G}_{ab}$ and $\mathcal{G}_{ba}$ occur solely as a product, the integrand vanishes rapidly in the UHP and the contribution from the semi-infinite contour is zero. Thus, the only contribution to the integral comes from the poles of the Fermi Function, which are known as the Matsubara Frequencies. These are located at regular intervals along the imaginary

energy axis: $E_r = E_F + \frac{i\pi(2r+1)}{\beta}, r = 0, 1, 2, ...$ [2]. We can expand the integrand in a Laurent series valid on a small ball centred at E_r. As the temperature T decreases, the separation between the Matsubara Frequencies shrinks and so does the domain of validity of each of these expansions. However as long as we consider the limit of $T \to 0$, the poles remain distinct and the use of the Residue Theorem is still justified. Summing over the residues,

$$J(D) = -\mathrm{Im} \sum_m \sum_{r=0}^{\infty} C_m(E_r) \frac{e^{imk(E_r)D}}{\beta} \quad . \tag{4.25}$$

If $D >> 1$ then the integral is rapidly suppressed in the Upper Half Plane[3]. Consequently; only the Matsubara Frequencies close to the real energy axis make any appreciable contribution to the integral. As a result we can regard the energy dependence as only influencing the exponential factor, and,

$$\begin{aligned}
J(D) &= -\mathrm{Im} \sum_m C_m(E_F)\, e^{imk_F D} \sum_{r=0}^{\infty} \frac{\exp(imk'_F(E_r - E_F)D)}{\beta} && (4.26)\\
&= -\mathrm{Im} \sum_m C_m(E_F)\, e^{imk_F D} e^{-m\pi k'_F D/\beta} \sum_{r=0}^{\infty} \frac{\exp(-2m\pi r k'_F D/\beta)}{\beta} && (4.27)\\
&= -\mathrm{Im} \sum_m C_m(E_F)\, e^{imk_F D} \frac{\exp(-m\pi k'_F D/\beta)}{\beta(1 - \exp(-2m\pi k'_F D/\beta))} && (4.28)\\
&= -\mathrm{Im} \sum_m C_m(E_F) \frac{e^{imk_F D}}{2\beta \sinh(\frac{m\pi k'_F D}{\beta})} \quad . && (4.29)
\end{aligned}$$

The final step is to take the zero temperature limit $\beta \to \infty$, so that,

$$J(D) = -\mathrm{Im} \left[\frac{1}{2\pi k'_F D} \sum_m \frac{C_m(E_F)}{m} \exp(imk_F D) \right] \quad . \tag{4.30}$$

From Eq.(4.30) it is clear that the coupling displays an oscillatory behaviour with period k_F and an overall $1/D$ decay. The period is determined by the Fermi-Surface, which consists of six discrete points lying at the vertices of the First Brillouin zone of graphene (c.f. fig. 3.1(b)). The $1/D$ decay is the predicted rate for a quasi 1-dimensional system.

For higher dimensional systems each point on the Fermi Surface will contribute with an oscillatory component, the summation of which leads to interference effects

[2] We should note that the success of such a venture relies on the logarithm being analytic. Were this not the case, the residue theorem could not be used since $\log(f(z))$ cannot be represented as a holomorphic function about the zeros of $f(z)$.

[3] This necessitates that the Fourier Coefficients for which $m < 0$ must be zero. This is correct since we can regard the Fourier Series as a Laurent Series in e^{ikD}. Since the function is analytic in the UHP it can be represented by a Taylor Series i.e. the negative terms in the Laurent Series vanish.

that reduce the range of the coupling. Perhaps the most interesting feature of Eq.(4.30) is that its derivation involved no reference to whether the impurities are substitutional or adsorbed. It states that the period of oscillation and the decay rate are solely properties of the host material. It nevertheless seems reasonable that the particular impurity species or the type of interaction should influence the coupling. As we shall see, for the most part these affect only the amplitude of the oscillation. In some cases they can also change the overall phase of the oscillation. In situations where the exchange coupling is particularly strong, the shape of the oscillation can become quite complex as higher order Fourier Coefficients begin to contribute.

Since D describes the lattice separation we are limited to probing the function at integer spacings. As a result, whenever the wavevector satisfies $\frac{2\pi p}{q}$ then the coupling will be periodic with a q atomic layer period. For non rational wave-vectors the strict periodicity of Eq.(4.30) will not manifest itself if we restrict ourselves to integer spacings, although the behaviour will still be oscillatory.

For nanotubes the derivation outlined above has to be adjusted slightly to account for the fact that the Green Function propagators do not oscillate with a single period but rather as a function of the $2N$, in general incommensurate, wavevectors k_m seen in Chapter 3. By incommensurate it is meant that two wavevectors k_n and k_m are not related by a simple fraction. The presence of incommensurate wavevectors destroys the strict periodicity of the Green Function. Such functions are referred to as being quasi-periodic and in order to deal with such cases we must introduce a number of pseudo variables D_m, each of which is associated with the single wavevector k_m. The Green Function $\mathcal{G}(D_1, D_2, ..., D_{2N})$ is periodic with respect to each variable separately. This does not bring about any major alteration to Eq.(4.30) since, for nanotubes, most of the wavevectors are evanescent for any given energy. However it does lead to considerable notational congestion, which is why discussion of it has been postponed until now.

If we regard the integrand in Eq.(4.18) as being a function of the $2N$ pseudo variables, $D_1, D_2, ..., D_{2N}$, then each variable D_i oscillates as a function of the corresponding wavevector k_i. We must therefore perform a multi-dimensional Fourier Series expansion,

$$\frac{1}{\pi}\ln(1+4V_{\mathrm{x}}^2 G^{\uparrow}_{AB} G^{\downarrow}_{BA}) = \sum_{n_1,n_2,...,n_{2N}} C_{n_1,n_2,...,n_{2N}} e^{in_1k_1D_1} e^{in_2k_2D_2} \cdots e^{in_{2N}k_{2N}D_{2N}} \ . \quad (4.31)$$

Within the first sub-band only two wavevectors, labelled k_1 and k_2, give rise to non-evanescent contributions, so that the only relevant Fourier Coefficients are $C_{n_1,n_2,0,0,...,0}$. Setting $n_1 = n$, $n_2 = m$ and each of pseudo variables equal to D,

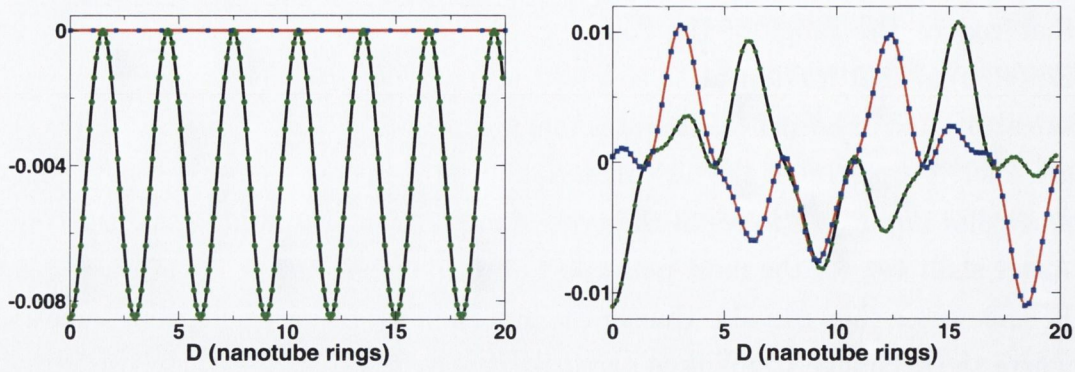


Figure 4.4: Real (black line/green dots) and imaginary (red line/blue dots) components of $\ln(1+4V_x^2 G^{\uparrow}_{AB} G^{\downarrow}_{BA})$ as a function of D on a $(5,5)$ armchair for 2 different values of E_F. The left panel shows $E_F = 0.0$, the right $E_F = -0.5\,\gamma$, where γ is the carbon-carbon hopping energy. In both cases the integrand is given by the solid lines. The dotted lines are the sum over the Fourier coefficients $m, n = -2, -1, 0, 1, 2$. The only contributions come from $(n, m) = (0, 2), (2, 0), (1, 1)$. The contribution from higher coefficients is negligible. For $E_F = 0.0$, the imaginary part of the integrand is seen to be zero.

then the integrand can be written as,

$$\frac{1}{\pi}\ln(1+4V_x^2 G^{\uparrow}_{AB}(E,D)G^{\downarrow}_{BA}(E,D)) = \sum_{n,m} C_{n,m}(E)e^{i(nk_1+mk_2)D} \quad . \tag{4.32}$$

In direct analogy with Eq.(4.30) we can write the coupling for this quasi-periodic case as,

$$J(D) = -\mathrm{Im}\sum_{n,m} \frac{C_{n,m}(E_F)}{2\pi(nk'_{1F}+mk'_{2F})D}\exp(i(nk_{1F}+mk_{2F})D) \quad . \tag{4.33}$$

Figure 4.4 shows the integrand in Eq.(4.22) as a function of the separation D for two different values of E. The tube in question is a (5,5) armchair. The case of $E = 0$ displays a simple period three oscillation. This results from the commensurability of the two wavemodes, $k = \pm 2\pi/3$, at the charge neutrality point. Moving away from $E = 0$, this commensurability is broken and the integrand is no longer a perfectly periodic function of the single variable D.

In the next section we examine the coupling for armchair and zigzag nanotubes.

4.5 Results

4.5.1 Armchair Nanotubes

For armchair nanotubes only two wavemodes, $k_{\pm}$, have non-evanescent contributions in the immediate vicinity of $E_F = 0$. From figure 4.5 it is seen that at $E_F = 0$ the propagating wavevectors are $k_{\pm} = \pm 2\pi/3$. This gives rise to a regular period

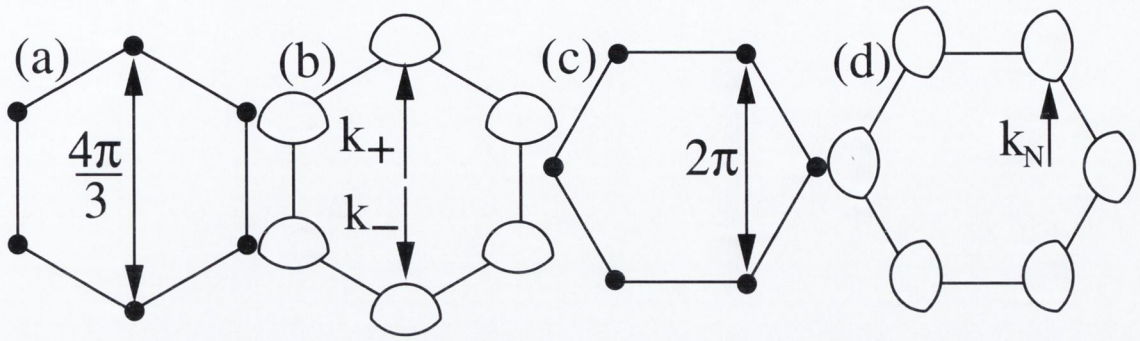


Figure 4.5: Propagating wavevectors for armchair and zigzag nanotubes as a function of the Fermi-Energy: (a) armchair with $E_F = 0$ (b) armchair with $E_F \neq 0$ (c) zigzag with $E_F = 0$ (d) zigzag with $E_F \neq 0$. For armchair nanotubes, changing E_F is seen to break the commensurability between the plus and minus wavevectors.

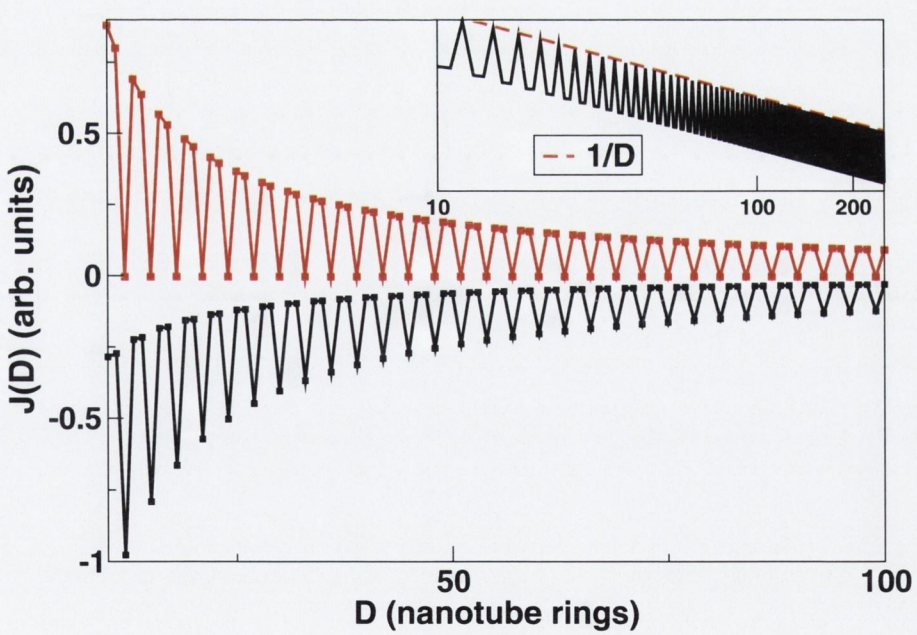


Figure 4.6: $J(D)$ for a $(5,5)$ armchair with 2 substitutional impurities at $E_F = 0.0$ for cases where the impurities reside on the same sublattice of graphene (black line) and on different sublattices (red line). The inset shows a log-log plot of the coupling. The decay is seen to be $1/D$. The magnitude of the coupling is given in terms of an arbitrary energy unit and the separation in the number of nanotube rings separating the impurities.

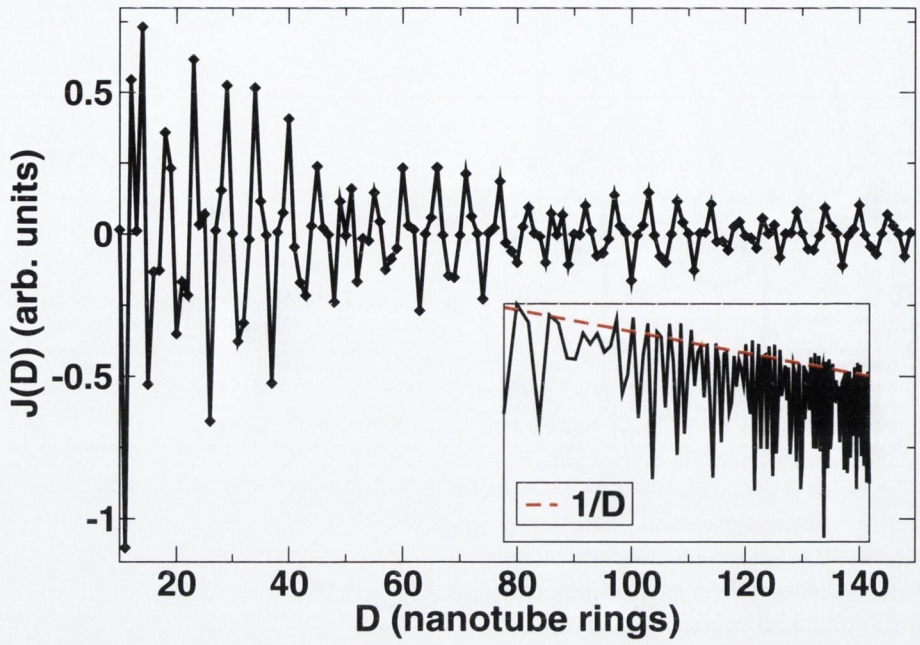


Figure 4.7: $J(D)$ for a $(5,5)$ armchair nanotube with 2 substitutional impurities at $E_F = -0.5\gamma$. The impurities reside on the same sublattice. Coupling is measured in arbitrary units, the separation in number of nanotube rings. The inset is a log-log plot of the coupling. It confirms that the rate of decay is 1/D.

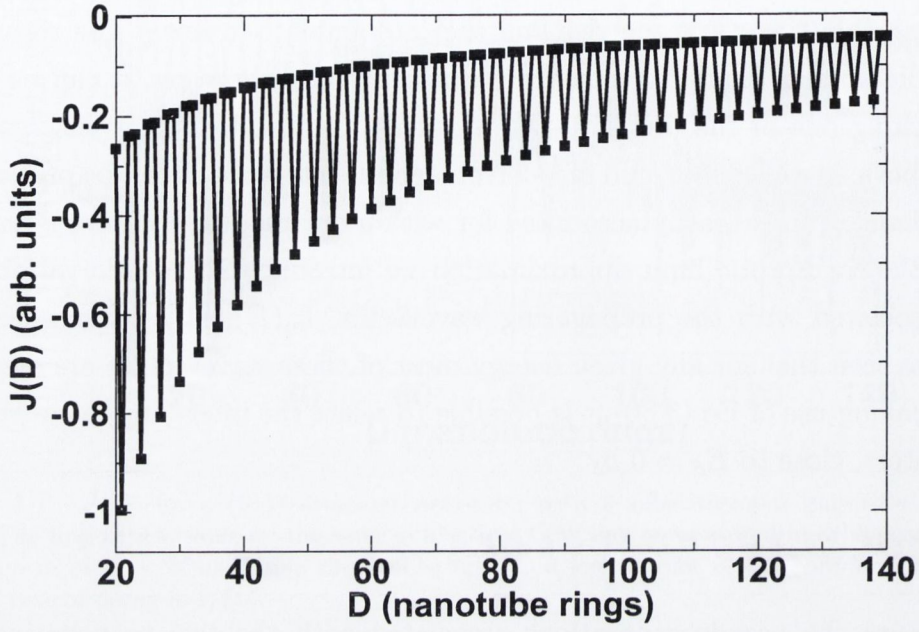
3 oscillation seen in figure 4.6, which shows the coupling as a function of D along the tube's longitudinal axis. Since we are examining the separation dependence, the actual magnitude of the coupling is not crucial and the results are written in arbitrary energy units. E_F and V_x are normalised by the carbon-carbon hopping, γ. In chapter 6 we will attempt to simulate the presence of real transition metal atoms and at this stage it will become necessary to introduce the appropriate physical energy unit. The coupling in figure 4.6, although technically oscillatory, does not exhibit any change in sign. This results from mixing of the $k_\pm$ wavemodes in Eq.(4.33). In cases with a single propagating mode the leading Fourier Coefficient, $C_0(E)$, must vanish, since a non-zero value would bias the coupling. Consequently, a change in sign should be a general feature of the coupling. However, from Eq.(4.33) with $k_+ = -k_-$, whenever $m = n$ the oscillatory contribution vanishes. In this case, no biasing will result since these terms still exhibit an overall decay: it is merely the oscillation that is suppressed. This is something of a subtle point. It might seem that since the 2 wavevectors are commensurate, the coupling could equally well be described by a single wavevector. However this is only true at $E_F = 0$, whereas the derivation of Eq.(4.33) involves an integration over all energy contributions. As such, the two situations are not equivalent. The overall oscillation, in the case of a nanotube, can thus be thought of as comprising the sum of an oscillatory decay sitting on a monotonic decay. The inset in figure 4.6 shows that in the asymptotic limit the coupling decays with the predicted rate of $1/D$.

Due to the bi-partite nature of the graphene lattice two distinct cases arise: in the first the moments are placed on the same sublattice, in the second they reside on different sublattices. The distinct sublattices are labelled black ($\bullet$) and white ($\circ$). The coupling for both cases has been included in figure 4.6. The black line shows the intra-sublattice case, the red line the inter-sublattice one. The results show that while no sign change results from changing the separation, it can be induced by switching one of the impurities to a different sublattice. This ensures that in general both ferromagnetic and anti-ferromagnetic interactions can be present. Such a sign change can be easily accounted for within our model. We have already seen how in the asymptotic limit approximation we introduce 2N pseudo variables, D_n, each associated with the propagating wavevector, $k_n(E)$, at a given energy. We have also seen that for any given energy most of these wavevectors are evanescent. Thus, making use of Eq.(3.30) it is possible to relate the inter- and intra- sublattice propagators, close to $E_F = 0$ by

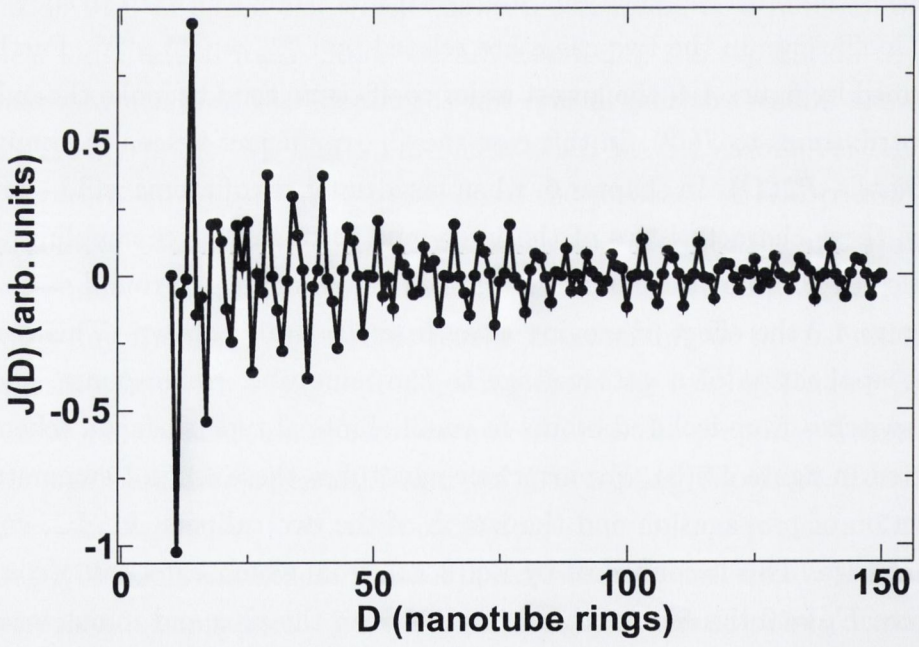
$$\mathcal{G}^{\bullet\circ}(D_+, D_-) = \mathcal{G}^{\bullet\bullet}(D_+, D_- + \pi/k_-) \quad . \tag{4.34}$$

D_+, D_- are the pseudo separations associated with the two propagating modes around $E_F = 0$. With this relation established it is straightforward to show that the Fourier Coefficients in the two cases are related by $C^{\bullet\circ}_{n,m} = C^{\bullet\bullet}_{n,m} e^{im\pi}$. Furthermore, as confirmed by figure 4.4, the lowest order coefficients tend to make the only significant contributions to $J(D)$. In this case the $C_{1,1}$ coefficient is seen to dominate and so $J^{\bullet\circ}(D) \approx -J^{\bullet\bullet}(D)$. In chapter 6, when large numbers of atoms will be present on the tube, these characteristics of the inter- and intra-sublattice couplings are seen to give rise to an interesting property of the overall magnetic ground state.

In figure 4.7 the effect of moving away from $E_F = 0$ is shown. This could arise from the application of a gate voltage to the nanotube. In response, the Fermi-Surface switches from isolated points to small elliptical type surfaces, schematically represented in figure 4.5(b). For armchair nanotubes these are not symmetric along the direction of propagation and the length of the two calipers, k_+, k_-, will consequently change. This is confirmed by Eq.(3.22), from which $k_+ = \cos^{-1}(\cos k_- + E)$. Away from $E_F = 0$ the commensurability between the plus and minus wavevectors is thus broken. As a result, the true oscillatory character of the coupling returns, but is no longer regular since the function is now quasi-periodic. This is accentuated by the short oscillation period which results in quite an untidy oscillation when restricted to integer spacings. This does not affect the rate of decay however, which is shown from the inset to retain a $1/D$ dependence. This quasi-periodicity was also seen in figure 4.4(b), which is a plot of the integrand in Eq.(4.18). Here, the separation D is allowed to assume non integer values. Although the pattern is



(a)



(b)

Figure 4.8: J(D) for a (5,5) armchair with 2 adsorbed impurities. (a) $E_F = 0$. (b) $E_F = -0.5\gamma$. The coupling $J(D)$ is plotted in arbitrary units and D refers to the number of armchair rings separating the impurities.

oscillatory, it is not exactly periodic.

The effect of switching from substitutional to adsorbed impurities is shown in figure 4.8. The switch does not introduce any qualitative differences in the behaviour of the coupling. At first this might seem surprising, but it is exactly in line with the predictions of the previous section, which restricts the impact of this change to the actual amplitude of the oscillation. The main features of the coupling were predicted to result solely from the properties of the host nanotube. With this in mind we consider, in the next section, the effect of replacing the host with a zigzag nanotube.

4.5.2 Zigzag Nanotubes

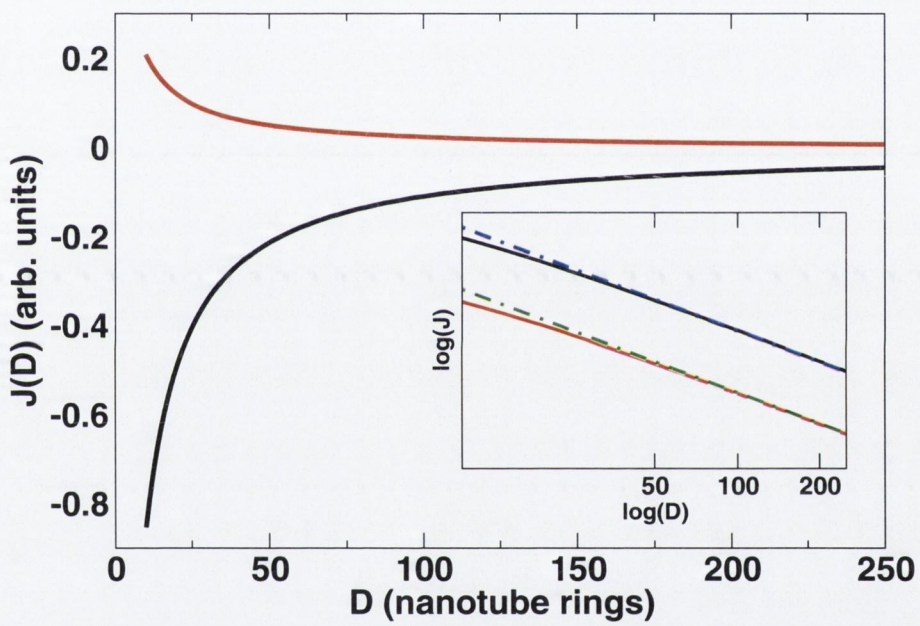


Figure 4.9: $J(D)$ for a $(6,0)$ zigzag at $E_F = 0.0$ with two adsorbed impurities. The black line represents the case where the impurities lie on the same sublattice, the red line the case where the impurities lie on different sublattices. The log-log plot shown in the inset confirms that the asymptotic rate of decay is $1/D$.

Fig. 4.9 shows a plot of the coupling for two adsorbed impurities on a metallic zigzag nanotube. As in the case for armchairs, the change in sign of the coupling is absent. Not only this but the decay is actually monotonic. To understand why it is necessary to look at the Fermi-Surface for the zigzag nanotubes shown in figure 4.5(c,d). Referring to Eq.(3.22), for a metallic (3N,0) zigzag the modes described by $m = N, 2N$ give non-evanescent contributions with wavevectors $k_m = \pi, 2\pi$ respectively. Consequently, along the longitudinal axis of the tube the period of oscillation is 2π[4]. Any oscillatory behaviour is masked since we are restricted to probing the

[4]This is because separation along the longitudinal axis actually involves switching $D = \Delta\ell + \Delta j$ in multiples of 2.

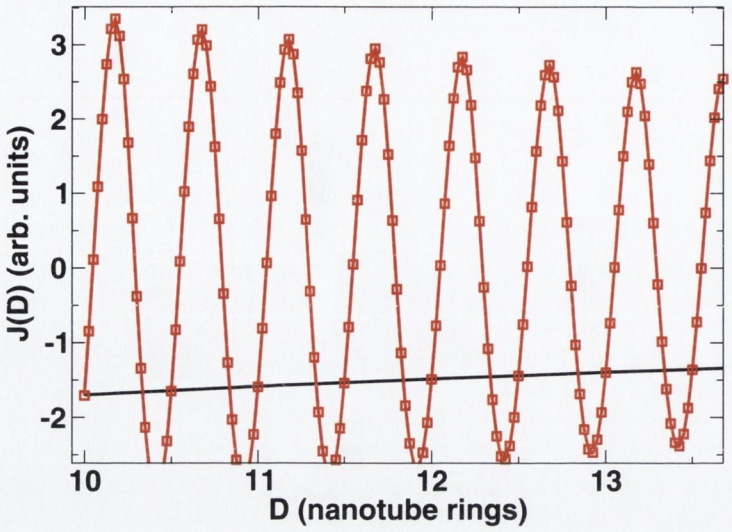


Figure 4.10: $J(D)$ for a $(6,0)$ zigzag at $E_F = 0.0$ with two adsorbed impurities. The separation is allowed assume non-integer values (red line), revealing the underlying oscillatory nature of the coupling. The black line shows the coupling with D restricted to integer values. J is measured in arbitrary units.

function at integer intervals. It is this commensurability between the propagating wavevector and the lattice spacing that results in the observed monotonicity. One way of revealing the underlying oscillation is to plot Eq.(4.18) for real values of D. This is shown in figure 4.10. The coupling is seen to be oscillatory with period of half a nanotube ring. This half lattice spacing arises because the propagators $\mathcal{G}_{ab}$ occur in Eq.(4.18) as products $\mathcal{G}_{ab}\mathcal{G}_{ba}$, so that the period of the integrand is in fact 4π. A second way of uncovering the oscillations is to change the Fermi-Energy, E_F. This might correspond to, say, the application of a small gate voltage. A small change in the Fermi-Energy results in the appearance of long-period oscillations. This is shown in figure 4.11 for the cases of $E_F = 0.1\gamma, 0.2\gamma$. The case of $E_F = 0$ can be viewed as an oscillation with an infinite period. As E_F changes the oscillation period gradually reduces. The overall oscillatory pattern is a lot smoother for zigzags than for armchairs, since the period is much longer. This might have a useful practical significance since it will thus be possible to find large areas in which the moments couple anti-ferromagnetically.

A second difference between armchair and zigzag tubes, evident from figure 4.11, is their behaviour away from $E_F = 0$. For armchairs the 2 propagating wavevectors become incommensurate and the overall coupling becomes quasi-periodic. For zigzags this is not the case. The wavevectors are related by $k_+(E) = k_-(E) + \pi$. Therefore, the coupling will oscillate with a single oscillation period. Again, this leads to a regular oscillatory pattern away from $E_F = 0$.

The final possibility we consider is the case of a semi-conducting zigzag nanotube. When the tube is semi-conducting the coupling is absent around $E_F = 0$ since there

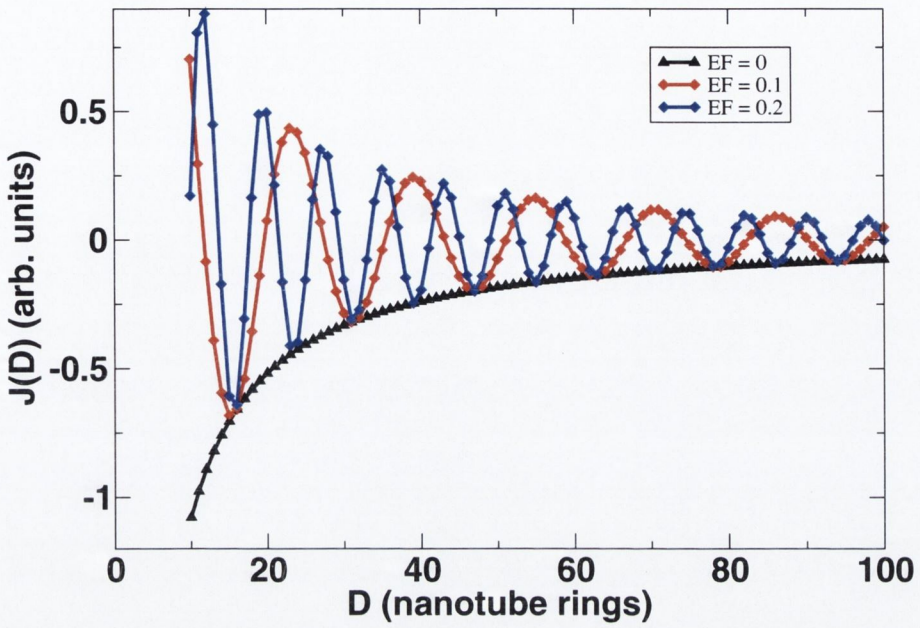


Figure 4.11: $J(D)$ for a $(6,0)$ zigzag with two substitutional impurities at $E_F = 0.0$ (black line), $E_F = 0.1\gamma$ (red line), $E_F = 0.2\gamma$ (blue line). Doping the tube reveals the underlying oscillatory character of the coupling. J is measured in arbitrary units, D is the separation in nanotube rings.

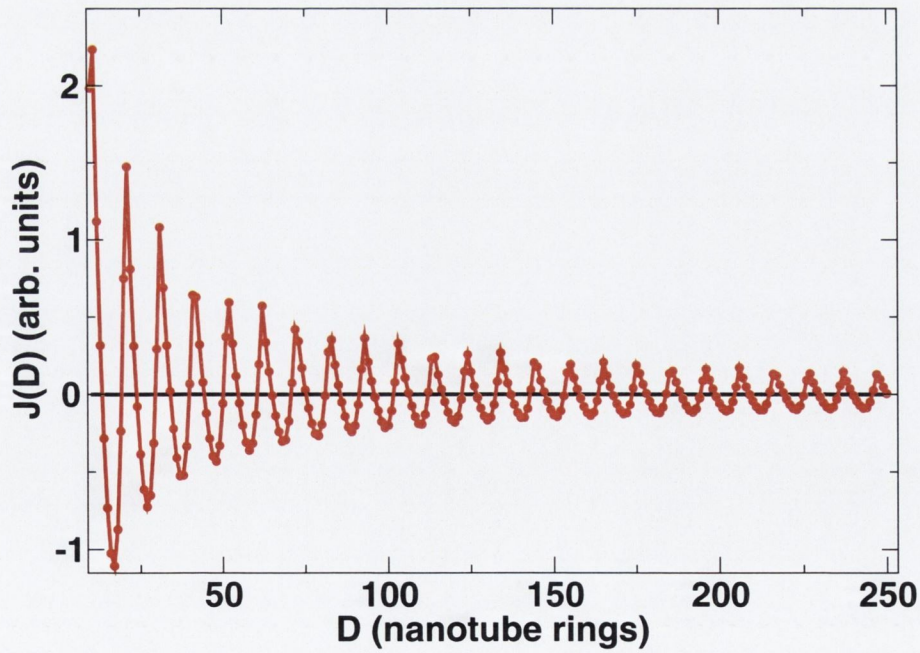


Figure 4.12: $J(D)$ for a $(7,0)$ semi-conducting zigzag with two adsorbed impurities at $E_F = 0.0$ (black line) and $E_F = 0.3\gamma$ (red line). J is measured in arbitrary units and D is the separation in nanotube rings.

are no extended states available to mediate the interaction. This is represented by the black line in figure 4.12 for a (7,0) tube. The coupling is exponentially suppressed. Applying a gate voltage will cause the Fermi-Surface to expand around the vertices of the graphene Brillouin zone. For the (7,0) tube, the surface will cross the first quantisation line at $E = \pm 0.26\gamma$. The red line in figure 4.12 shows the coupling at $E = 0.3\gamma$. The long range oscillation is indeed restored.

4.5.3 Effect of changing the Exchange Potential, V_x

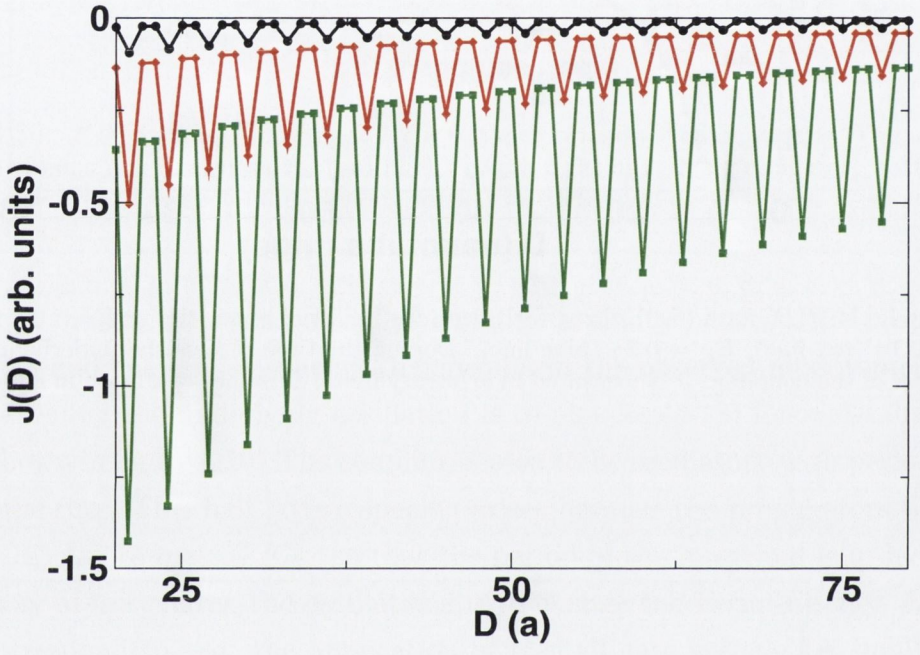


Figure 4.13: $J(D)$ for a (5,5) armchair with two adsorbed impurities at $E_F = 0.0$ for several values of V_x : 0.5γ (black), 1.0γ (red), 1.5γ (green). J is measured in arbitrary units, D is the separation in nanotube rings.

Using Eq.(4.33), the effect of changing D on the coupling could be seen in a particularly transparent fashion. In this section, the effect of changing V_x is investigated.

It is not immediately obvious from Eq.(4.33) how a change in V_x will influence the coupling since the dependence is encoded in the Fourier Coefficients. As such, broadly speaking, a change in V_x should alter the amplitude and the phase of the resulting oscillation. In figure 4.13 the coupling is plotted as a function of D for several different values of V_x for an armchair nanotube with two adsorbed atoms. The effect of changing the strength of the interaction is simply to change the amplitude of the oscillations. The question is whether this is a general statement or merely results from the particular values chosen. Additionally, do substitutional and adsorbed impurities behave differently as a function of V_x? From Eq.(4.18) it would appear that changing V_x should have an effect beyond simply scaling the oscillation,

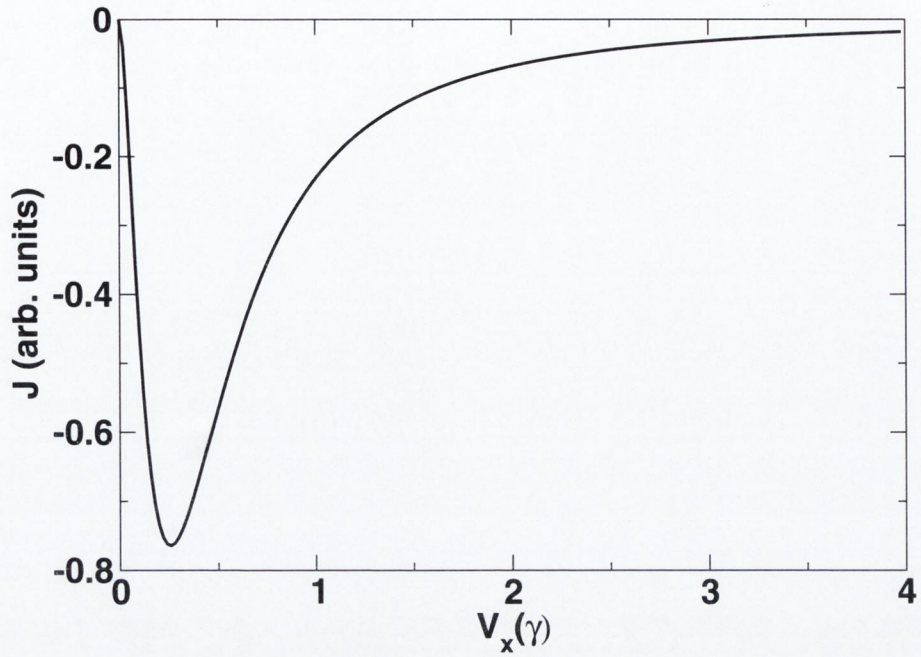


Figure 4.14: Coupling as a function of V_x on a (6,0) zigzag with two adsorbed impurities at $E_F = 0$. Two limiting regimes are evident: For small V_x the coupling increases quadratically while for large splittings the decoupling decreases quadratically.

and would in principle also change the phase of the oscillation. If it were solely the amplitude that was altered then the dependence of $J(D, V_x)$ on variables D and V_x must be separable, that is, the coupling can be expressed as a product of functions of D and V_x only. It is easy enough to see that this will not be true in general. However, there are regimes where it will be true and this explains the absence of any phase shift in figure 4.13. To help identify these regimes, figure 4.14 shows the coupling in the adsorbed case for a zigzag tube as a function of V_x with $D = 50$. The dependence is non-monotonic, and it is possible to identify 2 clear limiting cases: the case of small splitting where the increase is quadratic and the case of large splittings where the decrease is quadratic. These two regimes correspond to regions where the argument to the log in Eq.(4.18) can be expanded to low order terms in $V_x G^{\sigma}_{AB}$. As we shall see, this is not quite the same as saying that the integrand can be expanded in low order powers of V_x, because G_{AB} itself contains a dependence on V_x and will consequently behave differently in the two limits.

In figure 4.15 the coupling has been plotted as a function of separation for several values of V_x on a (6,0) zigzag with a small gate voltage applied to reveal the underlying oscillation. The results show a simple sinusoidal behaviour. Again, changing V_x simply alters the amplitude of the oscillation; the phase remains the same in each case. Figure 4.16 shows a similar plot for three smaller splitting values. Here the effect of changing V_x is more pronounced. Although the period of oscillation remains unchanged, the shape and phase is altered by decreasing V_x. This is particularly evident at $V_x = 0.3\,\gamma$ and $0.4\,\gamma$. The genesis of a sawtooth profile indicates the presence

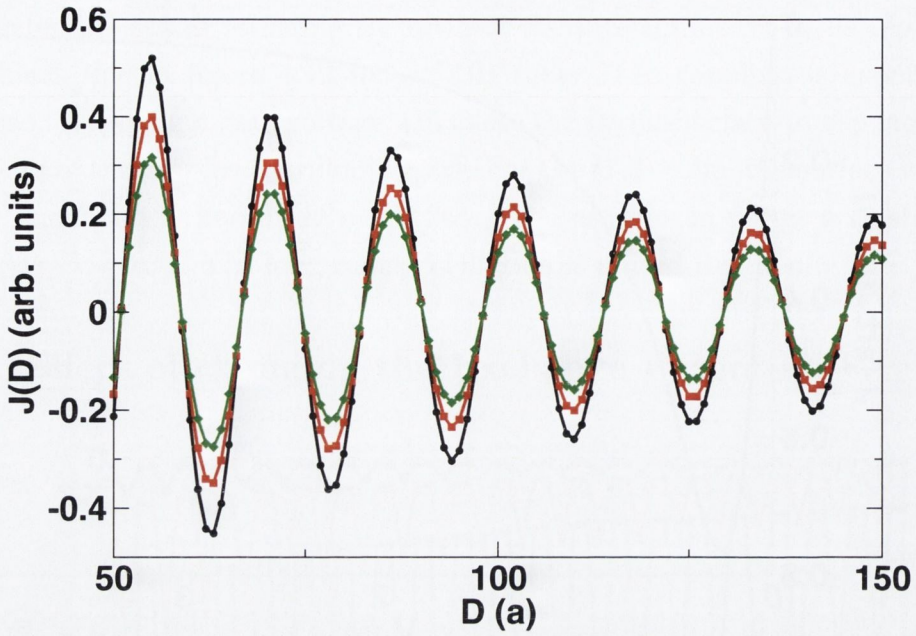


Figure 4.15: Coupling on a (6,0) zigzag nanotube with two adsorbed impurities for different values of V_x: Black line $3.5\,\gamma$; red line $4.0\,\gamma$; green line 4.5γ. $E_F = 0.10\gamma$. The effect of changing V_x is merely to scale the oscillation.

of higher order powers of $\mathcal{G}_{AB}(D) \sim e^{ik_F D}$ in the expansion. By contrast, in figure 4.15 the higher order harmonics make a negligible contribution and the behaviour is simple sinusoidal. In this region, the interaction strength, V_x, and separation, D, become separable in Eq.(4.18) and hence the effect of changing the strength of the splitting is only to scale the amplitude but not the shape or phase.

To see this a little more clearly we look at the expression for the propagator $V_x G^{\uparrow}_{AB}(D)$ given by Eq.(4.20). For adsorbed impurities, setting $t = 1$,

$$V_x G^{\uparrow}_{AB}(D) = V_x \frac{\mathcal{G}_{ab}(D)}{(E - V_x - \mathcal{G}_{aa})(E - V_x - \mathcal{G}_{bb}) - \mathcal{G}_{ab}(D)\,\mathcal{G}_{ba}(D)} \quad , \tag{4.35}$$

and describes how the interaction strength affects the profile of the coupling. When V_x is *small* the coupling will increase quadratically. In this context *small* is determined by the condition,

$$|V_x| \ll \left| \frac{(E - \mathcal{G}_{aa})(E - \mathcal{G}_{bb}) - \mathcal{G}_{ab}\mathcal{G}_{ba}}{2E - (\mathcal{G}_{aa} + \mathcal{G}_{bb})} \right| \quad , \tag{4.36}$$

which means the denominator is very weakly dependent on the exchange splitting. When this is satisfied V_x and $G^{\uparrow}_{AB}$ become separable

In the opposite limit, $V_x \to \infty$, the integrand decreases quadratically with V_x. The denominator no longer has any separation dependence and the decay is described by the simple oscillatory product $\mathcal{G}_{ab}(D)\mathcal{G}_{ba}(D)$ appearing in the numerator. Again, D and V_x become separable variables and the effect of V_x is simply to change

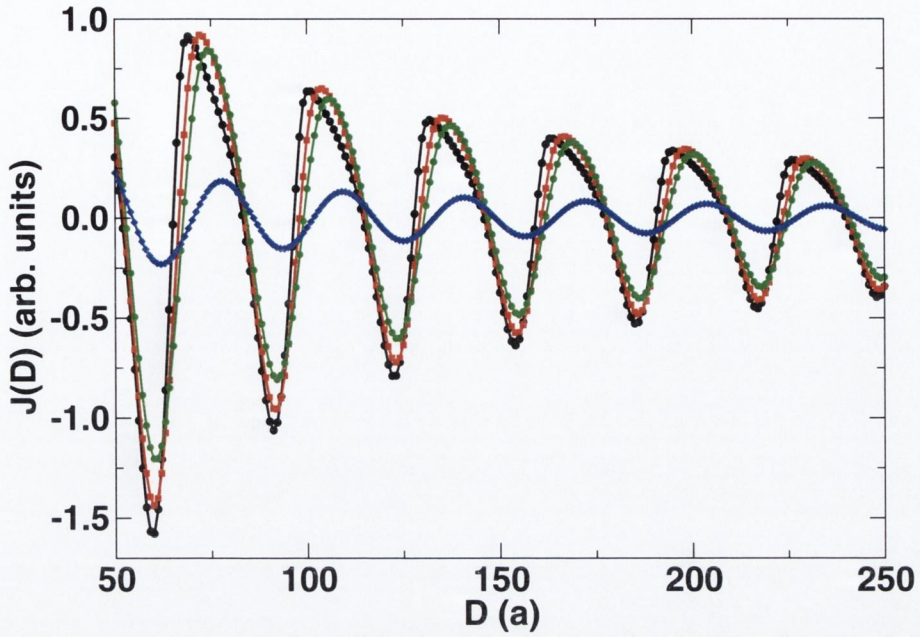


Figure 4.16: Coupling on a (6,0) zigzag nanotube with two adsorbed impurities for different values of V_x. Black line $0.3\,\gamma$; red line $0.4\,\gamma$; green line $0.5\,\gamma$; blue line $1.5\,\gamma$. The Fermi-energy is set at $E_F = 0.10\gamma$. In this regime the phase and shape of the coupling shows some sensitivity to the value of V_x.

the amplitude of the oscillation, as evidenced by figure 4.15.

The case of substitutional impurities is somewhat different. From Eq.(4.19) with $\lambda^{\uparrow}_{a,b} = -V_x$,

$$V_x G^{\uparrow}_{AB}(D) = V_x \frac{\mathcal{G}_{ab}(D)}{(1 + V_x\,\mathcal{G}_{aa})(1 + V_x\,\mathcal{G}_{bb}) - V_x^2\,\mathcal{G}_{ab}(D)\,\mathcal{G}_{ba}(D)} \quad . \tag{4.37}$$

It is clear that for small V_x the coupling will increase quadratically and as $V_x \to \infty$ the decay is quadratic. This is similar to the adsorbed case. However a striking difference between the two cases is seen in the width of the profile for substitutional impurities, shown in figure 4.17. The difference essentially results from a reciprocity between substitutional and adsorbed atoms. For adsorbed atoms, the condition for observing a leading order quadratic dependence is essentially that $|V_x| \ll |\mathcal{G}_{aa}|$, i.e., the denominator in Eq.(4.35) is not strongly dependent on V_x. For substitutional impurities it becomes $|V_x| \ll |\mathcal{G}_{aa}|^{-1}$. Since in general $|\mathcal{G}_{aa}| < 1$ this will be valid over a much wider range of V_x than in the case of substitutional impurities.

Another qualitative difference between the two cases can be seen by examining the limit of large exchange splitting. As already seen from figure 4.15, in the adsorbed case the coupling oscillates sinusoidally and only the amplitude of the oscillation is affected by the magnitude of the splitting. The substitutional case is shown in figure 4.18 for 4 different values of V_x in the range of $10.0 - 40.0\,\gamma$. Such strong splittings may not have much physical relevance but they nevertheless

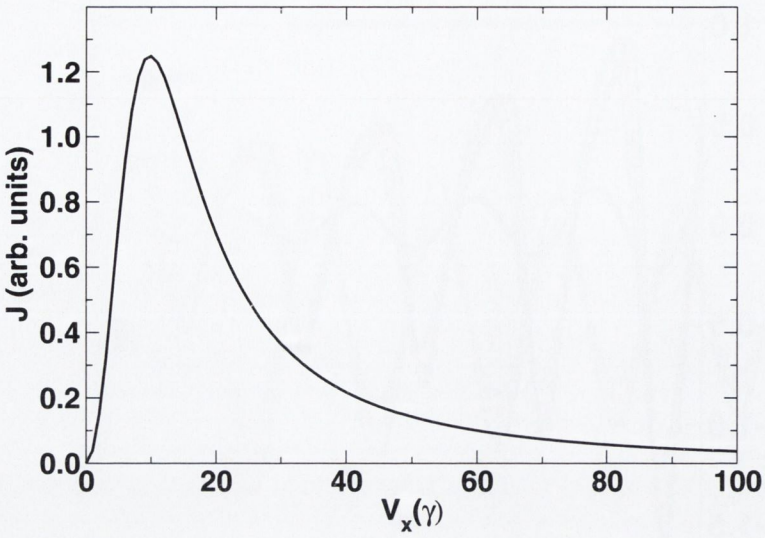


Figure 4.17: Coupling as a function of V_x for two substitutional impurities on a (6,0) zigzag at $E_F = 0.05\gamma$. The impurity separation is 50 layers.

constitute a valid limit. At $V_x = 10.0\,\gamma$, the coupling appears sinusoidal. As the exchange splitting is increased further still the coupling adopts a square like profile. As $V_x \to \infty$ a limiting shape is reached. In each case the period and rate of decay of the oscillation is unaffected. This is a particularly nice illustration of how a limiting value can still give rise to a more complicated oscillatory pattern. It amounts to the distinction between expanding Eq.(4.18) in low orders in $V_x G^{\sigma}_{AB}$ as against V_x. After implementing the former, D dependent propagators, $\mathcal{G}_{ab}(D)$, remain in the denominator and these may lead to deviations from simple sinusoidal behaviour. There is no reason to believe that these should be expandable to low order harmonics, since there is no parameter in the denominator to control such an expansion. Indeed for substitutional impurities, as $V_x \to \infty$, Eq,(4.37) will behave as,

$$\sim \frac{1}{V_x} \frac{\mathcal{G}_{ab}(D)}{(\mathcal{G}_{aa}\mathcal{G}_{bb} - \mathcal{G}_{ab}(D)\mathcal{G}_{ba}(D))} \quad . \tag{4.38}$$

This function will determine the limiting shape of the oscillation. Since there are no longer any terms in V_x in the denominator, the function should contain higher order powers in the harmonics $\mathcal{G}_{ab}(D) \sim e^{ik_F D}$ that a perturbative treatment, such as the RKKY theory, will not be able to account for. Of course, from the point of view of real substitutional dopants, we are far more likely to lie in the opposite regime with simple oscillatory behaviour. Nevertheless, it is interesting to see how in principle altering the exchange potential can lead to some highly non-trivial oscillatory patterns.

Thus we see that although the primary effect of the magnitude of the exchange splitting is in determining the amplitude of the oscillation, it can also influence the phase of the coupling and, when higher harmonics are important, the shape of the

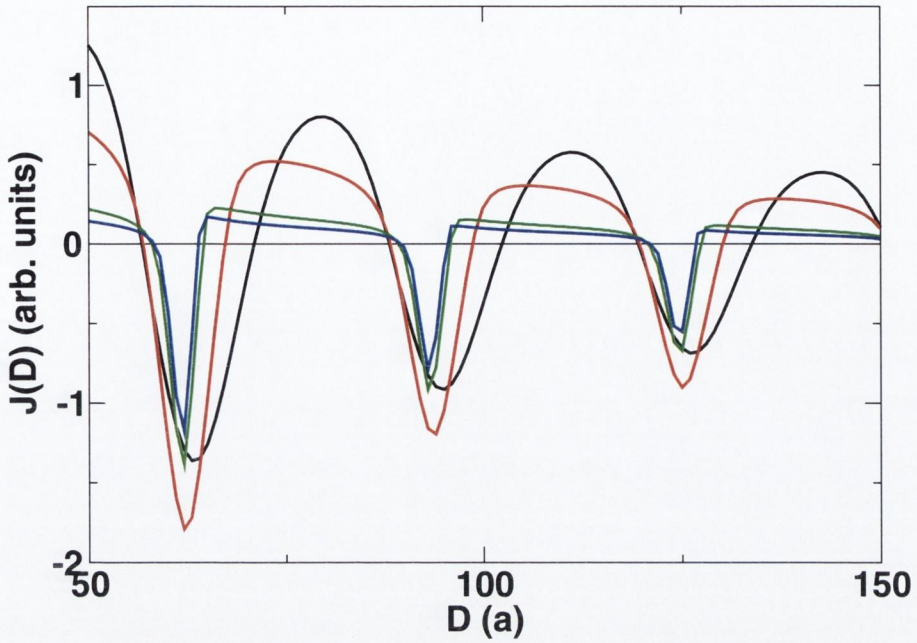


Figure 4.18: Coupling on a (6,0) zigzag nanotube with two substitutional impurities for different values of V_x at $E_F = 0.05\gamma$. Black line $V_x = 10.0\,\gamma$; red line $20.0\,\gamma$; green line $30.0\,\gamma$; blue line $40.0\,\gamma$. As $V_x \to \infty$ a non sinusoidal profile develops. This results from higher order contributions in $\mathcal{G}_{ab}(D)$ and represents deviations from the predictions of RKKY theory.

oscillation. These effects, particularly any shift in the overall phase of the coupling, are most clearly evident in the regime where the splitting has an intermediate strength such that V_x is coupled to D in a non separable fashion.

4.6 Summary of Chapter

In this chapter we examined the Indirect exchange coupling between localised magnetic moments on armchair and zigzag nanotubes. The results were in agreement with the predictions of the Quantum Well Theory as applied to multilayers. Specifically, the coupling was found to be non-oscillatory but this was seen to result from a commensurability between the propagating wavevector(s) and the lattice separation. This commensurability could be broken by changing the Fermi-Energy through, say, the application of a gate voltage. Additionally, switching from substitutional to adsorbed dopants was seen to bring about no qualitative changes. We also examined the effect of changing the magnitude of the exchange splitting. Primarily, this affected the amplitude of the coupling but over certain ranges it could give rise to non-trivial oscillatory profiles. Such profiles can not be accounted for using the RKKY theory.

Perhaps most importantly, a long range decaying rate of $1/D$ was observed in all cases. This confirms the prediction that the rate of decay is determined by the systems dimension. The content in this chapter has appeared in abridged form in

reference[60].

Chapter 5

Suppression of Indirect Exchange Coupling on Carbon Nanotubes

In chapter 4 the properties of IEC between a pair of magnetic impurities interacting with a nanotube host were examined quite extensively. The results were in complete agreement with the general characteristics predicted by the Quantum Well Theory. Specifically, the coupling was found to be oscillatory, although the oscillation could be masked by commensurability effects, and the period of oscillation was seen to be exclusively a property of the host Fermi-Surface. The rate of decay is determined by the dimensionality of the system and for a quasi 1-D metal like a nanotube is predicted to be $1/D$. These features were common to zigzag and armchair tubes with both substitutional and adsorbed impurities. Such a robust behaviour would suggest that the phenomena are well understood and should be general characteristics of all tube/impurity combinations. Nevertheless, attempts to reproduce such a long ranged decay using *ab-initio* techniques have been unsuccessful[35][61]. In this chapter this apparent discrepancy is resolved. In so doing an unexpected intrinsic characteristic of doped nanotubes is revealed.

5.1 Ab-initio Results

5.2 Failure of the Asymptotic Approximation

The derivation outlined in chapter 4 leading to Eq.(4.30) does not allow for a decay rate faster than $1/D$. As the derivation is quite general it is reasonable to assume that this would be one of the most robust characteristics of IEC on nanotubes. In an attempt to identify the source of any higher order decay, we return to Eq.(4.24) where the integrand had been expanded in a Fourier Series. Starting from this point, the only assumption made in arriving at Eq.(4.30) is that the Fourier coefficients

are slowly varying functions of energy and can hence be evaluated at $E = E_F$. This is perfectly valid. In fact it is the assumption underpinning the asymptotic approximation which allows for the analytic evaluation of the integral. However, there is an another, more subtle implication: that these coefficients are non-zero. To account for cases where the coefficients may vanish it is necessary to derive an extension to Eq.(4.30).

Returning to Eq.(4.24), if $C_m(E_F) = 0$ then it becomes necessary to consider the contribution to the integrand from $C_m(E)$ in the vicinity of E_F. Since the coefficients are slowly varying, with respect to the exponential term, we can expand them in a Taylor Series about $E = E_F$,

$$C_m(E) = \sum_{p=0}^{\infty} \frac{1}{p!} \left. \frac{d^p C_m}{dE^p} \right|_{E_F} (E - E_F)^p. \tag{5.1}$$

Inserting in Eq.(4.24) we have,

$$J(D) = \mathrm{Im}\left[\int_{-\infty}^{\infty} dE f(E) \sum_{p=0}^{\infty} \sum_{m} \frac{1}{p!} \left. \frac{d^p C_m}{dE^p} \right|_{E_F} (E - E_F)^p \exp(imk(E)D) \right]. \tag{5.2}$$

The coefficients, C_m, are now energy independent and we can move them outside the integral. As before, with $D \gg 1$, the exponential is well approximated by expanding $k(E)$ to first order,

$$J(D) = \mathrm{Im}\left[\sum_{p=0}^{\infty} \sum_{m} \frac{1}{p!} \left. \frac{d^p C_m}{dE^p} \right|_{E_F} \int_{-\infty}^{\infty} dE\, f(E)(E - E_F)^p e^{im(k_F + k'_F(E-E_F))D} \right]. \tag{5.3}$$

This can be written as,

$$J(D) = \mathrm{Im}\left[\sum_{p=0}^{\infty} \sum_{m} \frac{1}{p!} \left. \frac{d^p C_m}{dE^p} \right|_{E_F} \frac{e^{imk_F D}}{[imk'_F]^p} \frac{d^p}{dD^p} \left\{ \int_{-\infty}^{\infty} dE \frac{\exp(imk'_F(E - E_F)D)}{1 + e^{\beta(E-E_F)}} \right\} \right]. \tag{5.4}$$

The quantity in chain brackets can be evaluated by exactly the same method that was used in the previous chapter and therefore the integration can proceed in the same fashion, yielding,

$$\begin{aligned} \int_{-\infty}^{\infty} dE \frac{\exp(imk'_F(E - E_F)D)}{1 + e^{\beta(E-E_F)}} &= -\frac{1}{\beta} \sum_{r=0}^{\infty} \exp(-m\pi k'_F(2r+1)D/\beta) \\ &\overset{T \to 0}{=} -\frac{1}{2m\pi k'_F D}. \end{aligned} \tag{5.5}$$

Now,

$$J(D) = -\mathrm{Im}\left[\sum_{p=0}^{\infty}\sum_{m}\frac{1}{p!}\left.\frac{d^p C_m}{dE^p}\right|_{E_F}\frac{e^{imk_F D}}{[imk'_F]^p}\frac{d^p}{dD^p}\left\{\frac{1}{2m\pi k'_F D}\right\}\right] \quad . \tag{5.6}$$

Subsequent differentiation leads to a generalised expression for Eq.(4.30),

$$J(D) = -\mathrm{Im}\left[\sum_{p=0}^{\infty}\sum_{m}\left.\frac{d^p C_m}{dE^p}\right|_{E_F}\frac{i^p\, e^{imk_F D}}{2\pi(mk'_F)^{p+1}D^{p+1}}\right] \quad . \tag{5.7}$$

The two expressions are in agreement when $p = 0$.

This generalisation shows that the overall decay can be thought of as a sum over decay rates of all orders. Since we are considering the asymptotic limit, then the higher order decaying terms are suppressed rapidly and the decay rate is determined by the leading order term. The previous derivation had assumed that this was the first order term, however, if this is not true the decay may be more rapid. The obvious question is: under what circumstances will such a condition occur. A sufficient condition for $C_m(E_F)$ to vanish is if the integrand in Eq.(4.18) evaluated at $E = E_F$ vanishes. This in turn requires that $G^{\sigma}_{AB}(E)$ is zero. This simple argument establishes a criteria for determining whether the decay rate will be more rapid than expected.

This rescues the situation to the point that the model is now capable of producing high decaying rates. It does not yet attach any physical significance to the circumstances under which such a decay occurs, and crucially why *ab-initio* calculations might fail to produce long range coupling in the case of nanotubes. To address this we must return to the basic assumptions of our nanotube/impurity system. The only particular assumption made was that the adsorbed atom lay atop a single carbon atom. In reality, as seen from figure 5.1, an adsorbed atom can reside at several possible locations within the host. The atop position was chosen in the first instance for simplicity. Since the rate of decay was assumed to be determined by the dimensionality of the host, then the position of the impurity should be irrelevant. However, the apparent absence of long range coupling motivates the exploration of the effect of this additional degree of freedom.

5.3 Effects of Changing Adatom Location

Fig. 5.1 shows three possible locations for an itinerant atom adsorbed on a carbon nanotube. These positions are called the atop, bridge and centre position and correspond to the impurity sitting (a) atop a single carbon atom, (b) at a bridge site between carbon atoms and (c) at the centre of a hexagon of carbon atoms. A num-

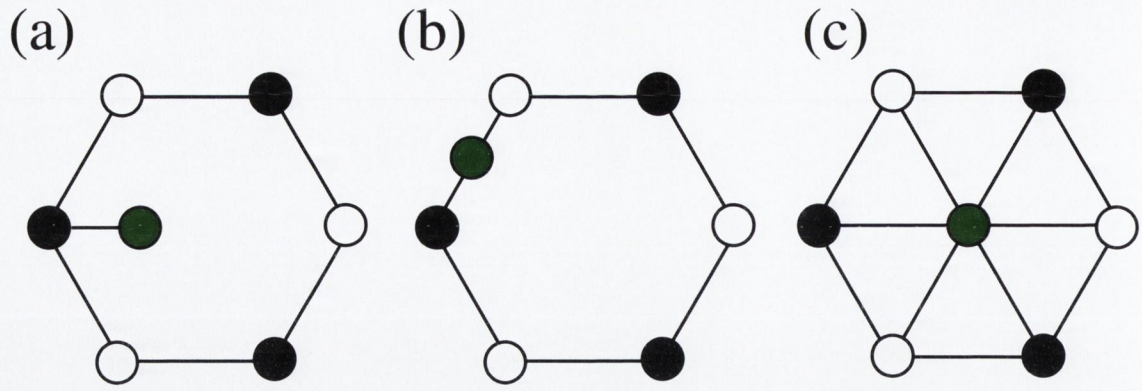


Figure 5.1: Three possible locations for an adatom (green) within a host nanotube: (a) atop a single carbon atom (b) a bridge site between atoms (c) at the centre of a hexagon of carbon atoms.

ber of *ab-initio* calculations have been conducted into the stability of each of these sites on armchair and zigzag nanotubes[36][37][38]. These studies have concluded that the centre location was the most stable configuration for all transition metal atoms surveyed. Certain atoms, for example Cobalt, have metastable states in the atop position although these were found to be very sensitive to factors such as the curvature of the tube.

The formalism developed in chapter 4 is easily capable of distinguishing between these three scenarios. We consider a general case of 2 adsorbed impurities A, B, each of which is in contact with n host atoms. The perturbation Hamiltonian for such a system is,

$$\hat{V} = \sum_{\ell=1}^{n} |A\rangle\, t_\ell\, \langle a\,\ell| + |a\,\ell\rangle\, t_\ell\, \langle A| + |B\rangle\, t_\ell\, \langle b\,\ell| + |b\,\ell\rangle\, t_\ell\, \langle B| \quad . \tag{5.8}$$

a, b labels the group of lattice atoms in contact with A, B respectively. The second index, ℓ, labels the individual host atoms. For the three cases shown in figure 5.1, $n = 1$ is the atop position, $n = 2$ for bridge sites and $n = 6$ for the centre location. For simplicity we assume that the interaction between the impurity and each host atom is equivalent. This amounts to setting $t_\ell = t$. The effect of relaxing this condition is addressed in section 5.6. We can then write,

$$\hat{V} = t(|A\rangle\, \langle a| + |a\rangle\, \langle A| + |B\rangle\, \langle b| + |b\rangle\, \langle B|) \tag{5.9}$$

where $|a\rangle = \sum_{\ell=1}^{n} |a\,\ell\rangle$. Written in this form $|a\rangle$ can be regarded as an effective lattice site and the expression for the propagator G_{AB} is identical to Eq.(4.20). The only difference is that the lattice-lattice propagator, $\mathcal{G}_{ab}$, is now a sum over $n \times n$ propagators between individual host atoms. To distinguish between the various

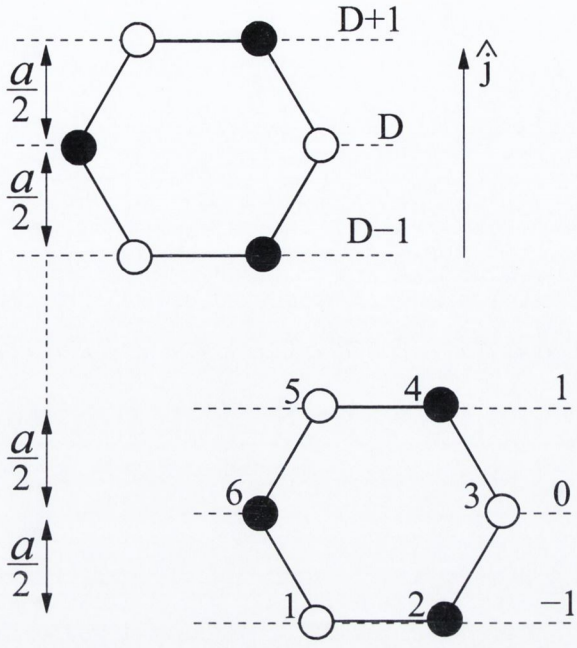


Figure 5.2: Two armchair nanotube hexagons separated in the longitudinal direction by $D\,\mathbf{a}_Z$. When impurities are centrally located they interact with host atoms on three adjacent lines of carbon atoms: $-1\,,0\,,1$. The atoms are labelled from 1-6 in a counterclockwise direction.

cases we introduce a generalised propagator,

$$\Gamma_{ab}^{(n)} = \sum_{\ell=1}^{n}\sum_{\ell'=1}^{n}\langle a\ \ell|\hat{\mathcal{G}}|b\ \ell'\rangle \quad . \tag{5.10}$$

If $n = 1$ then $\Gamma_{ab}^{(1)} = \langle a\ 1|\hat{\mathcal{G}}|b\ 1\rangle$ and the atop case is recovered. For $n = 6$ the sum extends over the 36 propagators linking each atom in hexagon a with all of the atoms in hexagon b. When computing this sum, the analytic expressions developed in chapter 3 will prove extremely useful. We now consider armchairs and zigzags in turn.

5.3.1 Armchair Nanotubes

For armchair tubes, when the Fermi-Energy (E_F) is close to zero, only two of the propagating wavevectors will rise to non-evanescent contributions. This is not meant in any limiting sense of E_F tending to zero. About $E_F = 0$ there is a finite region, its extent determined by the tube diameter, where only these two sub-bands will provide extended states. These bands are the two solutions with $m = 0$[1] in the dispersion relation for armchairs, Eq.(3.22),

$$E^2 = t_0^2(1 + 2\cos(k))^2 \quad , \tag{5.11}$$

[1]We have previously assumed that the mode index ran from 1,...,N, but we could equally have chosen 0,...,N-1. The only requirement is that we consider all the states in the 1st Brillouin Zone.

giving

$$\cos(k_{\pm}) = -\frac{1}{2} \pm \frac{E}{2t_0} \quad . \tag{5.12}$$

Neglecting the other sub-bands, Eq.(3.30) can be written in a much simplified form. Firstly the dependence on the transverse separation vanishes, since the $n = 0$ modes correspond to electrons travelling along the longitudinal axis of the tube. If we write the separation along this direction as $D = |\Delta\ell - \Delta j|$ then by labelling the black and white site on each line as $(\bullet, \circ)$, we can write

$$\mathcal{G}^{\bullet\bullet}(D) = \frac{i}{4Nt_o}\left(\frac{e^{ik_+D}}{\sin k_+} - \frac{e^{ik_-D}}{\sin k_-}\right) = \mathcal{G}^{\circ\circ}(D) \tag{5.13}$$

for intra-sublattice propagators. For propagators on different sublattices,

$$\mathcal{G}^{\bullet\circ}(D) = \frac{i}{4Nt_0}\left(\frac{e^{ik_+D}}{\sin k_+} + \frac{e^{ik_-D}}{\sin k_-}\right) = \mathcal{G}^{\circ\bullet}(D) \quad . \tag{5.14}$$

With such a simplified form for the propagators it is an easy matter to sum over the contributions from the $n \times n$ lattice sites. Fig. 5.2 shows that the hexagon of carbon atoms surrounding each impurity extends over three lines of carbon atoms. There are two atoms, from different sublattices, on each line. Considering the case where the 2 atoms are on the same line and defining a ket $|j \bullet/\circ\rangle$ as representing the $\bullet/\circ$ atom on line j,

$$\langle 0 \bullet |\hat{\mathcal{G}}| D \bullet\rangle + \langle 0 \bullet |\hat{\mathcal{G}}| D \circ\rangle = 2\frac{i}{4Nt_0}\frac{e^{ik_+D}}{\sin k_+} \quad . \tag{5.15}$$

But this is the same as the expression for the generalised propagator $\Gamma^{(2)}_{ab}$, for the bridge site in the case where the adatoms lie on a given line (e.g. between 1 and 2). The actual propagator will be twice this value since both atoms on the line contribute,

$$\Gamma^{(2)}_{ab} = 4\frac{i}{4Nt_0}\frac{e^{ik_+D}}{\sin k_+} \quad . \tag{5.16}$$

We note in passing that Eq.(5.16) is a function of k_+ only.

Returning to the centre ($n = 6$) sites and including the contributions from the propagators between the atoms on line 0 and those on lines $D-1, D+1$

$$\sum_{\ell=1}^{6}\langle 0 \bullet |\hat{\mathcal{G}}| b\,\ell\rangle = 2\frac{i}{4Nt_0}\frac{e^{ik_+D}(e^{-ik_+} + 1 + e^{ik_+})}{\sin k_+} = \langle 0 \bullet |\hat{\mathcal{G}}|\, b\rangle \quad . \tag{5.17}$$

This is also equal to the propagator $\langle 0 \circ |\hat{\mathcal{G}}| b\rangle$. All that remains is to include the contributions from line -1 and 1. Each will be identical to the above propagator only phase shifted by an amount $e^{-ik_\pm}$ and $e^{ik_\pm}$. Thus,

$$\Gamma^{(6)}_{ab} = 4\frac{i}{4Nt_0}(e^{-ik_+} + 1 + e^{ik_+})^2 \frac{e^{ik_+ D}}{\sin k_+} \quad . \tag{5.18}$$

From Eq.(5.18) it is clear that each of the 3 lines contributes an oscillatory component to $\Gamma^{(6)}_{ab}$, related by a simple phase shift. The total phase factor is given by $1+e^{-ik_+}+e^{ik_+} = 1+2\cos(k_+)$. However since the propagating wavevector at $E_F = 0$ is $2\pi/3$, the phase shift is exactly one third of a wavelength. Thus an interference effect arises which causes the generalised propagator $\Gamma^{(6)}_{ab}(E_F = 0)$ to vanish.

There is an alternative way of viewing this interference. In chapter 3, when calculating the band structure for graphene we saw that the hopping between intersublattice sites gave rise to a factor $t(\mathbf{k})$. For the $m = 0$ modes of an armchair tube, this factor equals $t(k_\pm) = t_0(1 + 2\cos(k_\pm))$, and from Eq.(3.22) it satisfies $E^2 = |t(k_\pm)|^2$. Therefore, Eq.(5.18) can be written as,

$$\Gamma^{(6)}_{ab}(E) = E^2 \frac{i}{Nt_0^3} \frac{e^{ik_+ D}}{\sin k_+} \tag{5.19}$$

$$= \left(\frac{E}{t_0}\right)^2 \Gamma^{(2)}_{ab}(E) \quad . \tag{5.20}$$

Eq.(5.20) gives a direct relationship between the bridge and hexagonal positions. It is evident that at $E = 0$, $\Gamma^{(6)}_{ab}$ vanishes to second order (assuming of course that $\Gamma^{(2)}$ is non-zero, which it is).

This alternative viewpoint is very important. Were we to view the fact that $\Gamma^{(6)}_{ab}$ vanishes simply as a commensurability effect between the propagating wavevector and the number of connecting atoms, then we might conclude that this effect was a peculiarity of armchair tubes. Since there are 3 lines of atoms then the sum over the contributions will only vanish if the propagating vector is $2\pi/3$ or some multiple thereof. However, Eq.(5.20), in relating the phase factor to the energy E suggests that this might be an effect intrinsic to the underlying graphene lattice. If this were so then it should also be observable for zigzag tubes.

5.3.2 Zigzag Tubes

Turning next to zigzag tubes, each impurity is in contact with atoms located on 4 lines of carbon atoms lying along the tube's longitudinal direction. These are labelled in figure 5.3 using the graphene scheme $(\ell, j\,; s)$, where the first two indices label the lattice cell and s is the intra-cell index. We need to adopt this more complicated labelling since, for zigzags, the separation in the transverse direction is

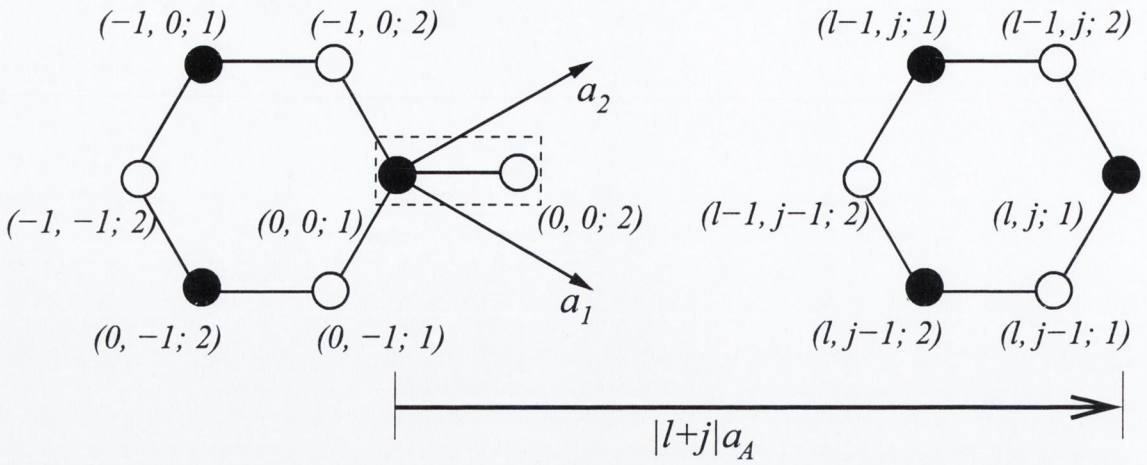


Figure 5.3: Two hexagons of carbon atoms belonging to a zigzag nanotube. The hexagons are separated by a distance $|\ell+j|\mathbf{a}_A$, along the tube's longitudinal axis. The carbon atoms are labelled in the graphene basis used in chapter 3. The foremost atom on hexagon A is overlaid with the origin of the underlying graphene sheet. There is no restriction that the circumferential separation must equal zero, as might be concluded from the figure.

no longer irrelevant. As before, we need to calculate the propagator $\Gamma^{(6)}_{ab}$. The atoms in contact with the first hexagon are labelled in a counterclockwise sense about the origin $(0,\,0\,;1)$. The second hexagon is labelled about$(\ell,\,j;1)$. For a metallic zigzag $(3N,0)$ only the $m = N$ (or alternatively the $m = 2N$) mode contributes around $E_F = 0$. From Eq.(3.22) this mode satisfies $E^2 = 2t_0^2(1+\cos(k_N))$. Once again simplified forms of the analytic expressions developed in chapter 3 can be employed and from Eq.(3.33) the simple lattice propagator $\langle 0,\,0;\,1|\hat{\mathcal{G}}|\ell,\,j;\,1\rangle$ is given by

$$\langle 0,\,0\,;1|\hat{\mathcal{G}}|\ell,\,j\,;1\rangle = \frac{i}{2Nt_0^2}\;E\;e^{-i\frac{\pi}{3}(\ell-j)}\frac{\exp(ik_N|\ell+j|)}{\sin k_N} \quad . \tag{5.21}$$

Including the contribution from all the • atoms on hexagon B, labelling the resultant ket as $|B\,\bullet\rangle = |\ell,\,j;\,1\rangle + |\ell-1,\,j;\,1\rangle + |\ell,\,j-1;\,1\rangle$ gives,

$$\begin{aligned}\langle 0,\,0\,;1|\hat{\mathcal{G}}|B\,\bullet\rangle &= \frac{i}{2Nt_0^2}\,E\,(1+[e^{i\pi/3}+e^{-i\pi/3}]e^{-ik_N})\frac{e^{-i\frac{\pi}{3}(\ell-j)}e^{ik_N|\ell+j|}}{\sin k_N} \\ &= \frac{i}{2Nt_0^3}\,E\,t^*(k_N)e^{-i\frac{\pi}{3}(\ell-j)}\frac{\exp(ik_N|\ell+j|)}{\sin k_N}\end{aligned} \tag{5.22}$$

Similarly the propagator $\langle 0,\,0\,;1|\hat{\mathcal{G}}|\ell,\,j\,;2\rangle$ is given by,

$$\langle 0,\,0;\,1|\hat{\mathcal{G}}|\ell,\,j;\,2\rangle = \frac{i}{2Nt_0^2}t(k_N)\exp(-i\frac{\pi}{3}(\ell-j))\frac{\exp(ik_N|\ell+j|)}{\sin k_N} \quad . \tag{5.23}$$

At first glance the presence of $t(k_N)$ instead of $t^*(k_N)$ might seem at odds with Eq.(3.33) since $\Delta s = -1$. However since $\Delta\ell$ and Δj are both negative $|\Delta\ell+\Delta j+\Delta s| = |\Delta\ell+\Delta j|-\Delta s$. Defining $|B\circ\rangle = |\ell-1,\,j\,;2\rangle+|\ell-1,\,j-1\,;2\rangle+|\ell,\,j-1\,;2\rangle$,

we can write

$$\langle 0,\, 0\,;1|\hat{\mathcal{G}}|B\circ\rangle = \frac{i}{2Nt_0^3}(t(k_N))^2 e^{-2ik_N} e^{-i\frac{\pi}{3}(\ell-j)} \frac{\exp(ik_N|\ell+j|)}{\sin k_N} \quad . \tag{5.24}$$

In much the same way,

$$\langle 0,\, 0\,;2|\hat{\mathcal{G}}|B\bullet\rangle = \frac{i}{2Nt_0^3}(t^*(k_N))^2 e^{-i\frac{\pi}{3}(\ell-j)} \frac{\exp(ik_N|\ell+j|)}{\sin k_N} \quad , \tag{5.25}$$

and

$$\langle 0,\, 0\,;2|\hat{\mathcal{G}}|B\circ\rangle = \frac{i}{2Nt_0^3} e^{-2ik_N}\, E\, t(k_N)\, e^{-i\frac{\pi}{3}(\ell-j)} \frac{\exp(ik_N|\ell+j|)}{\sin k_N} \quad . \tag{5.26}$$

All that remains is to complete the summation over all the sites in the first hexagon. The final result is,

$$\Gamma_{ab}^{(6)} = \frac{i}{2Nt_0^4}\left[2E^3 + [t(k_N)]^3 e^{-2ik_N} + [t^*(k_N)]^3 e^{2ik_N}\right] e^{i\frac{\pi}{3}(\Delta\ell-\Delta j)} \frac{e^{ik_N|\Delta\ell+\Delta j|}}{\sin k_N} \quad . \tag{5.27}$$

It remains to calculate the quantity $[t(k_N)]^3 e^{-2ik_N} + [t^*(k_N)]^3 e^{2ik_N}$. From the definition of $t(k_N)$ for zigzags, $t^3(k_N) = t_0^3(1+3e^{ik_N}+3^{2ik_N}+e^{3ik_N})$ and thus $(t(k_N))^3 e^{-2ik_N} = t_0^3(e^{-2ik_N} + 3e^{-ik_N} + 3 + e^{ik_N})$. Taking the real part[2],

$$\begin{aligned} 2\mathrm{Re}[(t(k_N))^3 e^{-2ik_N}] &= t_0^3[2\cos(2k_N) + 6\cos(2k_N) + 6 + 2\cos(k_N)\,] \\ &= t_0^3[4\cos^2(k_N) + 8\cos(k_N) + 4\,] \\ &= 4t_0^3[1+\cos(k_N)]^2. \end{aligned} \tag{5.28}$$

However, from the dispersion relation the quantity in Eq.(5.28) is equal to E^4/t_0. As a result,

$$\Gamma_{ab}^{(6)}(E) = \frac{i}{2Nt_0^4}\left[2E^3 + \frac{E^4}{t_0}\right] e^{i\frac{\pi}{3}(\Delta\ell-\Delta j)} \frac{e^{ik_N|\Delta\ell+\Delta j|}}{\sin k_N} \quad . \tag{5.29}$$

Since $\sin^2(k_N) = (E/t_0)^2(1-(E/2t_0)^2)$, $\Gamma_{ab}^{(6)}(E)$ will vanish to second order around $E_F = 0$. Therefore, a rapid decay should be observable for zigzag nanotubes. This derivation has been far less intuitive than in the case of armchairs, and it is difficult to picture the vanishing propagator in terms of simple interference effects. Nevertheless, it does vanish and the reason is that the phase factor can consistently be written in terms of $t(k_N)$, the magnitude of which is equal to E. This same condition arose for armchair tubes and it is difficult to see how it might arise from any peculiarity of the achiral tubes. In section 5.5 we will attempt to generalise the

[2]This is not strictly the real part since k_N has a small imaginary component. Nevertheless it is convenient to adopt the notation and should lead to no confusion.

above arguments and address this question specifically.

5.

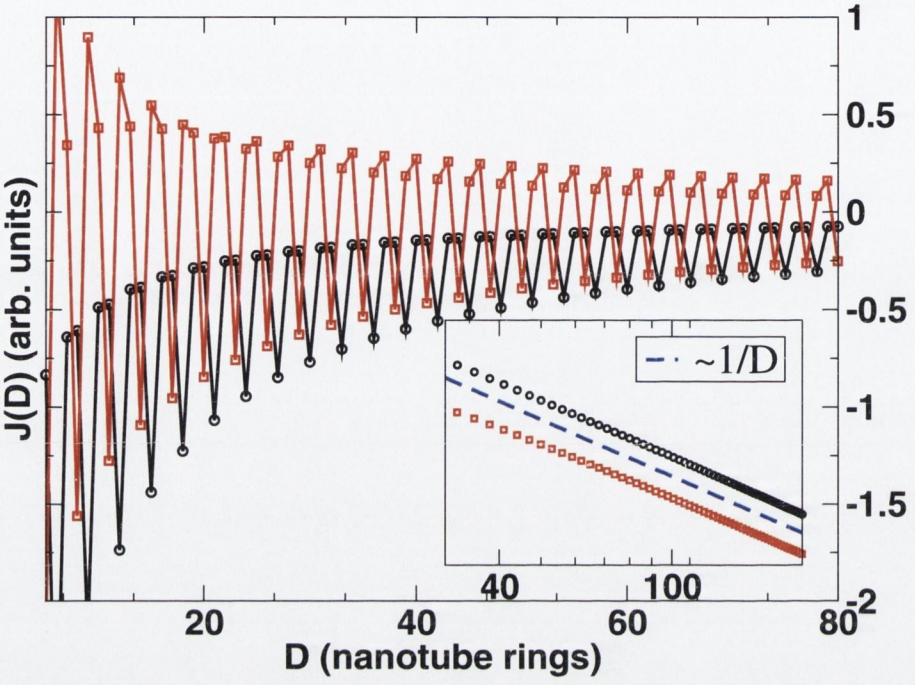


Figure 5.4: Coupling (in arbitrary units) as a function of separation for an armchair nanotube with the impurities placed in the atop (black line) and bridge (red line) positions. The inset is log-log plot of the coupling, confirming its long range character.

The leading order decay is determined by the degree to which the Fourier Coefficients vanish. In the atop case the Fourier Coefficients do not vanish and the decay is as $1/D$. We have seen that in this case the two expressions given by Eq.(4.30) and Eq.(5.7) are equivalent. When the Coefficients vanish to order p then the decay will be $1/D^{p+1}$. In figure 5.4 we plot the coupling as a function of D for both the atop and bridge sites for an armchair.

In the bridge site, the coupling is seen to be both long ranged and oscillatory. The appearance of an oscillation between ferromagnetic and anti-ferromagnetic coupling can easily be explained with reference to the previous section. As noted in Eq.(5.16), the generalised propagator $\Gamma^{(2)}_{ab}(E)$ is a function of a single period k_+ – the dependence on k_- cancels. This is because, by summing over the intra-cell degree of freedom, the bi-partite nature of the nanotube is not exposed. The inset confirms that in both cases the decay is the predicted rate of $1/D$.

In figure 5.5 we plot the coupling for the hexagonal case. It is immediately evident that the decay is extremely rapid. This is confirmed by the inset which shows a $1/D^5$ decay. Such a rapid decay is a consequence of Eq.(5.20), from which it is seen that $\Gamma^{(6)}_{ab}$ will vanish to at least second order in energy. This propagator

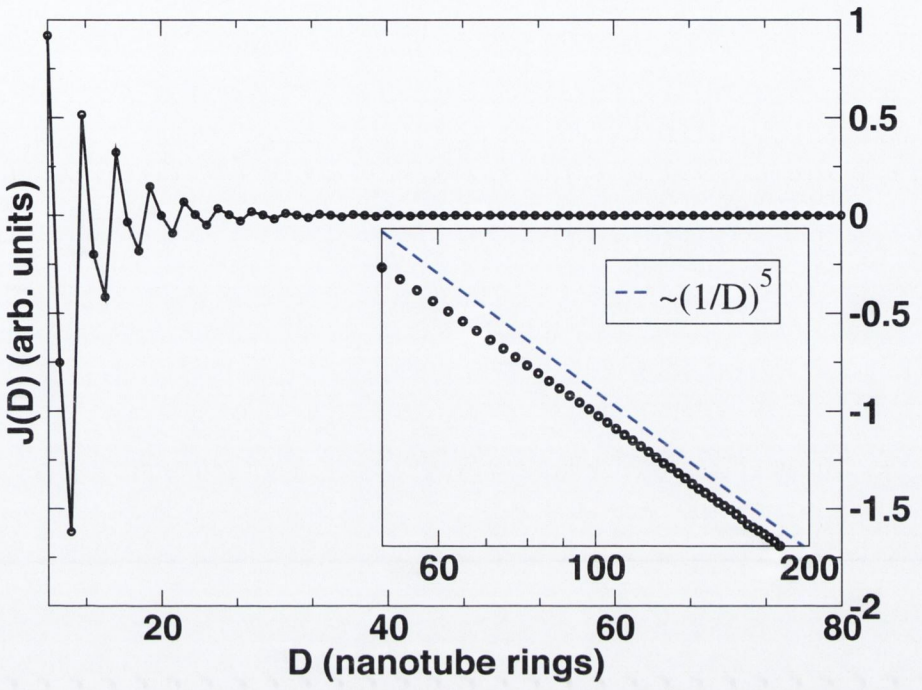


Figure 5.5: Coupling as a function of separation for an armchair nanotube with the impurities placed in the hexagonal position. The inset is a log-log plot which confirms the rapid decay.

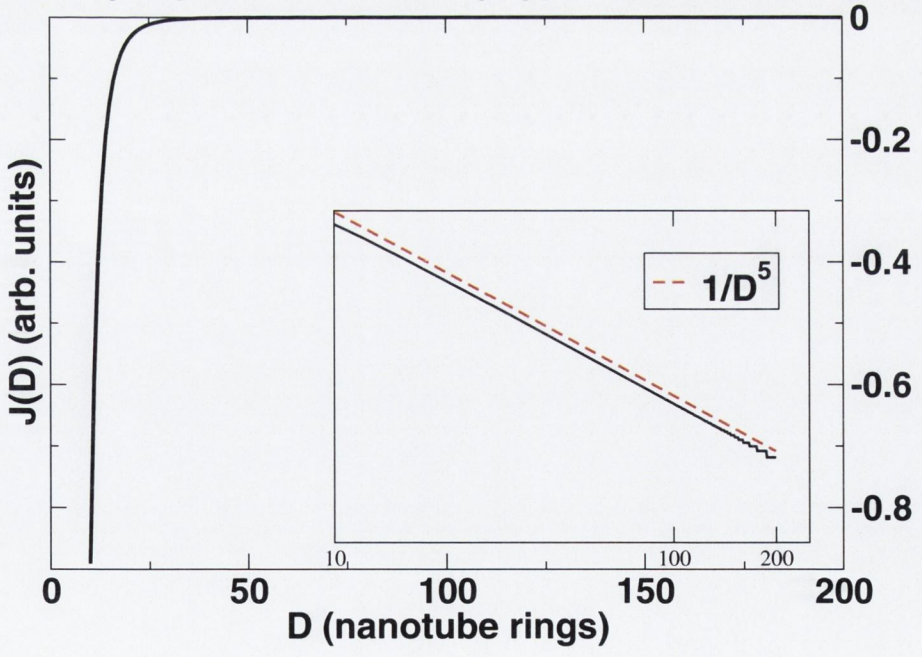


Figure 5.6: Coupling as a function of separation for metallic zigzag nanotube with the impurities placed in the hexagonal position. The inset is a log-log plot which confirms the rapid decay.

enters in Eq.(4.18) as a product $\Gamma^{(6)}_{ab}\Gamma^{(6)}_{ba}$. The composite term will vanish to order $p = 4$, which gives the observed decay rate. Fig. 5.6 shows the same plot for a metallic zigzag tube.

The observed rate of decay agrees exactly with the rate predicted by the generalised asymptotic limit, given by Eq.(5.7). This confirms that the position of the impurity within the host can play a crucial role in determining the long range order in doped nanotube systems.

This sensitivity to the location of the impurity has therefore been shown to be a formal property of our model. Before concluding this section, we compare these predictions with the results of first principles calculations[62]. These calculations were carried out with the SIESTA package using the generalized gradient approximation(GGA) for the exchange and correlation potentials[63]. In such calculations the total energy per unit cell in both the ferromagnetic and anti-ferromagnetic configurations is calculated and the energy difference gives the coupling. However, while our semi-empirical approach can generate a truly infinite system with two impurities, *ab-initio* approaches are limited to examining a section of the tube of length L. This section is then periodically repeated to produce an infinite tube with 2 atoms per unit cell. This presents some problems when trying to compare the two approaches since, because the coupling is long-ranged, the interaction between atoms in neighbouring cells will have to be accounted for in the *ab-initio* results. Therefore, in an attempt to relate them we write the total energy in the ferromagnetic configuration as,

$$E(FM) = \sum_{ij} J_{ij} \quad , \tag{5.30}$$

where J_{ij} is the coupling between the isolated pair i and j . The total energy in the anti-ferromagnetic configuration is then given by,

$$E(AFM) = \sum_{ij} (-1)^{(i-j)} J_{ij} \quad . \tag{5.31}$$

The energy difference $E(FM) - E(AFM)$, which we write as an effective coupling, J_{eff}, is given by,

$$\begin{aligned} J_{\text{eff}}(D) &= J(D) + 4J(L-D) + 4J(L+D) + 4J(2L-D) \\ &+ 4J(2L+D) + \cdots + 4J(nL+D) + 4J(nL-D) + \cdots \quad . \end{aligned} \tag{5.32}$$

n indicates the contribution from the n^{th} neighbouring cell and D is the intracell separation of the impurities. Eq.(5.32) gives us a systematic method of including the effect of all neighbouring terms. Obviously such an expression should converge, since

even with long range coupling eventually a point will be reached where the inclusion of additional terms will have a negligible impact. Three distinct cases are considered: adsorbed atop, adsorbed centre and substitutional. In the adsorbed cases the calculations were performed on a (4,4) armchair with Manganese impurities. In the substitutional case the nanotube was a (6,0) zigzag with Nickel impurities. For the armchair tube L was set to 10 rings, while for the zigzag $L = 5$ rings using the definition introduced in section 2.6. Assuming that the coupling between each individual pair of impurities adopts the form

$$J(D) = \frac{A}{D^{\alpha}} \quad , \tag{5.33}$$

where A is the amplitude of the coupling, then the decaying exponent, α, can be extracted from Eq.(5.32) using two distinct values for D. The *ab-initio* coupling values for the three cases are given in table 5.1. Inserting these in Eq.(5.32) yields

$D(a)$	ΔE (eV)		
	atop	centre	sub
1	———	———	-0.0728
2	0.027	0.064	-0.0658
3	0.011	0.009	———

Table 5.1: Table of coupling values, $\Delta E = E(FM) - E(AFM)$, for two Mn impurities adsorbed on a (4,4) armchair nanotube and two Ni impurities substituted in a (6,0) zigzag tube. The impurities are separated along the tube's longitudinal axis in units of the lattice constant: $a = 2.44\mathring{A}$ for armchairs and $a = 4.23\mathring{A}$ for zigzags.

the following values for the exponent: in the atop position $\alpha = 2.89$ while in the centre position $\alpha = 4.97$. The second exponent is remarkably close to the value of $\alpha = 5$ predicted by Eq.(5.7). Table 5.2 shows the effect on α of the interaction between neighbouring cells. For the centre case the exponent converges extremely rapidly as a function of n which results from the weakness of the interaction beyond the smallest separations. For the atop position the calculated exponent is somewhat faster than predicted by the standard theory. This is explained by the fact that the predicted $1/D$ decay refers to the asymptotic rate while the separations considered here are far from this limit. A second point to bear in mind is that for armchair nanotubes the form of $J(D)$ used represents the maximum possible decay rate. This is because the coupling actually oscillates with period $2\pi/3$ as a function of D. By assuming a monotonic form for $J(D)$ we are implicitly assuming that the phase of this oscillation is zero. Particularly for the atop case, where the coupling decays slowly, the oscillatory contribution may increase the extrapolated rate. This can be overcome be considering zigzag tubes. The oscillation is this case is masked and the decay is consequently monotonic. We consider the case of two nickel impurities substituted in a (6,0) zigzag. The values for α are given in the final column of table

5.2. With only the intra-cell interaction present the decay rate is $\alpha = 0.14$. To get closer to the predicated rate it is necessary to consider the contribution from a large number of periodic images. Convergence is very slow but a final rate of $\alpha \sim 1.30$ is obtained, which is much closer to the predicted rate.

Admittedly, it is difficult to infer behaviour from two points with complete certainty. Ideally we would like to have additional points, particularly for larger separations, which would for example allow for the evaluation of the phase of the oscillation. However this would require a significantly larger unit cell and was outside the scope of our calculations. Nevertheless, even from these limited results it is clear that the decay rate may be significantly faster when the impurities are in the centre position. Further comparisons with *ab-initio* results will be shown in section 6.6.2, where the dependence of the sign of the coupling on the sublattice on which the impurities are located can give rise to very striking effects.

n	$\alpha(n)$		
	atop	centre	sub
0	2.21	4.84	0.145
1	2.83	4.97	0.989
2	2.87	4.97	1.130
3	2.88	4.97	1.184
4	2.88	4.97	1.214
5	2.89	4.97	1.233
6	2.89	4.97	1.247
7	2.89	4.97	1.258

Table 5.2: Decaying exponent, α, as a function of number of interacting cells, n, for the three cases shown in table 5.1.

5.5 Graphene and Chiral Tubes

In this section we address the question of whether or not the vanishing of the propagator $\Gamma^{(6)}_{ab}(E = 0)$ is a feature common to all nanotubes. The derivation of this effect for zigzag tubes, and in particular the ability to relate the phase factor to the energy, would indicate that this is symptomatic of a more general property and not simply restricted to achiral tubes. In this section, we evaluate the propagator $\Gamma^{(6)}_{ab}$ for graphene. We consider graphene only because it provides the most general framework from which the behaviour of a graphene derivative, such as a nanotube, can be inferred.

To ease the notation slightly we will label each of the six hexagonal sites by an index i. Therefore $\mathcal{G}_{i,j}$ refers to the propagator between hexagon atoms i and j. The even numbered atoms all lie on the first graphene sublattice whilst the odd

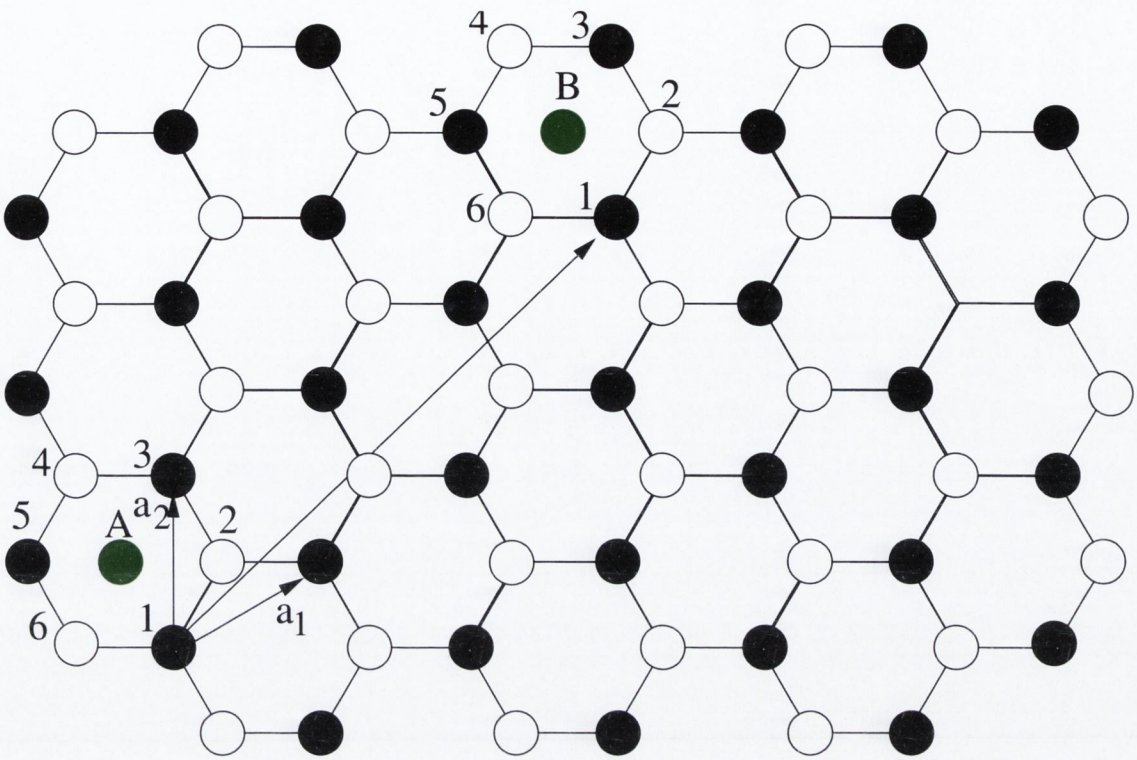


Figure 5.7: 2 centrally located impurities in a graphene sheet. Each atom is in contact with 6 lattice atoms, labelled 1,2,...,6 in a counter-clockwise direction. Atom 1 is fixed at the origin of the sheet. The 2 hexagons are displaced by a vector $\mathbf{R} = \ell\mathbf{a}_1 + j\mathbf{a}_2$.

numbered atoms lie on the second sublattice. From Eq.(3.11),

$$\mathcal{G}_{2i,2j} = \frac{1}{(2\pi)^2}\int d\mathbf{k}\,\frac{E\,\exp(i\mathbf{k}\cdot(\mathbf{r}_{1i}-\mathbf{r}_{2j}))}{E^2-|t(\mathbf{k})|^2} \tag{5.34}$$

$$\mathcal{G}_{2i-1,2j-1} = \frac{1}{(2\pi)^2}\int d\mathbf{k}\,\frac{E\,\exp(i\mathbf{k}\cdot(\mathbf{r}_{1i}-\mathbf{r}_{2j}))}{E^2-|t(\mathbf{k})|^2} \tag{5.35}$$

$$\mathcal{G}_{2i-1,2j} = \frac{1}{(2\pi)^2}\int d\mathbf{k}\,\frac{t^*(\mathbf{k})\,\exp(i\mathbf{k}\cdot(\mathbf{r}_{1i}-\mathbf{r}_{2j}))}{E^2-|t(\mathbf{k})|^2} \tag{5.36}$$

$$\mathcal{G}_{2i,2j-1} = \frac{1}{(2\pi)^2}\int d\mathbf{k}\,\frac{t(\mathbf{k})\,\exp(i\mathbf{k}\cdot(\mathbf{r}_{1i}-\mathbf{r}_{2j}))}{E^2-|t(\mathbf{k})|^2}\quad , \tag{5.37}$$

where the integration extends over the entire 1st-Brillouin zone. Without loss of generality, atom 1 on hexagon A is placed at the origin of the graphene lattice. The other sites in the hexagon are then located, in the counter-clockwise sense shown in

figure 5.7, at

$$(\mathbf{r}_1)_1 = \mathbf{0} \tag{5.38}$$

$$(\mathbf{r}_1)_2 = \mathbf{0} \tag{5.39}$$

$$(\mathbf{r}_1)_3 = \mathbf{a}_2 \tag{5.40}$$

$$(\mathbf{r}_1)_4 = -\mathbf{a}_1 + \mathbf{a}_2 \tag{5.41}$$

$$(\mathbf{r}_1)_5 = -\mathbf{a}_1 + \mathbf{a}_2 \tag{5.42}$$

$$(\mathbf{r}_1)_6 = -\mathbf{a}_1 \quad . \tag{5.43}$$

These are actually the locations of the graphene unit cell in which each carbon atom resides. The atoms in contact with hexagon B are related to those in contact with A by a simple translational vector, $(\mathbf{r}_2)_i = (\mathbf{r}_1)_i + \ell\,\mathbf{a}_1 + j\,\mathbf{a}_2$, representing a separation in an arbitrary direction.

We begin by summing over the propagators between odd numbered sites,

$$\mathcal{G}_{1,1} + \mathcal{G}_{1,3} + \mathcal{G}_{1,5} = \frac{1}{(2\pi)^2}\int d\mathbf{k}\frac{E\,e^{-i\mathbf{k}\cdot(\ell\mathbf{a}_1+j\mathbf{a}_2)}(1+e^{-ik_2}+e^{i(k_1-k_2)})}{E^2-|t(\mathbf{k})|^2} \tag{5.44}$$

$$= \frac{1}{(2\pi)^2}\int d\mathbf{k}\frac{E}{t_0}\frac{e^{-ik_2}\,t(\mathbf{k})\,e^{-i\mathbf{k}\cdot(\ell\mathbf{a}_1+j\mathbf{a}_2)}}{E^2-|t(\mathbf{k})|^2} \quad . \tag{5.45}$$

The contribution to $\Gamma^{(6)}_{ab}$ coming from all odd-odd terms, defined as $S_{\bullet\bullet}$ is,

$$S_{\bullet\bullet} = \sum_{i,j=1}^{3}\mathcal{G}_{2i-1,2j-1} = \frac{1}{(2\pi)^2}\int d\mathbf{k}\frac{E}{t_0}\frac{e^{-ik_2}\,t(\mathbf{k})e^{-i\mathbf{k}\cdot(\ell\mathbf{a}_1+j\mathbf{a}_2)}(1+e^{ik_2}+e^{-i(k_1-k_2)})}{E^2-|t(\mathbf{k})|^2}$$

$$= \frac{1}{(2\pi)^2}\int d\mathbf{k}\frac{E}{t_0^2}\frac{|t(\mathbf{k})|^2e^{-i\mathbf{k}\cdot(\ell\mathbf{a}_1+j\mathbf{a}_2)}}{E^2-|t(\mathbf{k})|^2} \tag{5.46}$$

Similarly the propagator $\mathcal{G}_{2,2} + \mathcal{G}_{2,4} + \mathcal{G}_{2,6}$ is given by

$$\mathcal{G}_{2,2} + \mathcal{G}_{2,4} + \mathcal{G}_{2,6} = \frac{1}{(2\pi)^2}\int d\mathbf{k}\frac{E\,e^{-i\mathbf{k}\cdot(\ell\mathbf{a}_1+j\mathbf{a}_2)}(1+e^{ik_1}+e^{i(k_1-k_2)})}{E^2-|t(\mathbf{k})|^2} \tag{5.47}$$

$$= \frac{1}{(2\pi)^2}\int d\mathbf{k}\frac{E}{t_0}\frac{e^{ik_1}\,t^*(\mathbf{k})\,e^{-i\mathbf{k}\cdot(\ell\mathbf{a}_1+j\mathbf{a}_2)}}{E^2-|t(\mathbf{k})|^2} \quad , \tag{5.48}$$

and the contribution coming from all even-even terms, $S_{\circ\circ}$ is,

$$S_{\circ\circ} = \sum_{i,j=1}^{3}\mathcal{G}_{2i,2j} = \frac{1}{(2\pi)^2}\int d\mathbf{k}\,\frac{E}{t_0^2}\frac{|t(\mathbf{k})|^2\,e^{-i\mathbf{k}\cdot(\ell\mathbf{a}_1+j\mathbf{a}_2)}}{E^2-|t(\mathbf{k})|^2} \quad . \tag{5.49}$$

Now we turn to the odd-even propagators. Firstly,

$$\mathcal{G}_{1,2} + \mathcal{G}_{1,4} + \mathcal{G}_{1,6} = \frac{1}{(2\pi)^2}\int d\mathbf{k}\frac{(t^*(\mathbf{k}))^2}{t_0}\frac{e^{ik_1}e^{-i\mathbf{k}\cdot(\ell\mathbf{a}_1+j\mathbf{a}_2)}}{E^2-|t(\mathbf{k})|^2} \quad , \tag{5.50}$$

and

$$S_{\bullet\circ} = \sum_{i,j=1}^{3} \mathcal{G}_{2i-1,2j} = \frac{1}{(2\pi)^2} \int d\mathbf{k} \, \frac{(t^*(\mathbf{k}))^3}{t_0^2} \, \frac{e^{i(k_1+k_2)} \, e^{-i\mathbf{k}\cdot(\ell\mathbf{a}_1+j\mathbf{a}_2)}}{E^2 - |t(\mathbf{k})|^2} \quad . \tag{5.51}$$

Finally, we can write down the even-odd propagator,

$$S_{\circ\bullet} = \sum_{i,j=1}^{3} \mathcal{G}_{2i,2j-1} = \frac{1}{(2\pi)^2} \int d\mathbf{k} \frac{(t(\mathbf{k}))^3}{t_0^2} \, \frac{e^{-i(k_1+k_2)} \, e^{-i\mathbf{k}\cdot(\ell\mathbf{a}_1+j\mathbf{a}_2)}}{E^2 - |t(\mathbf{k})|^2} \quad . \tag{5.52}$$

The expression for $\Gamma_{ab}^{(6)}(E)$ is simply equal to the sum of these terms,

$$\Gamma_{ab}^{(6)} = \frac{1}{(2\pi)^2} \int d\mathbf{k} \left(2E \, \frac{|t(\mathbf{k})|^2}{t_0^2} + 2 \, \frac{|t(\mathbf{k})|^3}{t_0^2} \cos(k_1 + k_2 - 3\phi(\mathbf{k})) \right) \frac{e^{-i\mathbf{k}\cdot(\ell\mathbf{a}_1+j\mathbf{a}_2)}}{E^2 - |t(\mathbf{k})|^2} \quad . \tag{5.53}$$

The factor $\phi(\mathbf{k})$ is the usual phase factor defined according to $\phi = -i \log(t(\mathbf{k})/|t(\mathbf{k})|)$. As in the case of nanotubes, integrating with respect to k_1 involves evaluating the zeros of the denominator, which defines a function $k_1^0(E, k_2)$

$$\begin{aligned} \Gamma_{ab}^{(6)} &= -\frac{i}{2\pi t_0^2} \int dk_2 \left[E \, |t(k_1^0, k_2)|^2 + |t(k_1^0, k_2)|^3 \cos(k_1^0 + k_2 + 3\phi(k_1^0, k_2)) \right] \\ &\times \left[\frac{\partial |t(\mathbf{k})|}{\partial k_1} \right]^{-1}_{k_1 = k_1^0} \frac{\exp(i(k_1^0|\ell| - k_2 j))}{|t(k_1^0, k_2)|} \quad . \end{aligned} \tag{5.54}$$

Now, $|t(k_1^0(k_2, E), k_2)|^2 = E^2$ and is independent of k_2. Therefore we can take this quantity outside the integral,

$$\begin{aligned} \Gamma_{ab}^{(6)} &= -\frac{i}{2\pi} \left(\frac{E}{t_0} \right)^2 \int dk_2 \left[1 + \cos(k_1^0 + k_2 - 3\phi(k_1^0, k_2)) \right] \\ &\times \left[\frac{\partial |t(\mathbf{k})|}{\partial k_1} \right]^{-1}_{k_1 = k_1^0} \exp(i(k_1^0|\ell| - k_2 j)) \quad . \end{aligned} \tag{5.55}$$

One might attempt to solve the integral with respect to k_2 by evaluating the zeros of $\partial |t(k_1^0, k_2)| / \partial k_1$. However this quantity contains a square root and it is not possible to treat it using the Residue Theorem. To some extent this is not important. The integral exists, irrespective of whether or not we can apply the Residue Theorem. With that in mind we notice that Eq.(5.55) can be written as,

$$\begin{aligned} \Gamma_{ab}^{(6)} &= 2 \left(\frac{E}{t_0} \right)^2 \Gamma_{ab}^{(1)} - \frac{i}{2\pi} \left(\frac{E}{t_0} \right)^2 \int dk_2 \cos(k_1^0 + k_2 - 3\phi(k_1^0, k_2)) \\ &\times \left[\frac{\partial |t(\mathbf{k})|}{\partial k_1} \right]^{-1}_{k_1 = k_1^0} \exp(i(k_1^0|\ell| - k_2 j)) \quad , \end{aligned} \tag{5.56}$$

that is, as a sum of the simple propagator, $\mathcal{G}_{11}$, between two sites and a second term which vanishes to second order in energy. In general, it does not seem possible to write $\cos(k_1^0 + k_2 - 3\phi(k_1^0, k_2))$ as an explicit function of energy, as had been the case with the achiral tubes. The only case in which the propagator might not vanish was if the integral diverged to second order at $E_F = 0$. However this should not arise. To see why, we note that the phase function $\phi(k_1^0, k_2)$ is a well defined function of k_2. It follows that the numerator is well defined with respect to k_2. If we assume that $\Gamma_{ab}^{(1)}(E = 0)$ does not diverge, which seems reasonable if the metal has no bound state at $E_F = 0$, then since both integrals share the same denominator the second integral should also be finite.

We have succeeded in showing that a vanishing Green Function at $E_F = 0$ is an intrinsic property of graphene and all graphene derivatives such as nanotubes. Crucially for nanotubes, it results from the identification of the sum over phase shifts with the energy,

$$|t(\mathbf{k})|^2 = E^2 \quad , \tag{5.57}$$

which arises from the integration in Eq.(5.53). This identity will hold irrespective of the particular quantisation direction defined by the chirality of the tube. What appears to happen is that in some sense, the particular form of the perturbation reproduces a symmetry of the graphene lattice. That is to say by summing over the contributing atoms we consistently reproduce the factor $t(\mathbf{k})$ which defines the characteristic equation for graphene (c.f. Eq.(3.3)).

If anything, the situation for a chiral tube is more simple than for graphene since there is only a single k-space integration. As shown in appendix[D] the phase factor is well defined for all chiralities. Therefore, rapid decay should be a property of any given metallic tube. The only point to raise about chiral nanotubes is that as the chirality increases, so does the size of the unit cell. The number of modes also increases. In this case we might be sampling the coupling at rather large separations, i.e. it is not possible to constantly change the separation along the tube's longitudinal direction.

5.6 Symmetry Breaking

The results of the previous section have shown that rapid decay results from the form of the interaction of the impurities with the host, which reproduces a symmetry of the electronic structure of the host. This symmetry obviously relies on the interaction between each host atom and the impurity being equivalent (c.f. Eq.(5.9)). It could be argued that this condition might not hold exactly for nanotubes due to,

for example, curvature in low-diameter tubes or from some other effect which might cause the impurity to shift slightly from the exact centre of the hexagon. In this section we examine the effect of such a symmetry breaking, particularly the effect on the decay rate.

We begin by letting atom 1 on each hexagon interact with a slightly different hopping strength $t \rightarrow t + \delta t$. As we shall see below, this should not involve any loss in generality, but does simplify the details somewhat.

The intention is not to begin afresh, but rather to take the system above as a starting point and allow deviations to occur. The perturbation Hamiltonian can be written as $\hat{V} = |a\ 1\rangle\, \delta t\, \langle A| + |b\ 1\rangle\, \delta t\, \langle B| + c.c.$. The reference Hamiltonian is that of the host interacting with two centrally located adsorbed impurities, with their magnetic moments aligned. This Hamiltonian is labelled H with corresponding Green Function G, and the Green Function for the perturbed system is labelled $\widetilde{G}$. As before, the energy change resulting from rotating one of the moments by an angle θ, can be written as,

$$\Delta\Omega(\theta, D) = \frac{1}{\pi} \int_{-\infty}^{E_F} dE\ \log(1 + 2(1 - \cos(\theta)) V_x^2\, \widetilde{G}^{\uparrow}_{AB}(E, D)\, \widetilde{G}^{\downarrow}_{BA}(E, D)) \quad . \tag{5.58}$$

Except for replacing G with $\widetilde{G}$, this is exactly the same expression as used previously, which stems from the fact that the spin rotation is still localised on the impurity at site B. The definition of $\Gamma^{(6)}_{ab}$ involves no assumptions about the form of the hopping matrix t_i. If all the hopping values are equal then the function is merely the sum over the 36 propagators, multiplied by t_0^2. Otherwise each term in the sum is weighted by the corresponding hopping, as is the case here. However, there is no need to re-derive the form of $\widetilde{G}^{\sigma}_{ab}$ using the decoupled tube-adatom system as a reference. Instead we use the symmetric, centrally located impurity case mentioned above. Before deriving the expression for the updated Green Function elements $\widetilde{G}_{AB}$, we note the following is true at $E = 0$.

$$\begin{aligned}
\langle A|\hat{G}|B\rangle &= 0 \\
\langle a_1|\hat{G}|B\rangle &= 0 \\
\langle b_1|\hat{G}|A\rangle &= 0 \\
\langle a_1|\hat{G}|b_1\rangle &= \langle a_1|\hat{\mathcal{G}}|b_1\rangle \\
\langle a_1|\hat{G}|A\rangle &= 0 \\
\langle b_1|\hat{G}|B\rangle &= 0
\end{aligned} \tag{5.59}$$

The first four statements follow directly from the symmetry arguments of the

last few sections. The last two are a little trickier to see (c.f. Appendix E), but are certainly true for armchair and zigzag nanotubes. Using Eq.(5.59) we see that at $E_F = 0$ the system described by H is equivalent to a nanotube decoupled from 2 impurities sitting atop lattice sites a_1 and b_1. Therefore the propagator $\widetilde{G}_{AB}$ is simply given by Eq.(4.20) with t replaced with δt,

$$\widetilde{\mathrm{G}}^{\sigma}_{AB} = \frac{(\delta t)^2\, \mathcal{G}^{\sigma}_{AA}\, \mathcal{G}_{a_1 b_1}\, \mathcal{G}^{\sigma}_{BB}}{[1-(\delta t)^2\, \mathcal{G}^{\sigma}_{AA}\, \mathcal{G}_{a_1 a_1}][1-(\delta t)^2\, \mathcal{G}^{\sigma}_{BB}\, \mathcal{G}_{b_1 b_1}] - (\delta t)^4\, \mathcal{G}^{\sigma}_{AA}\, \mathcal{G}_{a_1 b_1}\, \mathcal{G}^{\sigma}_{BB}\, \mathcal{G}_{b_1 a_1}} \quad . \tag{5.60}$$

We now make the assumption that δt is *small*. This should not be unduly restrictive, since if the symmetry is significantly broken then a description in terms of a centrally located impurity is no longer appropriate to begin with. With this assumption it becomes clear that the situation described by Eq.(5.60) is directly analogous to the case of a nanotube interacting weakly with the impurities adsorbed atop. The magnitude of the coupling will be very small due to the leading order $(\delta t)^4$, but it should exhibit its usual long range.

This is a nice comparison, but the conditions given by Eq.(5.59), in particular the last two, are more restrictive than they need to be. In an attempt to treat the system in a slightly more systematic way, we write $\hat{\widetilde{G}} = (\hat{G}^{-1} + \hat{V})^{-1}$. $\hat{G}$ describes the reference system in which the interaction between the adsorbed atoms and the host is symmetric. $\hat{V}$ is the perturbation Hamiltonian defined above. We can therefore write a general expression for the updated propagators,

$$\hat{\widetilde{G}} = \hat{G} + \begin{pmatrix} |L\rangle \\ |I\rangle \end{pmatrix} \delta t \begin{pmatrix} 0 & 1 \\ 1 & 0 \end{pmatrix} \left[\begin{pmatrix} 1 & 0 \\ 0 & 1 \end{pmatrix} - \delta t \begin{pmatrix} G_{LI} & G_{LL} \\ G_{II} & G_{IL} \end{pmatrix} \right]^{-1} \begin{pmatrix} \langle L| & \langle I| \end{pmatrix} \tag{5.61}$$

$|L\rangle = \{|a_1\rangle, |a_2\rangle\}, |I\rangle = \{|A\rangle, |B\rangle\}$ are generalised states representing the lattice and impurity states respectively. In the same way,

$$G_{II} = \begin{pmatrix} G_{AA} & G_{AB} \\ G_{BA} & G_{BB} \end{pmatrix} \tag{5.62}$$

and similarly for the other matrices. Since we are assuming δt is small Eq.(5.61) can be written as

$$\hat{\widetilde{G}} = \hat{G} + \begin{pmatrix} |L\rangle \\ |I\rangle \end{pmatrix} \delta t \left[\begin{pmatrix} 0 & 1 \\ 1 & 0 \end{pmatrix} + \delta t \begin{pmatrix} G_{II} & G_{IL} \\ G_{LI} & G_{LL} \end{pmatrix} + \mathcal{O}((\delta t)^2) \right] \begin{pmatrix} \langle L| & \langle I| \end{pmatrix} \tag{5.63}$$

We are interested in the terms in $\langle I|\hat{\widetilde{G}}|I\rangle = G_{II} + (\delta t)^2 G_{LL}$. From Eq.(5.63) it is clear that these propagators have a leading order term of $(\delta t)^2$. Writing the matrix

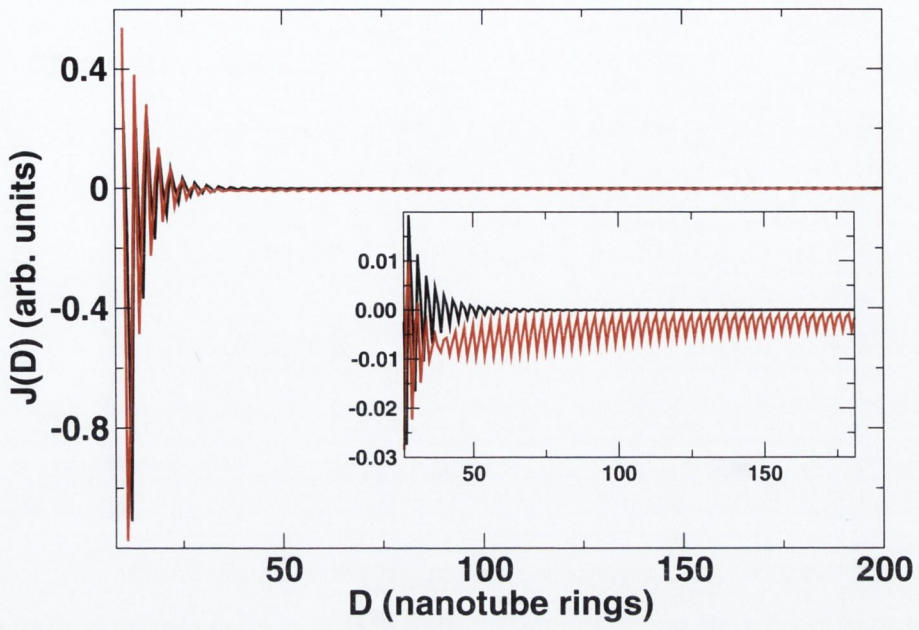


Figure 5.8: Coupling as a function of D for the case of a centrally placed atom (black line) and the case in which the hopping, t_3, between the impurity and hexagon atom 3 has been changed by 5%.

explicitly,

$$\begin{pmatrix} \widetilde{G}_{AA} & \widetilde{G}_{AB} \\ \widetilde{G}_{BA} & \widetilde{G}_{BB} \end{pmatrix} \approx \begin{pmatrix} G_{AA} & G_{AB} \\ G_{BA} & G_{BB} \end{pmatrix} + (\delta t)^2 \begin{pmatrix} G_{a_1a_1} & G_{a_1b_1} \\ G_{b_1a_1} & G_{b_1b_1} \end{pmatrix} \quad . \tag{5.64}$$

It is now simply a matter of selecting the appropriate propagator, which is,

$$\widetilde{\mathrm{G}}_{AB} \sim G_{AB} + (\delta t)^2 G_{a_1b_1} + \mathcal{O}((\delta t)^3) \tag{5.65}$$

and

$$\widetilde{\mathrm{G}}^{\uparrow}_{AB}\widetilde{\mathrm{G}}^{\downarrow}_{BA} \sim G^{\uparrow}_{AB}G^{\downarrow}_{BA} + (\delta t)^2 \left[G^{\uparrow}_{AB}G^{\downarrow}_{b_1a_1} + G^{\downarrow}_{BA}G^{\uparrow}_{a_1b_1}\right] + (\delta t)^4 G^{\uparrow}_{a_1b_1}G^{\downarrow}_{b_1a_1} \quad . \tag{5.66}$$

We have shown in detail that G^{σ}_{AB} vanishes at $E = 0$, but $G^{\sigma}_{a_1b_1} = \mathcal{G}_{a_1b_1}$ and is non-zero. Therefore,

$$\widetilde{\mathrm{G}}^{\uparrow}_{AB}\widetilde{\mathrm{G}}^{\uparrow}_{AB} \sim (\delta t)^4 G^{\uparrow}_{a_1b_1}G^{\downarrow}_{b_1a_1} + \mathcal{O}((\delta t)^5) \quad . \tag{5.67}$$

This leads to the following conclusion: As we have seen in the previous section, contributions from energies in the vicinity of E_F give rise to higher order decays. Eq.(5.67) indicates that we are now in the intermediate situation: although the leading order term is non-zero, the amplitude is suppressed by $\mathcal{O}((\delta t)^4)$. When we reach the fifth order term, contributions from G^{σ}_{AB} will begin to appear, independent of δt, but decaying rapidly. Therefore the overall decay can be viewed as a broken

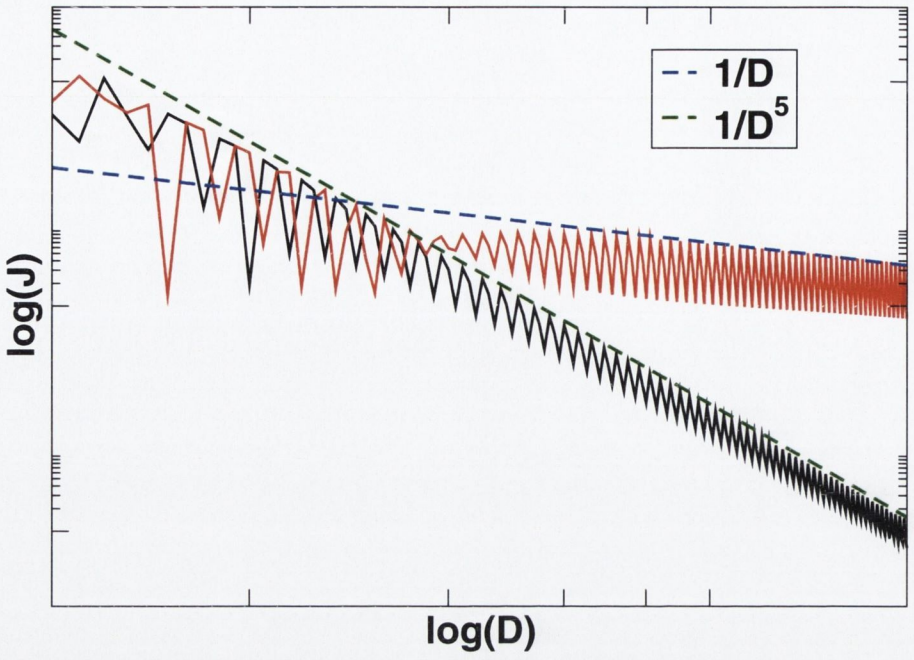


Figure 5.9: Log-log plot of coupling as a function of D for the case of centrally located impurities (black line) and the case in which the hopping, t_3, between the impurity and hexagon atom 3 has been changed by 5%. The guide lines show the respective asymptotic decay rates.

line dependence: an initial rapid decay giving way to a very small amplitude, long range decay in the asymptotic limit. The extent to which the rapid decay can be observed will depend on the value of δt. Obviously as $\delta t \rightarrow 0$, we would expect to recover the short range decay in the asymptotic limit. Fig. 5.8 shows the coupling for the case where the hopping is increased by 5%. The case with no asymmetry is also plotted for comparison. At first glance there seems to be no difference and the decay in both cases appears to be $1/D^5$. However, inspection of the inset shows that the coupling is longer ranged. This is confirmed by the log-log plot, shown in figure 5.9, which demonstrates that the coupling actually comprises two very distinct rates of decay: an initial rapid decay gives rise to a long range decay in the asymptotic limit. At a separation of around 40 rings the small amplitude, long range character of the coupling starts to dominate.

Since, in practice, *ab-initio* calculations are limited by the size of their unit cell to approximately 20 nanotube rings, any attempt to measure the coupling as a function of D should conclude that the decay was rapid, even in cases where the perfect symmetry was broken.

5.7 Summary and Conclusions

In this chapter we have studied the dependence of the range of the coupling on the impurity host location. It was found that the decay rate depends crucially

on this position; an observation which appears to be confirmed by first principles calculations. This would not have been predicted from the standard theory of IEC, since the specific nature of the impurity was seen to be far less significant than the properties of the nanotube in determining most of the features of the coupling. We have therefore extended the theory to allow for a faster decay and have related the rather formal and abstract condition for observing this property to the real physical condition of altering the host location of the impurity.

This sensitive dependence to host location was further shown to be an intrinsic feature of graphene by relating the generalised Green Function to the energy. Indeed there is nothing in the derivation of this relationship that should be particularly unique to graphene; it is likely that the same symmetry conditions could arise in a number of crystallographic lattices. Such considerations are outside the scope of this thesis. Finally, although strictly a symmetry effect it was nonetheless shown that the rapid decay is somewhat robust against symmetry breaking.

The content of this chapter has been published in references[64][65].

Chapter 6

Transport Properties of Magnetically Doped Carbon Nanotubes

6.1 Introduction

As outlined in chapter 1, the incorporation of nanotubes into spintronic devices is one of the many different possibilities driving the research in carbon nanotubes. Such attempts will inevitably require some understanding of how they interact with their surrounding environment, since real nanotubes display a range of structural imperfections[66]. In one sense these could be regarded as compromising the excellent transport characteristics of pristine tubes. At the same time, used in conjunction with these intrinsic properties, defects may provide an additional way of tuning nanotubes to a particular purpose. This has stimulated a substantial research effort into understanding how the electronic transport properties of nanotubes are affected by the presence of defects. Prominent amongst these are studies of heptagon-pentagon defects and heterojunctions[55][67][68], molecular nanotube junctions[69], effects of weak uniform disorder[70][71], substitutional doping[72][73], physisorbed molecules[74] and spin polarised transport[75]. A comprehensive review of theoretical developments in this area has recently been provided in reference[76].

In this chapter, our attention will focus on the magneto-transport characteristics of nanotubes in the presence of magnetic dopants. Whereas in previous chapters we have considered the effect of an isolated pair of impurity atoms, here we attempt to model a truly disordered system in which a large number of impurities are located on the nanotube. This is shown in figure 6.1. Such a system should represent the real physical environment far more closely. Modelling these large, truly disordered systems is only possible because of the lightweight computational approach we have

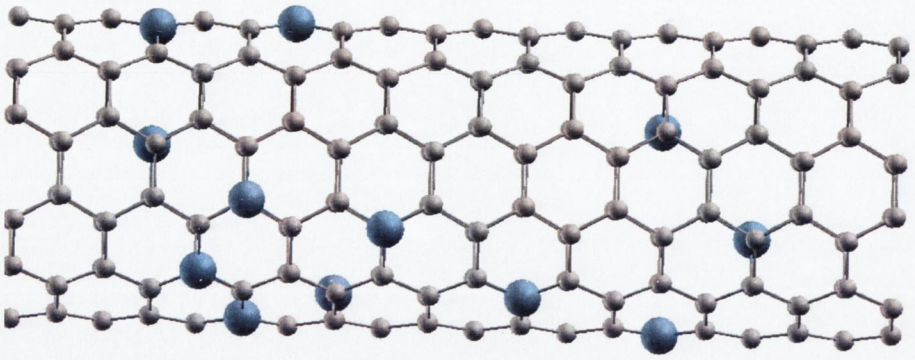


Figure 6.1: A section of a doped (6,6) nanotube. The large atoms represent substitutional impurities randomly distributed about the nanotube.

developed. To date, attempts to model similar systems using fully *ab-initio* methods, such as in[77], are restricted to either individual atoms or small numbers of impurities[78].

The magnetisation of the impurities should respond to the application of a magnetic field which can in principle lead to a giant-magnetoresistance (GMR). GMR was originally discovered in magnetic multi-layered systems and has been introduced in chapter 1. The effect was enabled in large part by the IEC between the magnetic regions, which allowed for a preferential anti-ferromagnetic coupling between magnetic layers. When a magnetic field is applied the magnetisation changes and consequently the transport properties are altered. In our case the situation is slightly different: Instead of well defined layers of a magnetic material we assume that the magnetic response results from the interaction of the tube with itinerant transition metal atoms. These atoms can be either adsorbed on the surface of the tube or, as in figure 6.1, embedded in the lattice as substitutional dopants. It would also be possible to consider a more conventional multi-layered approach by either placing the nanotube between ferromagnetic electrodes[75] or by placing large magnetic nanoparticles inside the tube. The motivation behind this particular approach is that most carbon nanotube growth techniques employ magnetic catalyst particles. After formation these particles will still reside in the vicinity of the nanotubes. The nanotube/catalyst particle system could then constitute a pre-fabricated spin-valve. The case of substitutional doping involves removing individual carbon atoms from the host and replacing them with magnetic impurities. The formation energy for such defects is presumably much larger than for adsorbed impurities but can be achieved using ion irradiation of the lattice[79].

Before calculating the magnetoresistance we need a formalism for calculating the conductance through a doped nanotube. This is provided by the Kubo formula[80], derived from linear response theory and correct in the limit of zero bias. The Kubo Formula provides a particularly convenient scheme for calculating transport through

nanotubes since it can be written in terms of Green Functions, which have been extensively studied in chapter 2 and 3. Once the conductance is known it remains to calculate the magnetoresistance. By convention, we define the magnetoresistance as the fractional change in conductance[1] arising from the application of a magnetic field H, divided by the zero field conductance.

$$\mathrm{MR} = \frac{\Gamma(H) - \Gamma(0)}{\Gamma(0)} = \Gamma(H)/\Gamma(0) - 1 \quad . \tag{6.1}$$

This is the *optimistic* definition of MR since, in general, it is expected that the conductance in the absence of an applied field will be less than with a field applied. The magnitude of the MR is thus amplified. More sober definitions of MR also exist: the so-called *pessimistic* definition with $MR' = (\Gamma(H) - \Gamma(0))/\Gamma(H)$ and the *realistic* definition for which $MR'' = (\Gamma(H) - \Gamma(0))/(\Gamma(H) + \Gamma(0))$ In this final case the magnitude of the MR is restricted to always being less than one. For our calculations we will choose the optimistic definition. Arguably it is not the most appropriate definition when $\Gamma(0)$ approaches zero. However, the primary requirement for useful MR characteristics is that the conductance in the presence and absence of applied field will differ substantially. This is most strikingly illustrated using the optimistic definition. As long as calculated values are viewed in the context of the actual conductance in both cases, this should not present any difficulties.

The underlying assumption is that the impurities in these magnetically doped structures are distributed randomly about the tube. Only the relation of the impurity to the host – substitutional, adsorbed atop or adsorbed centre – is specified. For a given impurity configuration we do not know the ground state orientation of the magnetic moments in the absence of an applied field. However, using the results of Chapters 4 and 5 the magnetic ordering between individual pairs of impurities can be obtained. These pairwise couplings, J_{ij}, can then be regarded as inputs in a classical Heisenberg Hamiltonian,

$$H = \sum_{ij} J_{ij}\, \mathbf{s}_i \cdot \mathbf{s}_j \quad , \tag{6.2}$$

in which the magnetic moments are represented by unit vectors, $\mathbf{s}_i$, in three dimensions. The ground state of such a system can be determined using a standard Monte Carlo or Simulated Annealing approach. Once the ground state orientation of the spins is known it becomes a simple matter to calculate the magnetoresistance. Because transport in nanotubes is coherent, the actual conductance will be extremely sensitive to the particular configuration adopted by the impurities. In contrast, for incoherent transport at a given concentration, the conductance does not depend on

[1] Arguably this would be more correctly described as the magnetoconductance.

the configuration of impurities. Thus, with large numbers of scatterers the results of individual simulations are of little statistical significance and it becomes necessary to average over the fluctuations. In low dimensional systems, these fluctuations can be substantial and it is normally necessary to average over more than a thousand simulations. Once again, the light-weight character of our model is crucial to the feasibility of performing such large ensemble averages. In what follows, this averaging will always be assumed. In cases where there may be some ambiguity the averaged quantity will be placed between angle brackets. For the conductance this is clear enough. For MR we consider two different averages. The ensemble averaged MR which is Eq.(6.1) averaged over all configurations,

$$\mathrm{MR} = \left\langle \frac{\Gamma(H)}{\Gamma(0)} \right\rangle - 1 \quad , \tag{6.3}$$

and a second which is the MR calculated for the average conductance,

$$\mathrm{MR}^* = \frac{\langle \Gamma(H) \rangle}{\langle \Gamma(0) \rangle} - 1 \quad . \tag{6.4}$$

In the next section we derive an expression for the Kubo Formula.

6.2 Kubo Formula

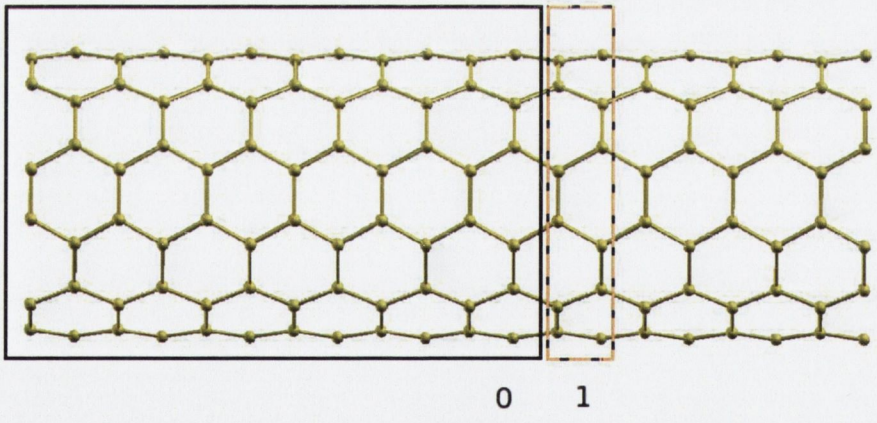


Figure 6.2: Illustration of transport through an armchair nanotube. The nanotube extends to infinity in both directions. The armchair unit ring is shown by the hatched box. This contains carbon atoms as well as potentially orbital and spin degrees of freedom. The left overlayer extends from $-\infty$ and terminates between ring 0 and ring 1. The conductance can be calculated by considering current elements crossing this imaginary boundary.

Standard linear response theory gives the following expression for the conduc-

tance at zero temperature[81],

$$\Gamma(\omega) = \frac{\pi}{\omega} \int dE \sum_{\substack{k,k' \\ \epsilon(k)<E_F<\epsilon(k')}} |\langle k|\hat{I}|k'\rangle|^2 \delta(E + \hbar\omega - \epsilon(k'))\delta(E - \epsilon(k)) \quad . \tag{6.5}$$

The sum extends over all eigenstates of the system satisfying $\epsilon(k) < E_F < \epsilon(k')$, where E_F is the Fermi-energy. $\hat{I}$ is the current operator, E is the energy and ω is the frequency. In order to perform actual calculations it is desirable to remove references to the eigenstates $|k\rangle$ – which are generally not known – by writing them in terms of more familiar Green Functions. Following the approach of Mathon[82] we write the current operator $\hat{I}$ as the rate at which charge crosses the surface S enclosing an arbitrary volume V. Using Heisenberg's Equation this can be written as,

$$\hat{I} = \frac{ie}{\hbar} \sum_{i \in V} \sum_{j \notin V} \{|i\rangle t_{ij} \langle j| - |j\rangle t_{ji} \langle i|\} \quad , \tag{6.6}$$

where the sum over i extends over all sites enclosed by S while the sum over j extends over those sites outside this region.

We assume the volume V encloses a semi-infinite nanotube extending from the left as far as ring 0. This is illustrated for an armchair nanotube in figure 6.2. The choice of ring is completely arbitrary due to charge conservation. The component of the surface S perpendicular to the tube lies between ring 0 and ring 1. This does not correspond to any physical separation of the system. Assuming nearest neighbour interactions, the current operator can then be written as

$$\hat{I} = \frac{ie}{\hbar} \sum_{a,b=1}^{N} \{|0\ a\rangle t_{0a,1b} \langle 1\ b| - |1\ a\rangle t_{1a,0b} \langle 0\ b|\} \quad , \tag{6.7}$$

where the first index labels the particular ring and the second labels the atoms within the ring. Note that $\hat{I}$ satisfies the Hermicity condition $\hat{I} = \hat{I}^\dagger$.

With the current operator defined, we remove the restriction on the sum over eigenstates in Eq.(6.5). This is accomplished by introducing the Heaviside function, defined according to

$$\Theta(x) \ = \ \begin{cases} 1 & x \leq 0 \\ 0 & x > 0 \end{cases} \quad . \tag{6.8}$$

Thus,

$$\sum_{\substack{k,k' \\ \epsilon(k)<E_F<\epsilon(k')}} |\langle k|\hat{I}|k'\rangle|^2 = \sum_{k,k'} |\langle k|\hat{I}|k'\rangle|^2 \Theta(\epsilon(k) - E_F)[1 - \Theta(\epsilon(k') - E_F)] \quad . \tag{6.9}$$

The Heaviside function can also be defined in terms of the low temperature limit of the Fermi-Dirac function: $\Theta(E - E_F) = \lim_{T\to 0} f(E)$. We can now write Eq.(6.5) as

$$\Gamma(\omega) = \frac{\pi}{\omega} \int dE \sum_{k,k'} |\langle k|\hat{I}|k'\rangle|^2 \delta(E + \hbar\omega - \epsilon(k'))\delta(E - \epsilon(k)) \times f(\epsilon(k))[1 - f(\epsilon(k'))] \quad . \tag{6.10}$$

Next we address the delta functions. From the initial definition of the LDOS (c.f. Eq.(2.8)), we know that the imaginary part of the on-site Green Function is a delta-function. This is most easily seen using Dyson's Equation, which allows us write

$$\hat{G}^A - \hat{G}^R = 2i\eta\, \hat{G}^R \hat{G}^A \quad . \tag{6.11}$$

A and R label the advanced and retarded Green Function. These are defined in Eq.(2.1), with $+$ and $-$ signifying the retarded and advanced operators respectively. From Eq.(2.1),

$$\hat{G}^A - \hat{G}^R = 2i\,\eta \sum_k |k\rangle\langle k| \frac{1}{(E - \epsilon(k))^2 + \eta^2} \tag{6.12}$$

$$= 2i\pi \sum_k |k\rangle\, \delta(E - \epsilon(k))\, \langle k| \quad . \tag{6.13}$$

Defining $\widetilde{G}_{ij} = \frac{1}{2i}(G^A_{ij} - G^R_{ij})$ gives trivially,

$$\widetilde{G}_{ij} = \pi \sum_k \langle i|k\rangle\delta(E - \epsilon(k))\langle k|j\rangle \quad . \tag{6.14}$$

Returning to the current operator,

$$|\langle k|\hat{I}|k'\rangle|^2 = -\frac{e^2}{\hbar^2}\left(\sum_{a,b=1}^{N} \langle k|0\ a\rangle t_{0a,1b}\langle 1\ b|k'\rangle - \langle k|1\ a\rangle t_{1a,0b}\langle 0\ b|k'\rangle\right) \times \left(\sum_{c,d=1}^{N} \langle k'|0\ c\rangle t_{0c,1d}\langle 1\ d|k\rangle - \langle k'|1\ c\rangle t_{1c,0d}\langle 0\ d|k\rangle\right) \tag{6.15}$$

So

$$|\langle k|\hat{I}|k'\rangle|^2 = -\frac{e^2}{\hbar^2}\sum_{a,b,c,d=1}^{N}\{\langle k|0\ a\rangle t_{0a,1b}\langle 1\ b|k'\rangle\langle k'|0\ c\rangle t_{0c,1d}\langle 1\ d|k\rangle$$
$$-\langle k|0\ a\rangle t_{0a,1b}\langle 1\ b|k'\rangle\langle k'|1\ c\rangle t_{1c,0d}\langle 0\ d|k\rangle$$
$$-\langle k|1\ a\rangle t_{1a,0b}\langle 0\ b|k'\rangle\langle k'|0\ c\rangle t_{0c,1d}\langle 1\ d|k\rangle$$
$$+\langle k|1\ a\rangle t_{1a,0b}\langle 0\ b|k'\rangle\langle k'|1\ c\rangle t_{1c,0d}\langle 0\ d|k\rangle\}\quad . \tag{6.16}$$

It follows easily that,

$$-\frac{\pi^2\hbar^2}{e^2}\sum_{k,k'}\langle k|\hat{I}|k'\rangle\langle k'|\hat{I}|k\rangle\,\delta(E+\hbar\omega-\epsilon(k'))\,\delta(E-\epsilon(k))$$
$$=\mathrm{Tr}\Big[\widetilde{G}_{10}(E)t_{01}\widetilde{G}_{10}(E+\hbar\omega)t_{01}-\widetilde{G}_{00}(E)t_{01}\widetilde{G}_{11}(E+\hbar\omega)t_{10}$$
$$-\widetilde{G}_{11}(E)t_{10}\widetilde{G}_{00}(E+\hbar\omega)t_{01}+\widetilde{G}_{01}(E)t_{10}\widetilde{G}_{01}(E+\hbar\omega)t_{10}\Big]\quad . \tag{6.17}$$

The trace extends over all intra-ring degrees of freedom. These will include individual atoms, atomic orbitals and spin degrees of freedom. Due to the presence of the delta-functions in Eq.(6.10), it is possible to remove the explicit dependence of the Fermi-Dirac functions, $f(\epsilon(k))$, on the energy eigenvalues,

$$\int dE\,\delta[E+\hbar\omega-\epsilon(k')]\delta[E-\epsilon(k)]f(\epsilon(k))[1-f(\epsilon(k'))]$$
$$=\int dE\,\delta[E+\hbar\omega-\epsilon(k')]\delta[E-\epsilon(k)]f(E)[1-f(E+\hbar\omega)]\quad . \tag{6.18}$$

Eq.(6.17) then allows us to write the Kubo Formula for the conductance in terms of Green Function matrix elements,

$$\Gamma(\omega)=\frac{e^2}{\pi\hbar^2\omega}\int dE f(E)(1-f(E+\hbar\omega))$$
$$\times\mathrm{Tr}\,[\,-\widetilde{G}_{10}(E+\hbar\omega)t_{01}\widetilde{G}_{10}(E)t_{01}+\widetilde{G}_{00}(E)t_{01}\widetilde{G}_{11}(E+\hbar\omega)t_{10}$$
$$+\widetilde{G}_{11}(E)t_{10}\widetilde{G}_{00}(E+\hbar\omega)t_{01}-\widetilde{G}_{01}(E+\hbar\omega)t_{10}\widetilde{G}_{01}(E)t_{10}\,]\quad . \tag{6.19}$$

In the zero frequency limit, using the identity $-\beta f(E)(1-f(E))=f'(E)$, where $\beta=1/k_BT$ is the inverse temperature,

$$f(E)(1-f(E+\hbar\omega)) = f(E)(1-f(E)-f'(E)\hbar\omega) \tag{6.20}$$
$$= -\left(\frac{1}{\beta}+\hbar\omega f(E)\right)f'(E)\quad . \tag{6.21}$$

Taking the low temperature limit[2], and making use of the relation $\lim_{T\to 0} f'(E) = -\delta(E - E_F)$,

$$\lim_{T\to 0} f(E)(1 - f(E + \hbar\omega)) = \hbar\omega\ \Theta(E - E_F)\ \delta(E - E_F) \quad . \tag{6.22}$$

Thus,

$$\begin{aligned}\Gamma = \lim_{\omega\to 0} \frac{2e^2}{h} \int dE\, \Theta(E - E_F)\delta(E - E_F) \\ \times \mathrm{Tr}\,[\, -\widetilde{G}_{10}(E + \hbar\omega)t_{01}\widetilde{G}_{10}(E)t_{01} + \widetilde{G}_{00}(E + \hbar\omega)t_{01}\widetilde{G}_{11}(E)t_{10} \\ + \widetilde{G}_{11}(E + \hbar\omega)t_{10}\widetilde{G}_{00}(E)t_{01} - \widetilde{G}_{01}(E + \hbar\omega)t_{10}\widetilde{G}_{01}(E)t_{10}\,] \quad .\end{aligned} \tag{6.23}$$

The limit can now be taken trivially. The integration is also trivial, and gives the following expression for the DC conductivity,

$$\begin{aligned}\Gamma(\omega = 0) = \frac{2e^2}{h}\mathrm{Tr}\,[\, -\widetilde{G}_{10}(E)t_{01}\widetilde{G}_{10}(E)t_{01} + \widetilde{G}_{00}(E)t_{01}\widetilde{G}_{11}(E)t_{10} \\ + \widetilde{G}_{11}(E)t_{10}\widetilde{G}_{00}(E)t_{01} - \widetilde{G}_{01}(E)t_{10}\widetilde{G}_{01}(E)t_{10}\,] \quad .\end{aligned} \tag{6.24}$$

Eq.(6.24) is the form of the Kubo formula which we shall use. Since it is written entirely in terms of Green Function propagators between discrete lattice sites it is a form that is easily evaluated using the methods outlined in Chapters 2 and 3. An alternative, yet equivalent expression can be deduced if we consider the effects of current conservation. Since in Eq.(6.15) the choice of overlayer is arbitrary, we can just as easily write[81],

$$\begin{aligned}\Gamma(\omega = 0) = \frac{2e^2}{h}\mathrm{Tr}\,[\, -\widetilde{G}_{i,j-1}t_{j-1,j}\widetilde{G}_{j,i-1}t_{i-1,i} + \widetilde{G}_{i-1,j-1}t_{j-1,j}\widetilde{G}_{j,i}t_{i,i-1} \\ + \widetilde{G}_{i,j}t_{j,j-1}\widetilde{G}_{j-1,i-1}t_{i-1,i} - \widetilde{G}_{i-1,j}t_{j,j-1}\widetilde{G}_{j-1,i}t_{i,i-1}\,] \quad .\end{aligned} \tag{6.25}$$

Now i, j are arbitrary rings. For calculational purposes it is generally easiest to set $i = j$, since using the recursive methods of Chapter 2 this requires only the evaluation of the propagators on two adjacent layers. From the point of view of analysis it is often easier to choose the i and j to lie far from the scattering region and on opposite sides, since around the Fermi level the propagators can be written in simplified form.

By choosing i, j far away from the scattering region, Fisher and Lee[83] were able

[2]Note that the limit should be applied to each term in the product separately. In fact, the introduction of the temperature dependence is unnecessary and we could just as easily work with the Heaviside function directly. However, we include the Fermi-Function to keep a connection to the standard derivation.

to relate the Green Function to the Transmission Matrix. It follows that in the DC limit the Kubo and Landauer-Buttiker formulas are equivalent[84]. One final point regarding the relationship between the two formalisms concerns the unit of quantum conductance. This is defined as $G_0 = e^2/h$ although it is often defined as $2e^2/h$ to account for spin degeneracy. The form of Eq.(6.24) would seem to suggest that we are accounting for this spin degeneracy. However this is not the case. The spin degree of freedom is accounted for by the trace. Indeed this has to be true since the spin degeneracy of the system will be broken. In case of confusion, we can always apply the formula in the case of a simple 1-D chain with a single propagating mode. The trace in Eq.(6.24) will evaluate to one half. This means that the transmission function $T(E)$ appearing in the Landauer formalism can be related to twice the trace appearing in the Kubo formula.

6.3 Monte Carlo Methods

Once the coupling between pairs of atoms is known it is necessary to determine the overall ground state orientation of the magnetic moments. The problem of finding such a ground state is commonly tackled using Monte Carlo techniques. What follows is a brief introduction to the method and the related technique of Simulated Annealing. A general introduction to Monte Carlo methods in Statistical Physics is given by Newman and Barkema[85], amongst others.

A standard problem in Statistical Physics is to estimate the equilibrium value of some physical observable, Q, in a system of N particles. Q might typically represent the total energy or magnetisation. Each specific microstate, μ, of the system contributes to this average with a weight given by a Boltzmann distribution,

$$\langle Q \rangle = \frac{\sum_\mu Q_\mu e^{-\beta E_\mu}}{\sum_\mu e^{-\beta E_\mu}} \quad . \tag{6.26}$$

The basic problem in evaluating these averages is that the number of states is normally so large that any attempt to average them directly is completely unfeasible. For example, even in the most simple case of a 1-D Ising ($S = \pm 1$) chain with N spins, the number of states increases as 2^N. If we take $N = 100$ then there are 1.27×10^{30} states contributing to the system. For continuous spin models, such as the Heisenberg Hamiltonian of Eq.(6.2), the situation is even worse.

Notwithstanding these difficulties, one might attempt to estimate the average by sampling over a small subset of the allowed states. This is unlikely to yield a good result since the weighting of the states in Eq.(6.26) is not uniform. This is particularly evident at low temperatures where virtually the entire contribution to $\langle Q \rangle$ comes from an extremely narrow energy window around the ground state, E_0.

Alternatively, choosing states according to a Boltzmann Distribution $e^{-\beta E_\mu}$ will not improve matters since we will end up rejecting almost all of the proposed states.

The Monte Carlo method circumvents these difficulties by generating states with a probability given by their corresponding weight. Now the approximation to Eq.(6.26) should be very good because the most important states in the average will appear most frequently. The way it does this is by generating a Markov Chain. Put simply, a Markov Chain takes an initial state, μ, and returns a new state, ν, chosen at random according to a transition probability $P(\mu \to \nu)$. If the states are allowed to evolve in this way for long enough then eventually the Markov Chain produces states at the frequency represented by the Boltzmann Distribution. There is some freedom in how the transition probabilities can be chosen but one of the most common is given by the Metropolis Algorithm. In this case the transition probabilities are defined according to

$$P(\mu \to \nu) = \begin{cases} 1 & E_\nu \leq E_\mu \\ e^{-\beta(E_\nu - E_\mu)} & E_\nu > E_\mu \end{cases} . \tag{6.27}$$

In the limit of temperature going to zero the ensemble averaging identifies the ground state, or global energy minimum of the system. As a method of finding ground state energies the Metropolis Algorithm makes intuitive sense. Movement towards more favourable energy configurations will always be accepted. However, there is still a finite probability that an *uphill* movement will be made. This is necessary to allow the state to escape from any local minimum it may find itself residing in. The likelihood of accepting an uphill move is determined by the temperature and the size of the movement. At high temperatures such moves are common, whereas at low temperatures it will take the system much longer to escape from a local minimum.

This motivates a second approach, adapted slightly from the first, which is a useful practical tool for evaluating ground state configurations. It is known as Simulated Annealing, a name which derives from the analogy to annealing processes in metallurgy. Instead of equilibrating the system at an extremely low temperature as in the standard Monte Carlo approach, the basic idea is to heat the system so that the spins are initially free to sample any configuration. This means that initially the system avoids spending long periods of time negotiating shallow minima. The temperature is gradually reduced by an amount $T \to RT$ with $0 \leq R \leq 1$. The temperature reduction progressively restricts the system to probing smaller regions around the current minimum. The rate of temperature reduction and the number of steps per temperature are parameters of a given simulation. If the temperature reduction is too abrupt then the system risks becoming frozen far from its actual ground state.

The implementation of the Metropolis Algorithm in our case is quite simple.

The energy is given by the Hamiltonian, which is a function of the $2N$ variables $\theta_1, \theta_2, ..., \theta_N; \phi_1, \phi_2, .., \phi_N$. These variables represent the angular orientation of the spins. $0 \leq \theta_i \leq \pi$ is the orientation of the i-th spin with respect to the z-direction; $0 \leq \phi_i < 2\pi$ is the orientation in the xy-plane. The energy can be written as,

$$E(\theta_i, \phi_i) = \frac{1}{2} \sum_{i,j=1}^{N} J_{ij} \mathbf{s}_i \cdot \mathbf{s}_j \tag{6.28}$$

$$= \frac{1}{2} \sum_{i,j=1}^{N} J_{ij} |\mathbf{s}_i| \left(\sin\theta_i \sin\theta_j \, \hat{\mathbf{n}}_i(\phi_i) \cdot \hat{\mathbf{n}}_j(\phi_j) + \cos\theta_i \cos\theta_j \right) , \tag{6.29}$$

where the factor of 2 accounts for double counting. The pairwise couplings, J_{ij}, are obtained from the total energy calculations given by Eq.(4.18). The on-site couplings, J_{ii}, are set to zero. The unit vectors, $\hat{\mathbf{n}}_i = \cos(\phi_i)\hat{\mathbf{e}}_\mathrm{x} + \sin(\phi_i)\hat{\mathbf{e}}_\mathrm{y}$, represent the projection of each moment onto the xy plane. Eq.(6.29) can also be written in cylindrical coordinates,

$$E = \frac{1}{2} \sum_{i,j=1}^{N} J_{ij} \left[s_{iz} s_{jz} + \sqrt{1 - s_{iz}^2} \sqrt{1 - s_{jz}^2} \cos(\phi_i - \phi_j) \right] \quad . \tag{6.30}$$

A new orientation for one of the spins is then chosen at random. If we label this spin i, then the rotation affects the projection of this vector onto the $N-1$ other vectors. Writing the projection vector as $\mathbf{S}_i = \sum_{j=1}^{N} J_{ij} \, \mathbf{s}_j$ then the energy change is given by,

$$\Delta E = (\mathbf{s}_i' - \mathbf{s}_i) \cdot \mathbf{S}_i \quad . \tag{6.31}$$

If this quantity is negative then the rotation is accepted. If not the move might be accepted with a probability dependent on both the temperature and the magnitude of the energy change. In our simulations the annealing schedule obeys $T(n) = T_0 R^n$. T_0 is the initial temperature; $R = 0.9$ is the temperature reduction factor and n is the temperature step. T_0 is chosen so as to be equal in magnitude to the largest pairwise coupling. The temperature is normally reduced after $4000N$ spin rotations.

Calculating ΔE after each rotation involves the evaluation of the $N-1$ cosine terms arising from the inner products in Eq.(6.30). Calculating these cosine functions is the most time consuming part of the simulation. However, it is possible to reduce the number of function evaluations by writing the energy change as

$$\Delta E = (s_{iz}' - s_{iz}) A_i + \mathrm{Re}\left[\left(\sqrt{1 - s_{iz}'^2} e^{i\phi_i'} - \sqrt{1 - s_{iz}^2} e^{i\phi_i} \right) B_i \right] \quad , \tag{6.32}$$

with $A_i = \sum_j J_{ij} s_{jz}$ and $B_i = \sum_j J_{ij} \sqrt{1 - s_{jz}^2} e^{-i\phi_j}$. This simplifies matters be-

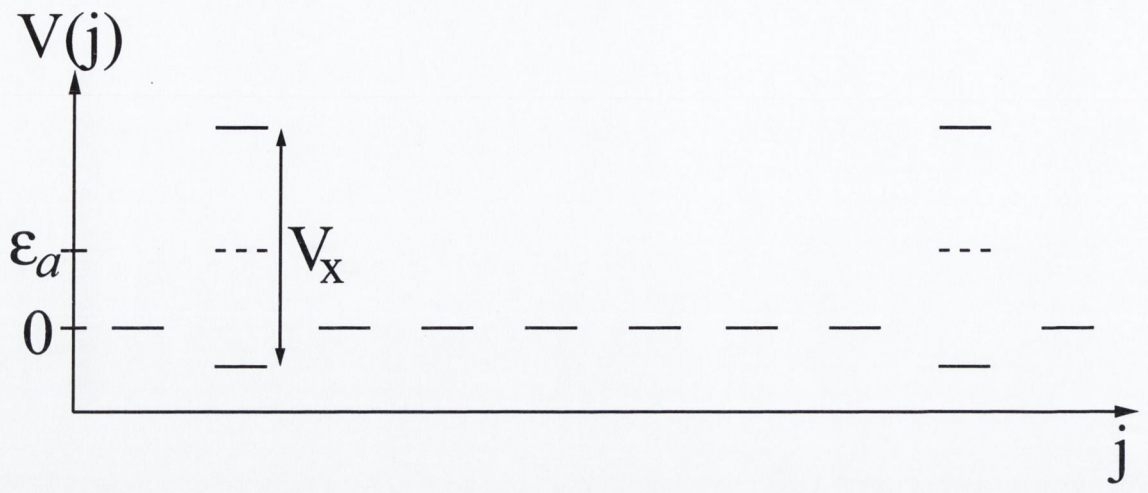


Figure 6.3: Magnetism at the site of impurity atoms is represented by introducing a spin-split potential. The separation between the bands is given by V_x, centred about the dashed line ϵ_a.

cause, assuming A_i and B_i are known, then we only need to evaluate s'_{iz} and $e^{i\phi_i}$ to determine the energy change. The values of A_k and B_k, $k \neq i$ will also need to be updated but this does not involve any function evaluations – merely a subtraction.

One final aspect to be considered before proceeding is in the generation of the random spin directions. The angular directions should be uniformly distributed about the surface of a unit sphere. This distribution is not satisfied if we choose the spin angles θ and ϕ at random: because the surface element on a sphere is given by $dA = \sin(\theta)d\theta d\phi = d(\cos(\theta))d\phi = dzd\phi$, so that choosing values for θ and ϕ uniformly would bias the moment towards the equator of the sphere. Therefore in order to sample the allowed orientations correctly, values for ϕ and z should be generated uniformly.

6.4 Parameterisation of the Hamiltonian

As outlined in section 4.2 magnetism within a mean field approximation is represented by a spin-split potential describing the intra-atomic Coulomb interaction. This is illustrated in figure 6.3. In a single band model, the splitting is normally described by two parameters: the magnitude of the splitting, V_x, and the band centre, ϵ_a. In our examination of the indirect coupling between magnetic moments the main consequence of changing the values of these parameters was to change the amplitude of the oscillation. Since the primary focus was on the rate of decay and period of oscillation, the specific parameterisation chosen was of no great importance. However, the transport properties should depend on the specific parameterisation. Since we wish to model interactions with real transition metal atoms we need to choose values of the parameters that will reproduce physical characteristics of these atoms: namely magnetisation and occupation. This can be accomplished

using a self-consistent approach. Within a single band model the nanotube itself is well described by a single parameter: the nearest neighbour hopping $t_0(\gamma)$. This parameter determines the width of the energy bands. Until now all energies were normalised in terms of this hopping. The actual value can be determined by fitting the bands to experimental or *ab-initio* results. For carbon nanotubes these yield $t_0 = 2.7\,\mathrm{eV}$[70]. This value is adopted from here on. The parameters describing the transition metals can be determined from *ab-initio* simulations in systems with one or two impurities. These values, obtained for this simple case, can then be used in the far larger doped systems we are considering.

Within the mean field approximation, the band centre of the magnetic atoms is located at $\epsilon_i = \epsilon_a + U\langle n_i\rangle/2$ while the exchange splitting is proportional to the magnetisation: $V_\mathrm{x} = U\langle m_i\rangle/2$. U is the Coulomb term which was introduced in chapter 2. Empirical fittings of the relationship between the splitting and the magnetisation find the constant of proportionality is $U \approx 1\mathrm{eV}/\mu_B$[86]. The magnetisation(occupation) can also be determined by integrating the difference(sum) of the LDOS of the spin-up and down bands up to the Fermi-Energy. This leads to the following self-consistency condition:

$$\begin{aligned}
\langle m_i\rangle &= \int_{-\infty}^{E_F} dE \left[\rho_i\left(E, \epsilon_a + \frac{U\langle n_i\rangle}{2} - \frac{U\langle m_i\rangle}{2}\right) - \rho_i\left(E, \epsilon_a + \frac{U\langle n_i\rangle}{2} + \frac{U\langle m_i\rangle}{2}\right)\right] \\
\langle n_i\rangle &= \int_{-\infty}^{E_F} dE \left[\rho_i\left(E, \epsilon_a + \frac{U\langle n_i\rangle}{2} - \frac{U\langle m_i\rangle}{2}\right) + \rho_i\left(E, \epsilon_a + \frac{U\langle n_i\rangle}{2} + \frac{U\langle m_i\rangle}{2}\right)\right]
\end{aligned} \tag{6.33}$$

If the total occupancy $\langle n_i\rangle$ is known, it is possible to deduce values for ϵ_a and V_x. However, we should really consider the effect of a third parameter in our problem: the host/impurity hopping, t. Extracting a value for t requires the introduction of a third equation of constraint. The most obvious choice is the expression for the pairwise coupling,

$$\Delta\Omega(\pi, D) = -J(D) = \int_{-\infty}^{E_F} dE\; E\; \Delta\rho(E, \epsilon_a, V_\mathrm{x}, t) \quad . \tag{6.34}$$

The coupling along with the correct occupation, labelled $\langle n\rangle_0$, can be obtained from first principles calculations. However, these can also provide the spin split occupation of the d-band and hence the magnetisation. It should therefore be possible to directly calculate the value of the exchange integral U. Unfortunately, standard *ab-initio* approaches can greatly over-estimate the magnitude of the coupling[87], and in general it does not seem possible to satisfy the three constraint equations using these values. For these cases; in the absence of a set of accurate physical values we have to adopt an alternative approach. If we ignore the final constraint,

Nanotube	Location	Atom	$\langle n \rangle_0$	$\langle m \rangle_0$	J	t	$\langle m \rangle$	ϵ_a
(4,4)	atop	Mn	0.97	0.79	–	2.52	±0.79	-2.04
(4,4)	centre	Mn	0.98	–	0.064	1.66	±0.67	-2.14
(4,4)	sub	Mn	1.10	0.60	–	0.96	±0.60	-3.16
(5,5)	sub	Ni	1.60	0.14	–	0.63	±0.14	-4.92

Table 6.1: Table of self consistent parameters. The two transition metal atoms for which values were available are Manganese and substitutionally doped Nickel. $\langle n \rangle_0$ and $\langle m \rangle_0$ are the occupation and magnetisation obtained from *ab-initio* simulations. J is the pairwise coupling between two impurities placed on the tube at a specified distance. $\langle m \rangle$ is the self consistent value of the magnetisation. t is the host/impurity hopping and ϵ_a locates the centre of the exchange split level with respect to the nanotube band centre.

then we can modify the initial approach based on the first two constraints: since we now know the *ab-initio* value for the magnetisation we can adjust the value of t such the the self consistency condition gives the correct magnetisation.

In table 6.1 we present values for $V_{\mathrm{x}}, \epsilon_a$ and t for substitutional and adsorbed Manganese, and for substitutional Nickel. The *ab-initio* simulations for the Mn atoms were performed on a (4,4) armchair. In the case of substitutional Ni, a value for the magnetisation was taken from reference[39]. For manganese, they were provided by [62]. The value of U is taken as 5eV, which is the quoted value for Mn[86].

With the parameterisation complete all the necessary components required for the transport calculations are in place. The standard approach involves breaking the system into three regions: left, right and centre. This is shown schematically in figure 6.4. The central region hosts the disordered section of the tube. The left and right sections are semi-infinite leads, which couple the tube to external reservoirs. Using the decimation techniques developed in chapter 2 the effect of coupling the tube to each of the semi-infinite leads is restricted to the surface layers of the leads, which are described by the surface Green Function. These propagators are known as the self energies of the leads and are often written as $\Sigma_{L,R}$. In our model, the leads are also assumed to be nanotubes of the same diameter and chirality as the tube in the centre. As a result no back-scattering occurs at the interfaces and deviations from ballistic conductance are therefore solely due to the impurities located in the central region. From a computational standpoint, the great advantage of treating each of the leads as a semi-infinite nanotube is that using the expressions derived in chapter 3, the surface propagators of the nanotube leads are already known.

Once the self energies have been calculated, Eq.(2.57) can be employed to recursively update the surface Green Function to encompass the central region. The techniques for treating substitutional and adsorbed impurities on carbon nanotubes within the recursive scheme were discussed in section 2.6. The only difference is that now the impurities lift the spin degeneracy of the system. As a result the Green

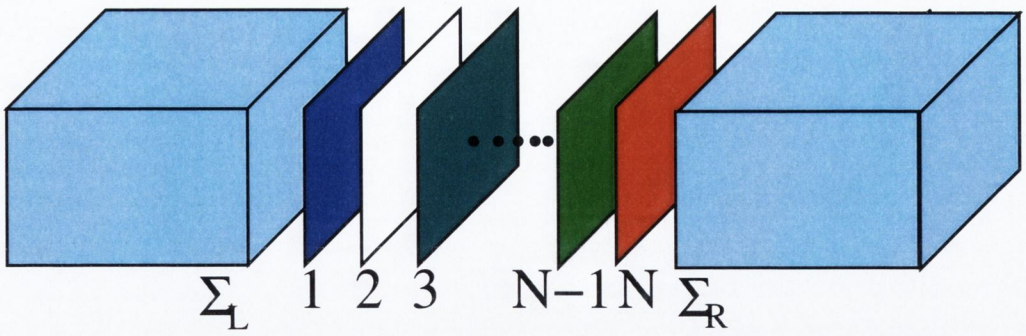


Figure 6.4: A schematic representation of a nanostructure. The system is broken into 3 sections with the central region comprising a series of N, possibly disordered layers. The left and right sections are semi-infinite leads. The central region couples to the leads via the surface layer and the effect of the leads can be incorporated into a self energy term, $\Sigma_{L,R}$, which is equal to the surface Green Function at each of the surfaces.

Function matrices contain a spin degree of freedom,

$$[G] \rightarrow \begin{bmatrix} G^{\uparrow\uparrow} & G^{\uparrow\downarrow} \\ G^{\downarrow\uparrow} & G^{\downarrow\downarrow} \end{bmatrix} \quad . \tag{6.35}$$

The spin degeneracy is lifted only at the sites of the impurities. Therefore, in place of a single matrix element, each impurity site is now a 2×2 matrix in spin space. The matrix operator for the i-th impurity is given by

$$\hat{H}_i = \epsilon_i \hat{I} - V_{\mathrm{x}}[\cos\theta_i \ \hat{\sigma}_z + \sin\theta_i(\cos\phi_i \ \hat{\sigma}_x + \sin\phi_i \ \hat{\sigma}_y)] \quad , \tag{6.36}$$

where σ_x, σ_y, σ_z are the usual Pauli matrices. θ_i and ϕ_i give the orientation of the moment. When the impurities are aligned the magnetic moment is taken to lie along the z-axis (i.e. $\theta_i = 0$). In the absence of an applied field the angles are the outputs of the Simulated Annealing routine. Writing the on-site matrix explicitly,

$$H_i \rightarrow \begin{bmatrix} H_i^{\uparrow\uparrow} & H_i^{\uparrow\downarrow} \\ H_i^{\downarrow\uparrow} & H_i^{\downarrow\downarrow} \end{bmatrix} = \begin{bmatrix} \epsilon_i - V_{\mathrm{x}}\cos\theta_i & -V_{\mathrm{x}}\sin\theta_i \ e^{-i\phi_i} \\ -V_{\mathrm{x}}\sin\theta_i \ e^{i\phi_i} & \epsilon_i + V_{\mathrm{x}}\cos\theta_i \end{bmatrix} \quad . \tag{6.37}$$

With $\theta_i = 0$, the moments are in a collinear alignment, the spin-up and down channels are decoupled and the conductance evaluates to the sum of the separate channels. When the moments are non-collinear the spin channels will experience mixing. Physically, this allows for the possibility of spin-flip scattering within the disordered region.

Once the left side lead has been extended to include the impurities all that remains is to attach the composite structure to the lead emanating from the right. If the structure on the left terminates at ring 0, then the matrices required to calculate the conductance, namely G_{00}, G_{01}, G_{10}, G_{11}, can easily be written in terms of the

surface propagators S_0, S_1,

$$G_{00} = (S_0^{-1} - t_{01}\, S_1\, t_{10})^{-1} \tag{6.38}$$

$$G_{01} = S_0\, t_{01}\, G_{11} \tag{6.39}$$

$$G_{11} = (S_1^{-1} - t_{10}\, S_0\, t_{01})^{-1} \tag{6.40}$$

$$G_{10} = S_1\, t_{10}\, G_{00} \quad . \tag{6.41}$$

Inserting these matrices in Eq.(6.24) gives the conductance. For a given impurity configuration the conductance is calculated twice: first with the moments aligned and then in their ground state orientation. Before proceeding to the calculations we introduce one final approach that will be useful in providing a qualitative understanding of some of the results obtained.

6.5 T-matrix Expansion

The simplicity of the tight-binding Hamiltonian we have adopted allows for the study of the dependence of the transport properties on the concentration of impurities. This dependence would be difficult, if not impossible, to determine using more sophisticated Hamiltonians, due to the sheer computational overhead involved. Before proceeding with the actual calculations we attempt to gain some qualitative insight into the form this dependence might be expected to take. In order to do this we must return to the T-matrix introduced in chapter 2 and defined as,

$$T = (I - \mathcal{G}V)^{-1} \quad . \tag{6.42}$$

The T matrix relates the Green Function of the perturbed system to that of the unperturbed system according to $G = T\mathcal{G}$. As such it contains all the information about scattering processes that can take place. If the system consists of a single substitutional impurity, with onsite energy λ, then the matrix is simply the scalar: $T_{11} = 1/(1 - \lambda\, \mathcal{G}_{11})$. The matrix for N substitutional impurities can be written in terms of these single particle matrices, by expanding the inverse in powers of T_{11}. Each term is associated with a higher order interaction. Thus, the first order interaction terms are the diagonal elements of the matrix, given by T_{ii}. The second order interaction matrix consists of terms of the form,

$$T_{ij}^{(2)} = \lambda\, T_{ii} \mathcal{G}_{ij} T_{jj} \quad . \tag{6.43}$$

Similarly the third order interaction matrix consists of the elements,

$$T_{ijk}^{(3)} = \lambda^2\, T_{ii} \mathcal{G}_{ij} T_{jj} \mathcal{G}_{jk} T_{kk} \quad , \tag{6.44}$$

which is cubic in the single particle term T_{ii}.

Expanding the T-matrix in this fashion we can write,

$$\hat{G} = \hat{\mathcal{G}} + \lambda \sum_{i,j=1}^{N} \hat{\mathcal{G}} \, |r_i \; a_i\rangle \, (T_{ij}^{(1)} + T_{ij}^{(2)} + \cdots) \, \langle r_j \; a_j| \, \hat{\mathcal{G}} \quad . \tag{6.45}$$

Considering the first order contributions,

$$\hat{G}^{(1)} = \lambda \sum_{i=1}^{N} \hat{\mathcal{G}} \, |r_i \; a_i\rangle \, T_{ii}^{(1)} \, \langle r_i \; a_i| \, \hat{\mathcal{G}} \quad . \tag{6.46}$$

The key point is to recognise that the single particle terms $T_{ii} = T_{11}$ do not depend on i, i.e. they do not depend on the configuration of the impurities. If we consider the limit where there is a large number of impurity sites, then the effect of the averaging over all sites is that we can write,

$$\sum_{r_i, a_i} |r_i \; a_i\rangle\langle r_i \; a_i| \approx \hat{I} \quad . \tag{6.47}$$

Therefore $\langle \hat{G}^{(1)} \rangle \approx \lambda N \, T_{11} \, \hat{\mathcal{G}}^2$, which is linearly proportional to the concentration.

Similarly for the second order term,

$$\hat{G}^{(2)} = \lambda^2 \sum_{i,j=1}^{N} \hat{\mathcal{G}} \, |r_i \; a_i\rangle \, T_{ii} \langle r_i \; a_i| \hat{\mathcal{G}} |r_j \; a_j\rangle T_{jj} \, \langle r_j \; a_j| \, \hat{\mathcal{G}} \quad . \tag{6.48}$$

Thus $\langle \hat{G}^{(2)} \rangle \approx \lambda^2 N^2 \, T_{11}^2 \, \hat{\mathcal{G}}^3$.

Continuing in this way,

$$\begin{aligned} \langle \hat{G} \rangle &\approx \hat{\mathcal{G}} + \lambda N T_{11} \hat{\mathcal{G}}^2 + (\lambda N T_{11})^2 \hat{\mathcal{G}}^3 + (\lambda N T_{11})^3 \hat{\mathcal{G}}^4 + \cdots \\ &= (\hat{I} - \lambda N T_{11} \hat{\mathcal{G}})^{-1} \hat{\mathcal{G}} \quad . \end{aligned} \tag{6.49}$$

Eq.(6.49) is just Dyson's Equation with $\hat{V} = \lambda N \mathcal{T}_{11} \hat{I}$. The net effect of the averaging is to introduce a self energy term $\lambda N T_{11}$. $\langle \hat{G} \rangle$ is diagonal when written in k-space, so that the mixing of the wavevectors induced by the impurities averages to zero. The self energy term depends both on the nature of the impurities and on the number of impurities present. When the transport can be described in terms of single particle scatterings the conductance should be seen to decrease linearly with concentration, for low concentrations. Alternatively, if the impurities are strong scattering centres then higher order interactions can be relevant even for low concentrations.

6.6 Results/Analysis

In this section we will look at the results for the ensemble averaged conductance and MR for armchair nanotubes doped with Mn and substitutional Ni impurities. The results are divided into three sections, separated according to the location of the impurity within the host. The three positions are adsorbed atop, adsorbed centre and substituted. The adsorbed bridge case is not considered since the qualitative features are not expected to differ from the atop case. Additionally the bridge site does not appear to represent a stable position for transition metal atoms.

For each of the three cases the emphasis is placed on the concentration dependence and energy dependence close to the band centre.

6.6.1 Adsorbed Impurities

Atop

The parameters of the Hamiltonian describing Mn impurities adsorbed atop are given in table 6.1. Using these parameters, the impurities are placed randomly on a (5,5) nanotube, in which the central disordered region is 200 rings ($\sim$ 50 nm) long. This system is replicated 1000 times with different impurity configurations and the ensemble average is taken. At zero bias the average conductance and MR was calculated as a function of concentration. The results are shown in figure 6.5. The lower panel shows the conductance both with an applied magnetic field (red line) and with no applied field (blue line). For both cases the conductance decreases monotonically. The rate of decrease is relatively slow, particularly for the case with zero field, and both cases can sustain an appreciable current at up to 10% doping. Interestingly, the conductance in zero field is greater than with an applied field. From the definition in Eq.(6.1), this gives rise to a negative MR with a minimum close to 6%. Figure 6.6 shows the same plot only with $E_F = -0.5\,\text{eV}$. By changing E_F we attempt to mimic the presence of a gate voltage. In this case the MR increases monotonically with a sign change close to c=1.5%.

To investigate the characteristics of the conductance in more detail we plot in figure 6.7 the spin-decomposed conductance for the case above. With an applied magnetic field the impurities are aligned and the up- and down-spin channels are decoupled. The total conductance, Γ, is simply the sum of the conductance of each channel separately, $\Gamma = \Gamma^{\uparrow} + \Gamma^{\downarrow}$. Changing the alignment of the impurities, such that they are no longer lying parallel and anti-parallel, induces mixing between the spin channels. The conductance is now the sum over the four spin components $\Gamma = \Gamma^{\uparrow\uparrow} + \Gamma^{\uparrow\downarrow} + \Gamma^{\downarrow\uparrow} + \Gamma^{\downarrow\downarrow}$, where the individual components are given by Eq.(6.24)

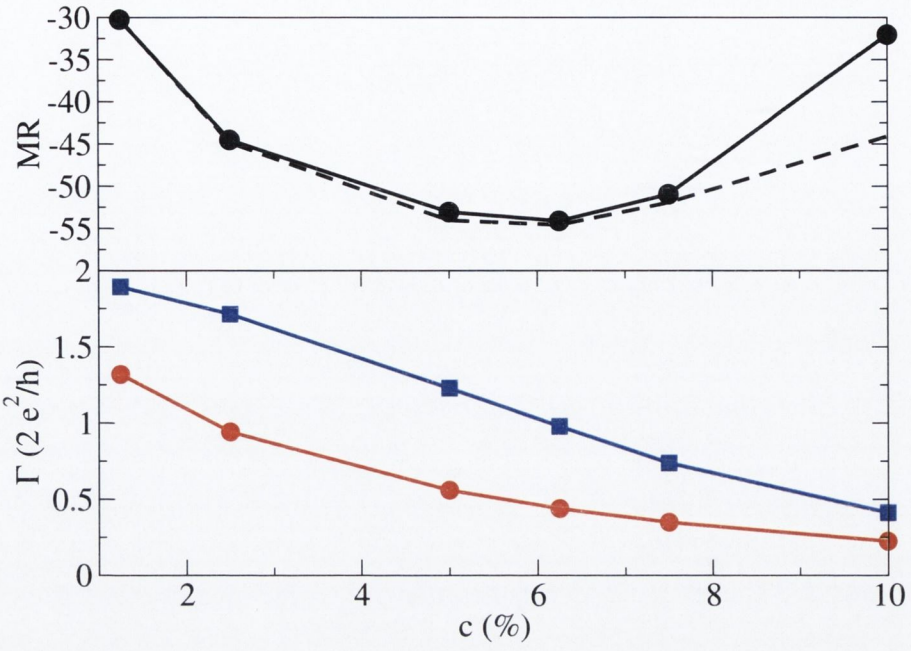


Figure 6.5: Conductance and MR vs impurity concentration on a 200 ring long (5,5) armchair. $E_F = 0$. The impurities are in the atop position. Top panel shows the average MR (solid line/circles) and the average MR* (hatched line). The lower panel shows the average conductance with $H > 0$ (red line) and $H = 0$ (blue line).

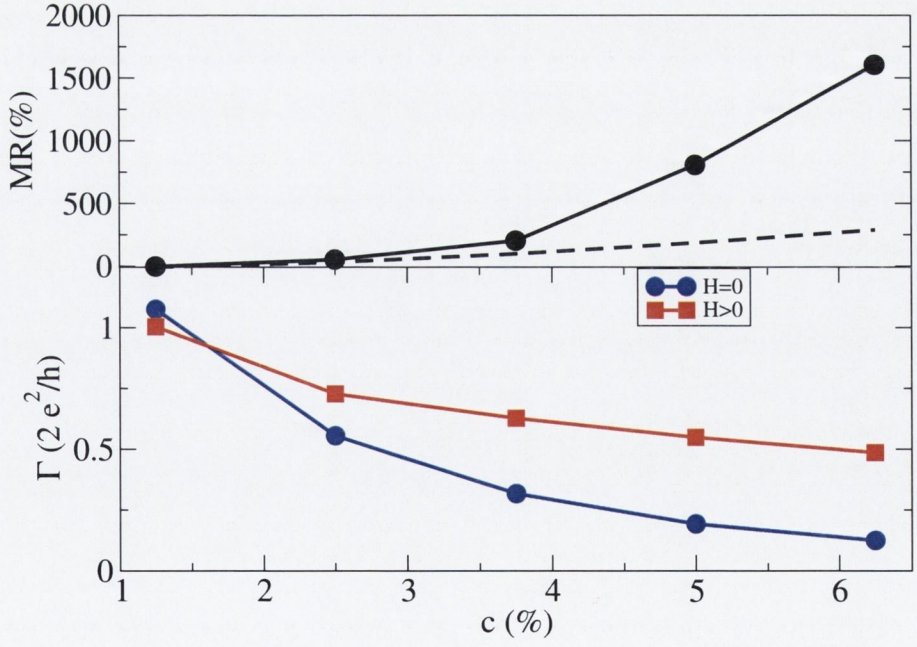


Figure 6.6: Conductance vs concentration of impurities on a 200 ring long (5,5) armchair. $E_F = -0.5$eV. The impurities are in the atop position. Top panel shows the average MR (solid line/circles) and the average MR* (hatched line). The lower panel shows the average conductance with $H > 0$ (red line) and $H = 0$ (blue line).

with the appropriate component of the spin resolved Green Function $G^{\sigma\sigma'}$ inserted,

$$\Gamma^{\sigma\sigma} = \frac{2e^2}{h}\mathrm{Tr}[\widetilde{G}^{\sigma\sigma}_{11}\, t_{10}\, \widetilde{G}^{\sigma\sigma}_{00}\, t_{01} + \cdots] \tag{6.50}$$

$$\Gamma^{\sigma\sigma'} = \frac{2e^2}{h}\mathrm{Tr}[\widetilde{G}^{\sigma\sigma'}_{11}\, t_{10}\, \widetilde{G}^{\sigma'\sigma}_{00}\, t_{01} + \cdots] \quad . \tag{6.51}$$

With these definitions, it is easy to show that $\Gamma^{\uparrow\downarrow} = \Gamma^{\downarrow\uparrow}$. Thus $\Gamma = \Gamma^{\uparrow\uparrow} + \Gamma^{\downarrow\downarrow} + 2\Gamma^{\uparrow\downarrow}$. From a physical standpoint these mixed currents can be thought of as the conductance arising from spin-flip scattering at the impurity sites. Thus $\Gamma = \Gamma^{\uparrow\uparrow} + \Gamma^{\downarrow\downarrow} + 2\Gamma^{\uparrow\downarrow}$.

The results of figure 6.7 can be understood with the aid of the previous section. Let us consider the aligned case first. The conductance for the spin-down channel is seen to decrease almost linearly as a function of concentration; whereas the up-spin channel is suppressed quite rapidly. The concentration dependence of the conductance for this channel is well approximated by a function of the form,

$$\Gamma = \frac{\Gamma_0}{1 + \alpha c + \alpha^2 c^2} \quad , \tag{6.52}$$

where c is the concentration and the parameter α is set to 1.3. This is represented by the dotted line in figure 6.7. The fitting is visual, but it is motivated by the form of the concentration dependence given by Eq.(6.49). The down-spin electrons are more weakly scattered, and Eq.(6.49) can be approximated to second order in c (hatched line). For up-spin electrons, the effect of multiple scattering terms appear to be far more important and the conductance is rapidly suppressed with increasing conductance. The three spin-decomposed conductance contributions for the case of $H > 0$ are also shown in the figure. The curves corresponding to $\Gamma^{\uparrow\uparrow}$ and $\Gamma^{\downarrow\downarrow}$ are almost degenerate, which indicates that the overall magnetisation of the system is very small. This is indeed the case: the ensemble averaged magnetisation, $\langle M \rangle$, is equal to $0.10\,\mu_B$ at c=2.5%, $0.09\,\mu_B$ at c=3.75% and $0.08\,\mu_B$ at c=5.00%. The conductance through the spin-up and down channels is seen to remain high over the range of concentrations: its value lying just below that of the spin-down band in the aligned case. As the concentration increases, scattering between the spin channels becomes increasingly significant and quickly leads to the positive MR seen in figure 6.6.

To examine the cause of the changing sign of the MR a little more closely the conductance is plotted as a function of E_F in figure 6.8. The impurity concentration is fixed at 3.33%. As usual, in the lower panel the red line shows the case with an applied field and the blue line the case with no field. The MR is shown in the upper panel. The conductance with applied field is not particularly sensitive to variations in E_F. In contrast, the conductance without field changes quite markedly and

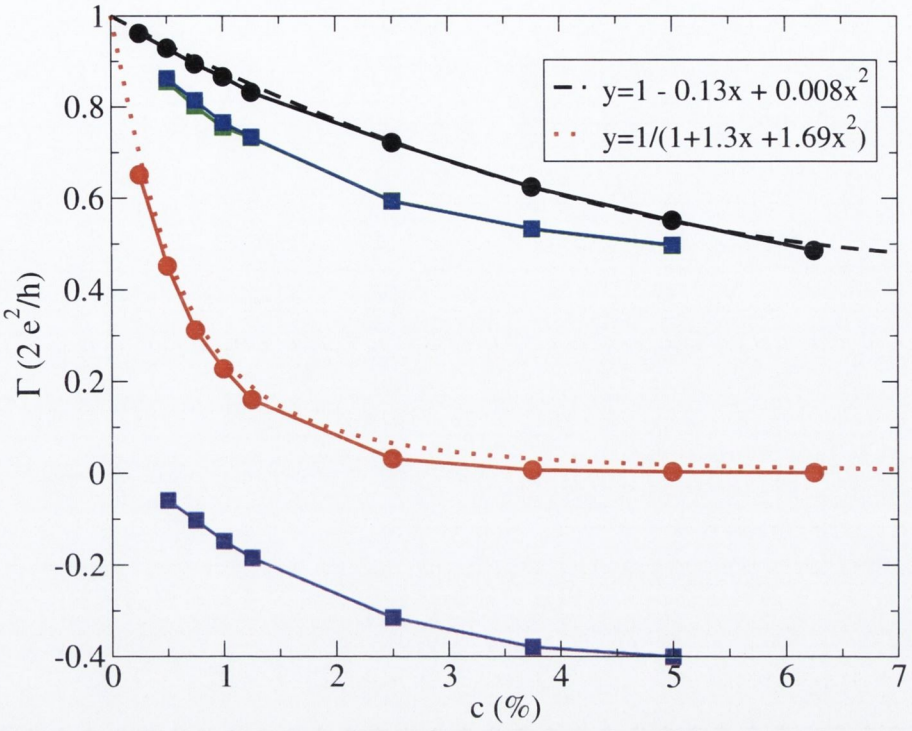


Figure 6.7: Channel decomposed conductance for the case of $E_F = -0.5\,\text{eV}$. The two solid/circle lines represent the down-down (black line) and up-up (red line) contributions for the case of $H > 0$. When $H = 0$ the conductance channels are allowed to mix. These are shown by the three solid/square lines. The down-down (blue) and up-up (green) components are now approximately equal. Scatterings between the up and down channels (indigo) reduce the conductance. The dotted and hatched lines are visual fittings of the down-down curve (black) and the up-up curve (red) for the case of $H > 0$.

displays a maximum around $E_F = 0.25\,\text{eV}$. This dependence is due to two factors. Firstly, for a given impurity configuration and a fixed ground state orientation of the moments the conductance will change as a function of E_F. Additionally, the pairwise couplings, J_{ij}, determining the ground state orientation are themselves dependent on the Fermi-Energy. The blue line (diamonds) in figure 6.8 includes the effect of both of these factors. In an attempt to separate the contributions from each of these components, the hatched line represents the case of $H = 0$, but the conductance is plotted using the pairwise couplings correct at $E_F = 0$. The two curves will obviously coincide at $E_F = 0$. For other energies the points are seen not to overlap but the qualitative features of both curves are similar. The changing sign of the MR is seen to arise from the changing energy. However the specific features of the MR, such as position of the sign change, depend on the magnetic ground state at a given energy.

Figure 6.9 shows the energy dependence of the transmission function for the same system with the spin channels decomposed. With $H > 0$ the two spin channels behave in a broadly anti-symmetric fashion as a function of the E_F. The crossover point is located near $0.25\,\text{eV}$ which is close to the band centre at $0.39\,\text{eV}$. This

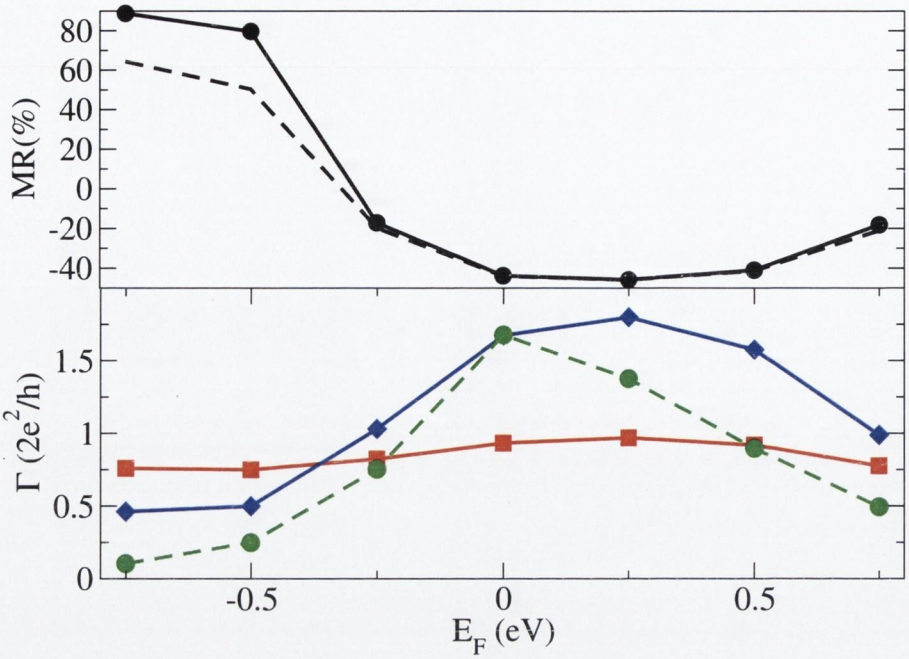


Figure 6.8: Conductance and MR vs E_F on a 160 ring long (5,5) armchair. The concentration of Mn impurities is 3.33%. The lower panel shows the conductance with $H > 0$ (red line) and $H = 0$ (blue line). The hatched line represents the effect of applying a gate voltage without changing the overall magnetisation. The upper panel shows the E_F dependence of the MR.

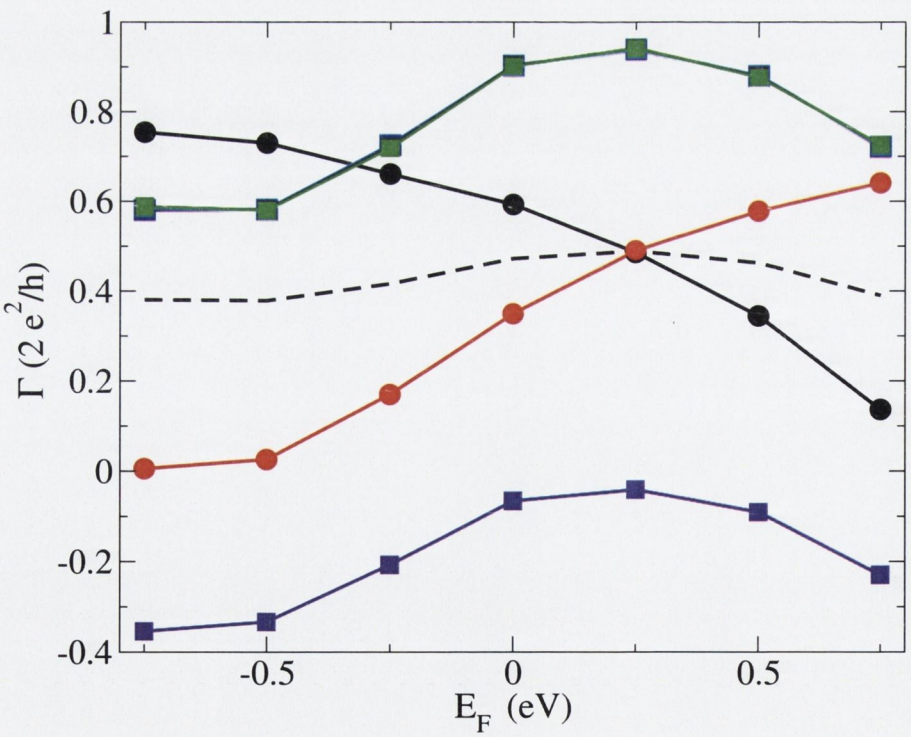


Figure 6.9: Channel decomposed conductance for the case in figure 6.8. The circles represent the down- (black) and up- (red) spin channels with $H > 0$. The squares are for the case with no applied field. The down-down (blue) and up-up (green) channels are degenerate. The violet line is the conductance arising from spin-flip scatterings. The hatched line is half the total conductance with $H > 0$.

leads to the overall conductance being relatively insensitive to E_F. In the absence of the applied field the degeneracy of the up-up and down-down channel conductance indicates the system is demagnetised over the range of the plot. For $E_F > 0$ the two channels transmit extremely effectively, with little spin-flip scattering in evidence. Indeed, both bands are more conductive than the corresponding bands with a field applied (hatched line). As the direction of the gate voltage is reversed, the effect of spin-flip scattering increases and the total conductance is reduced below the $H > 0$ value.

Centre

In chapter 5 it was shown that the location of the adsorbed impurity had a dramatic effect on the range of the coupling. This poses the question as to whether a similar effect should be present for the conductance. Naively we might assume that it should be because the Indirect exchange coupling and conductance can both be described in terms of scattering between the nanotube's conduction electrons and the impurities. Figure 6.10 is a plot of the energy dependence of the conductance and MR as a function of E_F on a (5,5) nanotube. Again, the size of the central region hosting the impurities is 200 rings. The impurity concentration is fixed at 1%(40 impurities). Rather surprisingly, the system displays no MR at $E_F = 0$. Away from this point the only non-zero MR seems to appear at specific energies. Inspection of the conductance shows that at $E_F = 0$ the transport is perfectly ballistic, both with and without applied field. This appears to be true independent of the impurity concentration and the parameters chosen to represent the transition metal atom.

To gain some understanding into why the conductance displays this ballistic character we make use of Dyson's Equation and the simplified form of the Green Function introduced in chapter 5. First, we consider the contribution to the transport from a single impurity. To determine the conductance we need to insert the updated Green Function propagator between ring i and j in Eq.(6.25). As mentioned in section 6.2 the positions of the two rings is arbitrary. In this case, we take the ring i to lie deep in the left lead and j deep in the right lead. This simplifies the details considerably, since, as with the case of asymptotic separation, we then need only consider the contributions arising from the two non-evanescent wavevectors around $E_F = 0$. As in chapter 5, the perturbation coupling the impurity to the nanotube is written as,

$$\hat{V} = |A\rangle\, t\, \langle a| + |a\rangle\, t\, \langle A| \quad , \tag{6.53}$$

where A labels the impurity site and $|a\rangle = \sum_{i=1}^{6} |a_i\rangle$ is the sum over the 6 carbon atoms surrounding the impurity. We adopt the labelling (R_i, s) for the sites with i

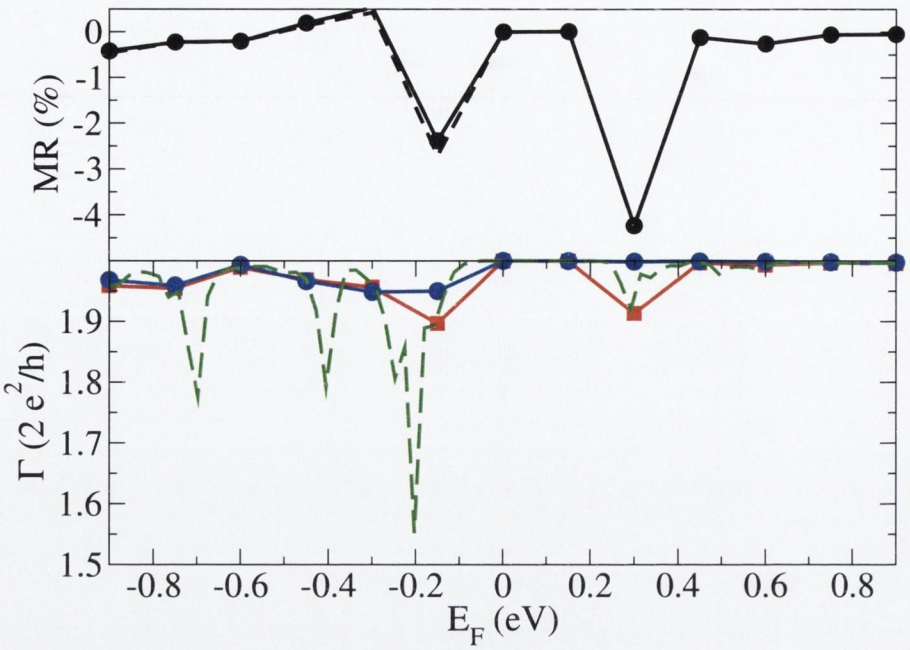


Figure 6.10: (5,5) nanotube with 200 rings. c=1% (40 impurities). Impurities are in the centre position. In the lower panel the red and blue lines show the conductance with $H > 0$ and $H = 0$ respectively. The dashed green line shows the conductance in the aligned configuration on a more densely plotted energy mesh. The upper panel shows MR (solid line/circles) and MR* (hatched line) as a function of E_F.

representing the nanotube ring and s the intra-ring atoms. Using Dyson's Equation, the propagators $G_{ij}(s, s')$ between rings i and j can be written in terms of propagators of the pristine tube,

$$\begin{aligned}\langle R_i\, s|\hat{G}|R_j\, s'\rangle &= \langle R_i\, s|\hat{\mathcal{G}}|R_j\, s'\rangle + \langle R_i\, s|\hat{\mathcal{G}}|a\rangle[VT]_{aa}\langle a|\hat{\mathcal{G}}|R_j\, s'\rangle \\ &= \langle R_i\, s|\hat{\mathcal{G}}|R_j\, s'\rangle + \langle R_i\, s|\hat{\mathcal{G}}|a\rangle\frac{t^2\mathcal{G}_{AA}}{1-t^2\mathcal{G}_{aa}\mathcal{G}_{AA}}\langle a|\hat{\mathcal{G}}|R_j\, s'\rangle \quad . \quad (6.54)\end{aligned}$$

Using the symmetry relations derived in section 5.3.1 (c.f. Eq.(5.17)), it is easily seen that $\langle R_\ell\, s|\hat{\mathcal{G}}|a\rangle = 0$ at $E_F = 0$ and thus

$$\langle R_i\, s|\hat{G}|R_j\, s'\rangle = \langle R_i\, s|\hat{\mathcal{G}}|R_j\, s'\rangle \quad . \quad (6.55)$$

For N impurities, Eq.(6.54) becomes,

$$\begin{aligned}\langle R_i\, s|\hat{G}|R_j\, s'\rangle &= \langle R_i\, s|\hat{\mathcal{G}}|R_j\, s'\rangle + \sum_{n,n'=1}^{N}\langle R_i\, s|\hat{\mathcal{G}}|a_n\rangle[VT]_{nn'}\langle a_{n'}|\hat{\mathcal{G}}|R_j\, s'\rangle \quad (6.56) \\ &= \langle R_\ell\, s|\hat{\mathcal{G}}|R_j\, s'\rangle \quad . \quad (6.57)\end{aligned}$$

In this context $|a_n\rangle = \sum_{i=1}^{6}|(a_n)_i\rangle$, where the first subscript refers to the n^{th} hexagon, the second to the individual carbon atoms in the hexagon. Since $\langle R_\ell|\hat{\mathcal{G}}|a_n\rangle = 0$, the transport is ballistic. Breaking spin degeneracy at the impurity sites will have

no effect since the unperturbed propagators have no spin dependence. As a result of Eq.(6.57) the MR will be zero when the impurities are placed in the centre position.

The next point to consider is the behaviour in the vicinity of $E_F = 0$. Once again, using the derivation in section 5.3.1 the Green Function close to this energy can be written as

$$\langle R_i, s|\hat{\mathcal{G}}|a\rangle = (E/t_0)\left(\langle R_i, s|\hat{\mathcal{G}}|a_1\rangle + \langle R_i, s|\hat{\mathcal{G}}|a_4\rangle\right) \quad . \tag{6.58}$$

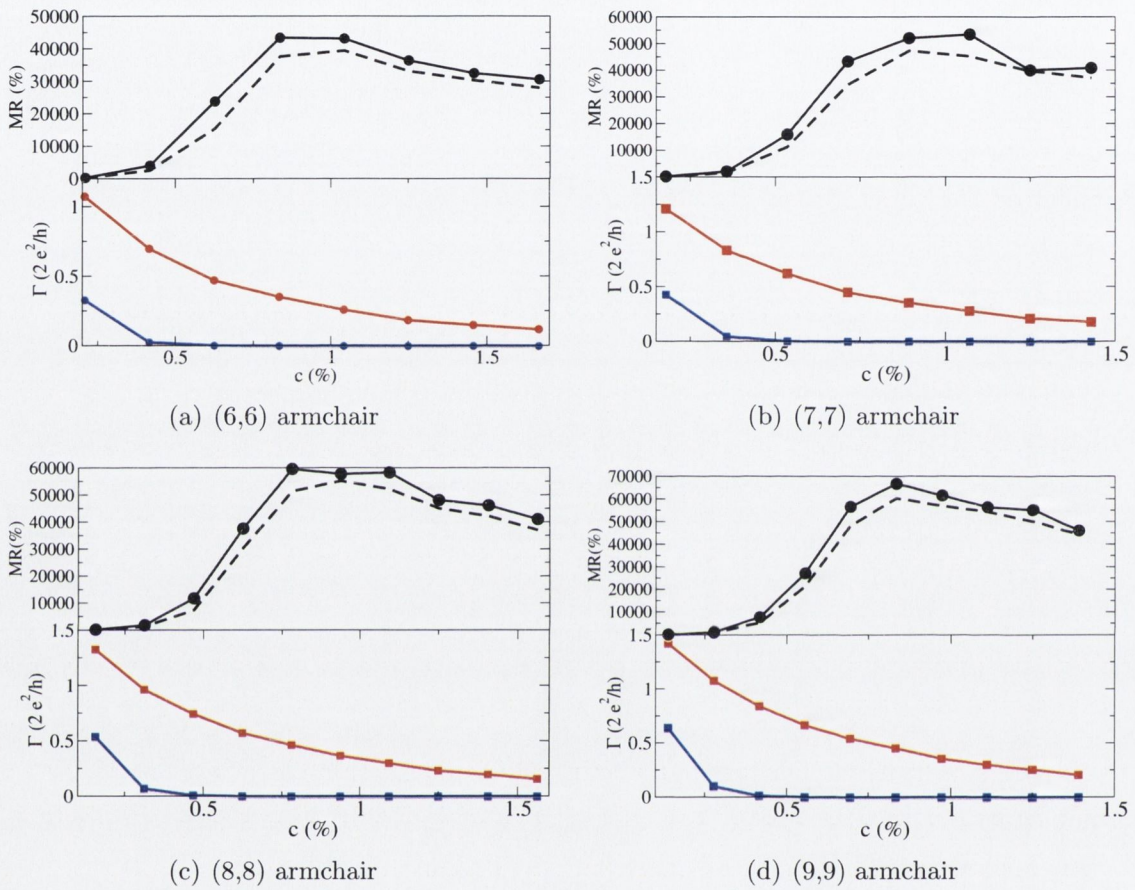
Thus, inserting this expression in Eq.(6.54) should result in the conductance changing from the ballistic limit as the Fermi-Energy changes. However, this has a weak effect on the conductance except at certain critical points. Considering only a single scattering channel, with the impurity on-site equal to V_x, the T-matrix in Eq.(6.54) can be written as $t^2/(E + i\eta - V_x - t^2\mathcal{G}_{aa})$. The on-site propagator $\mathcal{G}_{aa}$ cannot be treated within the two sub-band simplification, since the contribution from the attenuated modes will not be negligible when the separation is zero. In fact it can be shown that, $\mathcal{G}_{aa}(E) = iE^2g(E) + h(E)$, where $g(E)$ and $h(E)$ are real valued functions. This enables us to separate T into a real part, and an imaginary part which changes quadratically with E. Setting $f(E) = (E - V_x)/t^2 - h(E)$, we can write $T = 1/(f(E) - iE^2g(E))$, or

$$T = \frac{f(E) + iE^2g(E)}{f^2(E) + (E^2g(E))^2} \quad . \tag{6.59}$$

The conductance thus deviates from the ballistic value as $(\delta E)^2$. If Re$[T]$ does not contribute to the conductance – as is the case of armchair nanotubes with low concentrations of impurities – then the deviation is even slower: $(\delta E)^4$. The only place that this dependence breaks down is when $f(E)$ approaches zero. In this case, since $(\delta E)^2g(E)$ is small, the imaginary part of T displays Lorentzian like behaviour. To properly identify these features the conductance must be plotted on an extremely fine energy mesh. This is easily accomplished for the case of $H > 0$ and is shown as the dashed green line in figure 6.10. This detailed plot of the Transmission Function reveals a number of narrow dips in conductance at discrete energy levels. As the concentration increases, the frequency of these peaks should increase. However, in the immediate vicinity of $E_F = 0$, the same symmetry condition which resulted in short range coupling is seen to mask the impurities from the nanotube's conduction electrons. This confirms the intuitive prediction that a weak coupling should correspond to weak scattering. This is the origin of the zero value of the observed magnetoresistance. Within the context of our model this is a robust feature, unaffected by the particular parameterisation used to describe the transition metal atoms. Such a feature could have ramifications for the use of adsorbed impurities

in spintronic devices since the centre position is the most energetically favourable location for most, if not all, transition metal atoms. With this in mind, in the final section, we turn our attention to substitutional impurities.

6.6.2 Substitutional Impurities



(a) (6,6) armchair

(b) (7,7) armchair

(c) (8,8) armchair

(d) (9,9) armchair

Figure 6.11: Conductance and MR vs concentration, c, for armchair nanotubes doped with substitutional Mn impurities. $E_F = 0$. The nanotube is 200 rings long. For each case the upper panel shows MR (solid line/circles) and MR* (hatched line) and the lower panel shows the average conductance with $H > 0$ (red line) and $H = 0$ (blue line).

For substitutional impurities we consider a second atomic species: Ni. It has been recently shown that appreciable quantities of Ni can be substituted for carbon atoms in nanotubes[88]. According to the parameterisation in table 6.1, Ni has a relatively small exchange splitting, with both bands lying below the Fermi-Energy. Mn is strongly polarised with levels lying above and below the Fermi-Energy. Including a second species of impurities will allow for an exploration of the effect of changing parameters on the transport properties.

Figure 6.11 shows a plot of the conductance and MR vs concentration for armchair nanotubes of increasing diameter doped with substitutional Mn impurities. The effect of the doping on the MR is seen to be very strong: $\Gamma(H > 0)$ is still

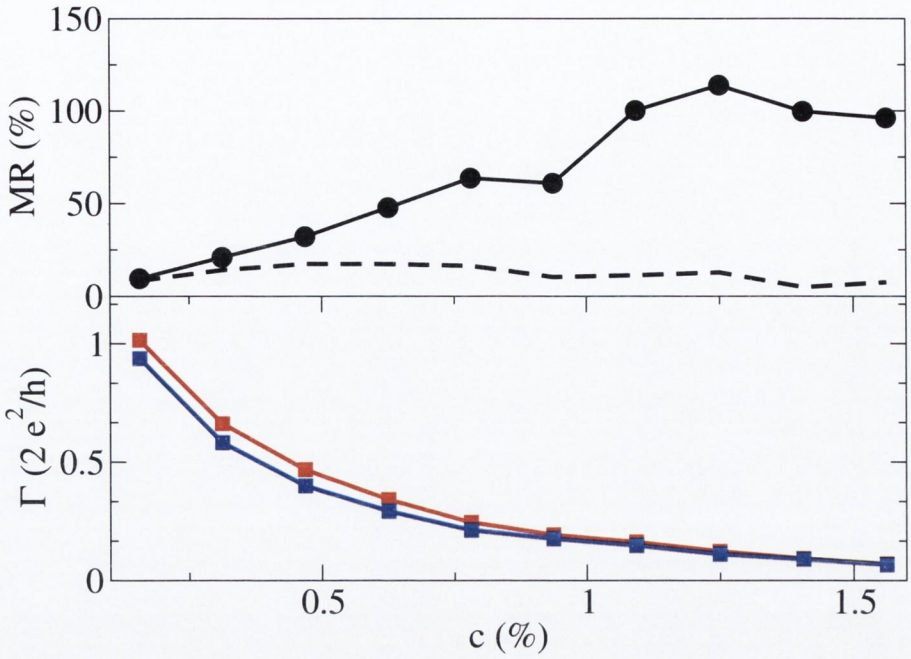


Figure 6.12: Conductance and MR as a function of concentration on a (7,7) armchair nanotube substitutionally doped with Ni impurities. The nanotube is 200 rings long. In the lower panel, the red line shows the conductance in an applied field, the blue line is the conductance with zero field. The upper panel shows MR (solid line/circles) and MR* (hatched line).

non-vanishing above concentrations of 1%. However $\Gamma(H = 0)$ is rapidly quenched and this leads to the enormous MR values seen. Changing the diameter of the nanotube seems to have no effect on the qualitative features of the magnetoresistance although the maximum value is seen to increase with increasing diameter. This increase should be bounded by the maximum value for the MR in the case of a graphene sheet, which is the limiting case of a large diameter nanotube. For a fixed number of impurities the conductance also increases with increasing diameter. This makes intuitive sense, since by increasing the diameter we also increase the number of paths along which the electrons can travel through the tube. However, unlike most conductors, the number of transmitting channels is fixed at 2 irrespective of the diameter of the nanotube. This will presumably reduce the effect of increasing the diameter. In figure 6.12, the Mn impurities have been replaced by Ni. Once again, the conductance and MR is plotted as a function of concentration. The magnitude of the resultant MR is radically different: for Ni the observed MR is much smaller. Additionally the average magnetoresistance(MR) and the magnetoresistance calculated from the average conductance(MR*) differ quite substantially in this case. This normally indicates that the fluctuations are large with respect to the mean value of conductance and is expected to occur as the value of $\Gamma(H = 0)$ approaches zero. For Ni, above 0.5% the conductance in both channels is so small the magnetoresistance is no longer usefully defined.

The difference in the magnitude of the MR between Mn and Ni doping is due

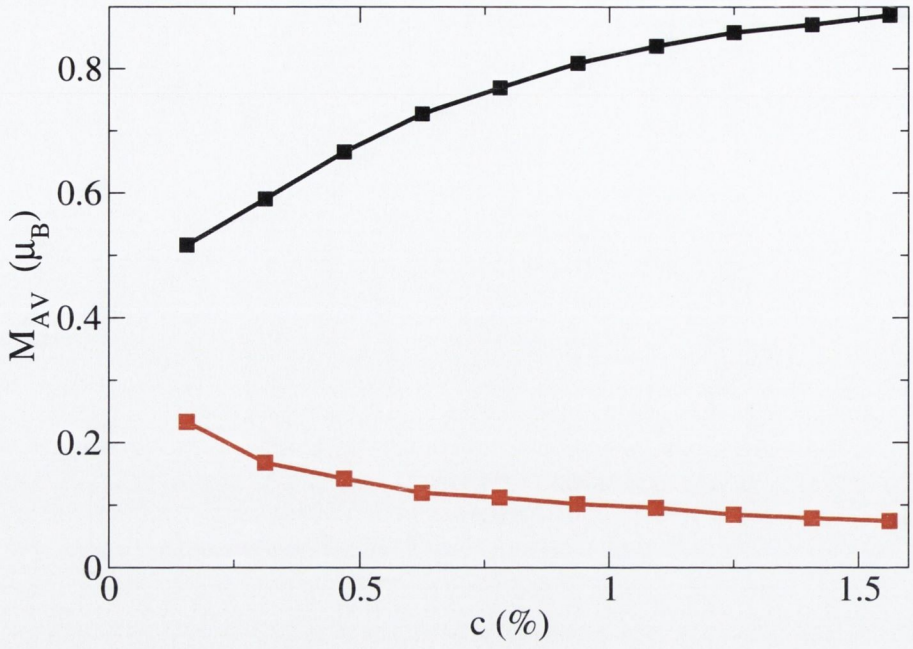


Figure 6.13: Ensemble averaged magnetisation vs concentration for a (7,7) armchair nanotube doped with substitutional Ni (black line) and Mn (red line) impurities

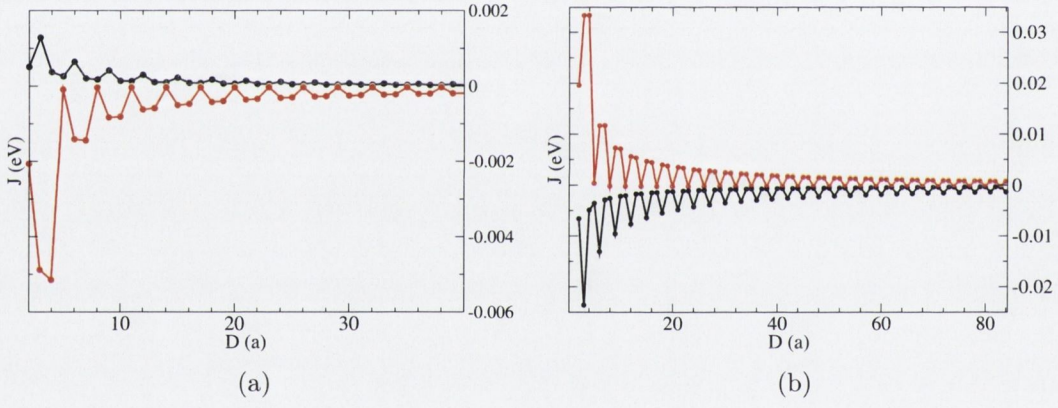


Figure 6.14: Coupling vs longitudinal separation for substitutional (a) Ni and (b) Mn impurities. In both cases the black line is the coupling when both impurities are placed on the same sublattice of graphene and the red line is for the case when they are placed on different sublattices

to the behaviour of the conductance with $H = 0$. For Mn this channel was rapidly suppressed, whereas for Ni the application of a magnetic field has little effect on the conductance, particularly as concentration increases. To see why this is the case, the average magnetisation as a function of concentration is plotted in figure 6.13 for both Ni and Mn. The difference is clear: with Ni impurities the system adopts an increasingly ferromagnetic configuration. For Mn there is little net magnetisation in the system.

To understand why the average magnetisation is so different for the two cases, we must look at the pairwise couplings, J_{ij}, which determine the ground state energy. These are obtained from the total energy calculations of chapter 4. For nanotubes, at $E_F = 0$, the sign of the coupling does not oscillate as a function of impurity

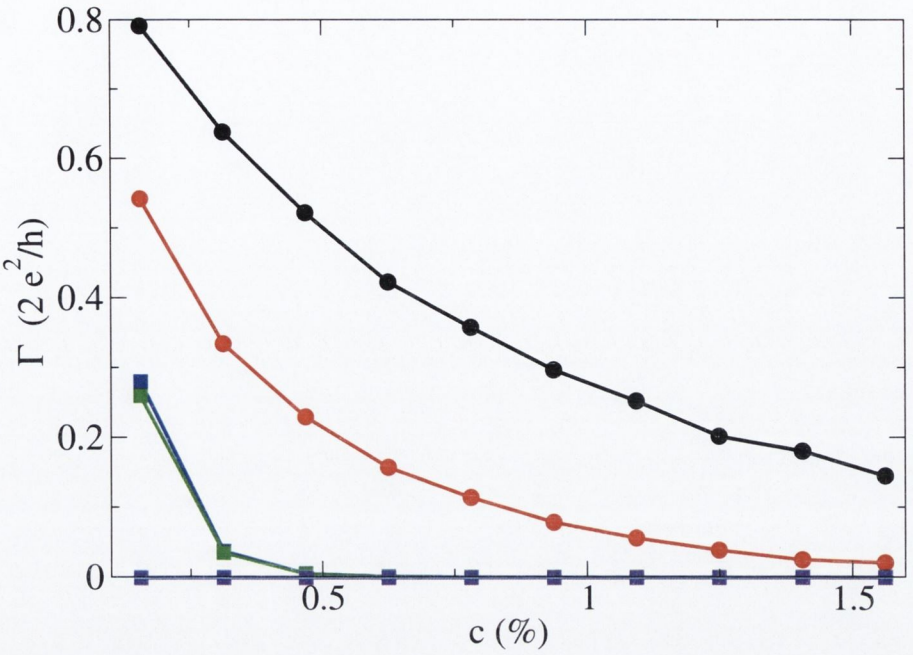


Figure 6.15: Channel decomposed conductance for a (7,7) armchair with substitutionally doped Mn impurities: With $H > 0$, the down-down channel is given by the black line and the up-up channel by the red. The same two channels for $H = 0$ are given respectively by the green and blue lines. The up-down channel (violet line) carries no current.

separation D and consequently the couplings are either all ferromagnetic ($J_{ij} < 0$) or anti-ferromagnetic ($J_{ij} > 0$). However, couplings of opposite sign can be introduced by placing impurities on different sublattices(c.f. figure 4.6). In general, since the impurities are not restricted to a single sublattice, this ensures that both ferromagnetic and anti-ferromagnetic couplings are present. However in the case of Ni, figure 6.14(a) shows that the amplitude of the ferromagnetic couplings are stronger than the anti-ferromagnetic ones. This is especially true at low separations. As the concentration is increased, these strong ferromagnetic interactions appear to become dominant and determine the magnetisation of the entire system. The situation for Mn is shown in figure 6.14(b). In this case the strength of the ferromagnetic and anti-ferromagnetic interactions are quite similar and a competition effect ensues which leads to much smaller overall magnetisation of the system.

But this is not the complete picture. In fact, for Mn, examination of the spin decomposed conductance shown in figure 6.15 indicates that not only is the average magnetisation close to zero, but that the moments are actually collinear. This is surprising since we would assume that the presence of ferro- and anti-ferromagnetic bonds of similar strength should lead to quite a randomised ground state. To see why this collinear, Ising type coupling is present it is necessary to examine the pairwise couplings for Mn impurities shown in figure 6.14(b). Impurities on the same sublattice have a preferred ferromagnetic orientation while those on opposite sublattices prefer an anti-parallel alignment. The situation is opposite in the case

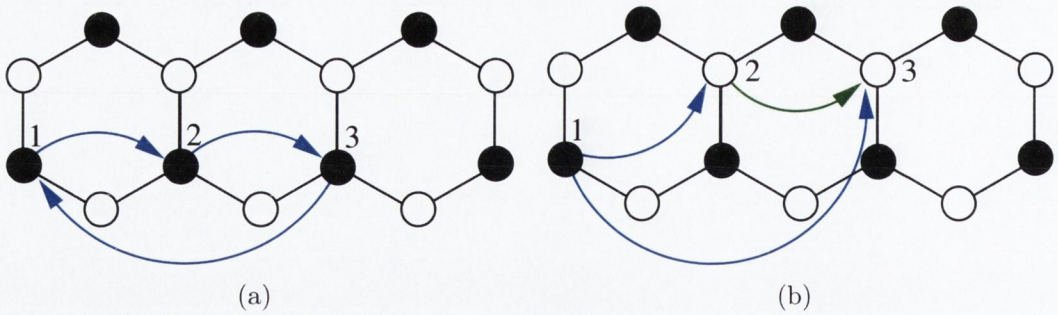


Figure 6.16: An example of frustration effects: (a) 3 magnetic moments are placed on the same sublattice and each has a preferential AFM coupling (blue) (b) the preferential AFM coupling is between moments placed on different sublattices. As a result no frustration need occur since the intra-sublattice moments now prefer to adopt a FM alignment (green).

of Ni (Fig. 6.14(a)). Consider three Ni impurities placed on the same sublattice of graphene. This is schematically represented in figure 6.16(a) . The first moment wants to align anti-ferromagnetically with the second and third. However the second and third moments also wish to align anti-ferromagnetically with respect to each other. These requirements cannot be mutually satisfied. In this case the magnetic alignment is said to be frustrated. Indeed the requirement for the appearance of magnetic frustration is the presence of two competing anti-ferromagnetic bonds. By contrast, for Mn the anti-ferromagnetic interaction is between impurities on different sublattices. This situation is shown in figure 6.16(b). Assume the first impurity is placed on the sublattice represented by the black sites and the second and third are on the sublattice represented by the white. The first impurity is strongly anti-ferromagnetically coupled to both the second and the third. However, the second and third impurities are located on the same sublattice and are ferromagnetically coupled. Therefore the preferred alignment of each of the individual bonds can be satisfied. The coupling cannot become frustrated because the production of two competing anti-ferromagnetic bonds necessarily involves the introduction of a ferromagnetic bond which facilitates the preferred alignment. This is a novel effect resulting from the properties of the IEC and the bi-partite nature of the graphene lattice. The absence of any spin-flip scattering in figure 6.15 confirms this interpretation.

Indeed, the robustness of such a feature has been borne out by *ab-initio* calculations for the coupling between substitutional impurities[89]. These examined the effect of switching the sublattice on which the second impurity was located, and are shown in table 6.2. The results are in perfect qualitative agreement with our model calculations. For Ni, atoms on the same sublattice are seen to be preferentially anti-ferromagnetically aligned, while for Mn the intra-sublattice coupling is ferromagnetic. Interestingly, for both cases switching sublattice changes the sign of the coupling, as predicted in section 4.5.1. Such a confirmation is important because

Impurity	$J_{\bullet\bullet}$(eV)	$J_{\bullet\circ}$(eV)
Ni	0.016	-0.023
Mn	-0.502	0.073

Table 6.2: *Ab-initio* results for pairs of Ni and Mn impurities located on different graphene sublattices. In both cases, the switching is seen to induce a change in the sign of the coupling.

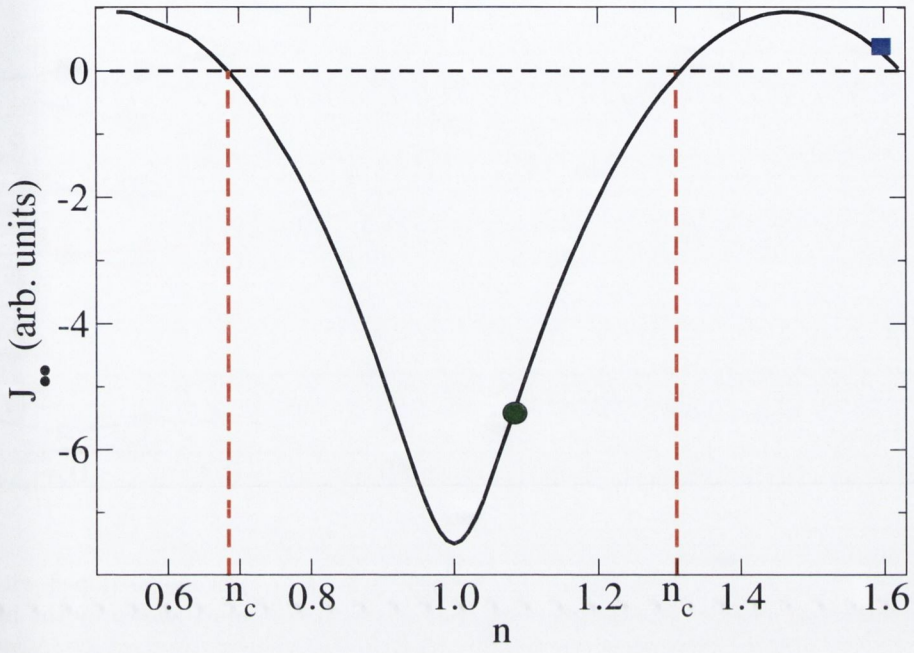


Figure 6.17: Coupling, $J_{\bullet\bullet}$, as a function of occupation, n. It is possible to identify regions, denoted by n_c, where the ground state will not be frustrated. The positions of Mn and Ni are indicated by the green ellipse and blue square respectively.

it indicates that it should be possible to identify a point at which the coupling will change sign as a function of the parameters used to describe the impurity. From figure 4.17 we have already seen that the sign of the coupling does not change as a function V_{x}. Therefore it must change as a function of the band centre, which is in turn determined by the occupation. By self-consistently calculating the coupling as a function of the occupation, n, we can identify a critical occupation, n_c, beyond which frustration effects will manifest themselves. This is seen in figure 6.17 which was plotted for $t = 0.63\,\mathrm{eV}$. The occupation for Mn and Ni are represented by the green ellipse and blue square respectively. The crossover is seen to occur at $n_c = 0.69$ and $n_c = 1.3$. Within this region the magnetic ground state will not be frustrated.

Away from $E_F = 0$ the true oscillatory character of the coupling returns and frustration effects should begin to emerge. These are seen in figure 6.18 which shows the spin decomposed conductance as a function of the Fermi-Energy in the case of Mn impurities. Significant spin-flip scattering is seen to develop as this energy moves away from zero. The total conductance and MR are shown in figure 6.19. With the spins in a collinear alignment and in the absence of an applied field, electrons propagating through the nanotube are subject to enormous back-

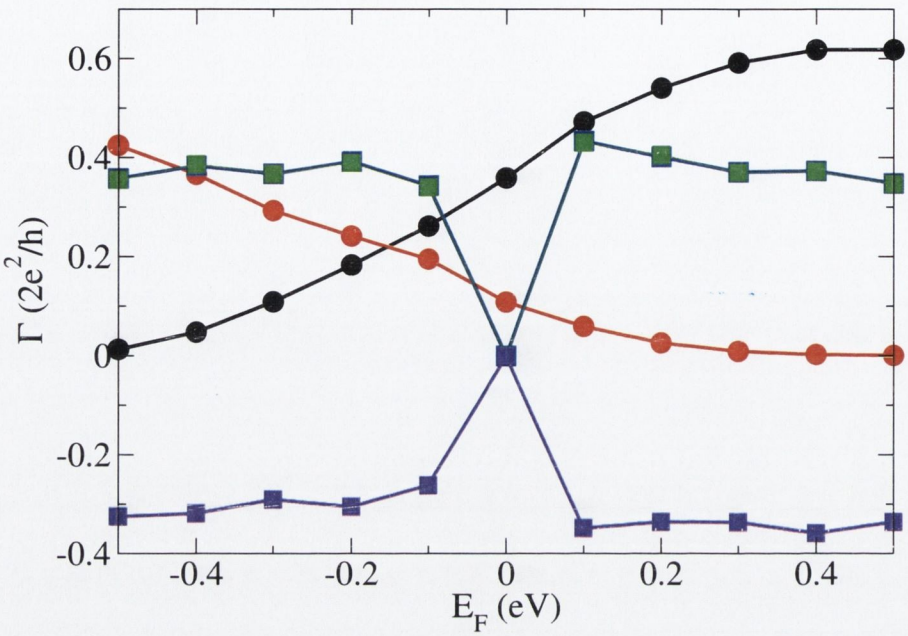


Figure 6.18: Band decomposed conductance vs E_F for a (7,7) armchair doped with 0.8% substitutional Mn impurities. The conductance channels with $H > 0$ are shown by the black and red lines (circles). The three bands corresponding to $H = 0$ are shown by the blue, green and violet lines (squares).

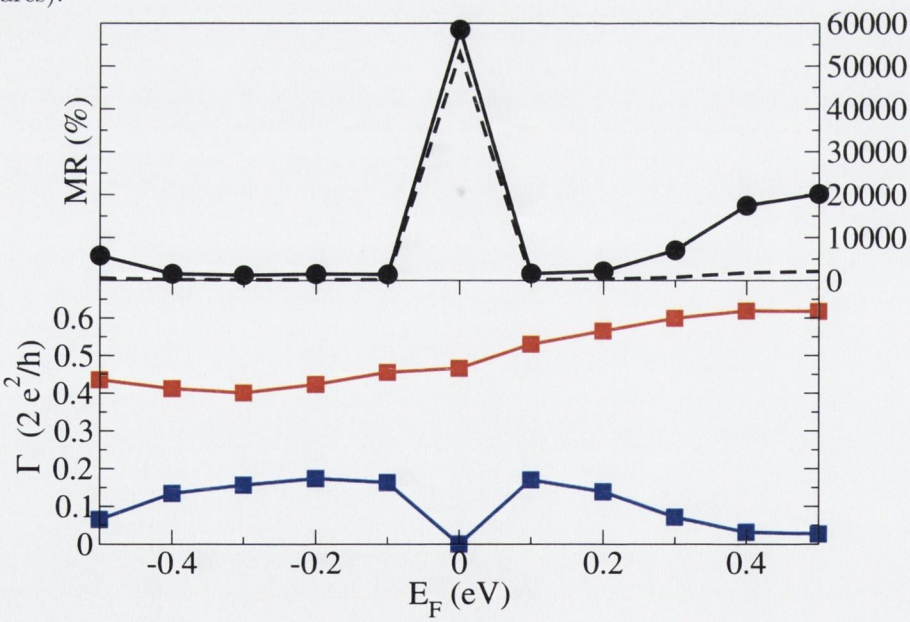


Figure 6.19: Conductance and MR vs E_F for a (7,7) for the case shown in figure 6.18. The MR (black line) is given in the upper panel. The conductance with $H > 0$ (red line) and $H = 0$ (blue line) are shown in the lower panel. The hatched line is the value of MR*, calculated using the ensemble average conductance.

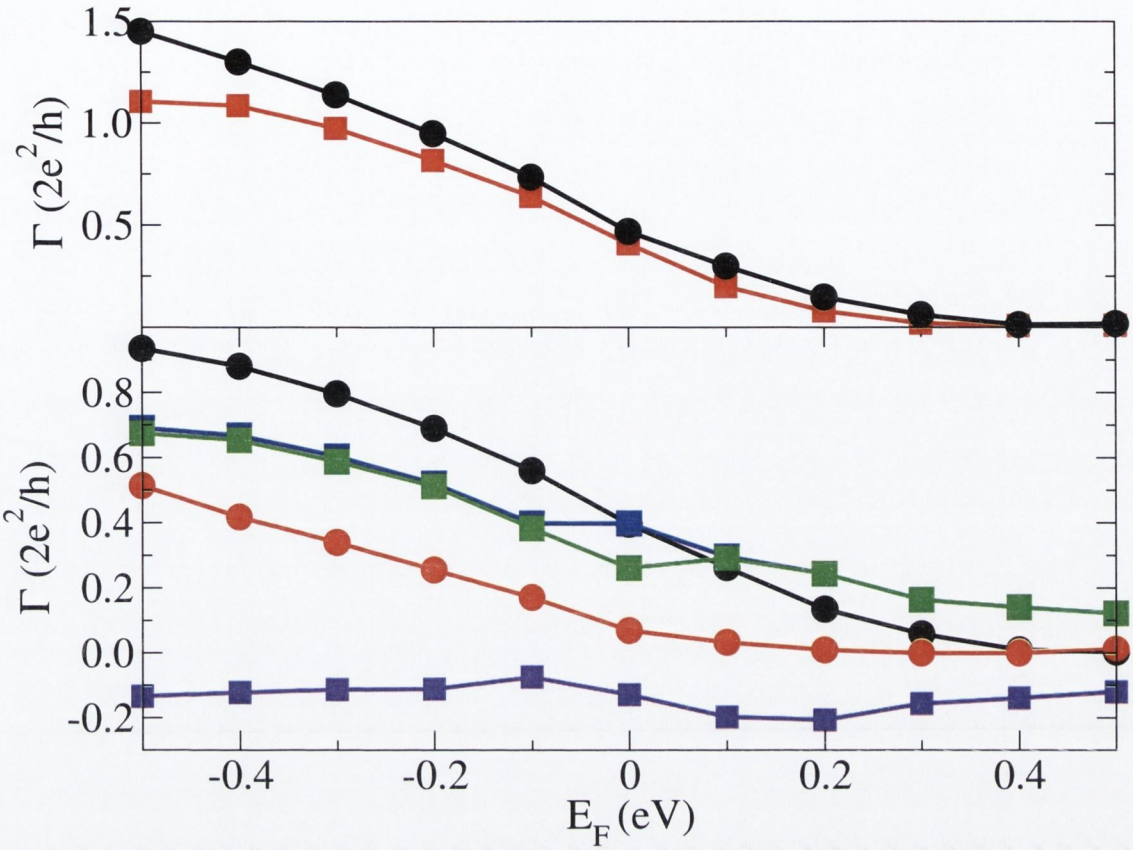


Figure 6.20: Conductance as a function of E_F on a (7,7) armchair nanotube substitutionally doped with 0.5% Ni impurities. The nanotube is 199 rings long. The lower panel shows the channel decomposed conductance: black and red lines (circles) for $H > 0$ and green, blue and violet (squares) for $H = 0$. The upper panel shows the total conductance for $H > 0$ (black) and $H = 0$ (red).

scattering and the conductance rapidly drops to zero. In response to a change in the Fermi-Energy, the moments adopt a non-collinear alignment in which the overall magnetisation remains low. This has the effect of enhancing the conductance in the up-up and down-down channels. Even with this enhancement the MR remains very large: the minimum value in figure 6.19 is 1500%. As was the case with impurities adsorbed atop, in the presence of an applied field the up- and down-spin channels display broadly anti-symmetric behaviour as a function of the gate voltage which leads to a reasonably constant value for $\Gamma(H > 0)$.

In figure 6.12, we saw that the small observed value for the MR in the case of Ni resulted from the large degree to which the moments were aligned, even in the absence of an applied field. This will obviously be sufficient to result in a small MR. An interesting question is whether the MR will remain small when the system demagnetises. This can be achieved by changing the Fermi-Energy and the results are shown in figure 6.20. The upper panel shows the total conductance and the lower panel shows the spin decomposed conductance. The concentration of Ni atoms is 0.5%. The presence of substantial spin alignment at $E_F = 0$ is evident. With

$E_F < 0$ the net magnetic moment in the ground state is much smaller. This leads to an increase in $\langle\Gamma(H)\rangle - \langle\Gamma(0)\rangle$, but the overall magnitude of the average MR will not be significantly affected since the normalisation factor also increases. With $E_F > 0$ the conductance in both cases becomes very small and again the magnetoresistance ceases to be usefully defined. This results from the fact that both the up- and down-spin bands lie below the Fermi-Energy. In contrast with Mn, the levels lie on opposite sides of the band centre which leads to the up- and down-spin bands behaving in a roughly anti-symmetric fashion when $H > 0$. With Ni, this does not occur and both bands display a broadly similar behaviour. In any case the results indicate that it is the magnitude of the exchange splitting, more so than the magnetisation of the ground state, which is primarily responsible for the size of the MR.

6.7 Chapter Summary and Conclusions

The results of the previous section have shown the richness of the magnetoresistance features displayed in carbon nanotubes. It has been seen that nanotubes can display enormous magnetoresistance although the observed value is sensitive to the particular atomic species doping the tube, the location of the dopants within the host and the properties of the magnetic ground state.

For the atop position a metallic nanotube was seen to display a sizeable magnetoresistance, with a conductance which is very robust to the addition of large quantities of impurities ($> 10\%$). The sign of the magnetoresistance was seen to be sensitive to a gate voltage applied to the tube. Near to, and above, $E_F = 0$ the transmission became enhanced when no magnetic field was applied. When the Fermi-Energy became negative, the MR became positive. Changing the ground state magnetisation as a function of E_F was seen to have some effect on both the size of the MR and the energy at which the sign change occurs. However it was also seen that the sign change occurred even in the absence of any changes in the ground state orientation of the moments.

For adsorbed atoms placed at the centre of the hexagon, the MR at $E_F = 0$ was seen to be strictly zero. In fact the transport both with and without an applied field was ballistic. The effect was seen to arise from same interference term which gave rise to the weak coupling experienced by impurities placed in this location. This makes some intuitive sense: the coupling arises from scatterings back and forth between the impurities. In the absence of this back-scattering the impurities are weakly coupled and the conductance is ballistic. Applying a gate voltage was seen to introduce some deviations from ballistic conductance. Close to $E_F = 0$, these occur as narrow resonances which were shown to correspond to the locations of additional

Van-Hove singularities in the density of states, introduced by the impurities. From the results of chapter 5 this absence of scattering is a robust feature within our model and should be present, independently of the impurity species or the chirality of the tube. Since the centre site is almost always favoured over the atop site, such an effect could have implications for the feasibility of any spintronic device based on adsorbed doping of nanotubes.

For substitutional impurities two distinct atomic species (Mn, Ni) were considered. This allowed for some examination of the effect that changing the tube parameters had on the properties of the conductance and the MR. It was seen that these were ultimately influenced by two factors: the overall magnetisation of the system and the actual strength of the exchange splitting. For Ni, at $E_F = 0$ the MR was small. This was seen to result from the fact that, even in the absence of an applied field, the impurities were mostly ferromagnetically aligned. While a substantial ground state magnetisation would certainly lead to small MR, the effect of the size of the exchange splitting is still important. For Ni this splitting was relatively small and led to modest MR values being observed, even when the ground state demagnetised.

For Mn doping, a novel property of the ground state magnetisation was uncovered: At $E_F = 0$ the coupling of the impurities was Ising like with a small overall magnetisation. This type of coupling prohibits spin-flip scattering. This confinement manifested itself in the form of enhanced back-scattering which greatly suppressed the conductance in the case of $H = 0$. The *ab-initio* results presented for the case of inter- and intra-sublattice coupling confirm the robustness of such a feature. Applying a gate voltage to the tube removed the restriction on spin-flip scattering and the MR regained a finite, although still sizeable value.

In the limit of high concentration doping, or when the impurities form large clusters[90] the effect of direct interaction between magnetic moments on adjacent sites may become important. In such cases, a competition would arise between the direct and indirect contributions to the pairwise couplings[61]. When the two contributions are of similar magnitude and acting in opposition, the impurity pairs may align at some intermediate angle between ferromagnetic and anti-ferromagnetic coupling. From a computational standpoint this would complicate matters somewhat since evaluation of the ground state of the disordered system in the presence of such effects would require detailed knowledge of the angular dependence of the pairwise couplings; it would no longer simply be a matter of rotating unit vectors in the Heisenberg Hamiltonian. From a qualitative standpoint, the effect of direct interactions would be to break the collinearity of the overall ground state. However, this should not be particularly detrimental to the spin-valve properties of such systems, since the collinearity is not necessary for observing workable values of the MR.

Certainly the extreme enhancement of the values arising from the lack of spin-flip scattering will vanish, but even in the absence of this enhancement, the MR has been seen to remain extremely large ($\sim$ 1000%)

Ultimately it would seem that the magnitude of the MR is determined by the size of the exchange splitting, although it can be influenced by the character of the ground state magnetisation of the system. The fact that substitutionally doped nanotubes are capable of displaying such large values of magnetoresistance – especially in light of the predicted ballistic properties of the adsorbed impurity systems – points to a probable route for applications.

Chapter 7

Conclusions

This thesis has presented a study of theoretical aspects of carbon nanotubes interacting with transition metal atoms. The emphasis has been placed on (1) the possibility of long range magnetic order in nanotubes and (2) the conductance and magnetoresistance through doped nanotubes. These are the two complimentary pillars which normally underpin the investigation of any potential spintronic device. Generally speaking, the oscillatory nature of coupling creates a spin dependent current which can be switched on or off by a comparatively weak magnetic field. If the two currents differ sizeably then the system may constitute a useful device. Carbon nanotubes possess many characteristics which make them desirable components in future electronic devices; among these are mechanical stability, high thermal conductivity, low dimensionality and a Fermi-velocity approximately two orders of magnitude greater than standard semi-conductors.

Amongst the myriad of possible ways in which nanotubes might be incorporated into spintronic devices, the interaction of the tubes with itinerant particles in their immediate vicinity is of great importance. This forms part of a larger effort to identify the effect of structural imperfections and disorder on the superlative physical properties of nanotubes. From another point of view, the composite nanotube/catalyst particle system might constitute a useful spintronic device in itself. This has been the viewpoint adopted throughout this work. What follows is a review of the thesis. The intention is to present a fully integrated summary of the work undertaken and the main conclusions. Finally, suggestions for possible extension to the work are considered.

Chapter 1 was a general introduction to carbon nanotubes and to the phenomena of IEC and GMR. The properties of nanotubes were discussed with particular emphasis on electronic properties. Following this there was a review of recent attempts to develop electronic devices which use nanotubes as components. While these have been successful in demonstrating that they can be incorporated in working devices, serious practical difficulties exist in producing, characterising and separating carbon

nanotubes. Until these can be resolved, the large scale development of nanotube based technologies cannot occur. It was finally argued that in light of these difficulties, theoretical methods could play in important role in guiding experiments.

Chapter 2 presented a theoretical method for treating disordered nanostructures. This was broken into three sections: Definition of the Green Function followed by a derivation of Dyson's Equation and the Lloyd Formula. The Green Function is a very general concept which can be used to determine many properties of condensed matter systems. Dyson's Equation and the Lloyd Formula are derived from the Green Function and provide techniques for treating disorder. The recursive method for generating Green Functions was introduced in some detail. The generality of these approaches was emphasised at all times. In later chapters the host was specified as a carbon nanotube and the disorder arose from individual transition metal atoms. However, the results of this chapter could just as easily treat any number of disordered nanostructures.

Chapter 3 presented an analytic method for determining the lattice Green Function propagators for achiral nanotubes. These lattice propagators form the building blocks for any calculations involving a disordered nanotube. As such, the existence of a closed form expression is extremely useful. It was also shown that these expressions can be extended to semi-infinite tubes. It is then possible to write down the self energy terms used to represent nanotube leads in the transport calculations of chapter 6.

Chapter 4 introduced IEC between localised magnetic moments on nanotubes. The chapter opened with an introduction to the Quantum Well Picture which provides the theoretical description of the coupling in terms of an indirect interaction mediated by the host's conduction electrons. The interaction of a pair of magnetic impurities mediated by a nanotube was treated in this picture. Surprisingly the predicted oscillation of the coupling as a function of the separation of the impurities was absent. This was found not to be an intrinsic property, but rather the result of a commensurability effect between the real space lattice and the Fermi-Surface, which can mask the underlying oscillation in certain cases. Next, the rate of decay as a function of the separation of the impurities was examined. The observed long range $(1/D)$ coupling was in exact agreement with the predictions of the Quantum Well Theory for a quasi one-dimensional structure. Finally, the effect of changing both the atomic species and the location of the impurity was examined. As expected, the qualitative features of the coupling were shown to be broadly independent of the properties of the particular impurity. Even the effect of switching between substitutional and adsorbed impurities had no impact on the rate of decay or oscillation period. The primary effect of altering the strength of the exchange potential, which parameterises the particular impurity species, was in changing the amplitude of the

oscillation. In certain cases it could also give rise to more complicated oscillatory patterns. These are the hallmark of higher order interactions between the moments and represent deviations from RKKY behaviour.

Chapter 5 treated the interaction between two impurities embedded in the host in yet more detail. This was motivated by the apparent absence of long range order found by some *ab-initio* calculations. To reconcile this within the QWT, it was necessary to generalise the derivation of the asymptotic limit approximation. This established a formal condition for the observance of a more rapid decay. The formal condition could be related to a simple physical condition on the nanotube and led to an interesting conclusion: the position of the impurity within the host could dramatically effect the range of the coupling. This had been overlooked in the original treatment of IEC, mainly because this degree of freedom was not available in multilayers. Within the context of the results of the previous chapter it was certainly unexpected, since switching between substitutional and adsorbed impurities produced no noticeable qualitative difference in the properties of the coupling.

The effect of changing host location was then examined in some detail. It was found that when placed at the centre of a hexagon of carbon atoms, the impurities are weakly coupled. This ultimately stems from an interference effect which renders the impurities effectively invisible to the host. The interference is clearly seen with armchair tubes, since the propagating wavemodes are in the longitudinal direction only. However, in subsequent sections this interference was seen to be an intrinsic property of the underlying graphene lattice. It was also seen to be robust to relatively small movements of the impurity from the centre of the hexagon.

In Chapter 6 attention was turned towards the transport properties of carbon nanotubes. The previous chapter had raised the possibility that a major qualitative difference would be observed when the location of the dopants within the host nanotube was altered. Before this could be addressed, a method for calculating the conductance through a doped carbon nanotube had to be selected. The formalism originally developed to treat magnetic multilayers could be applied to nanotubes in a straightforward fashion. This utilised the Kubo Formula, which is equivalent to the Landauer-Buttiker formalism. The fact that it can be written entirely in terms of lattice Green Functions made it particularly easy to implement within the existing theoretical framework.

The simple case of two impurities gave way to highly disordered systems containing up to 500 impurities, which were randomly distributed about the tube's surface. This was an attempt to model the truly disordered systems that exist experimentally. The value of the conductance was highly sensitive to the particular configuration of the moments; which necessitated the performance of large ensemble averages. Treating such levels of disorder was only possible due to the lightweight

computational approach adopted. The only factor limiting the size of the systems considered was the need to determine the ground state magnetic orientation of the moments, which involved performing Monte Carlo simulations. This places some restriction on the number of impurities, but not on the actual size of the nanotube.

The magnetoresistance was examined for both adsorbed and substitutional impurities. Impurities adsorbed atop individual carbon atoms were capable of exhibiting a substantial MR, although locating impurities in hexagonal positions had no effect on the ballistic conductance of the host nanotube, and yielded a MR that was formally zero. This fact, although seemingly very unusual, could easily be reconciled with the observation that the coupling between atoms in this position is also extremely weak. It was argued that this could have important implications for the potential use of such systems in spintronic applications. For substitutional impurities the situation was very different. Atoms with a strong exchange splitting, like Mn, demonstrated enormous MR. The results suggest that substitutional doping is the most promising mechanism for potentially developing spin-valves within the context examined. Of course, designing such a system will probably be more difficult since it will involve the dislocation of carbon atoms.

Ultimately, nanotubes present a unique system in which many of the novel features associated with low dimensional systems can be studied. The richness and variety of these features, and their comparative simplicity make them a fascinating playground for the theoretician. At the other end of the spectrum, these novel features display a degree of sensitivity and tunability that will become increasingly important as true nano-scale devices, which rely critically on their quantum mechanical character, start to find application in real world technology.

7.1 Extensions and Future Work

Throughout much of the presentation of this work, the generality of the methods employed has been emphasised. In the end, a single band picture, with the nanotube described by its π electrons was adopted. This is known to be a very accurate description for nanotubes and the transparency of such a model presents a unique arena in which to explore some novel features of low dimensional systems. An obvious generalisation would be to adopt a more complicated band picture approach. This would not be expected to radically alter the results and could provide a confirmation of the validity of the approach.

Since the ultimate aim of this work is to present a theoretical study of the properties of nanotubes with a view to guiding possible experimental approaches it would be desirable to extend the work of Chapter 6. Focusing on Manganese, we have demonstrated that a significant MR can exist and have also predicted difficulties in

observing MR with adsorbed dopants. However the MR was also seen to be strongly dependent on the actual magnetic impurity chosen. Ideally we would like to attempt to characterise the behaviour of transition metal atoms in a more systematic way. This could serve both as a guide to experiment and a check on the applicability of our model. Such an undertaking would involve extensive parameterisation of the model with a comprehensive set of *ab-initio* results. It might also prove necessary to extend the parameterisation in the model; particularly for substitutional impurities where the interaction with the nanotube may need to be treated to further nearest neighbours. This would allow for a mapping, or at least sampling of the parameter space of possible impurities, and the effect of changing these parameters on the resultant MR. Another obvious extension would be to apply the foregoing considerations to zigzag tubes.

The above paragraphs set out what could be considered refinements to the existing calculations. The other approach lies in the way of extensions. Again such a general formalism can be easily adapted to treating a wide range of interactions; particularly in systems which can be well described by a localised basis of atomic orbitals. An example of an extension which could be implemented very quickly is modelling ferromagnetic electrodes placed at the ends of the tube, or nanoparticles inserted in the tubes. These would recover a connection with the standard description of IEC and GMR in terms of layered structures. Another extension would be to look at the effect of dynamic coupling, in which the moments precess in time. This is thought to display an even longer range than the static case. A third extension lies in the general area of magnetic interactions in graphene based systems. There has been a recent explosion in activity into both graphene itself and graphene nanoribbons. These nanoribbons differ from tubes in that they can display edge effects – like the ones seen for semi-infinite zigzag nanotubes in chapter 3 – which lead to whole host of interesting physical effects. Another fashionable topic, which can easily be examined, is defect induced magnetism in which the defects themselves have no intrinsic magnetic character. In graphene systems it has been suggested that magnetism can be induced by the removal or addition of carbon atoms. This would involve treating the system within a full Hartree-Fock picture, but the comparative simplicity of our approach might provide a transparent physical picture in which to examine the veracity of these claims.

Appendix A

Differentiation of the Log of an Operator

If $\hat{A}(E)$ is a linear operator which depends on a variable E, then the derivative of this operator with respect to E can be written as [91],

$$\frac{d}{dE}e^{\hat{A}} = e^{\hat{A}}\left\{\hat{A}' - \frac{1}{2!}[\hat{A},\hat{A}'] + \frac{1}{3!}[\hat{A},[\hat{A},\hat{A}']] - \cdots\right\} \tag{A.1}$$

Therefore,

$$\hat{A}\frac{d}{dE}\hat{A}^{-1} = \frac{d}{dE}\log\hat{A}^{-1} - \frac{1}{2!}[\log\hat{A}^{-1}, \frac{d}{dE}\log\hat{A}^{-1}] + \cdots \quad . \tag{A.2}$$

Using the properties of the trace, the commutators vanish, and

$$\mathrm{Tr}\left[\hat{A}\frac{d}{dE}\hat{A}^{-1}\right] = \mathrm{Tr}\left[\frac{d}{dE}\log\hat{A}^{-1}\right] \quad . \tag{A.3}$$

Appendix B

Proof that $\mathrm{Tr}(\log(A)) = \log(\det(A))$

Let A be a diagonalisable matrix. Then there exists a diagonal matrix D s.t. $A = PDP^{-1}$. It follows that

$$e^A = Pe^D P^{-1} \quad . \tag{B.1}$$

Since $\log e^A = A$ we have

$$\log(Pe^D P^{-1}) = PDP^{-1} \quad . \tag{B.2}$$

Now if D' is a diagonal matrix. Then $D = e^{D'}$ is also a diagonal matrix with entries $D_i = e^{D'_i}, \forall i = 1, 2..., n$. In this way we see that for each diagonal matrix D we can construct a diagonal matrix D' s.t. $D = e^{D'}$, whose elements are given by $D'_i = \log D_i$. Thus,

$$\begin{aligned} A &= PDP^{-1} && \text{(B.3)} \\ &= Pe^{D'}P^{-1} && \text{(B.4)} \\ \log A &= \log(Pe^{D'}P^{-1}) && \text{(B.5)} \end{aligned}$$

which from Eq.(B.2) gives,

$$\log A = PD'P^{-1} \quad . \tag{B.6}$$

Therefore

$$
\begin{aligned}
\mathrm{Tr}(\log A) &= \mathrm{Tr}(PD'P^{-1}) && \text{(B.7)}\\
&= \mathrm{Tr}(D') && \text{(B.8)}\\
&= \sum_i D'_i && \text{(B.9)}\\
&= \sum_i \log D_i && \text{(B.10)}\\
&= \log\left(\prod_i D_i\right) && \text{(B.11)}\\
&= \log(\det(D)) && \text{(B.12)}\\
&= \log(\det(P^{-1}AP)) && \text{(B.13)}\\
&= \log(\det(A)) && \text{(B.14)}
\end{aligned}
$$

Appendix C

Imaginary-Axis Integration

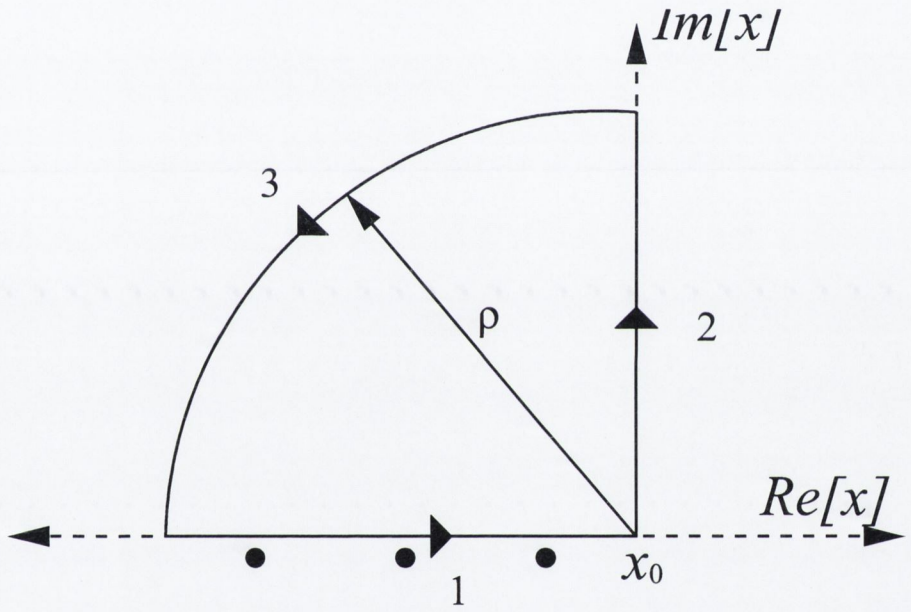


Figure C.1: Contour of integration. The integrand is assumed to vanish along the semi-circular contour, labelled as 3. The black dots mark the locations of poles of the function in the lower half plane.

Low dimensional systems exhibit singular behaviour for certain energies (the 1-D Van-Hove Singularities). The presence of a non-zero imaginary energy component, η, in the definition of the Green Function ensures these singularities don't lie on the real energy contour, but they can lie close enough to present considerable practical challenges when attempting numerical integrations over energy.

However, if the singularities are known to be confined to one half of the plane, the lower half say, the integral about any closed contour in the upper half plane is zero. Therefore, provided the integrand vanishes sufficiently rapidly in the upper half plane, then the integral along the real energy axis equals the negative of the integral evaluated along the imaginary axis. The contour is shown in figure C.1. Along the real axis the function still feels the presence of the nearby poles, however

along the imaginary axis the behaviour is very smooth.

Consider a function $f(z)$ of a complex variable z which has no singularities in the upper half plane. Then,

$$\begin{aligned} \oint dz f(z) &= \lim_{\rho\to\infty}\left[\int_{-\rho}^{x_0} dx f(x) + i\int_0^{\rho} dx f(x_0+ix) + i\rho\int_{\frac{\pi}{2}}^{\pi} d\theta e^{i\theta} f(x_0+\rho e^{i\theta})\right] \\ &= 0 \end{aligned} \tag{C.1}$$

Now if the third integral vanishes as $\rho \to \infty$ then

$$\int_{-\infty}^{x_0} dx f(x) = -i\int_0^{\infty} dx f(x_0+ix) \quad , \tag{C.2}$$

and

$$\mathrm{Im}\left[\int_{-\infty}^{0} dx f(x)\right] = -i\mathrm{Re}\left[\int_0^{\infty} dx f(x_0+ix)\right] \tag{C.3}$$

$$= -i\int_0^{\infty} dx\, \mathrm{Re}\left[f(x_0+ix)\right] \quad . \tag{C.4}$$

As a simple, yet illustrative example consider the case of

$$f(E) = \frac{1}{\sqrt{1-E^2}} \quad , \tag{C.5}$$

which represents the on-site Green Function for a linear chain. This function has singular points at $E = \pm 1$. However along the imaginary axis the function is

$$g(E) = f(iE) = \frac{1}{\sqrt{1+E^2}} \quad , \tag{C.6}$$

which is perfectly smooth and well defined for all energies.

When calculating the indirect coupling, $\Delta\Omega(D)$, between magnetic impurities, the contribution from the semi-circular contour is always zero. This is because the Green Function propagators occur in Eq.(4.18) as products. However, if the intention had been to calculate binding energies then some care would need be taken when dealing with this contour. For example, for the case of the change in energy resulting from introducing a single substitutional impurity, with on-site energy λ,

$$\Delta E = \int_{-\infty}^{0} dE\, \log(1-\mathcal{G}_{00}\lambda) \quad . \tag{C.7}$$

The propagator $\mathcal{G}_{00}$ behaves as $\mathcal{G}_{00} \sim \rho^{-1}e^{-i\theta}$ along the semi-circular contour for large values of ρ. Although this vanishes as $\rho \to \infty$, the integral along the contour

is not zero because,

$$i\int_{\frac{\pi}{2}}^{\pi} d\theta\, \rho e^{i\theta}(-\frac{\lambda e^{-i\theta}}{\rho}) = -i\lambda\frac{\pi}{2} \quad . \tag{C.8}$$

Therefore the contribution from the outer contour is seen not to be zero, unless the integrand vanishes faster than $1/\rho^2$. As mentioned above this is always satisfied for coupling calculations. In effect, since the coupling is equal to $E^{\uparrow\uparrow} - E^{\uparrow\downarrow}$, which is the energy difference between the two distinct magnetic alignments, the contribution from the outer term cancels.

Appendix D

Phase factor $\phi(E)$ for a Nanotube

For graphene $t(\mathbf{k}) = 1 + e^{ik_1} + e^{ik_2}$, which satisfies $E^2 = |t(k)|^2$, where E is the energy. $t(\mathbf{k})$ can be written as $|t(\mathbf{k})|e^{i\phi(\mathbf{k})}$, with,

$$\tan(\phi) = \frac{\sin(k_1) + \sin(k_2)}{1 + \cos(k_1) + \cos(k_2)} \quad . \tag{D.1}$$

In order to define a value for the phase $\phi(E)$ at $E = 0$ it is necessary to look at the behaviour as $E \to 0$. The Fermi-vector is given by $(k_1^F = 2\pi/3, k_2^F = 4\pi/3)$. Therefore expanding Eq.(D.1) about this point we have,

$$\tan(\phi) \approx \frac{\cos(k_1^F)\delta k_1 + \cos(k_2^F)\delta k_2}{-\sin(k_1^F)\delta k_1 - \sin(k_2^F)\delta k_2} \tag{D.2}$$

$$= -\frac{1}{2}\frac{\delta k_1 + \delta k_2}{-\frac{\sqrt{3}}{2}\delta k_1 + \frac{\sqrt{3}}{2}\delta k_2} \tag{D.3}$$

A general (n, m) nanotube is quantised according to $k_2 = ak_1 + b$ where $a = -n/m$ and $b = 2\pi r/m$. r is an integer. Therefore $\delta k_2 = a\delta k_1$ and,

$$\tan(\phi) = -\sqrt{\frac{1}{3}}\frac{(1+a)\delta k_1}{(1-a)\delta k_1} \overset{\delta k_1 \to 0}{=} -\sqrt{\frac{1}{3}}\frac{(1+a)}{(1-a)} \quad . \tag{D.4}$$

The quotient is well defined except when a=1 (i.e. a zigzag tube) in which case $\phi = \pi/2$.

Appendix E

Expression for the Generalised On-site Green function Propagator

In chapter 5 we showed that the generalised Green Function propagator $\Gamma^{(6)}_{ab}(E_F)$ vanishes when the Fermi-Energy, E_F, is equal to zero. This derivation was made subject to the assumption that the two hexagons did not have the same longitudinal separation. In cases where the longitudinal separation is zero, then there are two differences which need to be considered. Firstly the effect of the modulus in the analytic expressions for the lattice propagators become significant. Secondly, all the wave-modes contribute. In this section, we derive the generalised on-site propagator $\Gamma_{aa}(0)$ for an armchair tube.

Before beginning we make use of the very useful identity from chapter 3,

$$\sum_{p=\pm} \frac{1}{2\cos(k_m^p) + \cos(\frac{m\pi}{N})} = 0 \quad , \tag{E.1}$$

for all values of m. Now using Eq.(3.30) and summing over the intra-sublattice propagators on the first sublattice, and setting $t_0 = 1$,

$$\begin{aligned}
\sum_{j,j'=1}^{3} \mathcal{G}_{2j-1,2j'-1} &= \frac{i}{4N} \sum_{m=1}^{N} \sum_{p=\pm} E \frac{1 + 2e^{i\frac{m\pi}{N}} e^{ik_m^p} + 2e^{ik_m^p}(2\cos k_m^p + e^{-i\frac{m\pi}{N}})}{(\cos(\frac{m\pi}{N}) + 2\cos(k_m^p))\sin(k_m^p)} \\
&= \frac{i}{4N} \sum_{m=1}^{N} \sum_{p=\pm} E \frac{E^2 + 2i(\{2\cos(k_m^p) + \cos(\frac{m\pi}{N})\} + \cos(\frac{m\pi}{N}))\sin(k_m^p)}{(\cos(\frac{m\pi}{N}) + 2\cos(k_m^p))\sin(k_m^p)} \\
&= E^2 \mathcal{G}_{11} - E \quad .
\end{aligned} \tag{E.2}$$

Summing over the inter-sublattice propagators, from the first to second sublattices,

$$\begin{aligned}
\sum_{j,j'=1}^{3} \mathcal{G}_{2j-1,2j'} &= \frac{i}{4N} \sum_{m=1}^{N} \sum_{p=\pm} t_m^* \frac{e^{i\frac{m\pi}{N}}(2e^{ik_m^p} + e^{i\frac{m\pi}{N}}) + 2e^{ik_m^p}(2\cos(k_m^p) + e^{i\frac{m\pi}{N}})}{(\cos(\frac{m\pi}{N}) + 2\cos(k_m^p))\sin(k_m^p)} \\
&= \frac{i}{4N} \sum_{m=1}^{N} \sum_{p=\pm} t_m^* \frac{e^{2i\frac{m\pi}{N}}(1 + 2e^{-i\frac{m\pi}{N}}e^{ik_m^p}) + 2t_m^* e^{i\frac{m\pi}{N}}e^{-ik_m^p}}{(\cos(\frac{m\pi}{N}) + 2\cos(k_m^p))\sin(k_m^p)} \\
&= \frac{i}{4N} \sum_{m=1}^{N} \sum_{p=\pm} \frac{(t_m^*)^3 e^{2i\frac{m\pi}{N}} + 2ie^{i\frac{m\pi}{N}}((t_m^*)^2 + t_m^*)\sin(k_m^p)}{(\cos(\frac{m\pi}{N}) + 2\cos(k_m^p))\sin(k_m^p)} \qquad \text{(E.3)}
\end{aligned}$$

Eq.(E.3) will vanish at $E = 0$ since t_m^* vanishes. However it is does not seem possible to write the inter-sublattice propagator in terms of a single site propagator as in the case of the intra-sublattice propagator. The final two contributions to $\Gamma_{aa}^{(6)}$ can be evaluated in exactly the same way.

Bibliography

[1] S. Iijima. Helical microtubules of graphitic carbon. *Nature*, 354:56–58, 1991.

[2] S. Iijima and T. Ichihashi. Single shell carbon nanotubes of 1-nm diameter. *Nature*, 363:603–605, 1993.

[3] R. Saito, M. Fujita, G. Dresselhaus, and M. S Dresselhaus. Electronic structure of chiral graphene tubules. *Applied Physics Letters*, 60:2204–2206, 1992.

[4] S. J. Tans, M. H. Devoret, H. Dai, A. Thess, R. E. Smalley, L. J. Geerligs, and C. Dekker. Individual single-wall carbon nanotubes as quantum wires. *Nature*, 386:474–477, 1997.

[5] R. Saito, G. Dresselhaus, and M. S. Dresselhaus. *Physical Properties of Carbon Nanotubes*, pages 152–158. Imperial College Press, first edition, 1998.

[6] M. F. Yu, B. S. Files, S. Arepalli, and R. S. Ruoff. Tensile loading of ropes of single wall carbon nanotubes and their mechanical properties. *Physical Review Letters*, 84:5552 – 5555, 2000.

[7] S. Iijima, C. Brabec, A. Maiti, and J. Bernholc. Structural flexibility of carbon nanotubes. *The Journal of Chemical Physics*, 104:2089–2092, 1996.

[8] M. Fujii, X. Zhang, H. Xie, H. Ago, K. Takahashi, T. Ikuta, H. Abe, and T. Shimizu. Measuring the thermal conductivity of a single carbon nanotube. *Physical Review Letters*, 95:065502, 2005.

[9] P. Kim, L. Shi, A. Majumdar, and P. L. McEuen. Thermal transport measurements of individual multiwalled nanotubes. *Physical Review Letters*, 87:215502, 2001.

[10] S. M. Bachilo, M. S. Strano, C. Kittrell, R. H. Hauge, R. E. Smalley, and B. R. Weisman. Structure-assigned optical spectra of single-walled carbon nanotubes. *Science*, 298:2361–2366, 2002.

[11] J. A. Misewich, R. Martel, Ph. Avouris, J. C. Tsang, S. Heinze, and J. Tersoff. Electrically induced optical emission from a carbon nanotube FET. *Science*, 300:783–786, 2003.

[12] P. Grünberg, R. Schreiber, Y. Pang, M. B. Brodsky, and H. Sowers. Layered magnetic structures: Evidence for antiferromagnetic coupling of Fe layers across Cr interlayers. *Physical Review Letters*, 57:2442–2445, 1986.

[13] S. S. P. Parkin, N. More, and K. P. Roche. Ocsillations in exchange coupling and magnetoresistance in metallic superlattice structures: Co/Ru, Co/Cr, Fe/Cr. *Physical Review Letters*, 64:2304–2307, 1990.

[14] S. S. P. Parkin. Systematic variation of the strength and oscillation period of indirect magnetic exchange coupling through the 3d, 4d, and 5d transition metals. *Physical Review Letters*, 67:3598 – 3601, 1991.

[15] M. S. Ferreira. *Oscillatory interlayer exchange coupling in metallic magnetic multilayers.* PhD thesis, Department of Mathematics, Imperial College London, 1997.

[16] D. M. Edwards, J. Mathon, R. B. Muniz, and M. S. Phan. Oscillations of the exchange in magnetic multilayers as an analog of de Haas-van Alphen effect. *Physical Review Letters*, 67:493–496, 1991.

[17] D. M. Edwards, J. Mathon, R. B. Muniz, and M. S. Phan. Oscillations of the exchange coupling of ferromagnetic layers separated by a non–magnetic metallic layer. *Journal of Physics: Condensed Matter*, 3:4941–4958, 1991.

[18] M. A. Ruderman and C. Kittel. Indirect exchange coupling of nuclear magnetic moments by conduction electrons. *Physical Review*, 96:99–102, 1956.

[19] P. Bruno and C. Chappert. Oscillatory coupling between ferromagnetic layers separated by a nonmagnetic metal spacer. *Physical Review Letters*, 67:1602–1605, 1991.

[20] P. Bruno and C. Chappert. Ruderman-kittel theory of oscillatory interlayer exchange coupling. *Physical Review B*, 46:261–270, 1992.

[21] M. S. Ferreira, R. B. Muniz, J d'Albuquerque e Castro, and D. M. Edwards. The nature and validity of the RKKY limit of exchange coupling in magnetic trilayers. *Journal of Physics: Condensed Matter*, 6:L619–L623, 1994.

[22] M. S. Ferreira, J. d'Albuquerque e Castro, D. M. Edwards, and J. Mathon. Fundamental oscillation periods of the interlayer exchange coupling beyond the

RKKY approximation. *Journal of Physics: Condensed Matter*, 8:11259–11276, 1996.

[23] G. A. Prinz. Spin–Polarised transport. *Physics Today*, 48:58–63, April 1995.

[24] M. N. Baibich, J. M. Broto, A. Fert, F. Nguyen Van Dau, F. Petroff, P. Etienne, G. Creuzet, A. Friederich, and J. Chazelas. Giant magnetoresistance of (001)Fe/(001)Cr magnetic superlattices. *Physical Review Letters*, 61:2472 – 2475, 1988.

[25] R. Schad, C. D. Potter, P. Beliën, G. Verbanck, V. V. Moshchalkov, and Y. Bruynseraede. Giant magnetoresistance in Fe/Cr superlattices with very thin Fe layers. *Applied Physics Letters*, 64:3500–3503, 1994.

[26] P. A. Grünberg. Exchange anisotropy, interlayer exchange coupling and GMR in research and application. *Sensors and Actuators A: Physical*, 91:153–160, 2001.

[27] S. J. Tans, A. R. M. Verschueren, and C. Dekker. Room-temperature transistor based on a single carbon nanotube. *Nature*, 393:49–52, 1998.

[28] R. Martel, T. Schmidt, H. R. Shea, T. Hertel, and Ph. Avouris. Single- and multi-wall carbon nanotube field-effect transistors. *Applied Physics Letters*, 73:2447–2449, 1998.

[29] A. Javey, J. Guo, Q. Wang, M. Lundstrom, and H. Dai. Ballistic carbon nanotube field-effect transistors. *Nature*, 424:654–657, 2003.

[30] Ph. Avouris. Electronics with carbon nanotubes. *Physics World*, 20:41–45, March 2007.

[31] Ph. Avouris, Z. Chen, and V Perebeinos. Carbon-based electronics. *Nature Nanotechnology*, 2:605–615, 2007.

[32] K Tsukagoshi, B. W. Alphenaar, and H. Ago. Coherent transport of electron spin in a ferromagnetically contacted carbon nanotube. *Nature*, 401:572–574, 1999.

[33] L. E. Hueso, J. M. Pruneda, V. Ferrari, G. Burnell, J. P. Valdés–Herrera, B. D. Simons, P. B. Littlewood, E. Artacho, A. Fert, and N. D. Mathur. Transformation of spin information into large electrical signals using carbon nanotubes. *Nature*, 445:410–414, 2007.

[34] J. C. Charlier and S. Iijima. *Growth Mechanisms of Carbon Nanotubes*, volume 80 of *Topics in Applied Physics*, pages 55–81. 2001.

[35] S. B. Fagan, R. Mota, A. J. R. da Silva, and A. Fazzio. An ab initio study of manganese atoms and wires interacting with carbon nanotubes. *Journal of Physics: Condensed Matter*, 16:3647–3661, 2004.

[36] S. B. Fagan, R. Mota, A. J. R. da Silva, and A. Fazzio. *Ab-initio* study of an iron atom interacting with a single-wall carbon nanotube. *Physical Review B*, 67:205414, 2003.

[37] E. Durgun, S. Dag, V. M. K. Bagci, O. Gülseren, T. Yildirim, and S. Ciraci. Systematic study of adsorbtion of single atoms on a carbon nanotube. *Physical Review B*, 67:201401, 2003.

[38] Y. Yagi, T. M. Briere, M. H. F. Sluiter, V. Kumar, A. A. Farajian, and Y. Kawazoe. Stable geometries and magnetic properties of single-walled carbon nanotubes doped with 3d transition metals: A first principles study. *Physical Review B*, 69:075414, 2004.

[39] E. J. G. Santos, A. Ayuela, S. B. Fagan, J. Mendes Filho, D. L. Azevedo, A. G. Souza Filho, and D. Sánchez-Portal. Switching on magnetism in Ni-doped graphene. 2008, arXiv:0809.2901v1 [cond-mat.mes-hall].

[40] M. S. Ferreira and S. Sanvito. Contact-induced spin polarization in carbon nanotubes. *Physical Review B*, 69:035407, 2004.

[41] O. Céspedes, M. S. Ferreira, S. Sanvito, M. Kociak, and J. M. D. Coey. Contact induced magnetism in carbon nanotubes. *Journal of Physics: Condensed Matter*, 16:L155–L161, 2004.

[42] M. Weissmann, G. García, M. Kiwi, R. Ramírez, and C. C. Fu. Theoretical study of iron filled carbon nanotubes. *Physical Review B*, 73:125435, 2006.

[43] C. K. Yang, J. Zhao, and J. P. Lu. Magnetism of transition-metal/carbon-nanotube hybrid structures. *Physical Review Letters*, 90:257203, 2003.

[44] F. Banhart, N. Grobert, M. Terrones, J. C. Charlier, and P. M. Ajayan. Metal atoms in carbon nanotubes and related nanoparticles. *International Journal of Modern Physics B*, 15:4037–4069, 2001.

[45] Y. Ma, A. S. Foster, A. V. Krasheninnikov, and R. M. Nieminen. Nitrogen in graphite and carbon nanotubes: Magnetism and mobility. *Physical Review B*, 72:205416, 2005.

[46] P. O. Lehtinen, A. S. Foster, A. Ayuela, A. Krasheninnikov, K. Nordlund, and R. M. Nieminen. Magnetic properties and diffusion of adatoms on a graphene sheet. *Physical Review Letters*, 91:017202, 2003.

[47] G. Mpourmpakis, G. E. Froudakis, A. N. Andriotis, and M. Menon. Carbon-nanotube tips with edge made of a transition metal. *Applied Physics Letters*, 87:193105, 2005.

[48] P. Lloyd. Wave propagation through an assembly of spheres: II. the density of single-particle eigenstates. *Proceedings of the Physical Society*, 90:207–216, 1967.

[49] S. Datta. *Electronic Transport in Mesoscopic Systems*, pages 132–140. Cambridge University Press, First edition, 1995.

[50] M. C. Desjonquéres and D. Spanjaard. *Concepts in Surface Physics*, pages 464–467. Springer, second edition, 1996.

[51] A. Wall. *Theoretical studies of doped carbon nanotube based materials.* PhD thesis, School of Physics, Trinity College Dublin, 2008.

[52] C. G. Rocha, A. Wall, and M. S. Ferreira. Electronic properties of nanotube-based sensors: An inverse modeling approach. *Europhysics Letters*, 82:27004, 2008.

[53] M. S. Ferreira, G. E. W. Bauer, and C. P. A. Wapenaar. Recursive green functions technique applied to the propagation of elastic waves in layered media. *Ultrasonics*, 40:355–359, 2002.

[54] E. Kreyszig. *Advanced Engineering Mathematics*, pages 770–795. Wiley, 8th edition, 1999. Alternatively, consult any text on engineering mathematics.

[55] J. C. Charlier, T. W. Ebbesen, and Ph Lambin. Structural and electronic properties of pentagon-heptagon pair defects in carbon nanotubes. *Physical Review B*, 53:11108–11113, April 1996.

[56] K. Nakada, M. Fujita, G. Dresselhaus, and M. S. Dresselhaua. Edge state in graphene ribbons: Nanometer size effect and edge shape dependence. *Physical Review B*, 54:17954–17961, 1996.

[57] Y. Kobayashi, K. Fukui, T. Enoki, K. Kusakabe, and Y Kaburagi. Observation of zigzag and armchair edges of graphite using scanning tunneling microscopy and spectroscopy. *Physical Review B*, 71:193406, 2005.

[58] R. M. White. *Quantum theory of magnetism.* Springer, third edition, 2007.

[59] K. Yosida. *Theory of magnetism*, chapter 4. Springer, 1996.

[60] A. T. Costa, D. F. Kirwan, and M. S. Ferreira. Indirect exchange coupling between magnetic adatoms in carbon nanotubes. *Physical Review B*, 72:085402, 2005.

[61] A. T. Costa, C. G. Rocha, and M. S. Ferreira. Noncollinear coupling between magnetic adatoms in carbon nanotubes. *Physical Review B*, 76:085401, 2007.

[62] C. G. Rocha. private communication, 2007.

[63] J. P. Perdew, K. Burke, and M. Ernzerhof. Generalized gradient approximation made simple. *Physical Review Letters*, 77:3865 – 3868, 1996.

[64] D. F. Kirwan, C. G. Rocha, A. T. Costa, and M. S. Ferreira. Sudden decay of indirect exchange coupling between magnetic atoms on carbon nanotubes. *Physical Review B*, 77:085432, 2008.

[65] D. F. Kirwan, C. G. Rocha, A. T. Costa, and M. S. Ferreira. Suppression of long ranged coupling between magnetic atoms on carbon nanotubes. *Physica Status Solidi (b)*, 245:2169–2172, 2008.

[66] J. C. Charlier. Defects in carbon nanotubes. *Accounts of Chemical Research*, 35:1063–1069, 2002.

[67] L. Chico, L. X. Benedict, S. G. Louie, and M. L. Cohen. Quantum conductance in carbon nanotubes with defects. *Physical Review B*, 54:2600–2606, 1996.

[68] L. Chico, M. P. López Sancho, and M. C. Muñoz. Carbon nanotube based quantum dot. *Physical Review Letters*, 81:1278–1281, 1998.

[69] M. Terrones, F. Banhart, N. Grobert, J. C. Charlier, H. Terrones, and P. M. Ajayan. Molecular junctions by joining single-walled carbon nanotubes. *Physical Review Letters*, 89:075505, 2002.

[70] C. T. White and T. N. Todorov. Carbon nanotubes as long ballistic conductors. *Nature*, 393:240–242, 1998.

[71] M. P. Anantram and T. R. Govindan. Conductance of carbon nanotubes with disorder: A numerical study. *Physical Review B*, 58:4882–4887, 1998.

[72] S. Latil, S. Roche, D. Mayou, and J. C. Charlier. Mesoscopic transport in chemically doped carbon nanotubes. *Physical Review Letters*, 92:256805, 2004.

[73] Ch. Adessi, S. Roche, and X. Blase. Reduced backscattering in potassium-doped nanotubes: Ab initio and semiempirical simulations. *Physical Review B*, 73:125414, 2006.

[74] S. Latil, S. Roche, and J. C. Charlier. Electronic transport in carbon nanotubes with random coverage of physisorbed molecules. *Nano Letters*, 5:2216–2219, 2005.

[75] S. Krompiewski. Spin-polarised transport through carbon nanotubes. *Physica Status Solidi (b)*, 242:226–233, 2005.

[76] J. C. Charlier, X. Blase, and S. Roche. Electronic and transport properties of nanotubes. *Reviews of Modern Physics*, 79:677–732, 2007.

[77] H. J. Choi, J. Ihm, S. G. Louie, and M. L. Cohen. Defects, quasibound states and quantum conductance in metallic carbon nanotubes. *Physical Review Letters*, 84:2917–2920, 2000.

[78] A. R. Rocha, M. Rossi, A. Fazzio, and A. J. R. da Silva. Designing real nanotube-based gas sensors. *Physical Review Letters*, 100:176803, 2008.

[79] A. V. Krasheninnikov, K. Nordlund, M. Sirviö, E. Salonen, and J. Keinonen. Formation of ion-irradiation-induced atomic-scale defects on walls of carbon nanotubes. *Physical Review B*, 63:245405, 2001.

[80] R. Kubo. A general expression for the conductivity tensor. *Canadian Journal of Physics*, 34:1274–1277, 1956.

[81] P. A. Lee and D. S. Fisher. Anderson localization in two dimensions. *Physical Review Letters*, 47:882–885, 1981.

[82] J. Mathon, A. Umerski, and M. Villeret. Oscillations with Co and Cu thickness of the current–perpendicular–to–plane giant magnetoresistance of a Co/Cu/Co(001) trilayer. *Physical Review B*, 55:14378–14386, 1997.

[83] D. S. Fisher and P. A. Lee. Relation between conductivity and transmission matrix. *Physical Review B*, 23:6851–6854, 1981.

[84] S. Datta. *Electronic Transport in Mesoscopic Systems*, page 158. Cambridge University Press, First edition, 1995.

[85] M. E. J. Newman and G. T. Barkema. *Monte Carlo Methods in Statistical Physics*. Oxford University Press, 1999.

[86] F. J. Himpsel. Correlation between magnetic splitting and magnetic moment for 3d transition metals. *Journal of magnetism and magnetic materials*, 102:261–265, 1991.

[87] A. Akande and S. Sanvito. Exchange parameters from approximate self-interaction correction scheme. *The Journal of Chemical Physics*, 127:034112, 2007.

[88] M. Ushiro, K. Uno, T. Fujikawa, Y. Sato, K. Tohji, F. Watari, W. J. Chun, Y. Koike, and K. Asakura. X-ray absorption fine structure (XAFS) analyses of Ni species trapped in graphene sheet of carbon nanofibers. *Physical Review B*, 73:144103, 2006.

[89] V. M. de Menezes. private communication, 2009.

[90] C. Bittencourt, A. Felten, J. Ghijsen, J. J. Pireaux, W. Drube, R. Erni, and G. Van Tendeloo. Decorating carbon nanotubes with nickel nanoparticles. *Chemical Physics Letters*, 436:368–372, 2007.

[91] E. Merzbacher. *Quantum Mechanics*, page 41. John Wiley & Sons, third edition, 1998.